

RICE UNIVERSITY

**Chemistry of Nanostructured Carbon: I. Fluorination, Cutting and
Derivatization of Single-Wall Carbon Nanotubes; II. Fluorination and
Characterization of Polymeric C₆₀**

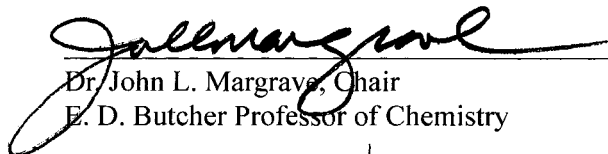
by

Zhenning Gu

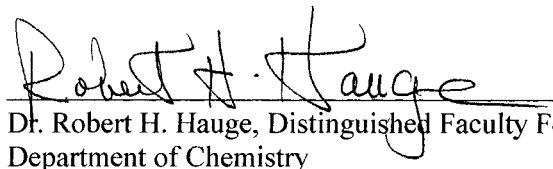
A THESIS SUBMITTED
IN PARTIAL FULFILLMENT OF THE
REQUIREMENTS FOR THE DEGREE

Doctor of Philosophy

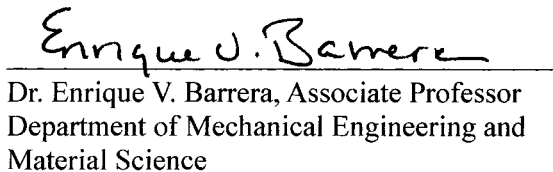
APPROVED, THESIS COMMITTEE:



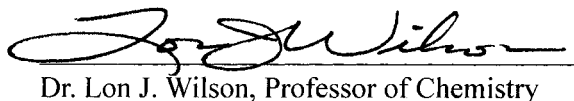
Dr. John L. Margrave, Chair
E. D. Butcher Professor of Chemistry



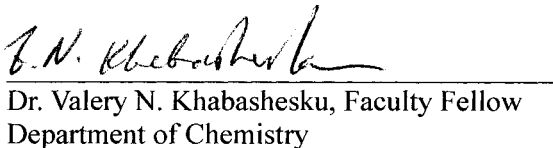
Dr. Robert H. Hauge, Distinguished Faculty Fellow
Department of Chemistry



Dr. Enrique V. Barrera, Associate Professor
Department of Mechanical Engineering and
Material Science



Dr. Lon J. Wilson, Professor of Chemistry



Dr. Valery N. Khabashesku, Faculty Fellow
Department of Chemistry

HOUSTON, TEXAS

MAY 2003

UMI Number: 3090153



UMI Microform 3090153

Copyright 2003 by ProQuest Information and Learning Company.

All rights reserved. This microform edition is protected against
unauthorized copying under Title 17, United States Code.

ProQuest Information and Learning Company
300 North Zeeb Road
P.O. Box 1346
Ann Arbor, MI 48106-1346

ABTRACT

Chemistry of Nanostructured Carbon: I. Fluorination, Cutting, and Derivatization of Single-Wall Carbon Nanotubes; II. Fluorination and Characterization of Polymeric C₆₀.

by

Zhenning Gu

Purified HiPco SWNTs have been fluorinated with elemental fluorine under various conditions to control the stoichiometry of the resultant Fluorotubes. The partially fluorinated SWNTs with stoichiometry CF_x ($x \leq 0.3$), which were originally microns in length and extensively bundled, when pyrolyzed in an argon atmosphere to high temperatures ($> 800\text{ }^{\circ}\text{C}$) are cut into short pieces (mostly $< 50\text{ nm}$). The “cut” nanotubes have been characterized with Raman, ATR-IR, EDAX and AFM. The reactivities of the “cut” SWNTs have been explored through re-fluorination, acidification (reflux in dilute nitric acid) and hexylation (with hexyl lithium).

The reactions of ozone with SWNTs on both gas-solid interface and on gas-solution interface have been studied. Ozone was found to oxidize the nanotube on both ends and sidewall forming functional groups such as epoxy groups and carboxylic acid groups. Intermittent ozone treatment of individually dispersed SWNTs in aqueous surfactant solution was found to effectively “cut” the nanotubes into short pieces. The effects of pH, surfactant types, and other factors on the reactions were investigated in situ with Raman and UV-vis.-NIR spectroscopy. In an acidic environment, the reactions can develop to

such an extent that the nanotubes were gradually “etched” away as CO₂.

The process of using diluted gaseous HCl to treat the softly oxidized HiPco SWNT raw materials at high temperature to remove the metal impurities (especially carbon shell encapsulated Fe nanoparticles) has been studied by EDAX, Raman, UV-vis-NIR and ESEM. Refluxing of pristine HiPco SWNTs in dilute HNO₃ (1-2 M) was found to remove most of the Fe catalyst from the SWNTs with less loss of SWNT mass and, as well, can add carbonyl, carboxylic, and hydroxyl group to the ends and sidewall of carbon nanotubes. The process and the products have been studied with TGA, ATR-IR, microscopic Raman, and TGA/MS. The solubility of the treated SWNTs in alcohol solvents such as ethanol was found greatly improved. The pristine HiPco SWNTs have been fluorinated and/or hexylated and the products suspended in organic solvents such as THF or chloroform to extract derivatized giant fullerene species formed as byproduct in the HiPco process. The hexylated giant fullerenes were also pyrolyzed in argon atmosphere to study the chemical desorption of the hexyl- functionalities. Such recovered pristine giant fullerenes were also studied with IR, Raman spectroscopy and were compared with SWNTs.

The transformation of SWNTs under high pressure and high temperature (HPHT) treatment was studied by characterizing the treated SWNTs samples with Raman and X-ray diffraction (XRD). The characterization provided evidence for covalent interlinking between SWNTs through sp^3 C – C bond formation under HPHT treatment. The “depolymerization” of the interlinked SWNTs with ultrasonication was also studied.

The fluorination of the 1D and 2D structures of polycrystalline polymeric C₆₀ synthesized from the fullerene monomer (C₆₀) under high temperature-high pressure (HPHT) conditions has been studied. The fluorinated C₆₀ polymers have been characterized with IR, Raman, XRD, VTP-MS, SEM, and EDAX to determine their structures and stoichiometries. The polymeric C₆₀ and their fluorinated derivatives were dissolved/suspended in organic solvents and the UV absorption spectra of thus formed solutions/suspensions were studied.

Acknowledgement

At this special moment, when I am ready to summarize my research work during the past four year, I'd like to express my acknowledgement to those people who have been indispensable for the completion of my Ph.D.. The first one I need give my gratitude to is my advisor, Dr. Margrave. I can still clearly remember the first time I talked with Dr. Margrave, and the deep impression I had about the amiable, knowledgeable professor. The enthusiasm Dr. Margrave has about chemistry and his infinite curiosity about the unknown have been inspiring to me during my study. Also his encouragement and recognition of my work are important propellants for my progress. Dr. Hauge is my advisor in practical work. He knew all the details about my research projects with single-wall carbon nanotubes, and gave me very useful and instructive suggestions. I've learned a lot from Dr. Hauge through his guidance and help on my research, both theoretically and experimentally. Dr. Khabashesku has guided me in several of my research projects. I really enjoy working with him and discussing the chemistry of nanoscale carbon materials. I thank Dr. Wilson and Dr. Barrera for being my thesis committee member and for their concerns about my research progress. My thanks also to Dr. Smalley and CNL members for their help. Collaboration with the Smalley research group has been important for my research. I'd like to thank all the members in our research group. Dr. Zimmerman and Dr. Chiang gave me great help with the start-up of my research. Haiqing Peng has been a great partner to work along with. Yu Liu and Lei Zhang has also helped me with my research work. There are many other people in

Chemistry Department and at Rice to whom I would give my thanks. Their help has been important for the completion of my graduate study here.

I give my most soulful gratitude to my husband, Zhiwei. He is always my strong backbone and my constant encourager. His love and support have lightened my way forwards. He has shared every moment of success and frustration during my graduate study. I couldn't have been where I am now without his great care and permanent patience. Also, I am very lucky to have had my parents-in-law to be with us during the past six months. Their taking care of all the details in our life allowed me to concentrate on my thesis writing. Finally, I'd like to thank my family in China. Their love has supported my life and study here in the United States.

Table of Contents

Abstracts	
Acknowledgements	v
List of Figures and Tables	xi
 Chapter 1 - Introduction to the nanostructured carbon materials	 1
1.1 Single-Wall Carbon Nanotubes (SWNTs)	2
1.2 Giant Fullerenes	3
1.3 Phase Transition of SWNTs under High Temperature – High Pressure (HPHT) treatment	4
1.4 Crystalline Polymerized Phases (CPP's) of C ₆₀	6
 Chapter 2 - Fluorination and Pyrolysis Cutting of Single-Wall Carbon Nanotubes	 12
2.1 Controlled Fluorination of HiPco Single-Wall Carbon Nanotubes	12
2.1.1 Introduction	12
2.1.2 Experimental	14
2.1.3 Results and Discussions	16
2.1.4 Conclusion	33
2.2 Pyrolysis Cutting of the partially fluorinated Single-Wall Carbon Nanotubes	36
2.2.1 Introduction	36
2.2.2 Experimental	38
2.2.3 Results and Discussions	39

2.2.4 Conclusion	55
2.3 Derivatization of the Cut Single-Wall Carbon Nanotubes	56
2.3.1 Introduction	56
2.3.2 Experimental	57
2.3.3 Results and Discussions	60
2.3.4 Conclusion	67
Chapter 3 - Ozonolysis of Single-Wall Carbon Nanotubes	71
3.1 Introduction	71
3.2 Ozonolysis of Purified Single-Wall Carbon Nanotubes at the Gas-Solid Interface	77
3.2.1 Experimental	77
3.2.2 Results and Discussions	78
3.2.3 Conclusion	87
3.3 Intermittent ozonolysis of Individually Dispersed Single-Wall Carbon Nanotubes at the Gas-Aqueous Solution Interface: Cutting Effects	87
3.3.1 Experimental	87
3.3.2 Results and Discussions	90
3.3.3 Conclusion	102
3.4 Spectroscopic Studies of Continuous Ozonolysis of Individually Dispersed Single-Wall Carbon Nanotubes	102
3.4.1 Experimental	102
3.4.2 Results and Discussions	103

3.4.2.1 Spectral Analysis	103
3.4.2.2 Non-buffered System	108
3.4.2.3 Buffered System	122
3.4.2.4 Purified-SWNTs system	134
3.4.2.5 pH Effect in SWNTs/Pluronic-108 System	138
3.4.2.6 Influence of Surfactants	141
3.4.3 Conclusion	142
3.4.4 Future Work	146
 Chapter 4 - Other Studies of HiPco Single-Wall Carbon Nanotubes	 147
4.1 High Temperature Gaseous HCl Process	147
4.1.1 Introduction	147
4.1.2 Experimental	148
4.1.3 Results and Discussions	148
4.1.4 Conclusion	153
4.2 Dilute HNO ₃ Refluxing Process	153
4.2.1 Introduction	153
4.2.2 Experimental	155
4.2.3 Results and Discussions	156
4.2.4 Conclusion	165
4.3 Extraction and Characterization of Giant Fullerene Species from HiPco process	 165
4.3.1 Introduction	165

4.3.2	Experimental	167
4.3.3	Results and Discussions	167
4.3.4	Conclusion	174
Chapter 5 - Characterization of the High Pressure – High Temperature Treated (HPHTT) Single-Wall Carbon Nanotubes		175
5.1	Introduction	175
5.2	Experimental	175
5.3	Results and Discussions	176
5.4	Conclusion	188
Chapter 6 - Fluorination and Characterization of Polymeric C ₆₀		189
6.1	Introduction	189
6.2	Experimental	190
6.3	Results and Discussions	191
6.4	Conclusion	220
References		224

List of Figures and Tables

Figure 1-1	Molecular structure models of some giant fullerenes	7
Figure 1-2	A perspective view of polymerized structure fragments of SWNTs	8
Figure 1-3	Phase diagram of C ₆₀ in the intermediate pressure range	9
Figure 1-4	Schematic structures of crystalline polymeric phases of C ₆₀	10
Figure 1-5	Overview of intermediate-pressure polymeric phases of C ₆₀ and their relationship to the fcc C ₆₀ structure.	11
Figure 2-1	Schematic diagram of the fluorination apparatus	19
Figure 2-2	SEM images of laser-oven grown SWNTs and HiPco SWNTs	20
Figure 2-3	SEM images of purified HiPco SWNTs before and after various extents of fluorinations.	21
Table 2-1	Atomic F/C ratio of HiPco SWNTs fluorinated at various temperatures	22
Figure 2-4	ATR-IR spectra of SWNTs fluorinated at various temperatures	23
Figure 2-5	Raman spectra of fluorinated SWNTs with various stoichiometry	26
Figure 2-6	ATR-IR spectra of SWNTs fluorinated at 100 °C for various hours	29
Figure 2-7	ATR-IR spectra of SWNTs fluorinated at 150 °C for various hours	30
Table 2-2	Influence of fluorination conditions on the stoichiometry of the fluorinated HiPco SWNTs	32
Figure 2-8	UV-vis.-NIR spectra of SWNTs before and after partial fluorination	34
Figure 2-9	TGA of <i>F-SWNTs</i> (C ₅ F) pyrolyzed in argon up to 1000 °C	41
Figure 2-10	In-situ IR spectra of the gaseous species released from the <i>F-SWNTs</i> during pyrolysis	42

Figure 2-11	Correlation of the TGA time derivative weight loss curve and the chemigrams during pyrolysis	43
Figure 2-12	TGA-MS plot of the volatile species from <i>F-SWNTs</i> during pyrolysis	44
Figure 2-13	Raman spectra of the SWNTs with partial fluorination and pyrolysis	46
Figure 2-14	ATR-IR spectra of the <i>F-SWNTs</i> before and after pyrolysis	47
Figure 2-15	AFM image of the <i>F-SWNTs</i>	48
Figure 2-16	AFM image of the <i>cut-SWNTs</i> – I	49
Figure 2-17	AFM image of the <i>cut-SWNTs</i> – II	50
Figure 2-18	AFM image of the <i>cut-SWNTs</i> – III	51
Figure 2-19	AFM image of the <i>cut-SWNTs</i> – IV	52
Figure 2-20	Histograms of length and bundle size distribution of the <i>cut-SWNTs</i>	54
Figure 2-21	Reactions to functionalize cut-SWNTs	58
Figure 2-22	TGA of <i>cut-SWNTs</i> vs. purified SWNTs heated in air up to 800 °C	59
Figure 2-23	Raman spectra of cut-SWNTs with brief oxidation up to 500 °C	62
Figure 2-24	ATR-IR spectra of cut-SWNTs with re-fluorination	64
Figure 2-25	Raman spectra of cut-SWNTs with re-fluorination	65
Figure 2-26	ATR-IR spectra of cut-SWNTs with HNO ₃ treatment	66
Figure 2-27	Raman spectra of cut-SWNTs with HNO ₃ treatment	68
Figure 2-28	ATR-IR spectrum of the hexylated cut-SWNTs	69
Figure 2-29	Raman spectra of cut-SWNTs with hexylation	69
Figure 3-1	Species formed in C ₆₀ ozonation reaction	75

Figure 3-2	Schematic demonstration of ozonation of SWNTs and subsequent cleavage of the sidewall ozonide with secondary reagents	76
Figure 3-3	TGA of SWNT bucky-paper during ozone exposure	79
Figure 3-4	ATR-IR spectra of SWNT bucky-paper with ozone exposure	80
Figure 3-5	Raman spectra of SWNT bucky-paper with ozone exposure	82
Figure 3-6	TGA of ozone treated SWNT bucky-paper annealed in argon up to 800 °C	84
Figure 3-7	ATR-IR spectra of SWNT bucky-paper with annealing	85
Figure 3-8	Raman spectra of SWNT bucky-paper with annealing	86
Table 3-1	Experimental conditions in the intermittent ozone reactions with <i>SWNTs/SDS</i>	89
Figure 3-9	Raman spectra of SWNTs/SDS suspension at each stage of the intermittent ozone treatment	93
Figure 3-10	UV-vis.-NIR spectra of SWNTs/SDS suspension with intermittent ozone treatment	94
Figure 3-11	AFM image of individually dispersed SWNTs	97
Figure 3-12	AFM image of individually dispersed SWNTs after intermittent ozone treatment – I	98
Figure 3-13	AFM image of individually dispersed SWNTs after intermittent ozone treatment – II	99
Figure 3-14	AFM image of individually dispersed SWNTs after intermittent ozone treatment – III	100
Figure 3-15	Histograms of length and bundle size distribution of individually dispersed SWNTs after intermittent ozone treatment	101
Figure 3-16	Schematic demonstration of the experiment set-up for in-situ spectroscopic monitoring the ozone reaction with individually dispersed SWNTs	105

Figure 3-17	Peak identities in Raman and fluorescence spectra of individually dispersed SWNTs	106
Figure 3-18	UV-vis.-NIR spectra of individually dispersed SWNTs (unbuffered) with 2-hour ozone treatment	107
Figure 3-19	Breakdown of the Raman spectra of SWNTs/SDS (unbuffered) during the first hour ozone treatment	111
Figure 3-20	Raman spectra of SWNTs/SDS (unbuffered) with 5.5-hour ozone treatment	112
Figure 3-21	Breakdown of the UV-vis.-NIR spectra of SWNTs/SDS (unbuffered) During the first 2 hours of ozone treatment	113
Figure 3-22	UV-vis.-NIR spectra of SWNTs/SDS (unbuffered) with 5.5-hour ozone treatment	114
Figure 3-23	Raman intensity trendline during a 2-hour continuous ozone treatment of SWNTs/SDS (unbuffered)	116-118
Figure 3-24	Raman spectra of SWNTs/SDS (unbuffered) with 2-hour ozone treatment	119
Figure 3-25	AFM images of SWNTs/SDS (unbuffered) with 80-minutes ozone treatment	121
Figure 3-26	Raman intensity trendline during a 2-hour continuous ozone treatment of SWNTs/SDS (buffered)	123-126
Figure 3-27	Raman spectra of SWNTs/SDS (buffered) with 2-hour ozone treatment	128
Figure 3-28	AFM images of SWNTs/SDS (buffered) with 2-hour ozone treatment	129
Figure 3-29	Raman spectra of SWNTs/SDS (buffered) with 215-minute ozone treatment	131
Figure 3-30	Raman intensity trendline of SWNTs/SDS (buffered) with 215-minute ozone treatment	132-133
Figure 3-31	Raman spectra of purified SWNTs/SDS (unbuffered) with 2-hour ozone treatment	135

Figure 3-32	Comparison of Raman intensity trendlines of as-prepared and purified SWNTs/SDS with ozone treatment	136-137
Figure 3-33	The pH effect on Raman intensity of SWNTs/Pluronic-108 with ozone treatment	139-140
Figure 3-34	The effect of surfactants on Raman intensity of SWNTs/Surfactant with ozone treatment	143-144
Figure 3-35	Raman spectra of SWNTs/DTAB (buffered) with 25-minute ozone treatment	145
Figure 4-1	SEM image of gaseous HCl purified HiPco SWNTs	150
Figure 4-2	Raman spectrum of gaseous HCl purified HiPco SWNTs	151
Figure 4-3	UV-vis.-NIR spectrum of gaseous HCl purified HiPco SWNTs	152
Figure 4-4	TGA of gaseous HCl purified HiPco SWNTs heated in air up to 800 °C	154
Figure 4-5	ATR-IR spectra of HNO ₃ treated as-prepared HiPco SWNTs	157
Figure 4-6	Raman spectra of as-prepared HiPco SWNTs with HNO ₃ treatment	158
Figure 4-7	TGA of HNO ₃ treated as-prepared HiPco SWNTs heated in air up to 780 °C	160
Figure 4-8	TGA-MS plot of HNO ₃ treated as-prepared HiPco SWNTs heated in air up to 780 °C	161
Figure 4-9	Raman spectra of HNO ₃ treated as-prepared HiPco SWNTs with annealing in argon up to 600 °C	163
Figure 4-10	UV-vis.-NIR spectra of HNO ₃ treated as-prepared HiPco SWNTs with annealing in argon up to 600 °C	164
Figure 4-11	Raman spectra of as-prepared HiPco SWNTs samples at various stages of giant fullerene extraction	168
Figure 4-12	TGA of hexylated giant fullerenes annealed up to 800 °C	171
Figure 4-13	ATR-IR spectra of hexylated giant fullerenes with annealing	172

Figure 4-14	Raman spectrum of hexylated giant fullerenes after annealing	173
Figure 5-1	Raman spectra of SWNTs treated under 1.5 GPa at various temperatures	177
Figure 5-2	XRD patterns of SWNTs treated under 1.5 GPa at various temperatures	179
Figure 5-3	SEM images of SWNTs treated under 1.5 GPa at various temperatures	180
Figure 5-4	Raman spectra of the HPHTT treated SWNTs with 2-hour ultrasonication	182
Figure 5-5	SEM images of the HPHTT treated SWNTs with 2-hour ultrasonication	183
Figure 5-6	AFM images of HPHTT treated SWNTs with 2-hour ultrasonication	184
Figure 5-7	XRD patterns of SWNTs treated under 8 GPa at various temperatures	186
Figure 5-8	XRD patterns of SWNTs treated under 9.5 GPa at 400 and 600 °C	187
Table 6-1	Atomic F/C ratio of C ₆₀ polymers fluorinated at various temperatures	193
Figure 6-1	SEM images of the T phase polymeric C ₆₀ with fluorination	195
Figure 6-2	SEM images of the R phase polymeric C ₆₀ with fluorination	196
Figure 6-3	IR spectra of O phase polymer with fluorination	200
Figure 6-4	IR spectra of T phase polymer with fluorination	203
Figure 6-5	IR spectra of R phase polymer with fluorination	205
Figure 6-6	XRD patterns of O phase polymer with fluorination	208
Figure 6-7	XRD patterns of T phase polymer with fluorination	210
Figure 6-8	XRD patterns of R phase polymer with fluorination	211

Figure 6-9	UV spectra of C ₆₀ - <i>n</i> -hexane solution	213
Figure 6-10	UV spectra of C ₆₀ -ODCB and of polymeric C ₆₀ S- <i>n</i> -hexane	215
Figure 6-11	UV spectra of fluorinated C ₆₀ and polymeric C ₆₀ S in <i>n</i> -hexane	216
Figure 6-12	UV spectra of R phase C ₆₀ polymer with various fluorination extents (in <i>n</i> -hexane)	217
Figure 6-13	UV spectra of fluorinated R phase C ₆₀ polymer in various solvents	219
Table 6-2	Thermal decomposition temperatures of C60 polymers and their fluorinated derivatives	221
Figure 6-14	VTP-MS of fluorinated R phase C ₆₀ polymer at 600 °C	222

Chapter 1

INTRODUCTION TO THE NANOSTRUCTURED CARBON MATERIALS

As the third elemental form of carbon, fullerene species have attracted enormous research interests since the discovery and characterization of C_{60} (Buckminsterfullerene) in 1985¹. The large closed-shell carbon structures^{2,3}, which have ball-shape structures⁴ and are nonvolatile even at high temperatures up to 800 °C in inert atmosphere⁵, so called giant fullerenes, are a direct extension of the fullerene family. The number of the family members kept increasing with the joining of tubular fullerenes (i.e. carbon nanotubes)^{6,7} and nested concentric fullerenes^{8,9}. The phase transitions of C_{60} ¹⁰⁻¹² and carbon nanotubes^{13,14} under high pressure – high temperature (HPHT) treatment have created new classes of materials: the crystalline polymeric phases (CPP's) of C_{60} and the covalently interlinked carbon nanotubes. These materials further enriched the species of fullerenes. The unique nanostructures of the fullerene species together with the graphene building block provide them with specific properties that arouse great research interest. Development of nanotechnology has enabled the research on properties of materials on a much smaller scale than it did several decades ago. The researches on the nanoscale are leading to the understanding and control over the fundamental building blocks of all physical things that are designed and made. This thesis concerns the characterization and chemistry of several different types of the nanostructured fullerene materials mentioned above. The following is a brief introduction to each of those areas.

1.1 SINGLE-WALL CARBON NANOTUBES (SWNTS)

The structure of single-wall carbon nanotubes (SWNTs) can be conceptually considered as a seamless hollow cylinder that is rolled up from a planar hexagonal network of carbon atoms. The length of the cylinder can be tens of microns, and the diameter can be as small as several angstroms. With walls only one atom in thickness, SWNTs possess distinctive electronic^{15,16} and mechanical properties¹⁷. Part of these are believed to originate from the graphene building blocks, while the other is related to their one-dimensional (1D) aspects. For example, carbon nanotubes possess in-plane properties of graphite such as high conductivity, excellent strength and stiffness, chemical specificity, and inertness¹⁸. Another characteristic parameter of SWNTs that determines their properties is the chiral angle θ ¹⁹, which correlates the direction of the tubular axis along which the graphene sheet are wrapped up in forming the tubular structure and the alignment direction of the hexagons on the graphene network. Three categories of SWNTs are defined according to their chiral angles: the armchair SWNTs with $\theta = 30^\circ$, the zigzag SWNTs with $\theta = 0^\circ$ and the helical SWNTs with $0^\circ < \theta < 30^\circ$. It was predicted by theoretical work¹⁹ and has been proved by the experimental observations^{20,21} that the electronic properties of the carbon nanotubes depend on their diameters and chiral angles. For the small diameter SWNTs, calculations have predicted that all the armchair tubes are metallic whereas the zigzag and helical tubes are either metallic or semiconducting. As for the large diameter SWNTs, the band gap between their valence and conduction bands tends to zero, which yields the zero-gap semiconductor electronically equivalent to the graphite¹⁸. In addition, the unique nanostructure of the SWNTs offer them a large surface area which is very important for

their applications as chemical probes and sensors. Also, the large volume of hollow channels in the SWNTs makes their density very low compared to graphite. The combination of the excellent mechanical strength and low density makes them an ideal option for material applications.

During last decade since the discovery of SWNTs⁷, there have been intense multidisciplinary researches on their growth mechanism²²⁻²⁴, their unique electronic structures²⁵⁻²⁷, their exceptional physical²⁸⁻³⁰ and chemical properties³¹⁻³⁴, and their potential applications³⁵ based on their remarkable properties. Among the experimentally realized applications are high-resolution nanoscale imaging probes^{36,37}, electron emission devices³⁸, reinforced composite materials³⁹, chemical sensors^{40,41}, nanostructured templates^{42,43}.

1.2 GIANT FULLERENES

Giant fullerenes are defined as the homologous series of hollow, closed-caged, molecules composed of elemental carbon only and with molecular weight larger than common fullerenes species such as C₆₀, C₇₀, C₇₆, etc. Structural models of some giant fullerene molecules are shown in Figure 1-1¹⁹. Large fullerenes such as C₈₄, C₉₄ etc. were theoretically predicted shortly after the discovery of C₆₀⁴⁴. Their stability was proposed to be dependent on a confluence of structure/strain and electronic orbital-filling considerations. In the early experimental observation of higher fullerenes², the characteristic pattern of C₂ losses seen in all mass spectra, in particular in the fast atom bombardment (FAB) spectra, of the higher all-carbon molecules was considered as strong evidence for their fullerene character. Scanning tunneling microscope (STM) work⁴

published shortly after indicated that the large carbon fullerenes with ball-shaped geometry had diameter up to ~ 2 nm, which corresponds to the molecule C_{330} . It was found that for structures having fewer numbers of carbon atoms smaller closed molecules are more stable than the planar graphite structure, because spherical shells have no dangling bonds^{45,46}. Under strong irradiation conditions or at high temperatures the spherical shells are also favored over tubular structures for small numbers of carbon atoms⁸. The proposed carbon nucleation scheme⁴⁷ suggests that giant fullerenes such as C_{240} and C_{540} could exist in pentagonal and hexagonal shapes, respectively. Other calculations predicted⁴⁸ that when $I_h - C_{240}$ is viewed from C_2 and C_3 symmetric axes, facet structures are seen, whereas when it is viewed along the C_5 axis, it is spherical. Giant fullerenes are closely related to other fullerene species. Especially, they might be important intermediates in carbon nanotube growth. The research on giant fullerenes could provide valuable information towards the understanding of carbon fullerenes and carbon nanotubes.

1.3 HPHT SWNTS

Phase transitions of elemental carbon materials from sp^2 hybridization states into sp^3 hybridization states under high pressure-high temperature (HPHT) conditions have been proved to be the essential mechanistic steps to form high-density superhard phases^{14,49,50}. The transformations from graphite to diamond and from *h*-BN to *c*-BN are classic examples. The special tubular structure of SWNTs means that the π -bonding geometry between the skeleton carbon atoms is distorted, i.e. the originally planar sp^2 configuration involves partially pyramidal character in SWNTs. This activation of the stable sp^2

configuration offers large number of reactive sites along the nanotube sidewall. It suggests that the configuration conversion of carbon atoms in SWNTs from sp^2 to sp^3 could occur at milder pressure and temperature conditions. This type of conversion has been found to occur by forming covalent bonding between nanotubes within bundles, which results in the polymerization of SWNTs by cross-linking. Polymerization of SWNTs has been theoretically studied^{51,52} following the 2 + 2 cycloaddition reaction mechanism proposed for the polymerization of crystalline C₆₀. Figure 1-2 shows the theoretically predicted perspective view of the polymerized structure (PS) fragments of a (10, 10) carbon nanotubes (at the top) and of a (6, 6) carbon nanotubes (at the bottom). HPHT polymerized SWNTs represent a series of intermediate states formed during the pressure-induced phase transition of elemental carbon from the metastable states (nanotubes) to the equilibrium states (graphite and diamond). The covalently cross-linked SWNTs could be good candidates for carbon nanofibers and nanocomposites because their mechanical properties should exceed the van der Waals force held nanotube ropes.

Recent studies of SWNTs under high pressure treatment have shown that the inter-nanotube distance varies with circumstance pressure⁵³⁻⁵⁷. However, the in situ Raman⁵⁸ and X-ray diffraction^{56,57} investigations of hydrostatic pressure (up to 13 GPa and 25.9 GPa) treatment of SWNTs at ambient temperature indicated that there was no inter-nanotube covalent cross-linking occurred. The nanotubes under the above treatment were always observed to recover from the pressure induced distortion on pressure release. The observation confirmed the theoretically predicted remarkable mechanical resilience of SWNTs.

1.4 CRYSTALLINE POLYMERIC PHASES (CPP) OF C₆₀

Polymeric C₆₀ is a new class of fullerene compounds that created by solid-state polymerization of C₆₀ monomers under high pressure-high temperature treatment (HPHTT) ¹⁰⁻¹². Depending on the temperature and pressure conditions of the process, chain-like one-dimensional (1D) phase and layered 2D phases of polycrystalline polymers were obtained ^{59,60}. Under even higher pressure (up to 13 GPa), 3D phase polymerized C₆₀ can be created ⁶¹. Figure 1-3 is an tentative phase diagram of C₆₀ according to the HPHT studies ⁶². The crystalline structures of various polymeric C₆₀ phases have been determined by combinative work from theoretical modeling of molecular packing patterns ⁶³ and from experimental X ray diffraction patterns ⁶⁴. The molecular packing structure of the 1D phase of the polymeric C₆₀ is described as orthorhombic (O-phase). Two different 2D phases are described as tetragonal (T-phase) and rhombohedral (R-phase), respectively (see Figure 1-4). The relation between the crystalline structures of fcc C₆₀ and O, T, R-phase polymers is shown in Figure 1-5 ⁶⁵. The vibrational ^{64,66,67}, electrical ⁶⁸ and magnetic ⁶⁹ properties of these polymeric C₆₀ species have been extensively studied since the successful preparation of pure single-phase samples. Some of these crystalline polymeric C₆₀ have demonstrated interesting mechanical ⁷⁰ and magnetic properties ⁶⁹. The 3D phase of polymeric C₆₀ that was synthesized at extremely high pressure has been found to be superhard, with hardness and bulk modulus exceeding those of diamond according to experimental and theoretical investigations ^{71,72}.

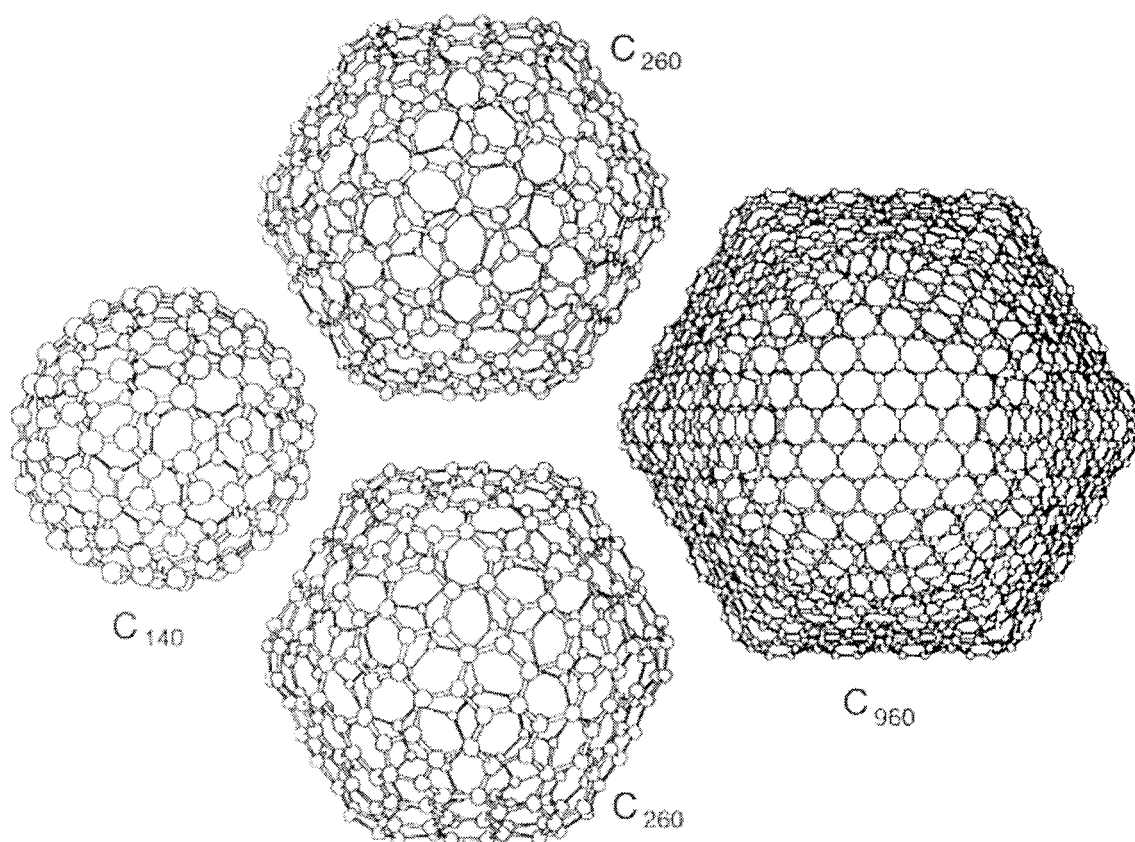


Figure 1-1 Molecular structure models of some giant fullerenes. (adapted from Dresselhaus, M. S.; Dresselhaus, G. and Eklund, P. C. *Science of Fullerenes and Carbon Nanotubes*; Academic: San Diego, 1996.)

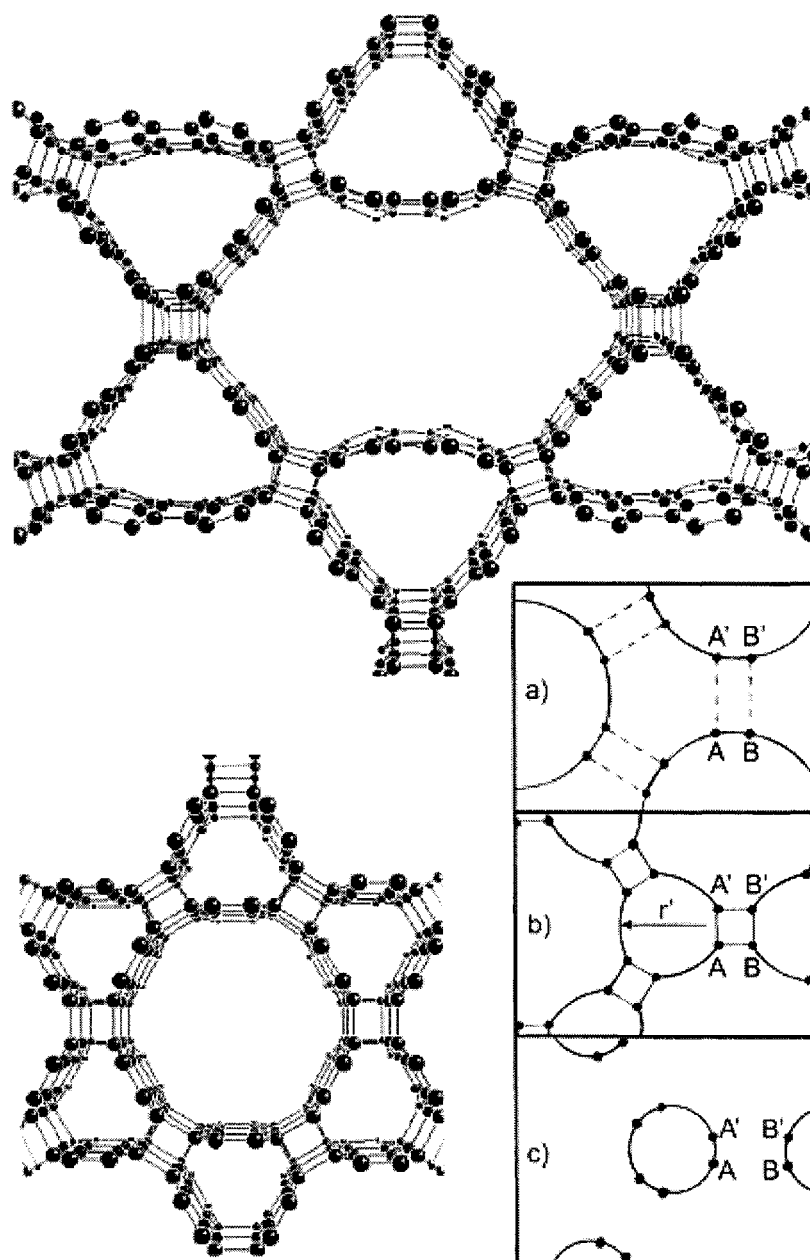


Figure 1-2 A perspective view of PS fragments of (10, 10) carbon nanotubes (at the top) and of (6, 6) carbon nanotubes (at the bottom). (adapted from Chernozatonskii, L. A. *Chem. Phys. Lett.* **1998**, 297, 257.)

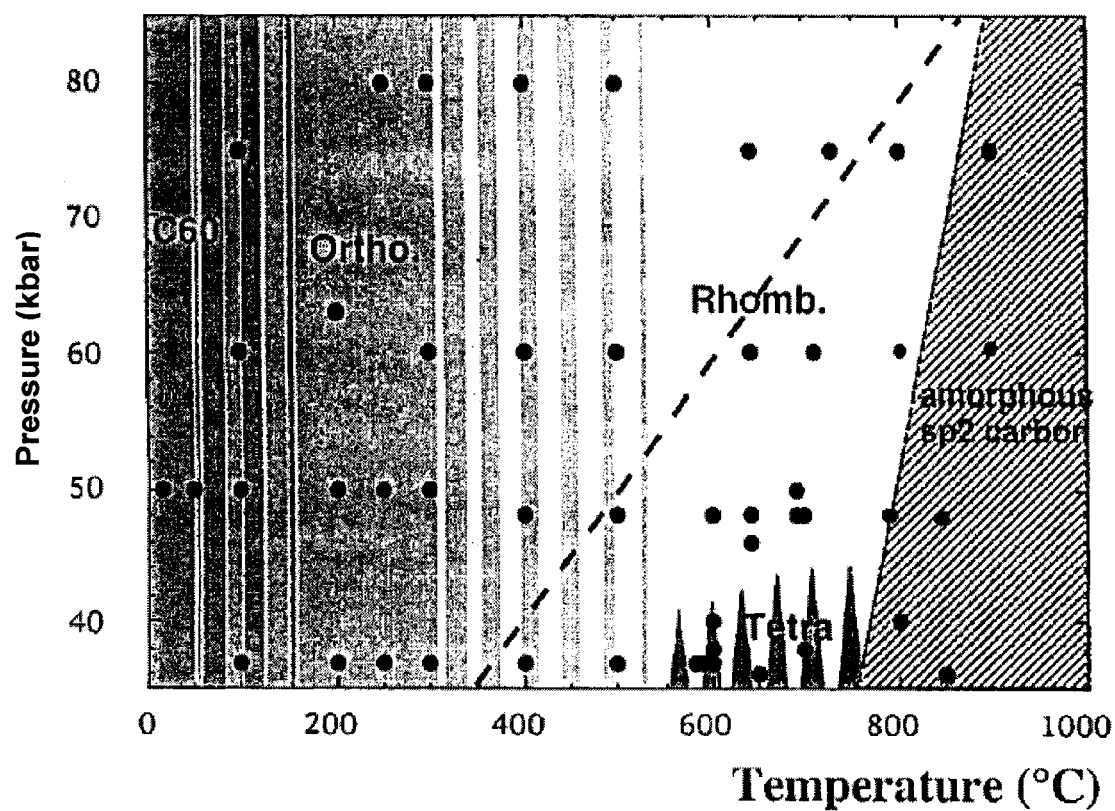


Figure 1-3 Phase diagram of C₆₀ in the intermediate pressure range. (adapted from Marques, L. et al *Phys. Rev. B* **1996**, 54, R12633.)

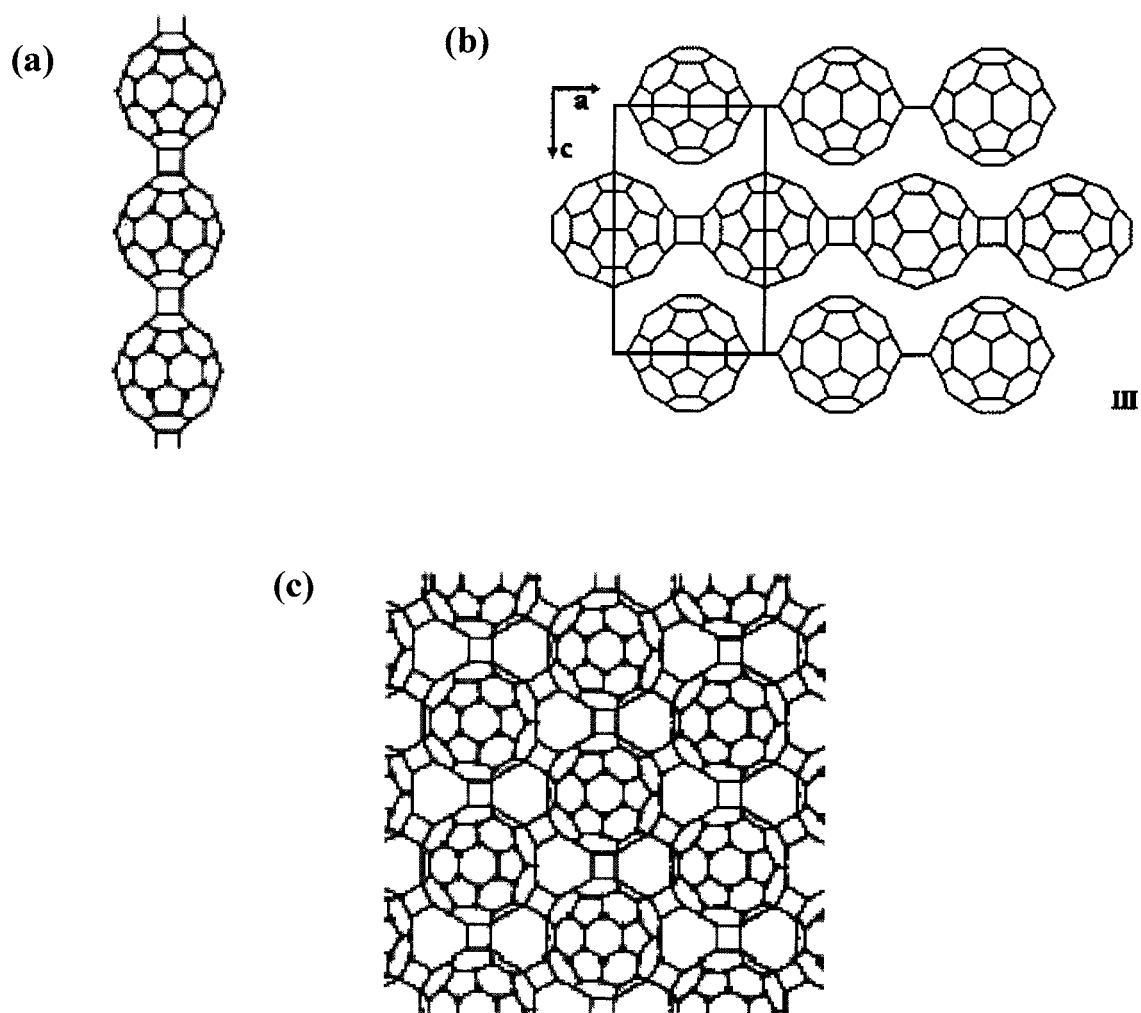


Figure 1-4 Schematic bonding structures of crystalline polymeric phases of C₆₀. (a) O phase; (b) T phase; (c) R phase. (adapted from Long, V. C. et al *Phys. Rev. B* **2000**, *61*, 13191; V. A. Davydov, et al *J. Phys. Chem. B* **1999**, *103*, 1800-1804.)

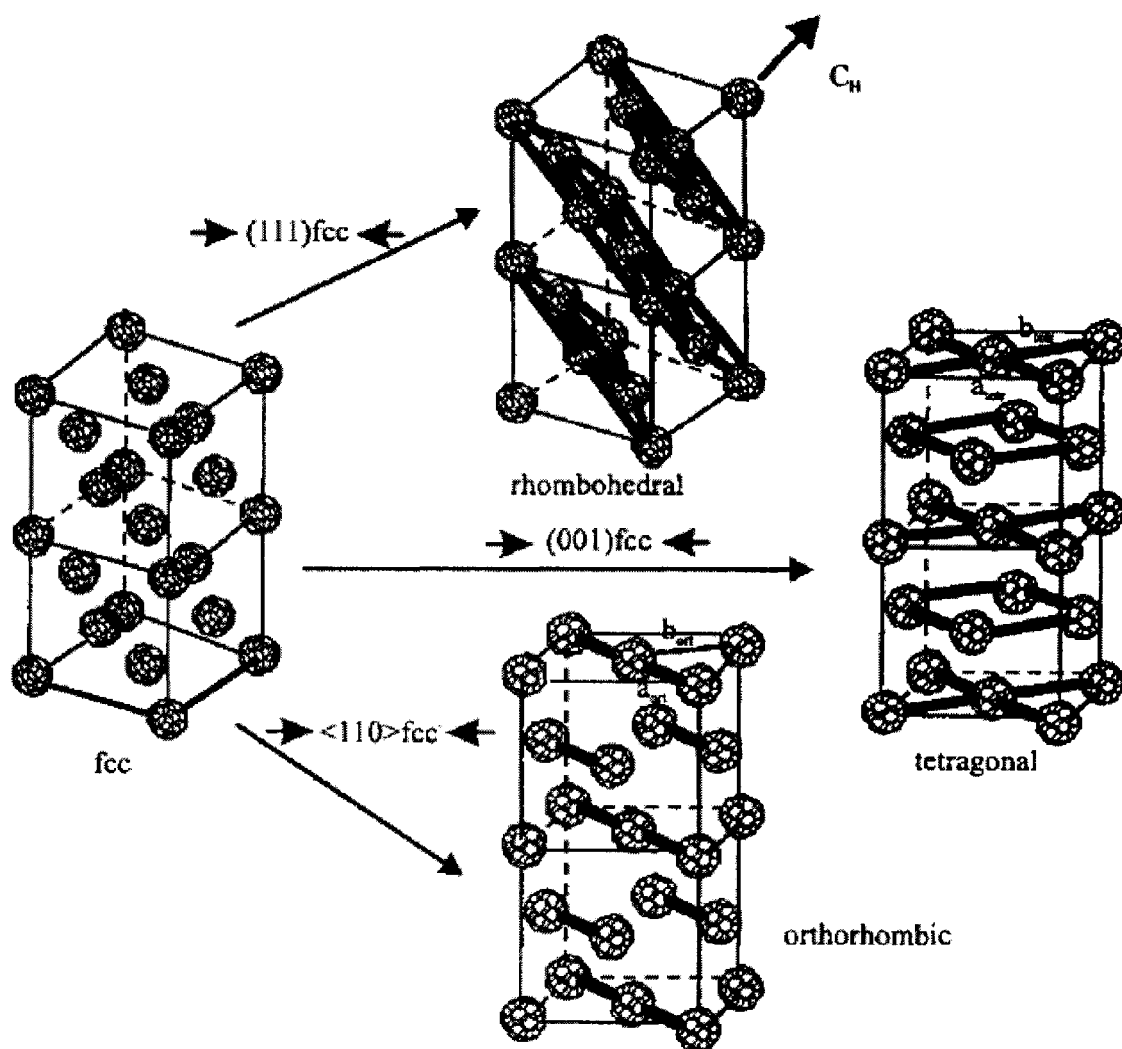


Figure 1-5 Overview of intermediate-pressure polymeric phases of C_{60} and their relationship to the fcc C_{60} structure. (adapted from Marques, L. et al *Molec. Mater.* **1996**, 8, 49.)

Chapter 2

FLUORINATION AND PYROLYSIS CUTTING OF HIPCO SINGLE-WALL CARBON NANOTUBES

2.1 CONTROLLED FLUORINATION OF HIPCO SINGLE-WALL CARBON NANOTUBES

2.1.1 Introduction

Single-wall carbon nanotubes (SWNTs) have become one of the research focuses in current nanoscience and nanotechnology. Their particular nanoscale structure and the one-dimensional (1-D) geometry make them not only a perfect model for studying nanoscale phenomena and quantum effects, but also they are promising nanomaterials with many potential applications³⁷⁻³⁹. However, the chemical inertness of SWNTs hampers their development into applicable materials in many fields. Although there have been many methods developed to synthesize^{73,74} and to purify^{75,76} single-wall carbon nanotubes on a large scale, the chemical manipulation of single-wall carbon nanotubes is still a big challenge. Since large scale syntheses of SWNTs have become available, there have been extensive research activities on the chemical modification of SWNTs^{31-34,77}. The motivations of the chemistry research on SWNTs include understanding the fundamental properties of the SWNTs from a chemistry viewpoint and seeking chemical methods to modify the properties of SWNTs for better performance and better compatibility. Since the electronic properties of carbon nanotubes are dependent on their diameter, helicity and defect distribution, the chemical reactivities are also determined by

those parameters. Research on the chemistry of SWNTs has been developing rapidly during the last two to three years. Original studies include utilizing the specific reactivities on the SWNTs ends for site selective derivatization; exploring the reactivities on the sidewall of SWNTs to modify the surface properties of SWNTs^{31,33,78}; noncovalent SWNTs sidewall functionalization such as polymer wrapping⁷⁹ for bio-applications⁸⁰, filling nanotube cavities with various substances forming novel hybrid materials, etc.

Among various approaches to the sidewall functionalization of SWNTs^{31,33,34}, fluorination has been shown to be able to covalently attach large amounts of fluorine to the SWNT structures³¹. Fluorination has proven to be an important derivatization precursor on the sidewall of SWNTs. Many other functional groups can be attached to the SWNTs sidewall through substitution reactions of the weak C – F bonds on the Fluorotubes³³. Alkyl groups such as methyl, butyl, and hexyl groups have been successfully attached to the SWNT sidewall using Fluorotubes as precursors⁸¹. Theoretical study of fluorinated SWNTs with stoichiometry C₂F indicates that the fluorination of SWNTs can yield insulating, semiconducting and metallic nanotube derivatives, depending on the fluorination pattern⁸². The same calculation also indicates that the fluorinated SWNTs are better electron acceptors than the bare carbon nanotubes and hence when reacting with reducing chemicals such as alkali metals the fluorinated SWNTs might be reduced to bare SWNTs⁸². Theoretical study on the thermochemistry of fluorinated SWNTs⁸³ found that thermodynamic stability of the fluorinated SWNTs increases with decreasing tube diameter, and the mean bond dissociation energies of the C – F bonds also increase with decreasing tube diameter. According to the calculation,

the C – F bond strength in a (5, 5) fluorinated SWNTs is similar to that in the “covalent” (CF)_n compounds. Recent study on the oxidative properties and chemical stability of Fluorotubes has revealed that the Fluorotubes are not chemically inert towards solid inorganic matrixes such as KBr, KI, LiI, etc. and exhibit significant oxidative properties in the redox reactions occurring under various temperatures depending on the nature of the inorganic matrixes ⁸⁴.

The specific SWNTs studied in this thesis were synthesized from the high pressure CO disproportionation (HiPco) process ⁷⁴. Using Fe(CO)₅ as a catalyst, the SWNTs produced from HiPco process have an average diameter of ~1.0 nm. Although the fluorination of Tubes@Rice (average diameter ~1.36 nm) has been thoroughly studied ³¹ and documented ⁸⁵, the fluorination of HiPco was only briefly explored ⁸⁶. In this chapter, a detailed study of the fluorination of HiPco SWNTs is described. It includes the optimization of reaction conditions for maximum fluorine attachment; temperature, reaction time, and fluorinating reagent concentration dependence of the stoichiometry of the fluorinated HiPco SWNTs; and exploration of stoichiometry controlled fluorination.

2.1.2 Experimental

The SWNTs samples used in this study are purified HiPco nanotubes. The purification is a two-step process: “soft-baking” and gaseous HCl leaching. The mechanism and experimental details of “soft-baking” is described in details elsewhere ⁸⁶. The gaseous HCl leaching process will be discussed in detail in a later chapter of this thesis. The final purified SWNTs are light-weight, porous, black flakes. The fluorination

apparatus is schematically demonstrated in Figure 2-1. The reaction chamber is made from two pieces of stainless steel flanges and is sealed with copper gasket. The chamber has been passivated with fluorine gas at ~ 300 °C before the first use. It is constantly purged with gaseous helium and is exposed to atmosphere only when loading and unloading samples. The chamber is located on a temperature controllable heating plate. The sample loading pan is fit into the chamber. To obtain uniform fluorine exposure, the sample pan is constantly rotated at a speed of ~ 3 rpm around the pole that is perpendicularly fixed on the bottom center of the pan during the reaction. The reagent gases include pure fluorine, 1% fluorine/helium mixture, and hydrogen. Hydrogen is used to react spontaneously with fluorine when they meet each other to form hydrogen fluoride, which is believed to facilitate the fluorination of SWNTs⁸⁶. The flow rates of the purging gas (helium) and reagent gases are controlled through a set of delicate mass flow controllers. The pressure inside the chamber is monitored through a pressure gauge. The outgoing gas from the reaction chamber is directed into a bottle with NaOH solution to absorb the unconsumed fluorine and hydrogen fluoride.

The nanotubes have been fluorinated at various temperatures (from 50 °C to 200 °C) for various period of time (2 hours to 12 hours), with various fluorine concentrations (0.2% to 10%) to explore the reaction initiation temperature and the optimized reaction conditions to get the fluorinated SWNTs with the highest F/C ratio without damaged the tubular structures.

Scanning electron microscopic (SEM) images of the samples were obtained with a Philips field emission gun (FEG) SEM. With its energy dispersive X ray analysis (EDAX) attachment, we obtained information on the elemental composition of the

samples. For each sample, EDAX data were collected at five different spots over the sample and were averaged to determine the overall elemental composition. The IR spectra of the samples were obtained with a Thermo Nicolet Nexus FT-IR spectrometer. With the attenuated total reflectance (ATR) accessory of the spectrometer, absorbance due to the vibration modes over the thin layer of the sample was directly detected. The Raman spectra of the samples were obtained with a Renishaw micro-Raman spectrometer using a 780 nm laser. The UV-vis.-NIR spectra were collected using a Shimadzu-UV-3101 PC spectrometer. The SWNT samples were suspended in *o*-dichlorobenzene (ODCB) for UV-vis.-NIR analysis.

2.1.3 Results and Discussion

The typical morphologies of SWNTs from laser oven synthesis process (Tubes@Rice) and from HiPco process under SEM are shown in Figure 2-2. Generally, Tubes@Rice SWNTs form larger bundles (ropes) than HiPco SWNTs. The HiPco SWNT bundles seem curved to a greater extent when formed in a mat-like bucky-paper, as shown in Figure 2-2(b). Also as mentioned before, the HiPco SWNTs have an average diameter about 2/3 that of the laser oven grown SWNTs. The three factors, i.e. the smaller individual tube diameter, the smaller bundle size, and the greater curved structure in solid form, account for the greater reactivity of the HiPco SWNTs with gaseous fluorinating reagents which is quite different from the laser oven grown SWNTs. It was found that the fluorination of HiPco SWNTs begins at about 50 °C, which is much lower than that of the laser oven grown SWNTs (over 150 °C, according to ref. 85). We believe

that the smaller individual nanotube diameter and the curved bundles lower the activation energy barrier for initiation of the fluorination reaction, and the smaller nanotube bundle size offers a larger surface area that is directly exposed to the reacting fluorine gas, as well as a more porous structure that allow more efficient penetration of fluorine throughout the samples. Overall, these factors facilitate the fluorination reaction of the HiPco SWNTs so that the reaction is initiated at a much lower temperature.

A comparison of the SEM images of HiPco SWNTs before and after fluorination is shown in Figure 2-3. The most important difference between the fluorinated SWNTs and the untreated ones is that the nanotube bundle size decreased significantly after fluorination. This debundling effect occurs even for nanotubes that have been treated with fluorine briefly, i.e. two hours at 50 °C. The debundling of SWNTs by fluorination probably due to the modification of nanotube surface properties with fluorine addition, which breaks the van der Waals interaction between sidewall of nanotubes and introduces the electrostatic repulsion between fluorine atoms on different nanotubes. The combination of these two effects could result in the separation of individual nanotubes that stay within the same bundle. Another apparent difference between the SEM images of the fluorinated SWNTs and the untreated ones is that there are evident bright zones over the fluorinated samples, which indicates the modification of electronic properties due to covalent fluorine addition to the sidewall of nanotubes. The extent of the modification is dependent on the amount of fluorine attached. As one can find out by comparing Figure 2-3(b) and (c), the higher F/C ratio of the sample, the greater the modification is.

The temperature dependence of the fluorination of HiPco SWNTs was studied by

fluorinating the HiPco SWNTs at four different temperatures between 50 °C and 200°C for 12 hours, respectively, and examining the fluorinated SWNTs with EDAX and IR. The stoichiometries of SWNTs fluorinated at different temperatures were determined with EDAX and are listed in Table 2-1. In brief, the F/C ratio increases with increasing fluorination temperature. The highest F/C ratio observed is about 1 to 2 when the fluorination occurs at 200 °C, where the Raman spectra indicate that the nanotube structure has been badly damaged under this condition (details in the following discussion). The IR spectra of the nanotubes fluorinated at various temperatures are compared in Figure 2-4. The broad, two-component peak spanning from $\sim 1050\text{ cm}^{-1}$ to 1220 cm^{-1} in Figure 2-4(a) indicates the formation of covalent C – F bonds when the nanotubes were fluorinated at 50 °C for 12 hours. The two components of the peak, centering around 1094 cm^{-1} and 1213 cm^{-1} , indicate that there are two types of C – F bonds formed on the nanotube sample, one is more semi-covalent in bond nature (the 1094 cm^{-1} one), the other is more covalent in bond nature (the 1213 cm^{-1} one). The formation of the two types of C – F bonds were also observed in the fluorination of graphite at mild reaction conditions⁸⁷. Ratio of these two types of bonds is about 1:1 in Figure 2-4(a). There is another peak around 1536 cm^{-1} in the spectrum. It was assigned as the vibrational mode from the activated C = C bonds. When there is no functionalization, all C = C bonds on the nanotubes are symmetric, therefore there is no IR active mode in this region. The fluorination breaks such symmetric geometry by forming C – F bonds on certain number of C atoms on the nanotubes. Most vibration of the remaining C = C bonds are not symmetric any more because of the influence of C – F bonds in their vicinity. Such vibration modes become IR active and cause the feature around

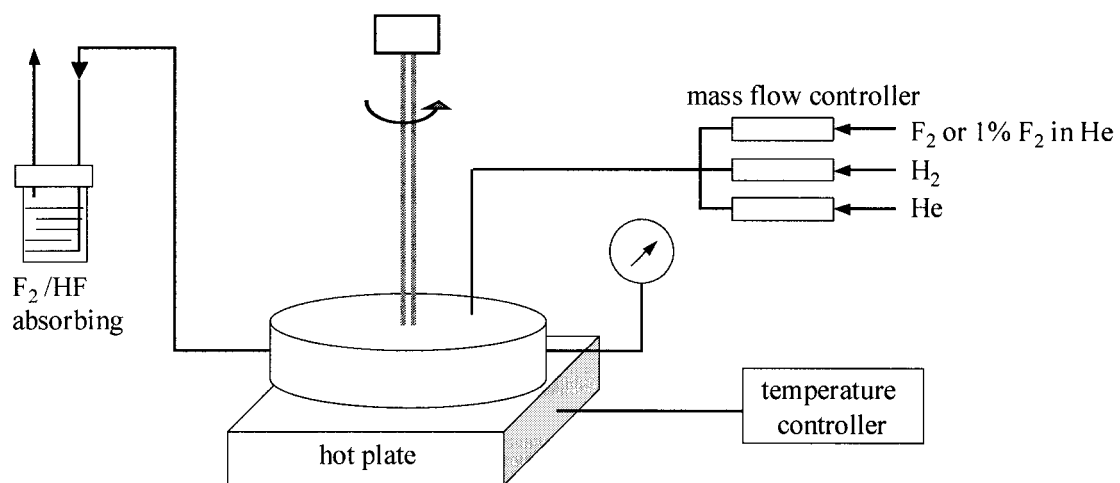


Figure 2-1 Schematic diagram of the fluorination apparatus.

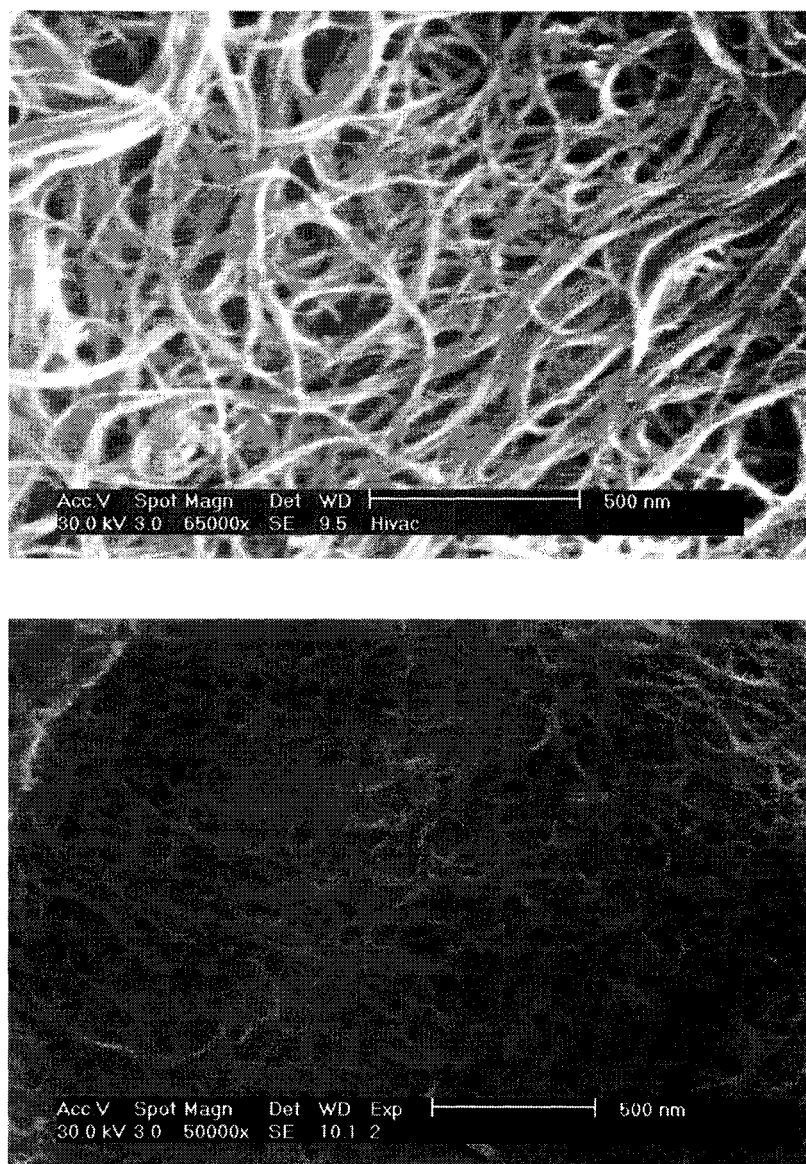


Figure 2-2 SEM images of laser-oven grown SWNTs (top) and HiPco SWNTs (bottom).

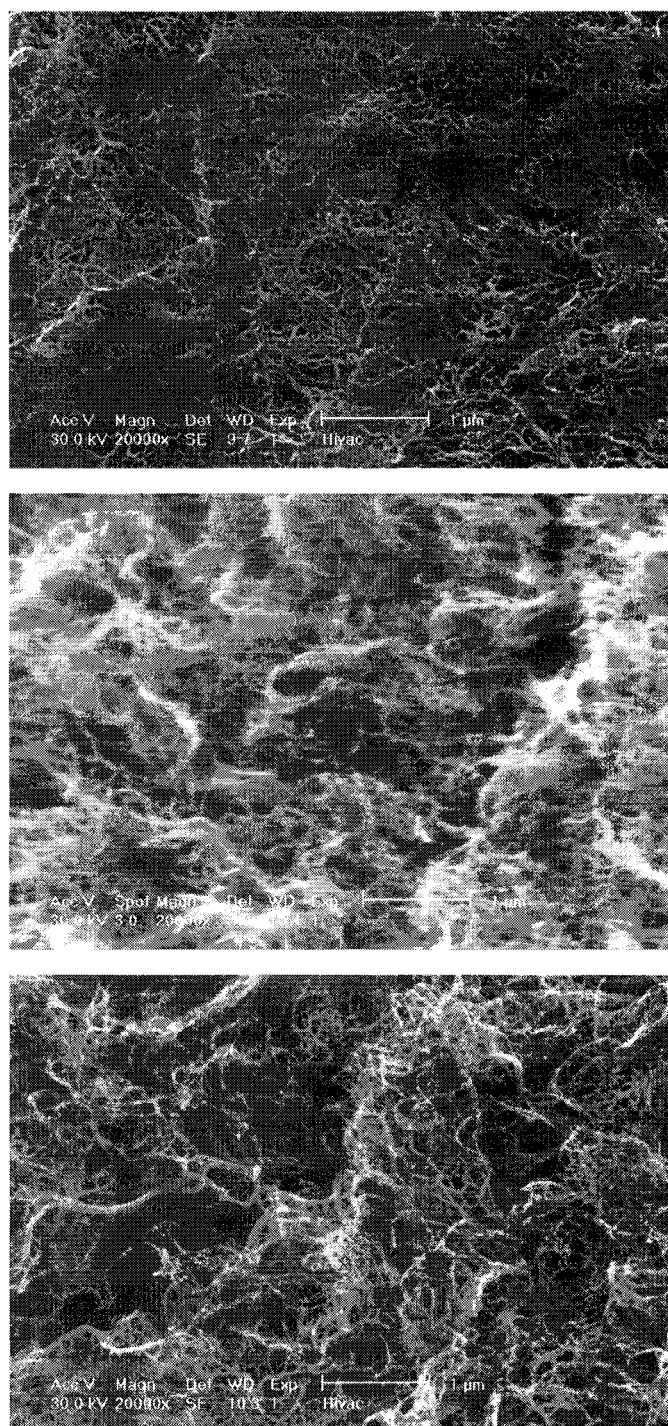


Figure 2-3 SEM images of purified HiPco SWNTs before and after various extents of fluorinations. (top: before fluorination; middle: $C_{2.5}F$; bottom: C_5F .)

Table 2-1 Atomic F/C ratio of HiPco SWNTs fluorinated at various temperatures ^{a, b}.

Temperature	50 °C	100 °C	150 °C	200 °C
Atomic F/C ratio	0.25	0.38	0.4	0.5

^a Values are determined with EDAX.

^b Fluorination time is 12 hours for all samples.

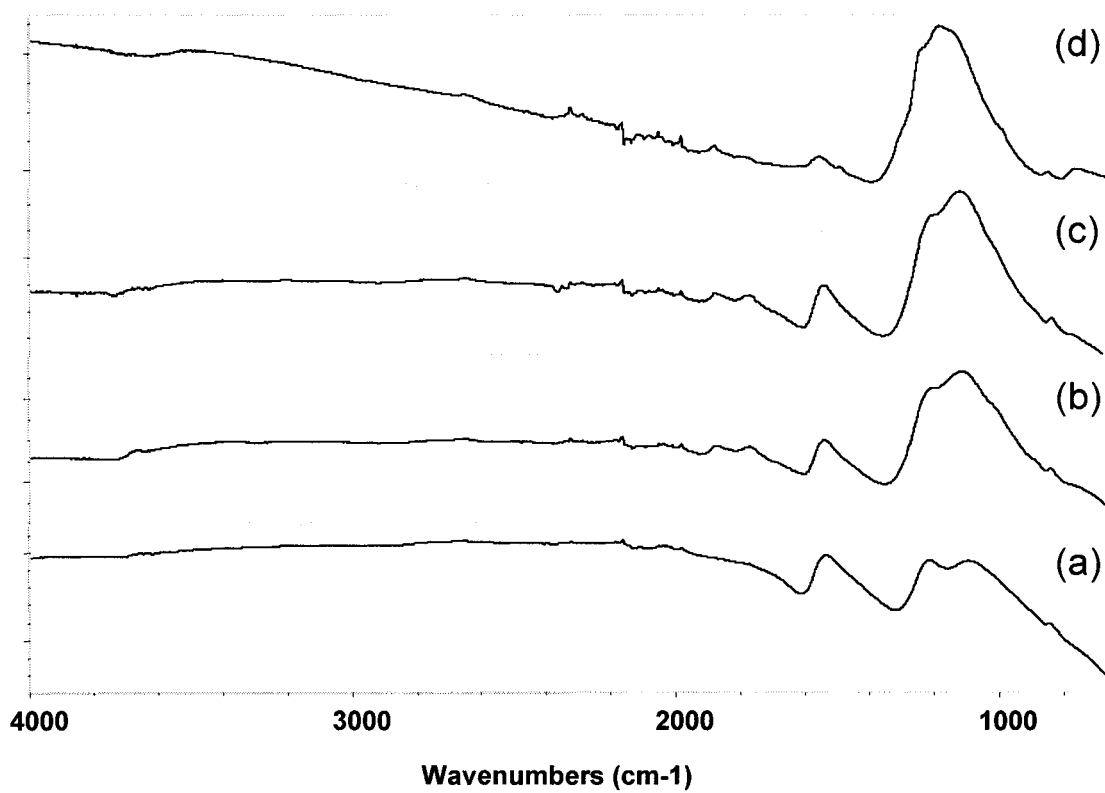


Figure 2-4 ATR-IR spectra of SWNTs fluorinated at various temperatures. (a) 50 °C; (b) 100 °C; (c) 150 °C; (d) 200 °C.

$\sim 1540\text{ cm}^{-1}$. Therefore, the relative intensity of the 1540 cm^{-1} mode is an indicator of the amount of intact $\text{C} = \text{C}$ bonds on the nanotube structure. When the SWNTs were fluorinated at $100\text{ }^{\circ}\text{C}$ for 12 hours, on their IR spectrum, the relative intensity of the semi-covalent bonding exceeds that of the covalent one and up-shift almost 20 wavenumbers to $\sim 1113\text{ cm}^{-1}$. The covalent component down-shifts ~ 5 wavenumbers to $\sim 1208\text{ cm}^{-1}$. Although it seems that the overall $\text{C} - \text{F}$ bonding property becomes less covalent by simply comparing the relative intensities of the two components, the center of the $\text{C} - \text{F}$ mode has up-shifted. It indicates that the overall bond strength increases when the SWNTs are fluorinated at $100\text{ }^{\circ}\text{C}$ versus that at $50\text{ }^{\circ}\text{C}$. Also the relative intensity of the 1540 cm^{-1} mode to that of the $\text{C} - \text{F}$ stretching mode in Figure 2-4(b) is much lower than that in Figure 2-4(a). It is a quantitative measurement that indicates the amount of intact $\text{C} = \text{C}$ bond decreases when fluorination is carried out at higher temperature. This tendency is maintained when the HiPco SWNTs were fluorinated at $150\text{ }^{\circ}\text{C}$ [Figure 2-4(c)] and $200\text{ }^{\circ}\text{C}$ [Figure 2-4(d)]. Actually in Figure 2-4(d), the $\text{C} = \text{C}$ feature almost disappeared completely, which implies that there is almost no intact $\text{C} = \text{C}$ bonds in this nanotube sample. The EDAX data of the SWNTs fluorinated at $200\text{ }^{\circ}\text{C}$ in Table 2-1 show that the F/C ratio is 0.5 in this sample, which means on average, one out of every two carbon atoms on the nanotubes have been bonded with fluorine. It explains the disappearance of the 1540 cm^{-1} mode. In Figure 2-4(c), the 1117 cm^{-1} component of the $\text{C} - \text{F}$ mode becomes dominant and the higher frequency component is not resolvable any more. It implies that the fluorination at $200\text{ }^{\circ}\text{C}$ forms $\text{C} - \text{F}$ bonds of more uniform bond strength. This trend is more apparent in Figure 2-4(d) where the $\text{C} - \text{F}$ mode has only one narrowed component centered at $\sim 1182\text{ cm}^{-1}$. By comparing the four spectra in

Figure 2-4, we conclude that the fluorination reaction of HiPco SWNTs shows a temperature dependence. At lower temperature, both semicovalent and covalent C – F bonds are formed, and there is still large number of intact C = C bonds on the nanotube sidewall. When fluorination occurs at higher temperature, the semicovalent C – F bonds become dominant and their vibration frequency up-shifts. At 200 °C, almost every C = C bond has been directly affected with fluorine addition and the C – F bonds around the nanotubes are more similar in bond strength.

The effect of fluorine addition to the structure of carbon nanotubes was examined with micro-Raman spectroscopy. In Figure 2-5, Raman spectra of fluorinated SWNTs with different F/C ratio are stacked and compared. Figure 2-5(a) is the typical Raman pattern of the purified HiPco SWNTs. It shows well defined radial breathing modes (RBM) in the region of 170 – 270 cm^{-1} , strong and sharp tangential mode at $\sim 1592 \text{ cm}^{-1}$ and a disorder mode with very low intensity at $\sim 1292 \text{ cm}^{-1}$. The Raman spectrum indicates that the purified SWNTs have long-range one-dimensional (1-D) order with very few defect sites along the sidewall ⁸⁸. Figure 2-5(b) is the Raman spectrum of the fluorinated HiPco SWNTs with stoichiometry C_8F . The distinctive increase in intensity of the disorder mode indicates the relative amount of sp^3 type carbon in this sample. Changes are also seen in the RBM and tangential mode regions, which indicates that bonding of fluorine to the carbon on the sidewall of the SWNTs changes the overall symmetry and bonding structure of the SWNTs. For example, the details of the RBM disappeared in Figure 2-5(b) due to the perturbation of fluorine addition. The tangential mode broadens and down-shifted almost 10 cm^{-1} , which implies the weakening of the bonding between carbon atoms on the nanotube framework. According to the

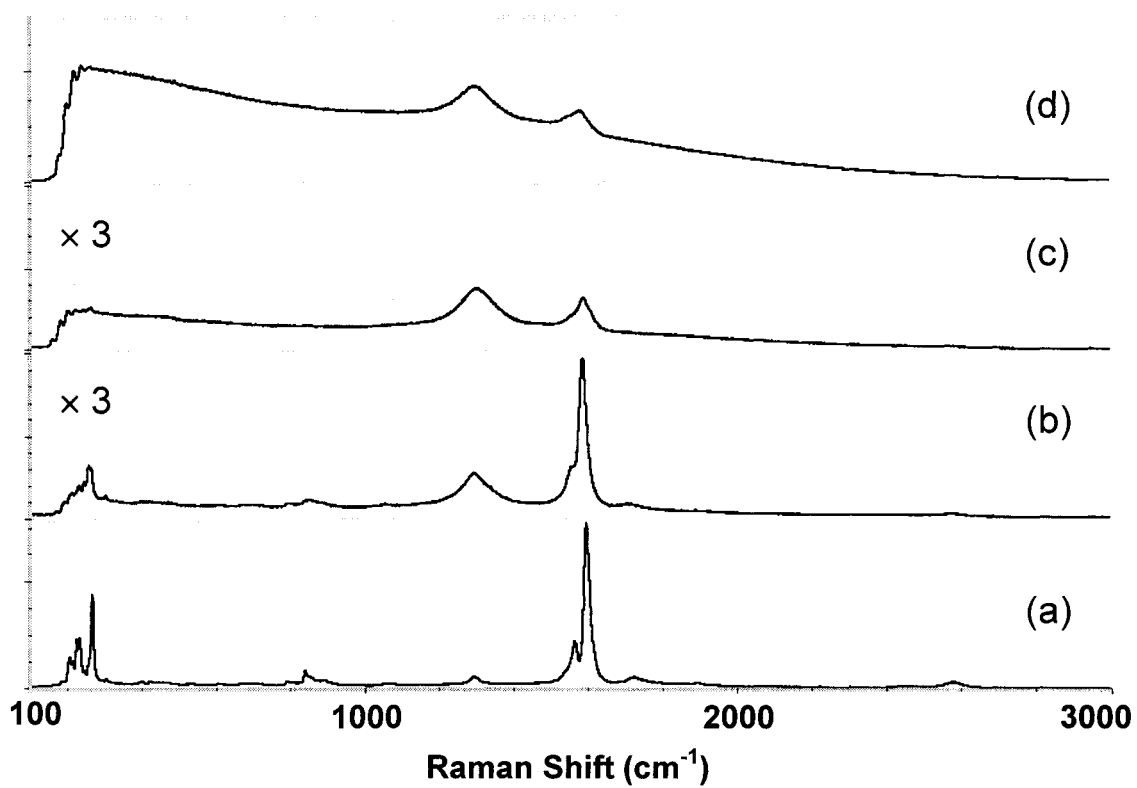


Figure 2-5 Raman spectra of fluorinated SWNTs with various stoichiometry (a) purified SWNTs; (b) C₈F; (c) C_{2.5}F; (d) C₂F.

density-function calculations by Kudin, et al ⁸², the addition of fluorine atoms to the single-wall carbon nanotubes changes the local bonding environments of the respective carbon atoms and this induces significant distortions from the pristine SWNT geometry. Also, the fluorinated SWNTs are buckled along the nanotube sidewall resulting in different distances of the sp^2 and sp^3 carbon atoms from the tube axis. The changes of Raman modes of the SWNTs after fluorination shown in Figure 2-5 are consistent with these calculations. The Raman spectrum of the SWNTs with stoichiometry $C_{2.5}F$ is shown in Figure 2-5(c). There is a dramatic change in Figure 2-5(c) compared to Figure 2-5(b): the RBM is almost featureless, and the intensity of disorder mode has surpassed that of the tangential mode. This suggests the fluorine addition to the nanotubes has approached a certain level, which has compressed the resonance Raman enhancement effect from SWNTs. We realized this stoichiometry ($C_{2.5}F$) marks the upper limit of F/C ratio that can be obtained from fluorination of HiPco SWNTs without damaging the tubular structures. Figure 2-5(d) is the Raman spectrum of HiPco SWNTs fluorinated at 200 °C for 12 hours, in which we resulted a product with atomic F/C ratio higher than 1:2. However, in its Raman spectrum there is no discernable RBM, and the tangential mode with extremely low intensity has down-shifted to $\sim 1576\text{ cm}^{-1}$. All the features from Figure 2-5(d) imply that there are no nanotube structures in this sample. To confirm that the tubular structures in this fluorinated sample have been severely damaged, a defluorination experiment was conducted. Defluorination of Fluorotubes with hydrazine has been shown to be able to restore the resonant Raman modes of SWNTs ³¹. The defluorination experiment on the sample mentioned above didn't restore SWNTs features in Raman spectra, which confirmed that the nanotube structures are destroyed in the

sample with F/C ratio over 1:2.

The reaction time dependence of the fluorination has also been investigated at reaction temperature 100 °C and 150 °C, respectively. Figure 2-6 shows the IR spectra of the HiPco SWNTs fluorinated at 100 °C for 4 hours, 8 hours and 12 hours, respectively. It can be seen that the C – F mode has two components (as discussed previously) in both the 4 hours and 8 hours cases. There is no detectable shift of the C – F mode between Figure 2-6 (b) and (a), and the overall C – F absorbance increased. That means the fluorination at 100 °C for 8 hours vs. 4 hours increase the amounts of both the covalent C – F bonding and the semicovalent ones, and there is no thermodynamic predominance of one type over the other during the time scale. However, fluorination at 100 °C for 12 hours changed the C – F bonding pattern on SWNTs. As shown in Figure 2-6(d), the semicovalent C – F bonding has taken dominance and has up-shifted about 10 cm^{-1} in vibration frequency. Meanwhile, the overall C – F absorbance has increased considerably relative to that of the C = C bonding. It seems that the fluorination at 100 °C for 12 hours reaches certain thermodynamic equilibrium. It also implies that the covalent C – F bonding with higher frequency IR absorbance on SWNTs is not the thermodynamically most stable state at 100 °C, so that if the reaction system is kept at this temperature for long enough time, it will gradually convert into the semicovalent type. At 150 °C, a similar situation was observed, as shown in Figure 2-7. The difference is that the semicovalent C – F bonding shows slight predominance even with a 2-hour reaction period. And after the 8-hour reaction, the semicovalent C – F bonding has already shown an up-shift. The overall up-shift of the C – F bonding is over 20 cm^{-1} between the 2-hour fluorination and the 12-hour one.

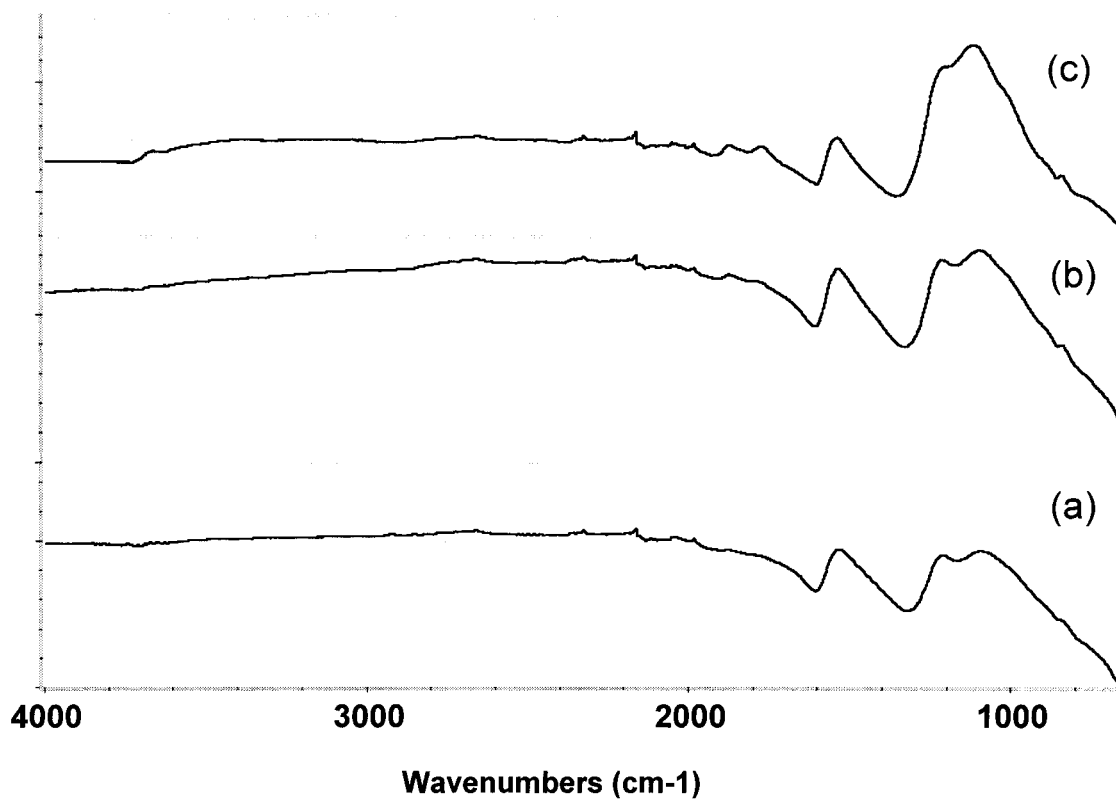


Figure 2-6 ATR-IR spectra of SWNTs fluorinated at 100 °C for various amounts of time. (a) 4 hours; (b) 8 hours; (c) 12 hours.

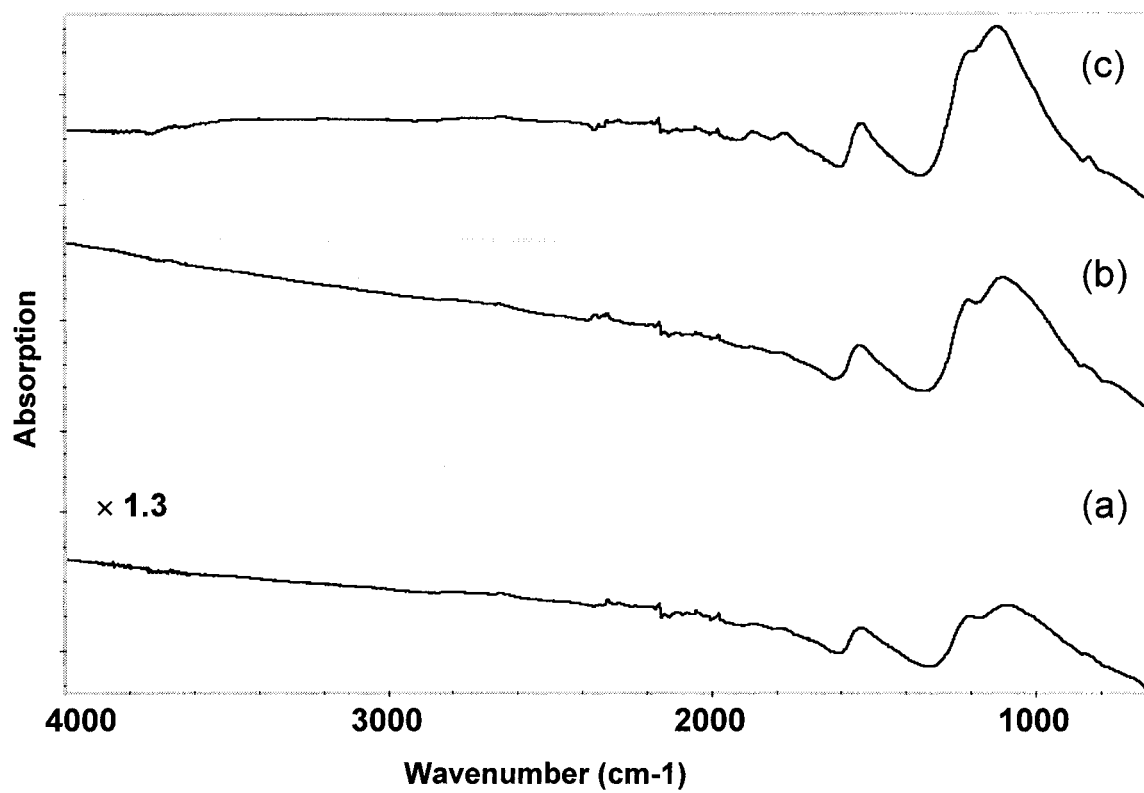


Figure 2-7 ATR-IR spectra of SWNTs fluorinated at 150 °C for various amounts of time. (a) 2 hours; (b) 8 hours; (c) 12 hours.

The study of temperature and reaction duration dependence of the fluorination reaction suggests that the fluorination can be controlled at certain levels so that the SWNTs are partially fluorinated (i.e. with atomic F/C ratio lower than 1:2). We carried out a series of experiments to investigate the influence of fluorination conditions, including reaction temperature, reaction duration and gaseous fluorine concentrations, on the stoichiometry of the fluorinated SWNTs. The results listed in Table 2-2 enable us to examine the effect of each of the three factors independently. For example, at 50 °C, when the F₂ concentration is 10%, the reaction duration has no notable effect on the stoichiometry of the fluorinated SWNTs. When F₂ concentration is 1%, reaction duration made a difference of an order of 2 between 1-hour reaction and 2-hour reaction, but there is no further effect beyond 2 hours. Reaction temperature makes a difference when the reaction duration is kept at 1 hour and F₂ concentration at 0.2%, fluorination at 100 °C resulted in a notably higher F/C ratio than that at 50 °C. The F₂ concentration has a considerable effect on the stoichiometry when the fluorination occurs at 50 °C for one hour, but there is no difference in the cases of longer reaction duration. According to the results shown in Table 2-1, the stoichiometry of fluorination reaction of HiPco SWNTs is temperature dependent when the reaction equilibrium is achieved. But terminating the reaction before it reaches its equilibrium can be achieved by using lower F₂ concentration and shortening reaction duration. Stoichiometries other than the ones shown in Table 2-1 could be obtained with these processes, as shown in Table 2-2. To be clear, the fluorinated HiPco SWNTs with atomic F/C ratio lower than 0.4 will be named as partially fluorinated HiPco SWNTs in the following sections.

Table 2-2 Influence of fluorination conditions on the stoichiometry of the fluorinated HiPco SWNTs.

Reaction Conditions			Atomic F/C Ratio of the Fluorinated SWNTs
Temperatures (°C)	Time (hours)	F ₂ conc. in gas mixtures	
50	1	10%	0.20
50	2	10%	0.20
50	3	10%	0.22
50	1	1%	0.10
50	2	1%	0.21
50	3	1%	0.20
100	1	0.2%	0.06
100	4	1%	0.30
50	1	0.2%	0.04

The van Hove singularities of the SWNTs are very sensitive to the chemical environment around the nanotube sidewalls. For example, the roped HiPco SWNTs in suspension only show several poor resolved, broad features in the range of 900 – 1400 nm⁸⁶, but the surfactant stabilized individual HiPco SWNTs show much sharper and well resolved spectrum in this range⁸⁹. The covalent derivatizations on the sidewall of nanotubes easily quench the overall van Hove transitions in the range of 300 – 1800 nm^{33,34}. Therefore, the UV-vis.-NIR absorption spectra of SWNTs can be used as an indicator of sidewall functionalization. We compared the UV-vis.-NIR spectra of the purified HiPco SWNTs and the partially fluorinated HiPco SWNTs with stoichiometry C₅F (corresponding to atomic F/C ratio of 0.2), as shown in Figure 2-8. The van Hove features of the purified HiPco SWNTs [Figure 2-8(a)] completely disappeared in the partially fluorinated SWNTs [Figure 2-8(b)]. The result indicates that even the partial fluorination is capable of modifying the electronic structure of the SWNTs significantly.

2.1.4 Conclusion

To conclude, the fluorination of HiPco SWNTs was studied at various circumstances to determine the optimized reaction conditions, such as fluorination temperature, reacting duration and F₂ concentration. The highest atomic F/C ratio obtained without severe damage to the nanotube structures was found to be 0.4, when SWNTs were fluorinated at 150 °C for 12 hours. Fluorination at higher temperature caused severe damage to the nanotube structure that could not be recovered with

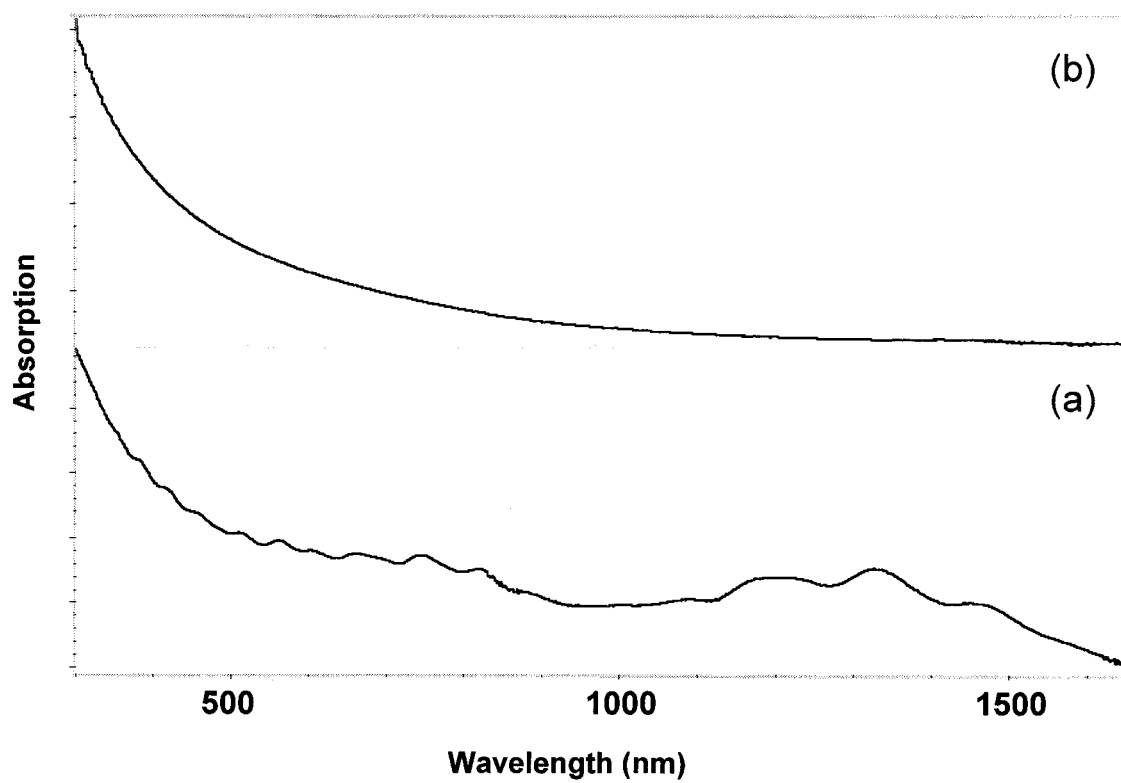


Figure 2-8 UV spectra of purified HiPco SWNTs (a) and fluorinated SWNTs C₅F (b).

hydrazine defluorination. The optimized fluorination temperature for HiPco SWNTs is significantly lower than that of the laser oven grown SWNTs. It is believed related to the smaller average diameter of HiPco SWNTs. The dependence of the fluorination on reaction conditions was examined by studying the variation of the IR, Raman spectra and the stoichiometry of the fluorinated SWNTs at different conditions. Partial fluorination can be achieved by terminating the reaction before it reaches its equilibrium. Decreased F_2 concentration and shorter reaction duration can be used to produce partial fluorination. Debundling was observed with purified HiPco SWNTs either partially fluorinated or completely fluorinated. We found that partial fluorination has already caused the significant modification of the electronic structures of HiPco SWNTs, which was confirmed by the observation that the van Hove singularities completely disappeared in a partially fluorinated SWNT sample.

2.2 PYROLYSIS CUTTING OF THE PARTIALLY FLUORINATED SWNTS

2.2.1 Introduction

Among the enormous research interest in their properties and potential applications, chemical manipulations of SWNTs has become a very important mission. To take full advantage of their mechanical, electrical, optical and other remarkable properties, SWNTs need to be incorporated into various chemical systems and to be fabricated into devices, sensors, composite materials, etc. Most of these research applications need individual or small ropes of nanotubes, and some of them prefer nanotubes with length less than 100 nm. The as prepared SWNTs from large-scale synthesis process are generally mat-like structure of tangled, huge bundles composed of tens, even hundreds of individual nanotubes. The van der Waals force between micron-long sidewalls of the nanotubes drives the spontaneous roping of these 1D nanostructures. Great efforts have to be taken to separate the nanotubes into individual ones⁸⁹, and the individual SWNTs can only be stabilized under “protection”, such as within surfactant micelles⁸⁹. For certain applications such as mechanically enhanced polymer composite materials, SWNTs need to be mixed into the polymer matrix uniformly. It is very difficult to incorporate tangled long ropes of SWNTs into such systems. The ideal interaction between the nanotubes and the polymer within the composite materials would be covalent linkages formed between both ends of the nanotubes and the polymer frameworks. This requires debundled SWNTs, as well as higher ends-carbon to sidewall-carbon ratio of nanotube samples, that means, shorter-length SWNTs. There are several aspects of research about SWNTs which mainly concern the chemistry on their ends. For example, aligning nanotubes on substrates is often based on end selective derivatization⁹⁰. Shorter pieces of nanotubes

have more ends to derivatize and manipulate. Another interesting research field for nanotubes is to fill the nanotube cavities with foreign materials to form hybrid structures^{91,92}. The experiment with original long nanotubes was not satisfactory and the yield of filled nanotubes was very low (about 2%). It is mainly because the aspect ratio of original nanotubes is too high, so that the probability of foreign materials entering the cavities through ends of nanotubes is too low. SWNTs have also been proposed to be promising drug delivering capsules, and it requires the dimension of nanotubes to be less than 20 nm. Because of the demand for short SWNTs in the research fields mentioned above, there have been studies of shortening and cutting SWNTs from length of several microns into shorter pieces. Previous work on chemically “shortening” the single-wall carbon nanotubes was based on oxidation of the SWNTs in a mixture of concentrated sulfuric and nitric acids⁹³. More recently, it was reported that sonication and homogenization of a mixture of single-wall carbon nanotubes and a monochlorobenzene (MCB) solution of polymethylmethacrylate (PMMA) increased the ratio of short and thinner SWNTs⁹⁴. We have developed a process that cuts the single-wall carbon nanotubes to an average length <50 nm. In this process, the purified single-wall carbon nanotubes were first partially fluorinated to a stoichiometry CF_x ($x \leq 0.2$). Then, by pyrolyzing the partially fluorinated nanotubes (*F-SWNTs*) up to 1000 °C in an argon atmosphere the fluorine was driven off the sidewall of the nanotubes in the form of CF_4 or COF_2 . This left behind the chemically cut nanotubes (*cut-SWNTs*). ATR-IR of the *cut-SWNTs* showed that all C – F bond features have disappeared. EDAX elemental analysis confirmed that the fluorine has been completely driven off during the pyrolysis. By comparing the Raman spectra of the *cut-SWNTs* and the *F-SWNTs* it was found that the sp^3 carbon feature decreased after

the pyrolysis whereas the resonant vibration modes of the nanotubes were restored. AFM images of the *cut-SWNTs* showed that the average length of these “cut” nanotubes was < 50 nm with ~ 80% of the SWNTs shorter than 60 nm.

2.2.2 Experimental

The *F-SWNTs* with a stoichiometry of CF_x ($x \leq 0.2$) were prepared with controlled fluorination discussed in previous section. When the F_2 concentration in the reacting gas mixture was ~ 1%, the reaction temperature was controlled at 50 ± 5 °C, and the SWNTs sample were exposed to the fluorinating gas mixture for ~ 2 h, *F-SWNTs* with atomic F/C ratio of 0.2 was produced.

The *F-SWNTs* were then pyrolyzed in an argon atmosphere to temperatures up to 1000 °C. To investigate the process in situ, the pyrolysis was conducted in the furnace of a thermogravimetric analysis (TA Model: TGA-DTA-2960 SDT and Model TGA-Q500) apparatus, which can be coupled with either an FT-IR spectrometer or a mass spectrometer (ThermoStar GSD 300T quadrupole MS). The sample was heated at a rate of 10 °C / min. to 1000 °C. The volatile species released from the sample during the pyrolysis were led into the FT-IR spectrometer or the mass spectrometer through a Teflon tubing or surface passivated capillary. The entire length of the tubing and the capillary were kept at 200 °C during the experiments. The setting enables us to monitor in situ the concentration variations of the volatile species during the pyrolysis with time and/or temperature.

Raman and ATR-IR spectroscopy were used to investigate the removal of C – F

bonding on the sidewall of the SWNTs and the changes caused on the structure of the SWNTs during pyrolysis. A DI MultiMode-SPM with scanner model 2570JV-Z was used at tapping mode atomic force microscopy (TM-AFM) settings for the length and bundle size distribution measurement of the *cut-SWNTs* and the precursor *F-SWNTs*. To prepare samples for AFM analysis, the nanotube samples were dispersed in an aqueous surfactant solution (1% Sodium Dodecyl Sulfate, SDS) with ultrasonic assistance. The dispersion was then deposited onto an aminopropyltriethoxysilane (APTES) monolayer coated silicon wafer using the “dip-rinse-blow dry” process.

2.2.3 Results and discussions

The pyrolysis of the *F-SWNTs* was in-situ monitored with a TGA-FTIR set up. The TGA results are shown in Figure 2-9. The percentage weight loss curve indicates that the overall weight loss during the process was $\sim 45\%$ and the time derivative percentage weight loss curve shows that there were two main weight loss steps. According to the heating program, the first weight loss step occurred between $\sim 300\text{ }^{\circ}\text{C}$ and $\sim 560\text{ }^{\circ}\text{C}$ and the second weight loss step occurred at temperatures over $560\text{ }^{\circ}\text{C}$. After isothermal heating at 1000°C for one hour, the weight loss curve has almost leveled out at $\sim 55\%$, showing that the defluorination of the *F-SWNTs* did not lead to complete destruction of the nanotubes even at $1000\text{ }^{\circ}\text{C}$.

With the TGA coupled FTIR spectrometer, we obtained information about the gaseous species released from the sample at various steps during the pyrolysis that account for the weight loss. By examining the IR spectra that were taken simultaneously

during the overall pyrolyzing process, it was found that there were mainly three gaseous species released at various time periods: CF_4 , COF_2 and CO_2 (the origin of some of the oxygen could be as impurity from the argon used in the experiment), as shown in Figure 2-10. The chemigrams in Figure 2-11 profile the variation of the relative concentration of each species versus time during the pyrolysis. According to the chemigrams, CO_2 and COF_2 were released from the sample within the temperature range of 300 °C and 560 °C, and CF_4 started evolving from the sample at a higher temperature, 560 °C. At that temperature, the release of CO_2 and COF_2 has already been completed. By putting together the chemigrams and the TGA curve on the same time scale, it can be seen that the two gas evolution steps are consistent with the two weight loss steps by TGA. Thus, the thermal defluorination of the *F-SWNTs* occurs in two steps: first, the evolution of CO_2 and COF_2 between ~ 300 °C and ~ 560 °C and second, the evolution of CF_4 at temperatures higher than 560 °C.

The pyrolysis was also in situ monitored with TGA-MS. Since only species with asymmetric vibration modes can be monitored with TGA-IR, TGA-MS provides complementary information if there are IR inactive species, such as F_2 , evolved from the sample. As the result of the TGA-MS measurement, there is no F_2 released from the *F-SWNTs* during the pyrolysis. The detected ion species were CO_2^+ (m/z 44), COF^+ (m/z 47), COF_2^+ (m/z 66) and CF_3^+ (m/z 49), which are consistent with the TGA-IR observation. Also the concentration trends of the ions versus time and/or temperature are very similar to the chemigrams from TGA-IR, as shown in Figure 2-12.

The TGA-IR and TGA-MS data showed that fluorine was driven off the nanotube structure during the pyrolysis of the *F-SWNTs*, and, the fluorine has taken a certain

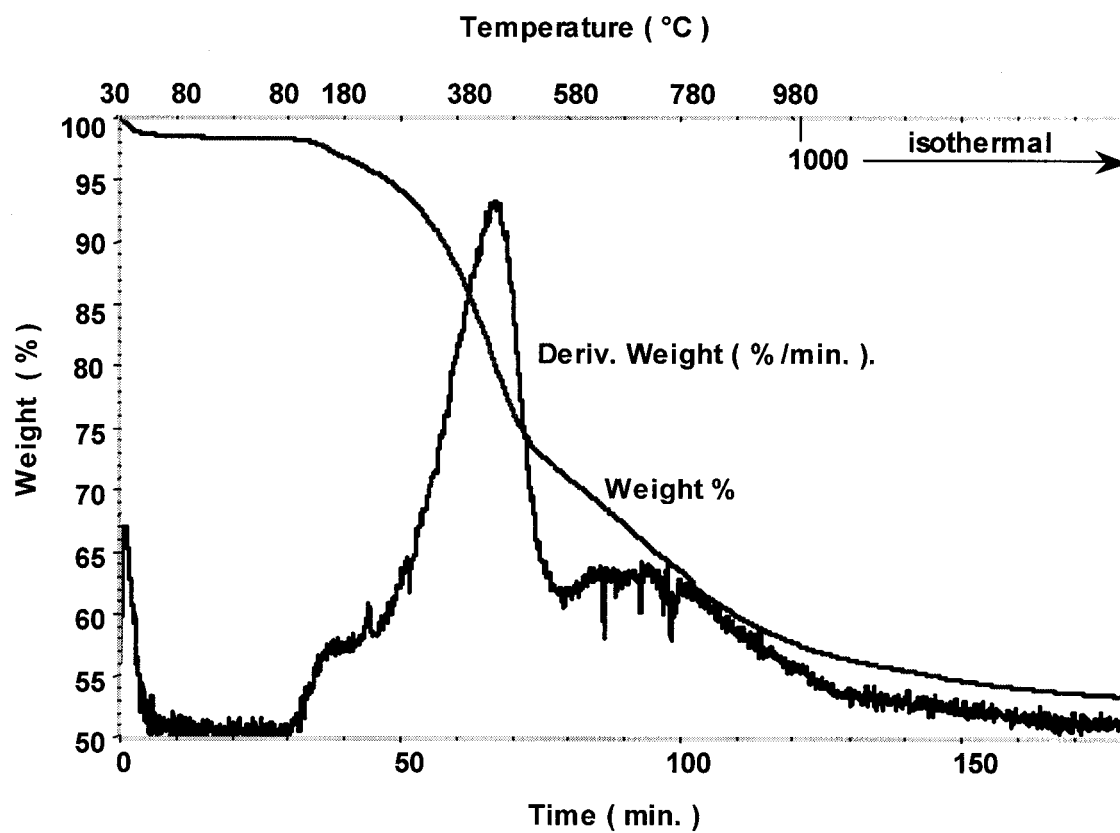


Figure 2-9 TGA of F-SWNTs (C₅F) pyrolyzed in argon up to 1000 °C.

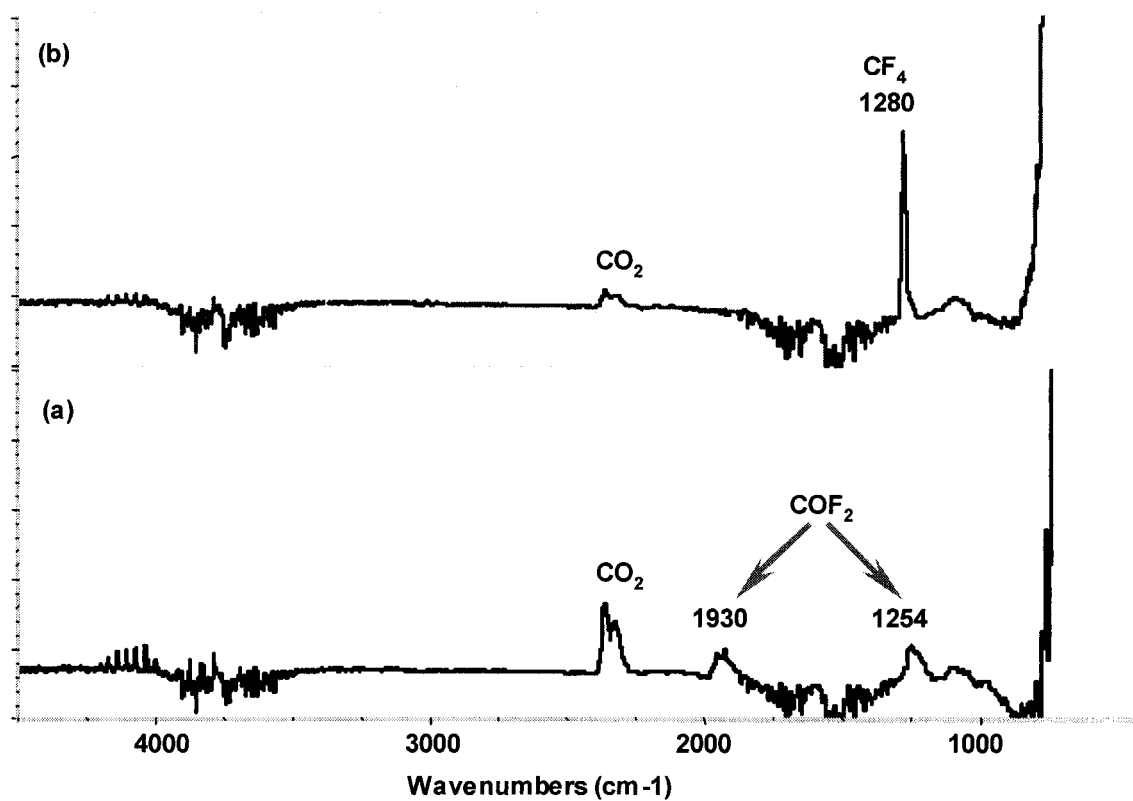


Figure 2-10 In-situ IR spectra of the gaseous species released from the *F-SWNTs* during pyrolysis. (a) spectrum during 300 – 650 °C; (b) spectrum during 560 – 900 °C.

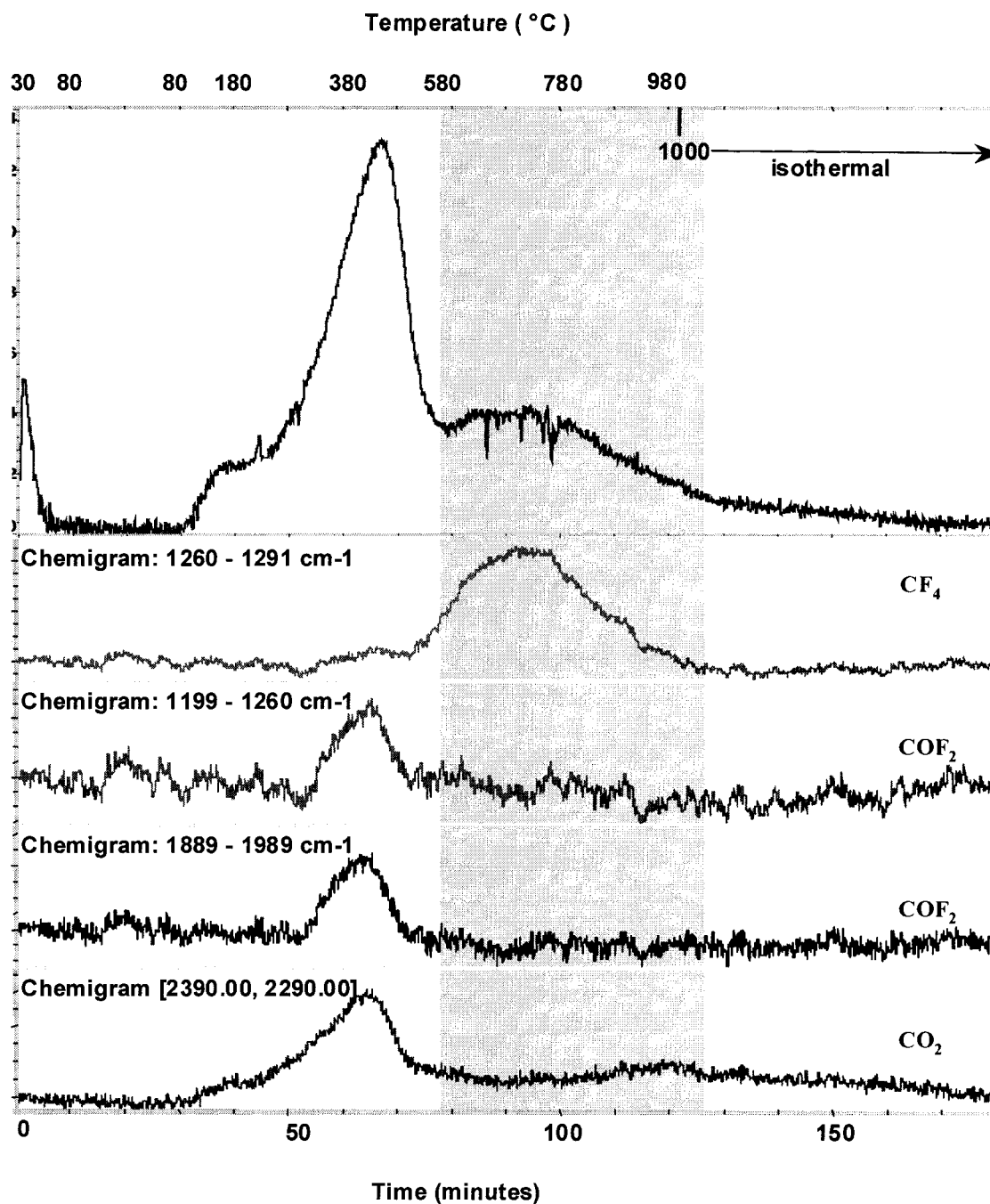


Figure 2-11 Correlation of the TGA time derivative weight loss curve and the chemigrams during pyrolysis.

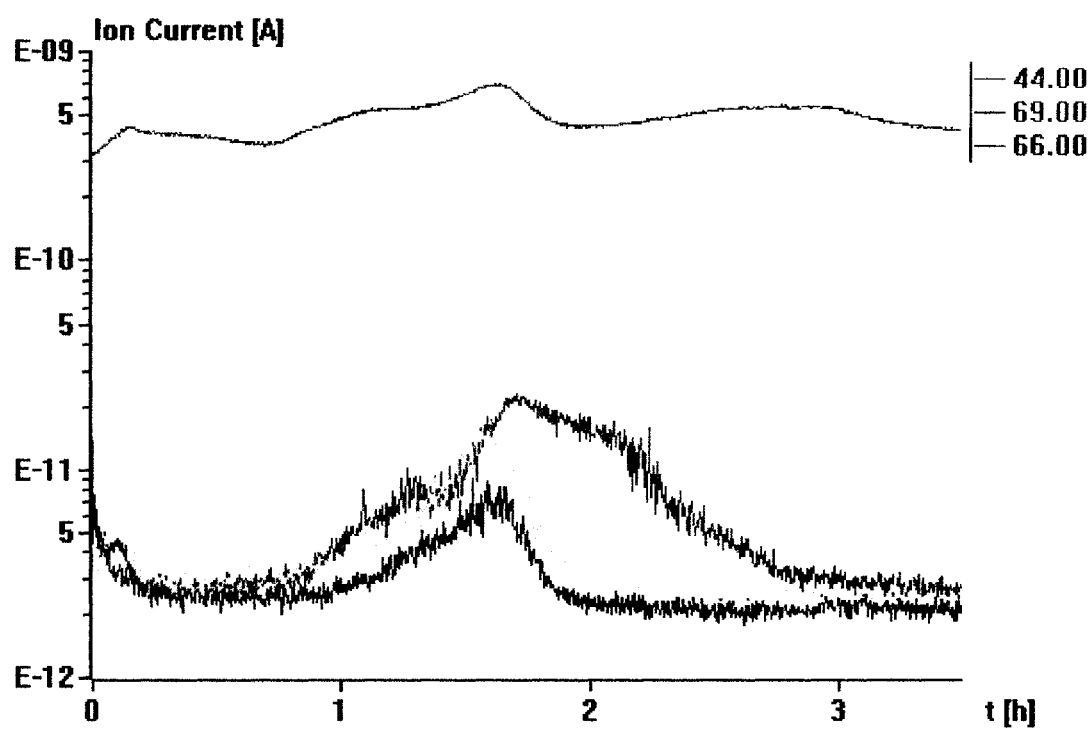


Figure 2-12 TGA-MS plot of the volatile species from *F-SWNTs* during pyrolysis.

amount of carbon from the nanotube sidewall. However, the loss of carbon didn't cause complete destruction and degradation of the SWNTs. Instead, $\sim 55\%$ of the mass survived as pristine nanotubes, even up to $1000\text{ }^{\circ}\text{C}$ in the heating process, as established by examining the residue from the pyrolysis.

In Figure 2-13, the Raman spectra of the SWNTs at each step of the process are stacked and compared. The Raman spectrum of the *cut-SWNTs* is shown in Figure 2-13(c). The relatively high intensity of the tangential mode compared with that of the disorder mode implies that the tubular structure of the SWNTs was maintained during the pyrolyzing process. The notable decrease in the relative intensity of the disorder mode reflects the variation in the relative amounts of sp^3 carbon and sp^2 carbon in the nanotube sample during the pyrolysis process. The remaining disorder mode in Raman spectrum of the *cut-SWNTs* indicates that there might be defects resulted from local carbon removal on the sidewall during the pyrolysis. A further investigation on the structures of the *cut-SWNTs* would provide a more detailed explanation of the Raman spectra.

The ATR-IR spectra of the *F-SWNTs* and *cut-SWNTs* are compared in Figure 2-14. Obviously, the C-F mode has disappeared after the pyrolysis and so has the C-F bond activated C = C mode. Also, elemental analysis of the *cut-SWNTs* by EDAX showed that the atomic percentage of fluorine was less than 0.2%. This information confirms that all the fluorine atoms that had been chemically bound to the SWNTs have been driven off during the pyrolyzing process.

Typical AFM images of the *cut-SWNTs* are shown in Figure 2-16 to Figure 2-19. As a contrast, the image of the *F-SWNTs* before the pyrolysis was also collected, as shown in Figure 2-15. By merely looking at the AFM images, the shortening of the SWNTs after

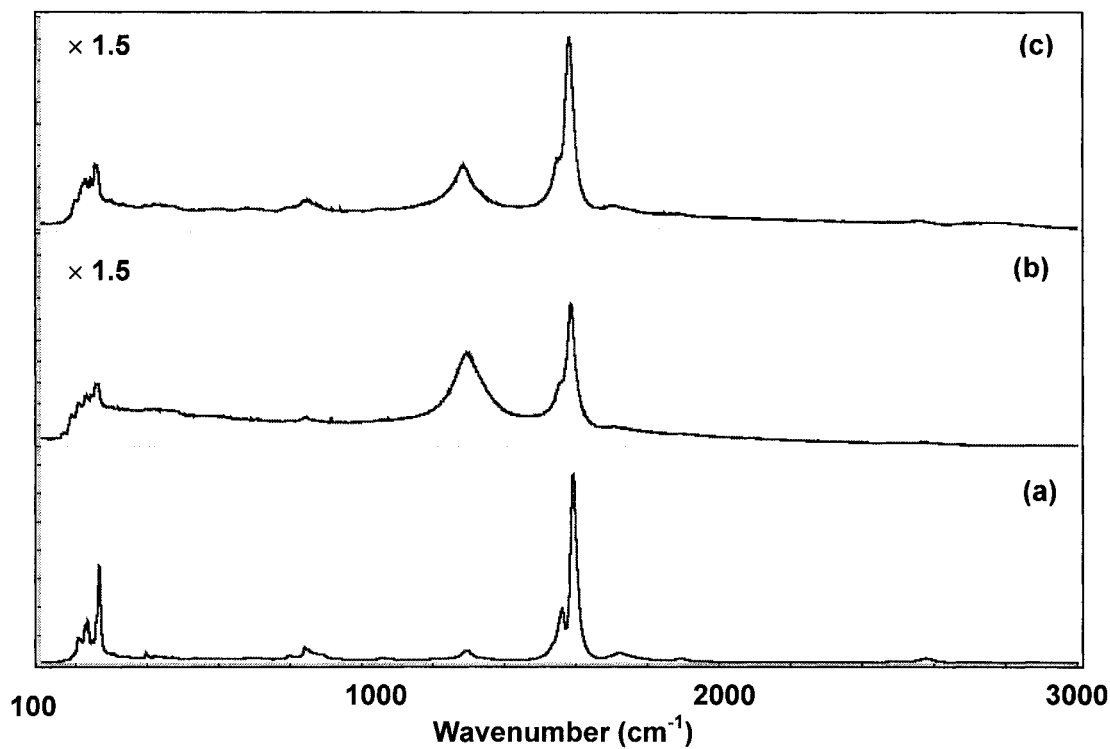


Figure 2-13 Raman spectra of the SWNTs with partial fluorination and pyrolysis. (a) purified SWNTs; (b) *F-SWNTs* (C_5F); (c) *cut-SWNTs*.

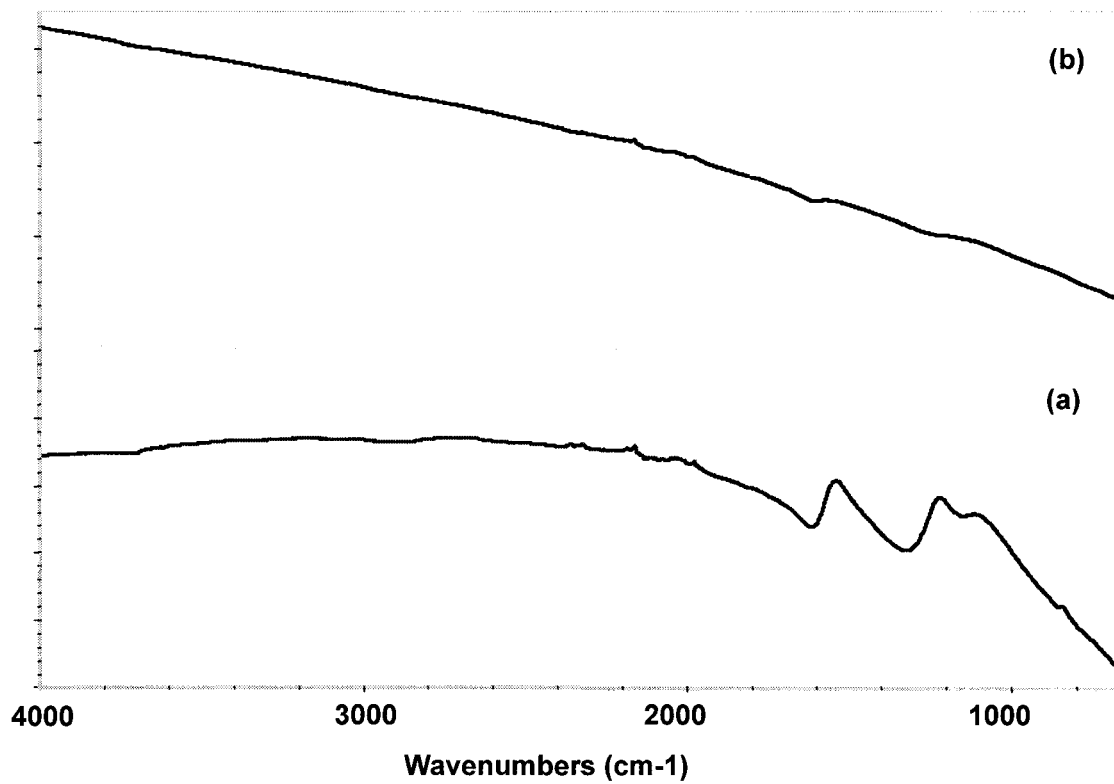


Figure 2-14 ATR-IR spectra of the F-SWNTs before and after pyrolysis. (a) *F-SWNTs* (C₅F); (c) *cut-SWNTs*.

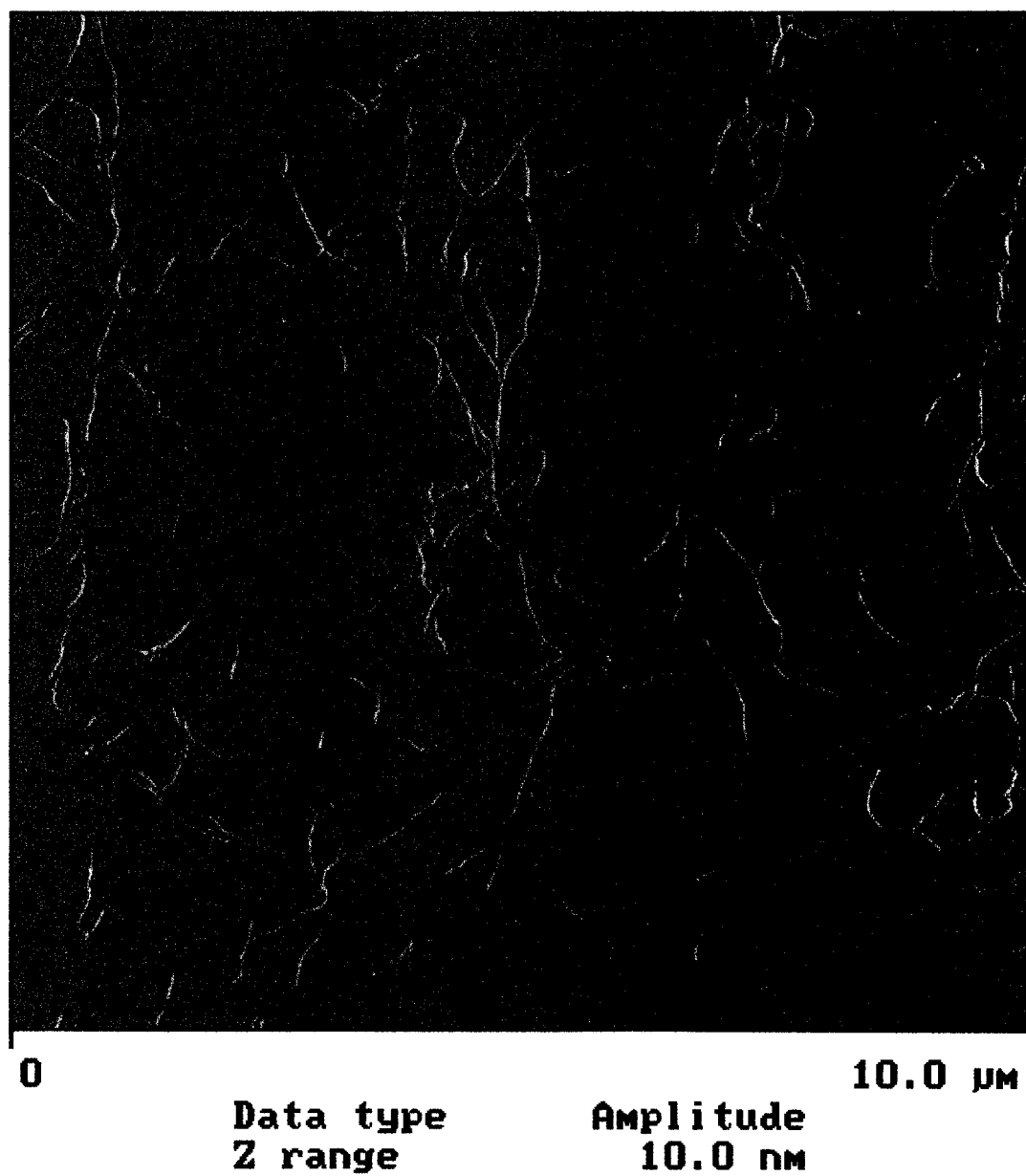


Figure 2-15 AFM image of the *F-SWNTs*.

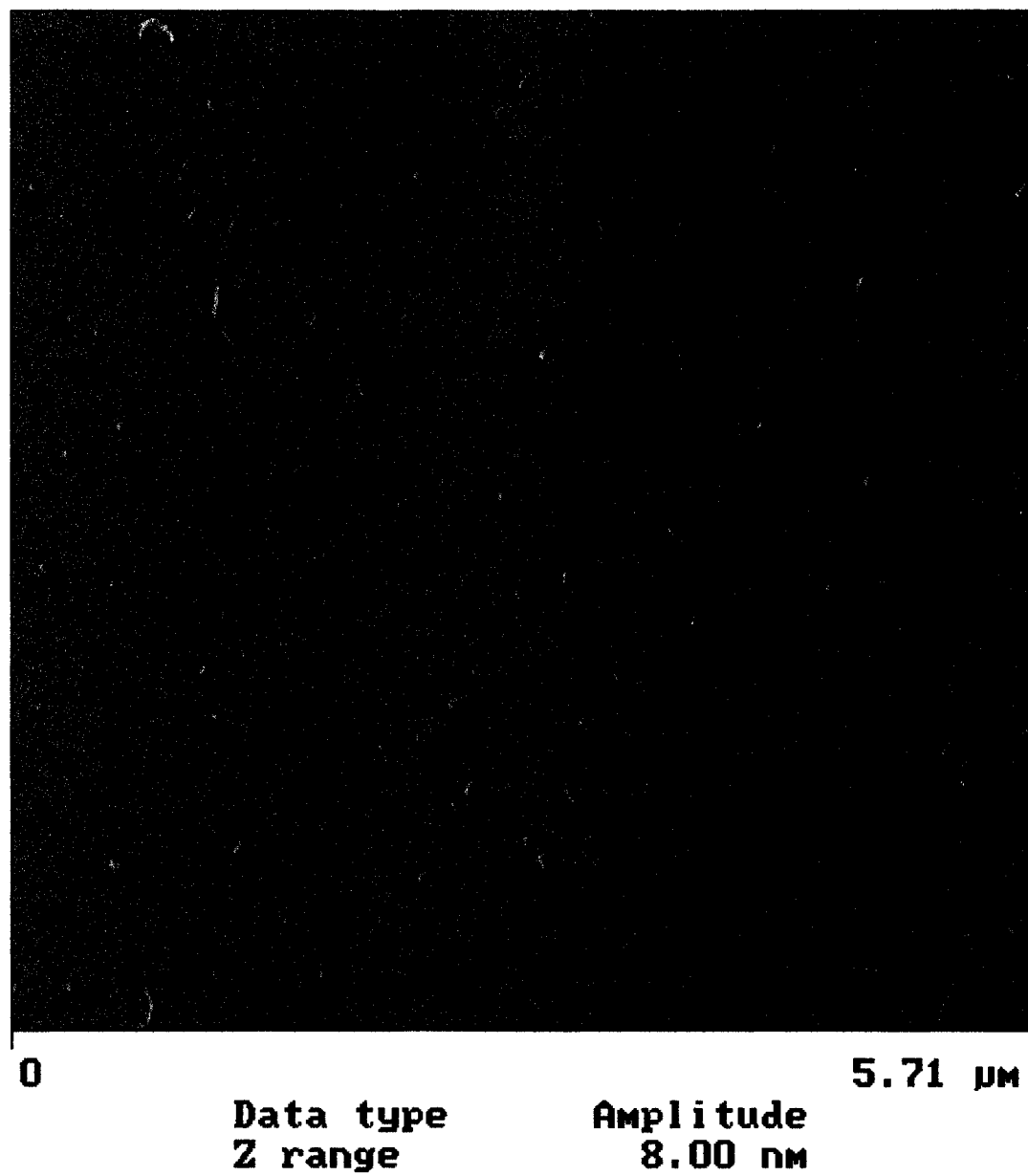


Figure 2-16 AFM image of the *cut-SWNTs* – I.

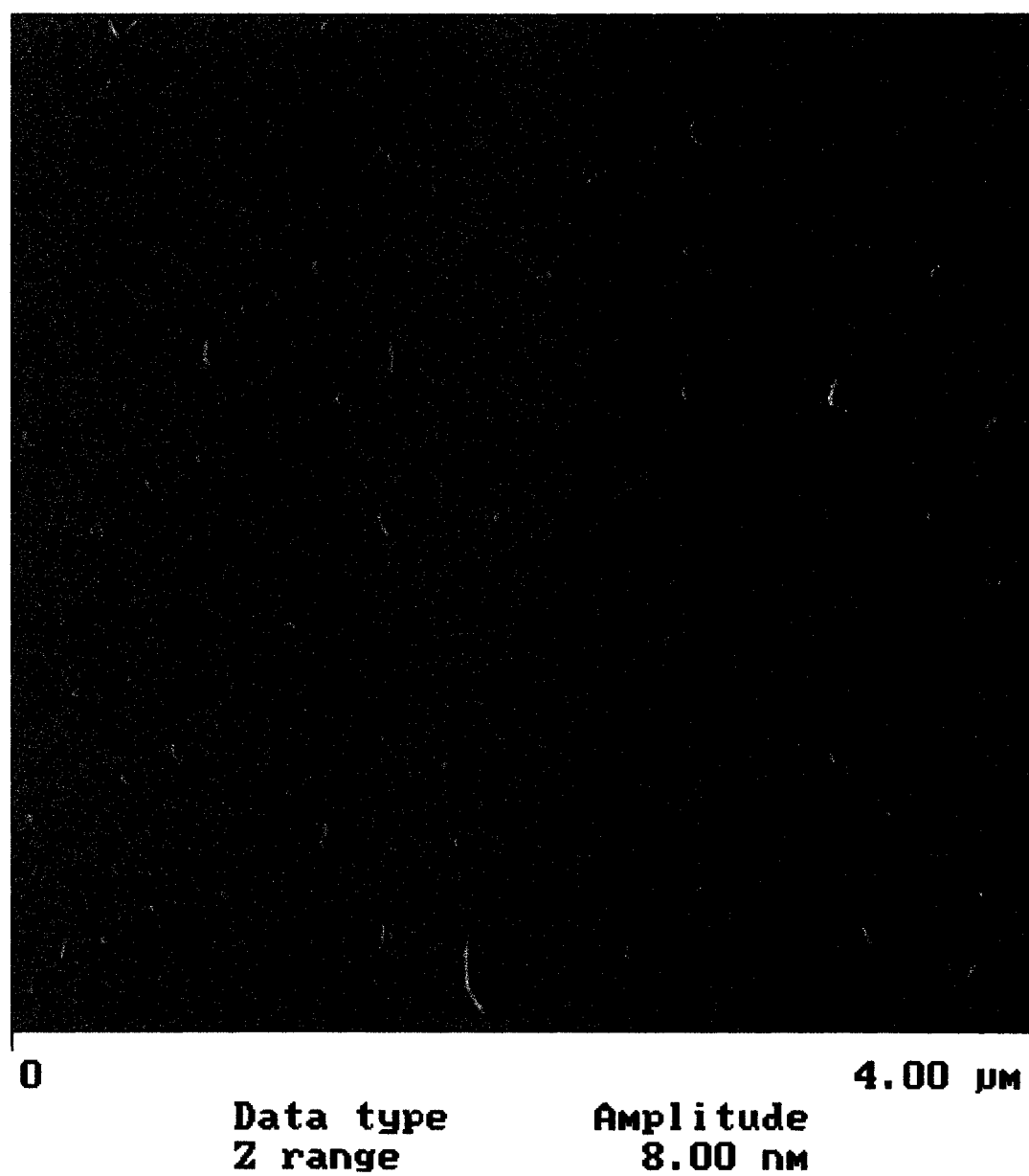


Figure 2-17 AFM image of the *cut-SWNTs* – II.

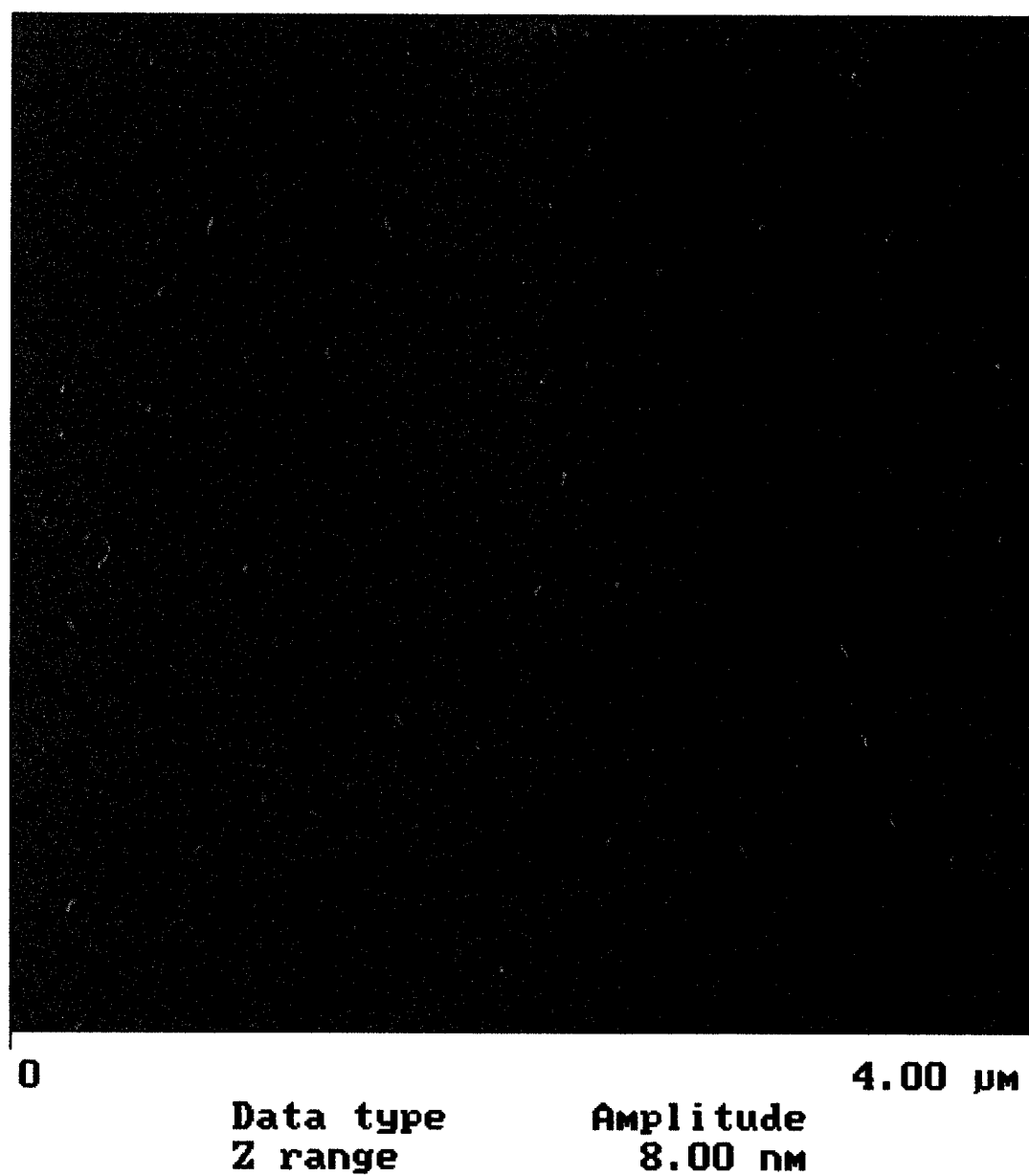


Figure 2-18 AFM image of the *cut-SWNTs* – III.

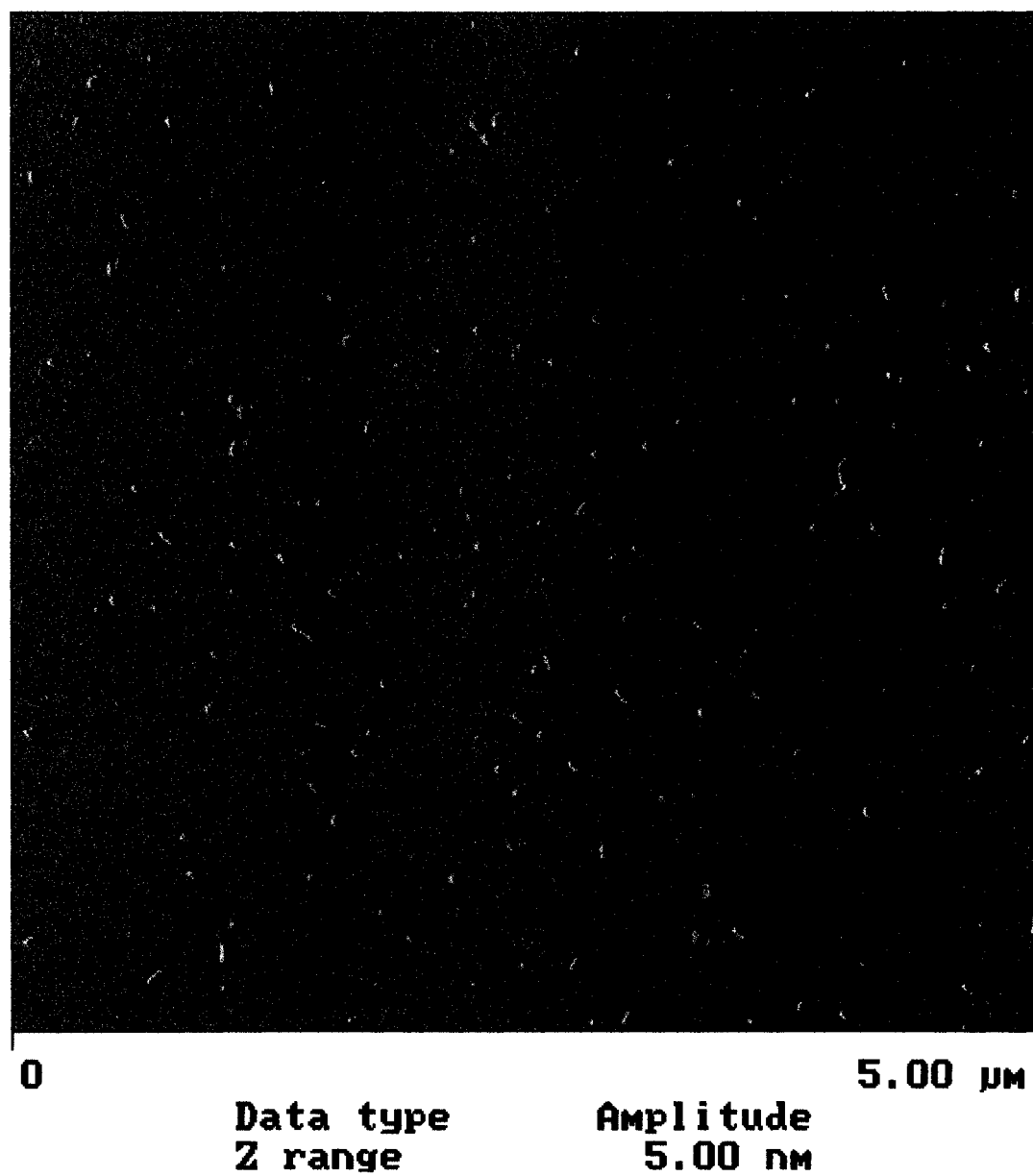


Figure 2-19 AFM image of the *cut-SWNTs* – IV.

the pyrolysis is apparent. The length distribution of the *cut-SWNTs* is shown in Figure 2-20(a). According to the AFM measurement, the average length of the *cut-SWNTs* bundles is ~ 40 nm, with $\sim 80\%$ of them shorter than 60 nm. In contrast, most of the *F-SWNTs* are longer than 1 μm as shown in Figure 2-15. AFM height analyses indicate that the average bundle size (i.e. the diameter of nanotube bundles) is ~ 8 nm for the *F-SWNTs* and is ~ 6 nm for the *cut-SWNTs*, as shown in Figure 2-20(b). Taking into consideration the effect that sidewall fluorine causes on the overall bundle sizes, there is no distinct change of the nanotube bundle sizes during the pyrolysis. It implies that the cutting in the pyrolysis process actually goes through the nanotube bundles.

We believe that the mechanism of the cutting is correlated with the C – F bond strength on fluorinated HiPco SWNTs and the distribution pattern of the fluorine atoms along the sidewall of the SWNTs. Theoretical calculations suggest that thermodynamic stability of *F-SWNTs* increases with decreasing tube diameter, and the mean bond dissociation energies of the C – F bonds increase as the nanotubes become thinner⁸³. It has been reported that the annealing of *F-SWNTs* with tube diameter ~ 1.35 nm at temperature as low as 100 °C could remove the sidewall fluorine groups and recover the pristine SWNTs⁹⁵. It implies that the C – F bonds dissociated to release fluorine in the larger diameter SWNTs. Whereas in our case, the “decomposition” of the *F-SWNTs* in inert atmosphere occurs at much higher temperature (i.e. ~ 300 °C), and there are considerable amounts of carbon atoms removed from the sidewall of nanotubes which are bound with fluorine. It is a clear contrast that indicates the C – F bond strength in our *F-SWNTs* is much higher than that of larger diameter SWNTs. According to the STM study of fluorinated SWNTs⁹⁶, the fluorine atoms tend to arrange around the

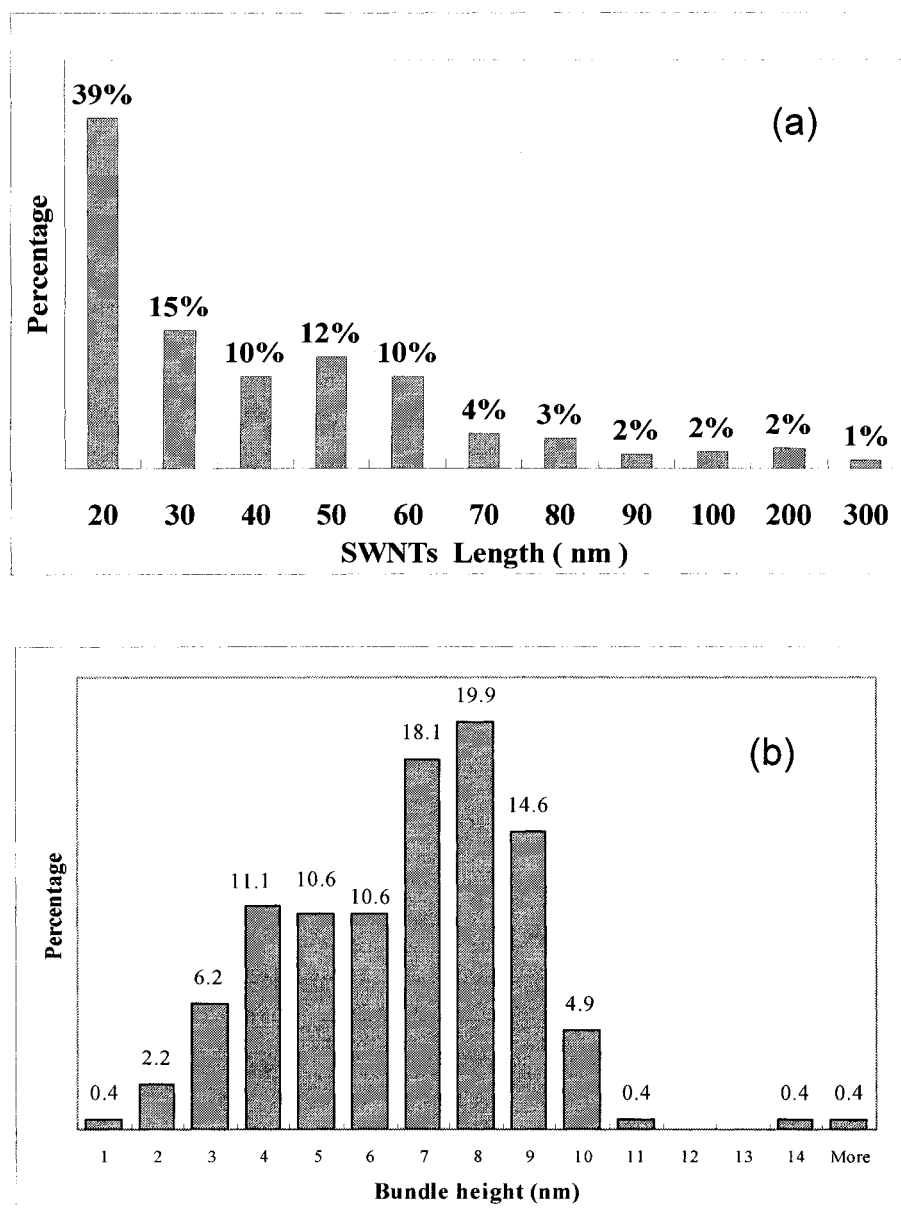


Figure 2-20 Histograms of length and bundle size distribution of the *cut-SWNTs*.

circumference of the nanotube and form band-like fluorinated areas along the nanotube sidewall. In the case of partially fluorinated SWNTs, the transition between the fluorinated and non-fluorinated bands typically remains quite abrupt and orthogonal to the SWNT axis. Since the fluorine atoms are localized in certain regions along the SWNTs sidewall and leave certain lengths of the SWNTs intact, one would expect that the pyrolysis would only affect the fluorinated part of the SWNTs and leave behind the intact parts of the SWNTs, resulting in the cut, short SWNTs. To explore this mechanism, a more detailed study of the correlation between the stoichiometry of the fluorinated SWNTs and the length distribution of the *cut-SWNTs* is needed.

2.2.4 Conclusion

To conclude, we have found that the originally microns long HiPco SWNTs can be cut into short pieces with an average length less than 50 nm by partial fluorination and pyrolysis. When the partially fluorinated SWNTs (C_5F) were pyrolyzed in argon atmosphere up to 1000 °C, volatile species such as COF_2 and CF_4 were released from the sample at different temperature ranges. Removal of carbon from the SWNT structure together with fluorine has broken the long-range tubular structure. Spectroscopic analyses and AFM measurements proved that the residues from the pyrolysis were short pieces of SWNTs without fluorine functionalities. The mechanism of the “cutting” was believed related to the specific distribution pattern of fluorine on the SWNT sidewalls in the partially fluorinated samples. The unique short lengths of the cut SWNTs will lead to specific reactivity on the ends and on the interior surface of the nanotubes. Effective

methods of sorting the *cut-SWNTs* to specific lengths will be required for many applications. One important step towards their application is to solubilize the *cut-SWNTs*. We have achieved this by chemical derivatization. Details are discussed next.

2.3 DERIVATIZATION OF THE CUT-SWNTS

2.3.1 Introduction

Cut-SWNTs are expected to possess interesting chemical properties due to their significantly smaller aspect ratio compared with the original SWNTs. It has been widely acknowledged that the carbon atoms at the ends of carbon nanotubes are chemically more reactive than the ones on the nanotube sidewall because the high curvature on the nanotube ends causes high bond strain. The high ends-to-sidewall carbon ratio of *cut-SWNTs* suggests that their chemical derivatizations could occur at milder chemical circumstances than that of the pristine SWNTs. One concern regarding the reactivities of the *cut-SWNTs* is whether they are thermally less stable than the pristine SWNTs in an oxidizing atmosphere. We have conducted a series of experimental studies to answer these questions, as schematically demonstrated in Figure 2-21. The *cut-SWNTs* have been refluorinated to atomic F/C ratio of 0.5. They were also refluxed in dilute HNO_3 to get them oxidized. Alkylation reactions were explored with refluorinated *cut-SWNTs*. These chemical manipulations were found capable of attaching specific functional groups on *cut-SWNTs*. Distinctively enhanced solubilities of the derivatized *cut-SWNTs* in various solvents such as isopropanol, ethanol, hexane and CHCl_3 were achieved.

2.3.2 Experimental

The thermal stability of the *cut-SWNTs* in an oxidizing atmosphere was tested by conducting TGA analysis of the sample in air. The sample was heated to 800 °C at a rate of 5 °C / minute. The results were compared with that of the purified SWNTs. The effect of brief sintering on the structure of the *cut-SWNTs* was examined by heating the sample to 500 °C at a rate of 5 °C / minute and keeping at 500 °C isothermally for 30 minutes. The sintered sample was examined by micro Raman spectroscopy and was compared with that of the *cut-SWNTs*.

The refluorination of the *cut-SWNTs* was conducted under the same conditions as the fluorination of purified uncut SWNTs, i.e., at 150 °C, for 12 hours. The refluorinated *cut-SWNTs* (*F-cut-SWNTs*) were characterized with micro Raman and ATR-IR. The dissolution of the *F-cut-SWNTs* was tested in 2-isopropanol (IPA), brief ultrasonication was involved.

The oxidative derivatization of the *cut-SWNTs* with HNO₃ was conducted by refluxing the *cut-SWNTs* sample in 1 M HNO₃ for ~15 hours. The sample was collected from the solution by vacuum filtration and was dried in vacuum oven at ~70 °C overnight before characterization with micro Raman and ATR-IR. The dissolution of the HNO₃ derivatized *cut-SWNTs* was tested in ethanol with brief ultrasonication.

The alkylation of the *cut-SWNTs* was achieved by reacting the *F-cut-SWNTs* with hexyl lithium at ~-40 °C. The hexylated *cut-SWNTs* were characterized with micro

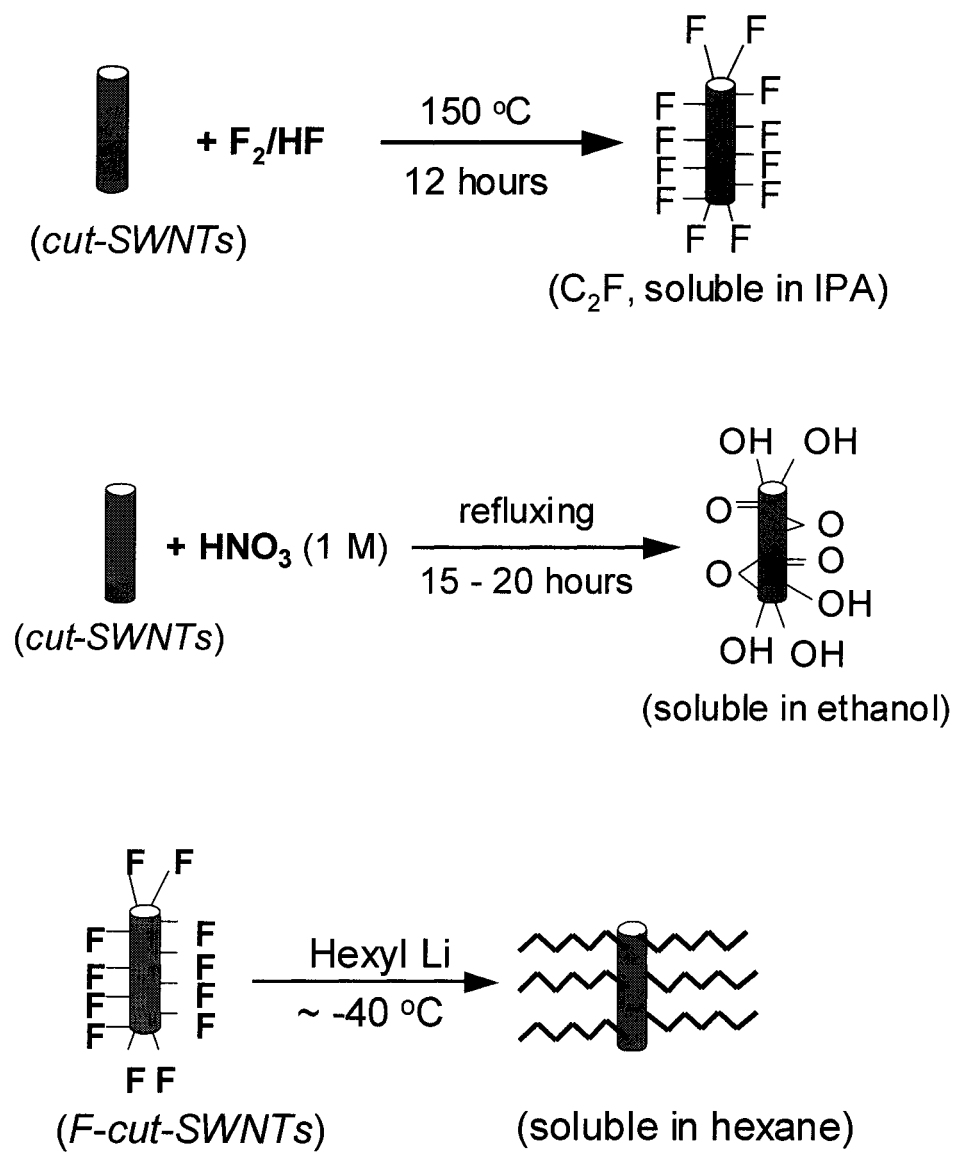


Figure 2-21 Schematic demonstration of derivatization of *cut-SWNTs*.

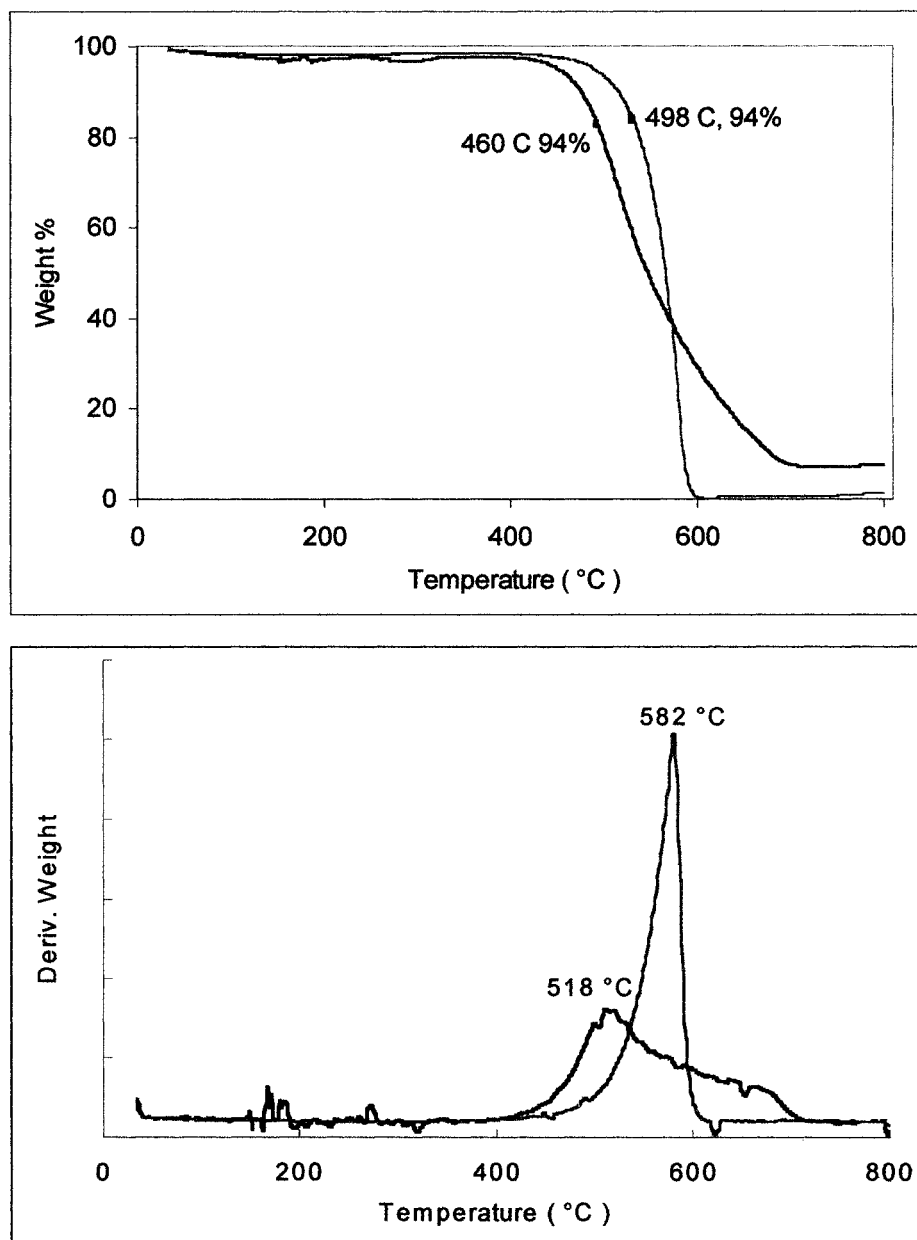


Figure 2-22 TGA plots of *cut-SWNTs* (pink curves) vs. purified SWNTs (dark blue curves): comparison of thermal stability in air.

Raman and ATR-IR. The dissolution of the hexylated *cut-SWNTs* was tested in hexane and CHCl_3 with very brief ultrasonication.

2.3.3 Results and Discussion

The TGA (in air) result of the *cut-SWNTs* was plot in Figure 2-21 and compared with that of the precursor, purified HiPco SWNTs. The weight loss curves (above one) indicates that the oxidation initiation temperature of the *cut-SWNTs* is $\sim 500^\circ\text{C}$, which is in the range of the typical oxidation initiation temperature of the purified HiPco SWNTs. It proves that the thermal stability of the *cut-SWNTs* in an oxidizing atmosphere is about the same as the precursor HiPco SWNTs. In other words, the increase in the relative amount of carbon at ends of nanotubes doesn't affect their thermal stability in an oxidative atmosphere. In the bottom plot in Figure 2-21, the derivate weight loss curves of the *cut-SWNTs* and of the precursor HiPco SWNTs are compared. The sharp feature of the *cut-SWNTs* peaking at 582°C in contrast with the much broader feature of the precursor HiPco SWNTs peaking at $\sim 518^\circ\text{C}$ indicates that the *cut-SWNTs* have a narrow distribution in thermal stability. It reflects a certain degree of selectivity during the partial fluorination and pyrolysis cutting processes. More specifically, the absence of the lower thermal stability part in the *cut-SWNTs* might be due to the consumption of the highly fluorinated part from the nanotube sample, which could be the consequence of certain type of selectivity during fluorination reaction. No matter what caused the difference in the derivate weight curves, the overall effect is minor compared with the major cutting result from the series of chemical treatment because the thermal decomposition behavior

of the *cut-SWNTs* in an oxidative atmosphere basically followed that of the precursor SWNTs.

The Raman spectra of the *cut-SWNTs* before and after sintering were compared in Figure 2-23. The notable difference between the two spectra is the decrease in intensity of the disorder mode of the sintered sample, also the decrease in intensity of the 264 cm^{-1} mode. We attribute the difference in the Raman spectra to the removal of the dangling carbon atoms by oxygen as CO_2 . The 264 cm^{-1} mode is generally believed to indicate the roping extent of the SWNT samples. In this case, the decrease of the 264 cm^{-1} mode implies that the roping in the *cut-SWNTs* was somehow disintegrated with sintering process. We believe this is also the effect of the removal of the dangling carbon because these unsaturated carbon atoms might tend to interlink between SWNTs and cause a denser roping pattern.

The refluorination of the *cut-SWNTs* at $150\text{ }^{\circ}\text{C}$ for 12 hours resulted the *F-cut-SWNTs* with stoichiometry $\text{CF}_{0.65}$. The atomic F/C ratio was considerably higher than that of the uncut SWNTs fluorinated under the same conditions. We believe this is due to the higher ratio of reactive carbon (i.e. the carbon on ends of nanotubes) in the *cut-SWNTs*. The ATR-IR spectra of the *cut-SWNTs* before and after refluorination are compared in Figure 2-24. The high intensity, one-component C – F mode and the absence of the C = C mode the Figure 2-24(b) indicate that the refluorination is complete. The Raman spectra of the *cut-SWNTs* before and after refluorination are compared in Figure 2-25. Figure 2-25(b) is very similar to the Raman of the fluorinated uncut HiPco SWNTs. The relatively high intensity of the disorder mode and the broad and low-intensity tangential mode symbolize the complete fluorination. The dissolution test of the

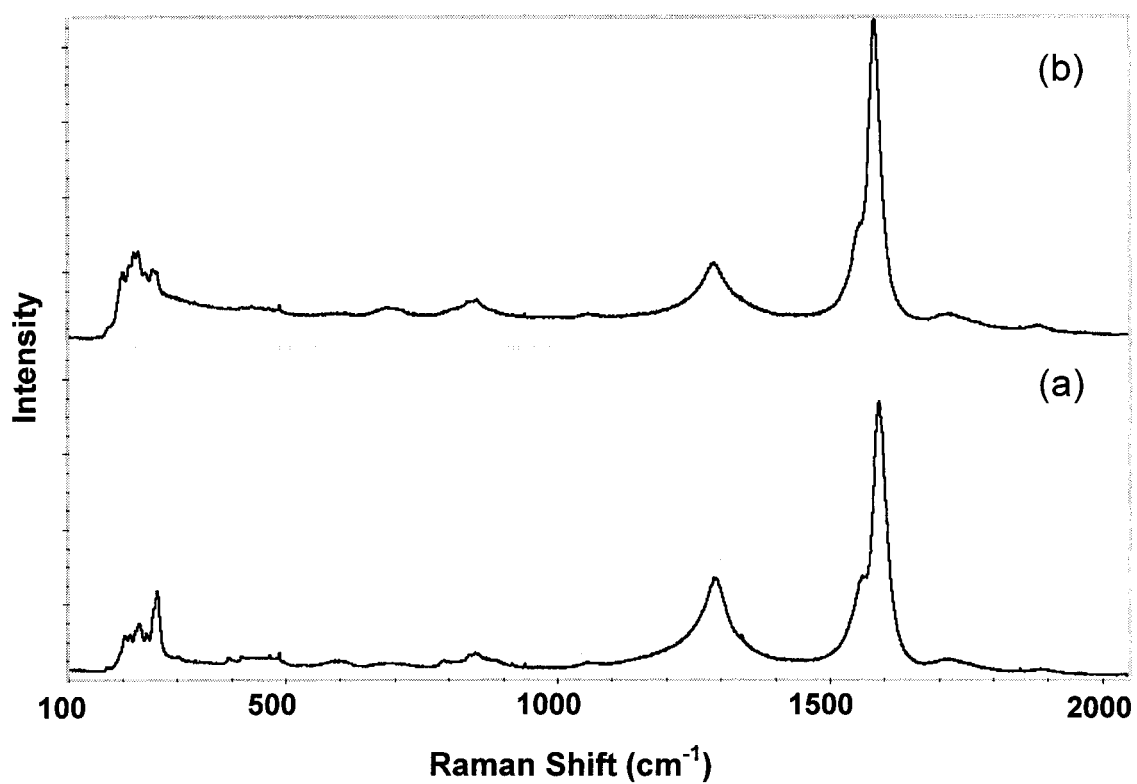


Figure 2-23 Raman spectra of *cut-SWNTs* before (a) and after (b) short period oxidation in air up to 500 °C.

F-cut-SWNTs in IPA showed that the *F-cut-SWNTs* could be easily dispersed in IPA and such a suspension was stable and no precipitation was observed for several months.

The ATR-IR spectra of the *cut-SWNTs* after HNO_3 refluxing process were shown in Figure 2-26. Because of the low intensities of the IR modes in the original spectrum, a baseline correction was conducted and the absorbance axis was scaled up by a factor of 10. Several carbon-oxygen related modes show up in the processed spectrum [Figure 2-26(b)]. The mode at 1120 cm^{-1} is assigned to the C – O – C bonding pattern, the mode at 1569 cm^{-1} belongs to the activated C = C bonds, the mode at 1708 cm^{-1} indicates the formation of C = O bonds, which, together with the broad mode centered at $\sim 3340\text{ cm}^{-1}$, suggest the formation of carboxylic acid groups. The low intensities of these modes might be because that most of them were located at the ends area of the *cut-SWNTs*, and their special orientations cause the low absorbance in the ATR-IR spectrometer. The modification of the sidewall functionalization on the SWNT structures was demonstrated in Figure 2-27. The fact that the disorder mode is higher in intensity than the tangential mode indicates that the amount of functional groups is relatively high. By comparing Figure 2-27(b) with Figure 2-25(b), the influence of the carbon-oxygen functional groups is apparently not as strong as that of the fluorine on the nanotube structures. The various carbon-oxygen functional groups formed on the *cut-SWNTs* actually have modified the SWNT properties of the nanotube sidewall significantly, because such derivatized *cut-SWNTs* have shown greatly enhanced solubility in ethanol.

The ATR-IR spectrum of the hexylated *cut-SWNTs* is shown in Figure 2-28. Comparing the IR spectrum of the precursor, *F-cut-SWNTs*, in Figure 2-24(b), the disappearance of the C – F mode and the appearance of the typical hexyl C – H modes in

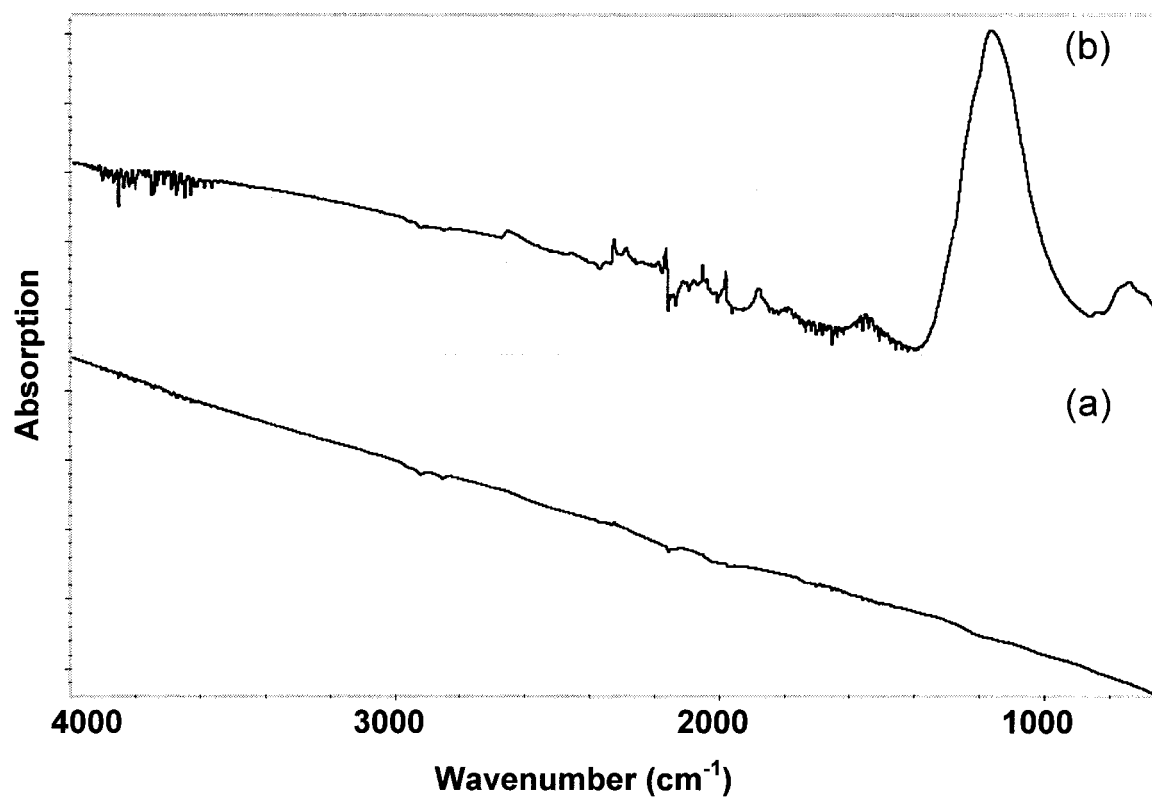


Figure 2-24 ATR – IR spectra of the re-fluorinated *cut-SWNTs* (b) vs. *cut-SWNTs* (a).

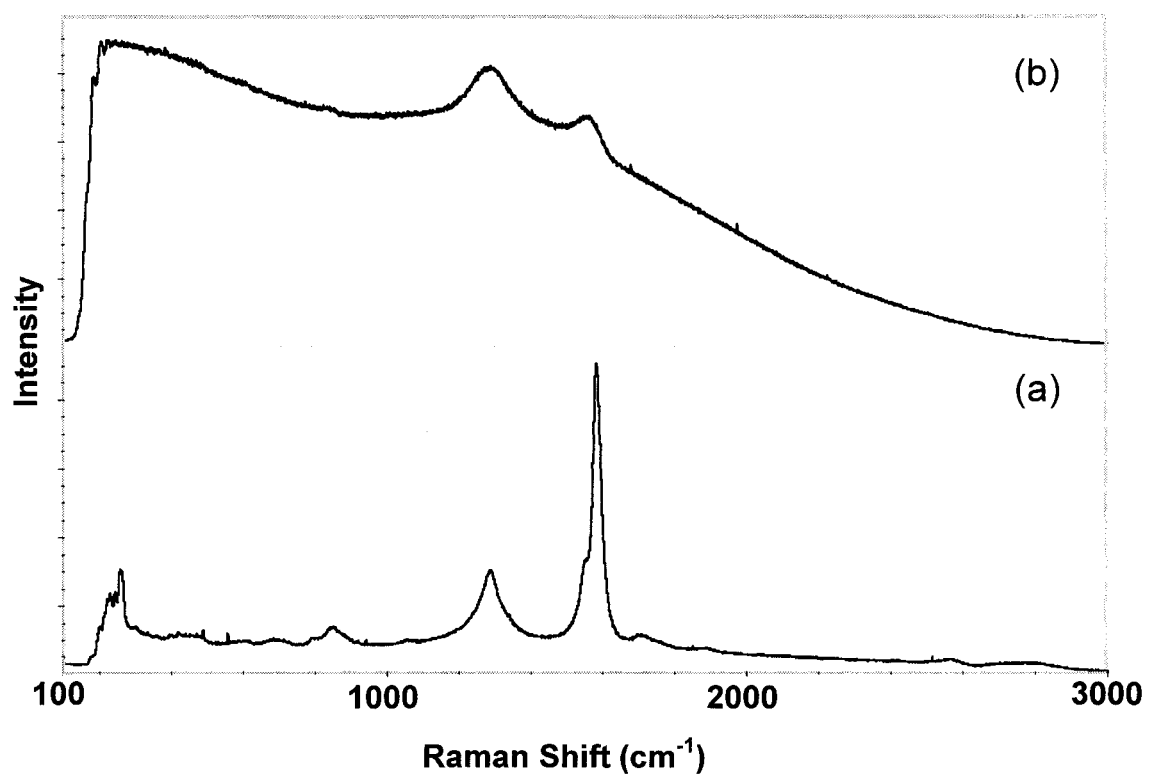


Figure 2-25 Raman spectra of the re-fluorinated *cut-SWNTs* (b) vs. *cut-SWNTs* (a).

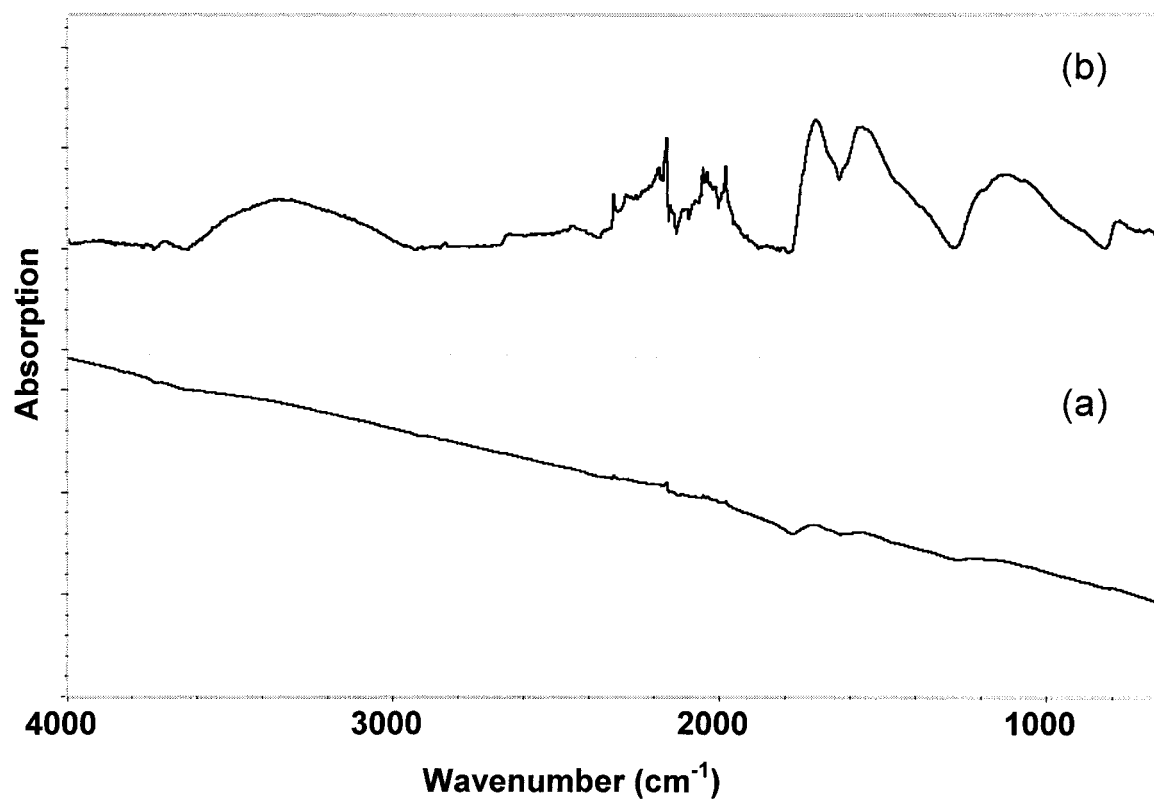


Figure 2-26 ATR-IR spectra of the nitric acid treated *cut-SWNTs* (a); (b) is (a) after baseline correction and $\times 10$.

the range of $2850 - 2960\text{ cm}^{-1}$ show strong evidence of the substitution of the fluorine functionalities by the hexyl groups on nanotube sidewalls. The vibration frequency of the C – H modes of the hexylated *cut-SWNTs* are at least 10 cm^{-1} lower than those of the *n*-hexane, which implies that the hexyl groups are covalently attached to the nanotubes in the hexylated *cut-SWNTs* samples. The 1565 cm^{-1} mode in Figure 2-28 is the typical activated C = C stretching mode in derivatized SWNT sample. The series of peaks in $1000 - 1500\text{ cm}^{-1}$ region was assigned to the bending modes and umbrella (rocking) modes of the methyl groups⁸¹. The Raman spectra of the hexylated *cut-SWNTs* and the precursor *F-cut-SWNTs* were compared in Figure 2-29. Again, the relatively high intensity of the disorder mode in Figure 2-29(b) indicates the degree of derivatization in this sample is high. The substitution of the fluorine with hexyl groups on the nanotube sample seems to decrease the distortion of the nanotube structure. This is reasonable because fluorine functionality is a very strong electron-withdrawing group, whereas hexyl functionality is an electron-pushing group. The hexylated *cut-SWNTs* form surprisingly high concentration suspensions in either hexane or CHCl_3 . We believe it is because the hexyl functional groups wrap around the nanotube sidewalls so that the surface properties of the hexylated *cut-SWNTs* are actually determined by the hexyl groups.

2.3.4 Conclusion

We have successfully derivatized the *cut-SWNTs* through chemical processes such as refluorination, refluxing in HNO_3 , and hexylation with hexyl Li. The refluorination of

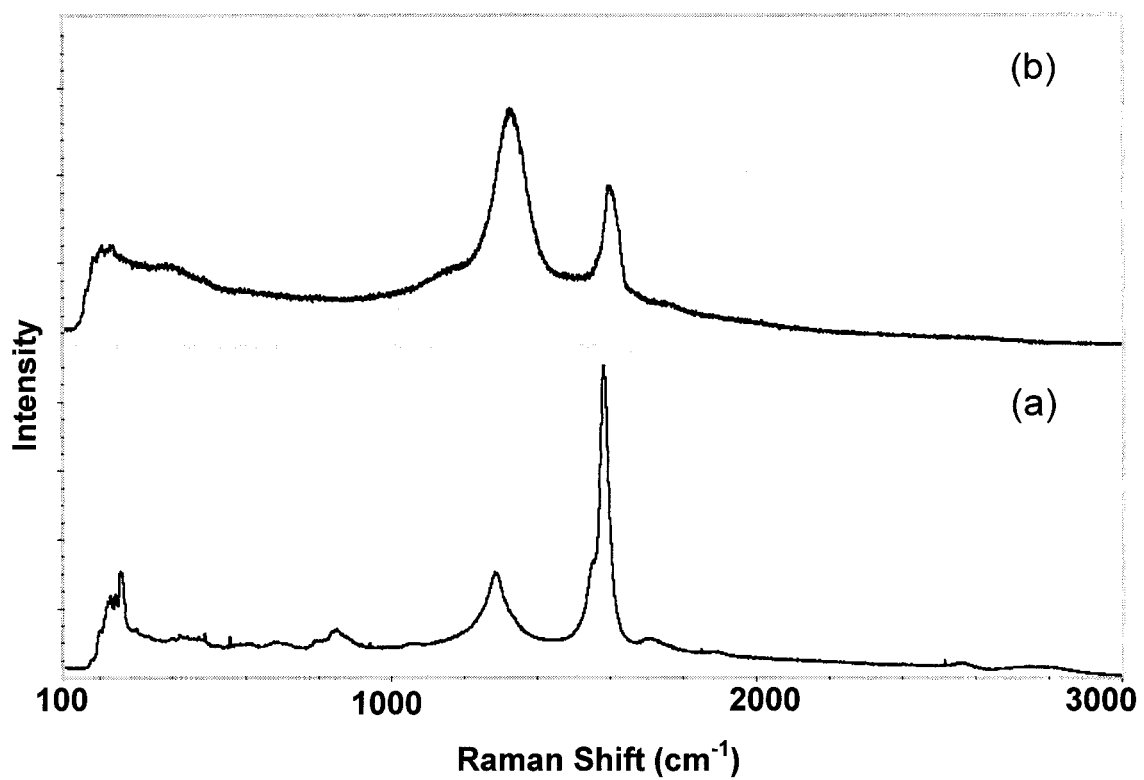


Figure 2-27 Raman spectra of HNO₃ treated *cut-SWNTs* (b) vs. *cut-SWNTs* (a).

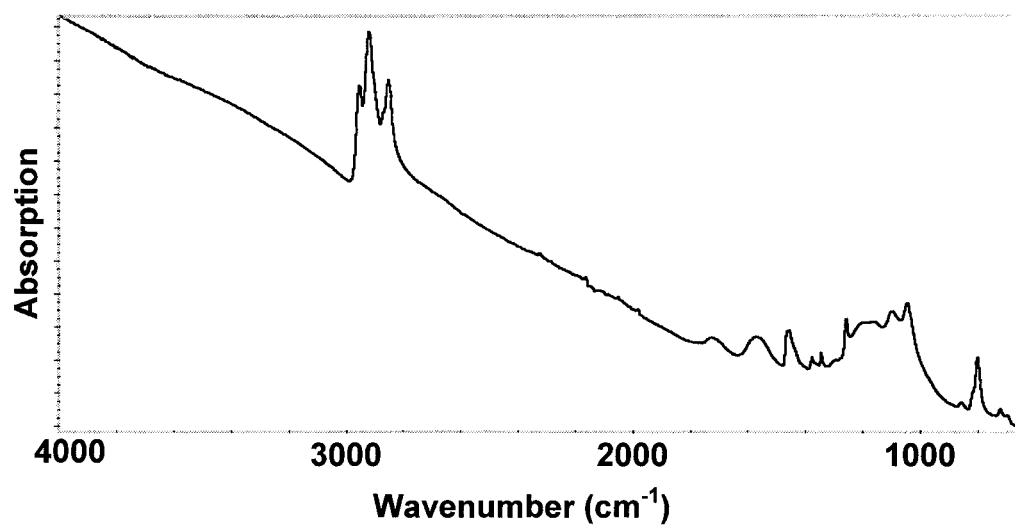


Figure 2-28 ATR-IR spectra of the hexylated *cut*-SWNTs

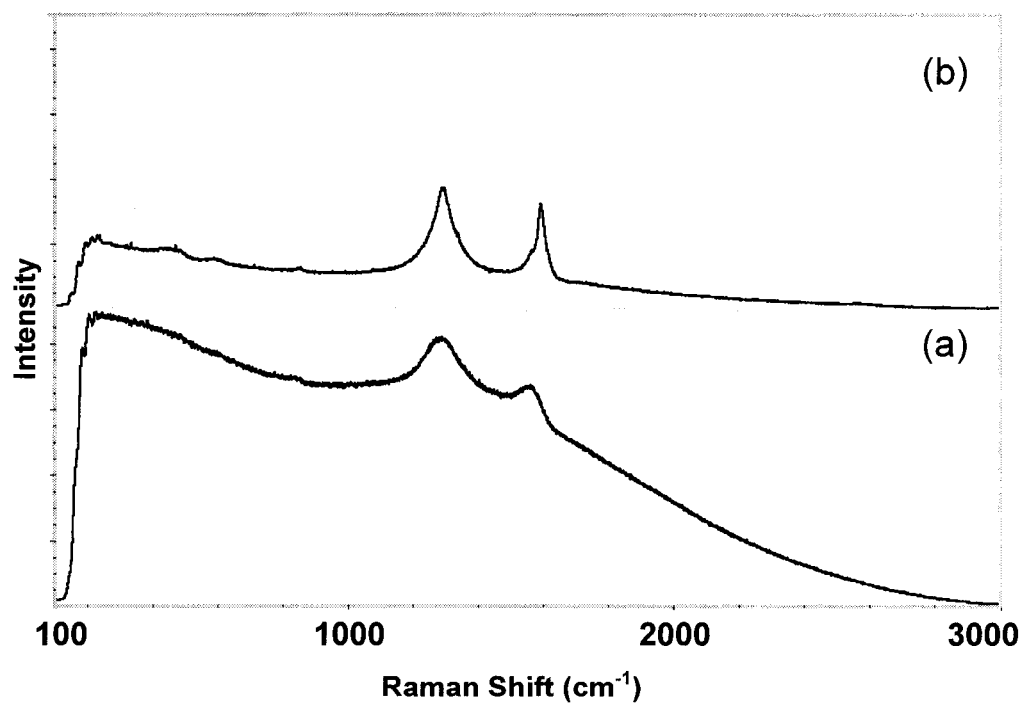


Figure 2-29 Raman spectra of the re-fluorinated *cut*-SWNTs (a) and after hexylation (b).

the *cut-SWNTs* created *F-cut-SWNTs* with stoichiometry $\text{CF}_{0.65}$, which is higher in atomic F/C ratio than the uncut HiPco SWNTs fluorinated under the same conditions. It indicates that the *cut-SWNTs* are more reactive in fluorination than the uncut SWNTs. The *F-cut-SWNTs* also show similar solubility in IPA as the fluorinated HiPco SWNTs with stoichiometry C_2F . The HNO_3 refluxing process resulted in the formation of carbon-oxygen functionalities such as $\text{C}-\text{O}-\text{C}$, $\text{C}=\text{O}$ and $\text{C}-\text{O}-\text{H}$ on the *cut-SWNTs*. These functional groups don't cause the same extent of distortion of the nanotube structures as fluorination, but the solubility of the HNO_3 treated *cut-SWNTs* in ethanol is greatly enhanced. The hexylation of the *cut-SWNTs* is achieved with *F-cut-SWNTs* as reaction precursor. The substitution of the fluorine with hexyl groups on the nanotube sample seems to decrease the distortion of the nanotube structure. The hexylated *cut-SWNTs* form concentrated and stable suspension in solvents such as hexane and CHCl_3 , which is believed related to the wrapping of the hexyl functionalities on the *cut-SWNTs* surfaces.

Chapter 3

OZONOLYSIS OF SINGLE-WALL CARBON NANOTUBES

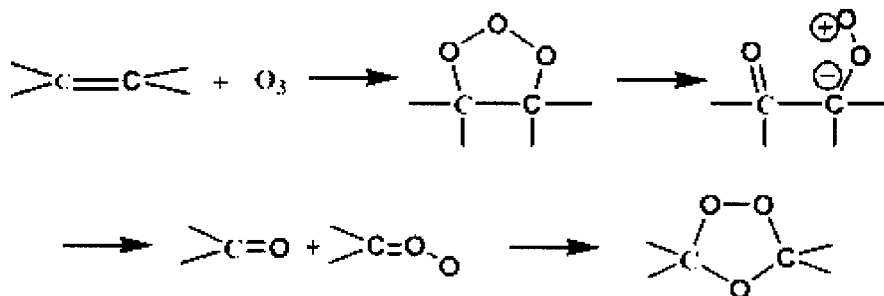
3.1 INTRODUCTION

The remarkable physical properties integrated into the 1D nanostructures makes SWNTs one of the most important building blocks in nanoscale world. However, because of their chemical inertness and the van der Waals attraction between sidewalls, the chemical manipulations of SWNTs become very challenging. Although there have been extensive studies on the chemical reactivities of SWNTs, most of them have been dealing with SWNT bundles. The diffusion process of chemical reagents through the stacked SWNT bundles might cause significantly different reaction circumstances for SWNTs on surface layer of the bundles and the ones in the core part. As a result, the reaction products could be mixture of highly derivatized SWNTs and the intact ones. It makes the characterization of SWNTs functionalization very complicated.

To study the reactivity of individual SWNTs, there has to be a system in which individual SWNTs instead of bundles are dispersed, so that they have equal exposure to the chemical reagents. Such a system recently became available due to the extraordinary discovery⁸⁹ that SWNTs suspended in aqueous surfactant solution such as SDS (sodium dodecyl sulfate) through high-power ultrasonication and high-speed centrifuging are mainly individual ones that have been isolated from each other with surfactant micelles. A series of important scientific phenomena have been observed about the individually dispersed SWNTs system, for example, distinctively enhanced and resolved van Hove

transition absorption spectra, the fluorescence emission from SWNTs. These observations have led to the detailed structure assignment of SWNT samples ⁹⁷, which provides a practical spectroscopic route for determination of detailed composition of bulk nanotube samples, and an important reference for theoretical predictions. The individually dispersed SWNT system also enables studies of SWNT reactivities on an unprecedented level. However, along with the individually dispersed SWNTs, there are many other factors worth consideration in such a system, for example, the reactivities of the surfactant molecules, the stability of the micelles, the pH effect and influence of absorbed ambient oxygen, etc. We have carried out a systematic study on the interaction between ozone and individually dispersed SWNTs at the gas-aqueous solution interface.

The reactions of ozone with fullerene species have been studied by many research groups during last decade. Early experiments were carried out by exposing fullerene in toluene solutions to ozone. McElvany et al ⁹⁸ found that ozone exposure of C₆₀ and C₇₀ can cause an opening of the fullerene cage and a subsequent reaction with another C₆₀ or C₇₀ to yield a larger carbon cluster. The authors suggested controlled ozone-catalyzed cage-opening reactions could be a new route to functionalize and derivatize fullerenes. Chibante and Heyman ⁹⁹ reported formation of [60]fullerene epoxides, C₆₀O_n (n = 1-5), which are soluble in toluene. Malhotra et al studied the “ozonolysis” of [60]fullerene under the similar conditions ¹⁰⁰. They found that even brief ozone exposure led to formation of highly oxidized derivatives of [60]fullerene, which precipitated from solution. According to the Criegee's mechanism of reaction between ozone and olefins ¹⁰¹, as shown in Scheme 1, ozone undergoes 1,3-dipolar cycloaddition reaction with olefins.



Scheme 1. Criegee's mechanism of ozone reacting with olefin.

Similar reaction was believed occurs when [60]fullerene exposes to ozone, which forms the initial C₆₀ molozonide, C₆₀O₃¹⁰⁰, as shown in Figure 3-1. More recent study revealed more detailed formation and dissociation behavior of the fullerene ozonide¹⁰², and reported the two C₆₀O isomers from the dissociation of C₆₀O₃ under different excitation conditions, as shown in Figure 3-1¹⁰³. Mawhinney et al¹⁰⁴ observed ozone “etching” SWNTs by depositing methanol suspension of SWNTs onto a CaF₂ crystal. Such prepared sample was then annealed to remove the residue oxygen-containing functional groups before it was exposed to ozone. The IR spectra they collected suggested that the reaction produced two distinct surface-bound functional groups, esters and quinines, as well as gas-phase CO₂ and CO. Cai et al carried out a gas-solid interface reaction of UV generated O₃ and bucky-paper SWNTs¹⁰⁵. They found that the ozonation of SWNTs resulted in improved solubility of SWNTs in water and increased resistance. Pristine SWNTs could be restored by annealing the ozone-treated SWNTs. The carboxylic groups formed on the SWNTs through ozonation could immobilize the nanotubes on surface of rigid molecule SAMs. Banerjee et al¹⁰⁶ studied the ozonolysis of SWNTs in methanol dispersion at -78 °C, followed by treating the ozonated SWNTs with various reagents to

generate a higher proportion of carboxylic acid/ester, ketone/aldehyde, and alcohol groups. Their proposed reaction sequence is shown in Figure 3-2.

This chapter describes our experimental study on the ozone reaction with SWNTs. First there is a brief summary of our observations on ozone reaction with bucky-paper HiPco SWNTs and the thermal decomposition behavior of the ozone treated bucky-paper. Then the main part is our spectroscopic and AFM investigations of ozone reaction with individually dispersed SWNTs on a gas-solution interface. This includes a short section about the cutting effect we have observed on intermittent ozone exposure of individually dispersed SWNTs, and a detailed in-situ Raman and UV spectroscopic study on the gas-solution reaction system. The behavior of the resonant Raman modes, the disorder mode, the fluorescence spectra, and the van Hove transition absorption of the individually dispersed SWNTs during ozone exposure are discussed. The influence of pH variation and surfactant types on the reaction system was also explored. Controlling of the ozonation in order to achieve effective cutting, instead of massive etching of SWNTs is proposed, as well as the possibility of creating distribution-controlled reactive sites with ozonation and “triggering” the cutting reaction with secondary reagents.

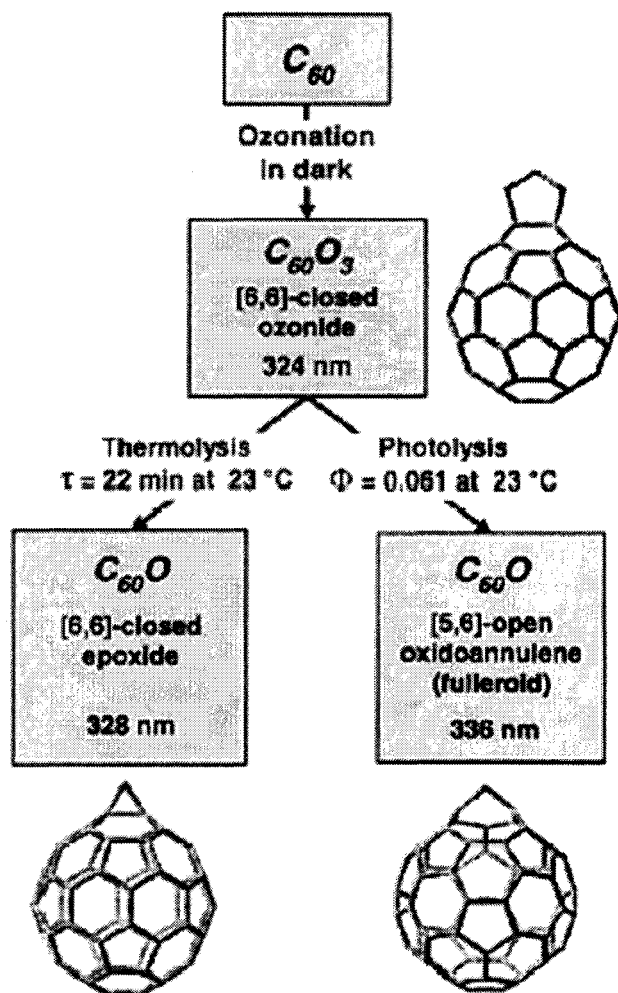


Figure 3-1 Species formed in C_{60} ozonation reaction. (Adapted from ref. Weisman, R. B. et al. *J. Am. Chem. Soc.* **2001**, 123, 9720.)

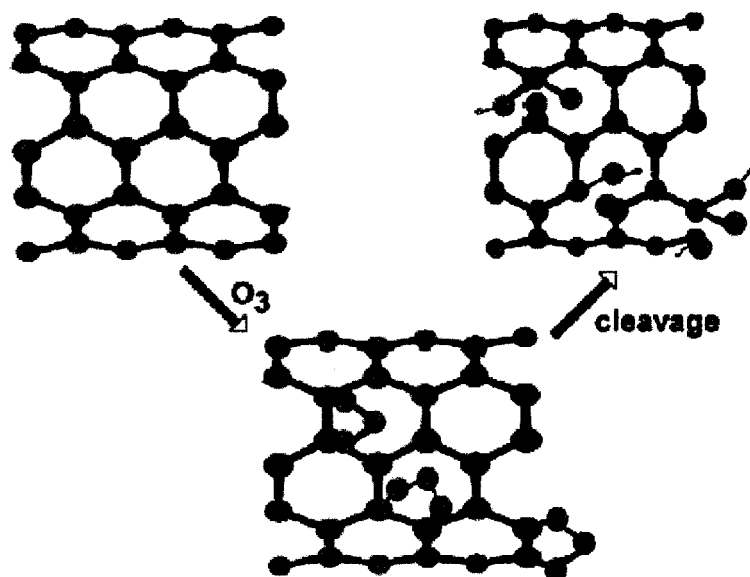


Figure 3-2 Schematic demonstration of ozonation of SWNTs and subsequent cleavage of the sidewall ozonide with secondary reagents. (adapted from ref. Banerjee, S. and Wong, S. S. *J. Phys. Chem. B* **2002**, *106*, 12144.)

3.2 OZONOLYSIS OF PURIFIED SWNTS ON GAS-SOLID INTERFACE

3.2.1 Experimental

The reaction of ozone with SWNTs on gas–solid interface was studied with bucky-paper of purified HiPco SWNTs. The sample was annealed in helium atmosphere up to 800 °C before use. The reaction was carried out in a TGA furnace that was isothermal at 50 °C during the reaction. The bucky-paper sample was loaded in a TGA sampling pan and delivered into the furnace. Gaseous mixture of ozone/oxygen was flowing through the TGA furnace for 100 minutes. Ozone was generated from oxygen gas through the GE60FM/12VDC ozonation system from Ozone Services. The total amount of ozone generated could be adjusted by controlling the flow rate of the starting oxygen, and by controlling the ozone concentration through varying the frequency of the discharge. In this experiment, the total flow rate of the ozone/oxygen gas mixture was 125 ml/min., and the ozone concentration in the mixture was 7 gram/m³. So the ozone fractional flow rate in the gas mixture was 1.82×10^{-5} (mol/min.). The weight variation of the sample during the ozone exposure was monitored with TGA. After the reaction, the sample was characterized with Raman and ATR-IR to determine the derivatization. The ozone treated sample was annealed in argon atmosphere up to 800 °C and its thermal decomposition behavior was monitored with TGA. Such annealed sample was analyzed with Raman and ATR-IR to study the desorption of the attached functional groups.

3.2.2 Results and discussions

The bucky-paper had gained over 8% weight (which is ~0.9 mg according to the absolute weight of the bucky-paper sample used in the experiment) during the 100 minutes ozone treatment, as shown in Figure 3-3. We've known that the bucky-paper didn't absorb oxygen under the experimental conditions, because when pure oxygen flew over the sample, there was no weight gain observed, as shown in the first 5 minutes of the TGA curve. Therefore the weight gain of the bucky-paper was caused by ozone only. The total amount of ozone flew through the sample during the 100 minutes experiment period was ~87.5 mg, so about 1% of the oxygen atoms from ozone were absorbed onto the bucky-paper sample. If we consider all the oxygen atoms were chemically bound to the SWNTs (which is a reasonable assumption because the post-experiment purging with argon at the same temperature didn't result in any weight loss of the ozone treated bucky-paper), then a simple calculation indicates that in average every 16 carbon atoms there was one formed bond with oxygen during the reaction. The number means that it's not possible that the oxygen only bound to the carbon at the ends, the kinked part, or the defect sites of the nanotubes. It denotes that ozone is reactive enough to add oxygen-containing functionalities to the sidewall of SWNTs at 50 °C. Also it is noticeable that the weight gain curve from TGA is not linear. The tendency implies that the reaction rate is determined by the active sites on the SWNTs. With more functional groups attached, the reaction rate decreased accordingly.

Figure 3-4 shows the ATR-IR spectra of the ozone treated bucky-paper. Surprisingly, we found that the experiment resulted highly functionalized surface layer and the almost intact inner part of the bucky-paper. On Figure 3-4(a), there are clear

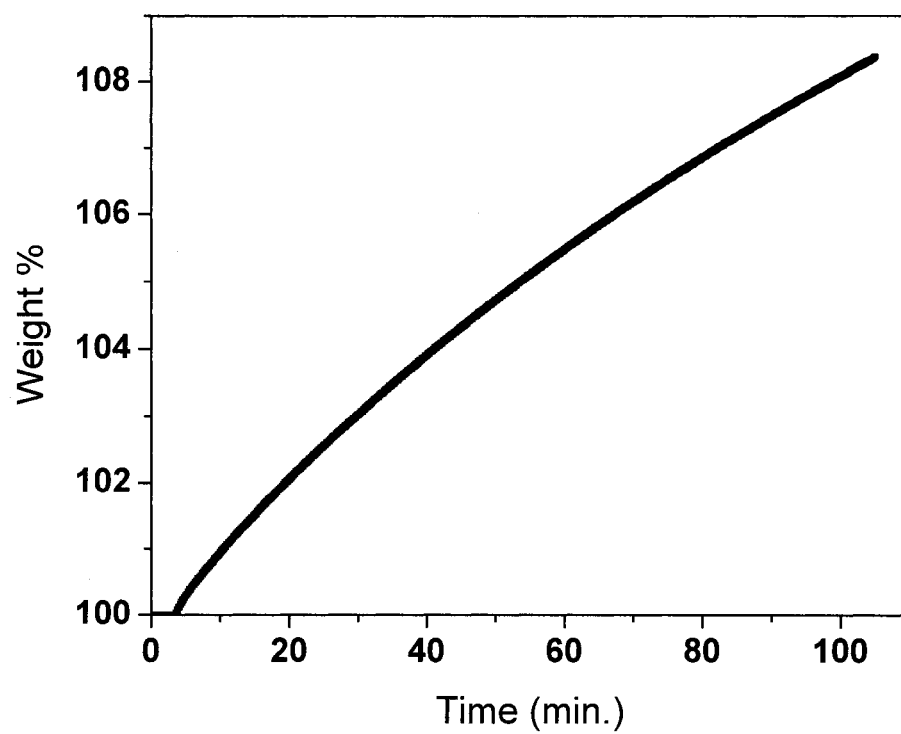


Figure 3-3 TGA of bucky-paper sample during ozone exposure.

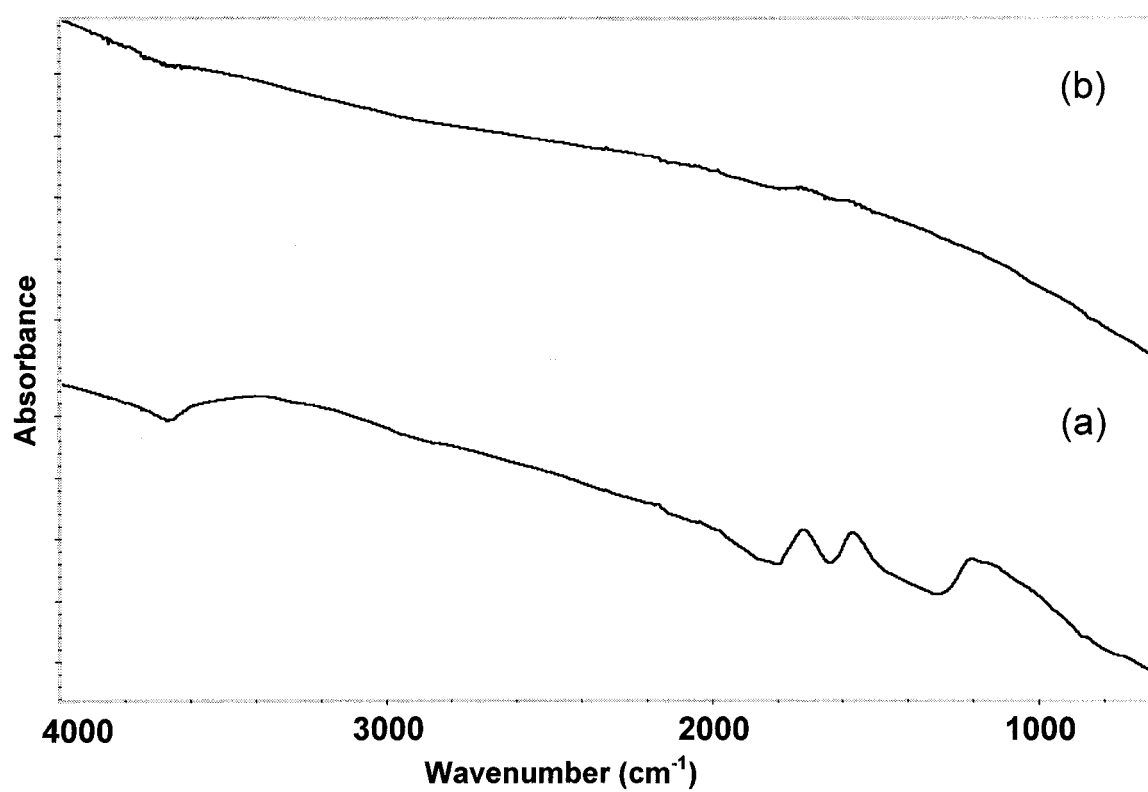


Figure 3-4 ATR-IR spectra of ozone treated bucky-paper SWNTs sample. (a) surface; (b) inner section.

evidence of functional groups such as the C – O – C mode around 1200 cm^{-1} , the C = O mode at 1720 cm^{-1} , the O – H mode around 3400 cm^{-1} , and the activated C = C mode at 1573 cm^{-1} . Whereas in Figure 3-4(b) none of these modes is discernable. The Raman spectra on the surface and inner part of the sample confirmed that the ozone reaction is not uniform throughout the bucky-paper. As shown in Figure 3-5, the disorder mode is strong from the surface of the sample. Combined with the distortion of the resonant Raman modes of SWNTs, it indicates the surface of the bucky-paper was highly derivatized. The Raman from the inner part of the sample, however, is exactly the same as the untreated SWNTs. It is well known that the bucky-paper is quite porous and there should be no difficulty for non-reactive gas species to diffuse through. Theoretical calculations found that the 1,3-dipolar cycloaddition of ozone onto the sidewall of a (5,5) SWNTs is facile¹⁰⁷. It is possible that when the first adsorbed ozone molecules form ozonides on the surface of the bucky-paper, they create secondary reactive sites that consume more ozone and impede their diffusion into inner part of the bucky-paper. It has been experimentally confirmed that ozone is able to remove carbon atoms from SWNTs by forming CO_2 and CO even at room temperature¹⁰⁴. If the sequence of reactions on the gas-solid interface between ozone and the SWNTs bucky-paper is: formation of ozonides; then formation of functionalities such as epoxy groups, carbonyl groups, and carboxylic acid groups by secondary ozone attack on the ozonides; then carbon removal from SWNTs as CO_2 and CO by further ozone attack on the oxygen-containing functionalities; then at any stage of the reaction, there will always be a highly derivatized surface layer and the intact inner part in the bucky-paper sample.

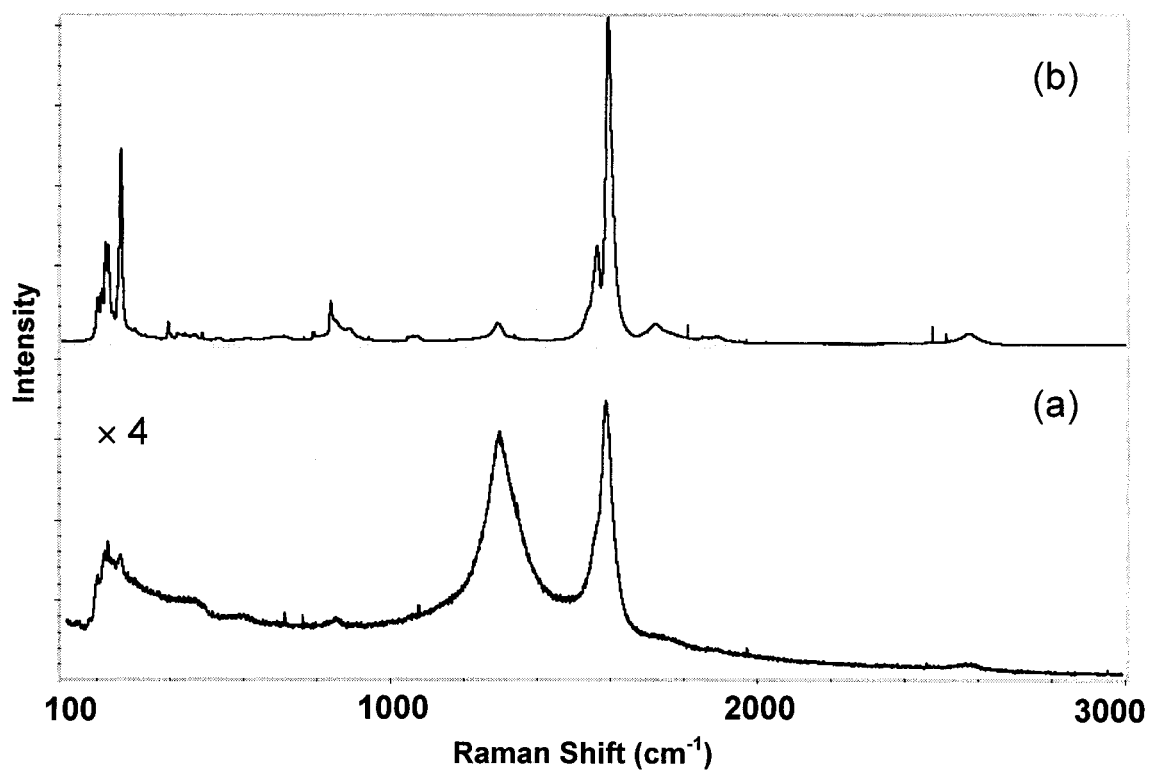


Figure 3-5 Raman spectra of ozone treated bucky-paper SWNTs sample. (a) surface; (b) inner section.

The thermal decomposition behavior of the ozone treated bucky-paper is demonstrated in Figure 3-6. The total weight loss is ~45% when the sample was heated to 800°C, which means that a large number of carbon were removed from the sample. The derivative weight loss curve indicates that there were four weight loss sections during the process. Two of them occurred at lower temperature: 101 °C and 150 °C, which contributed to ~15% of the total weight loss. The third section occurred during a wide temperature range between 350 to 700 °C, which contributed to ~20% of the total weight loss. The last section occurred at temperature over 700 °C and was responsible to ~10% of the total weight loss. The two most probable volatile species that would evolved from the sample during the annealing would be CO₂, and CO. Generally CO is only formed at relatively high temperature, at least over 600 °C. Unfortunately there was no measurement taken to identify the volatile species released during the annealing. The weight loss sections at various temperatures during the annealing might due to different carbon-oxygen containing functionalities that desorbed from the SWNTs at different temperatures. The ATR-IR spectrum of the annealed sample is shown in Figure 3-7. There is not much evidence of remaining functionalities from the original IR spectrum [Figure 3-7(a)]. The processed spectrum [Figure 3-7(b)] shows that there is only small amount of C – O – C bonds, represented by the IR mode around 1100 cm⁻¹, survived the annealing. The Raman spectra of the annealed sample show similar inhomogeneous features as those of the ozone treated bucky-paper. Part of this is the direct subsequence of the uneven ozonation. For example, the intact part of the sample during ozonation could remain intact during annealing, as shown in Figure 3-8(a). However, spectra in Figure 3-8(b) and (c) imply that the remove of carbon from the SWNT structure during

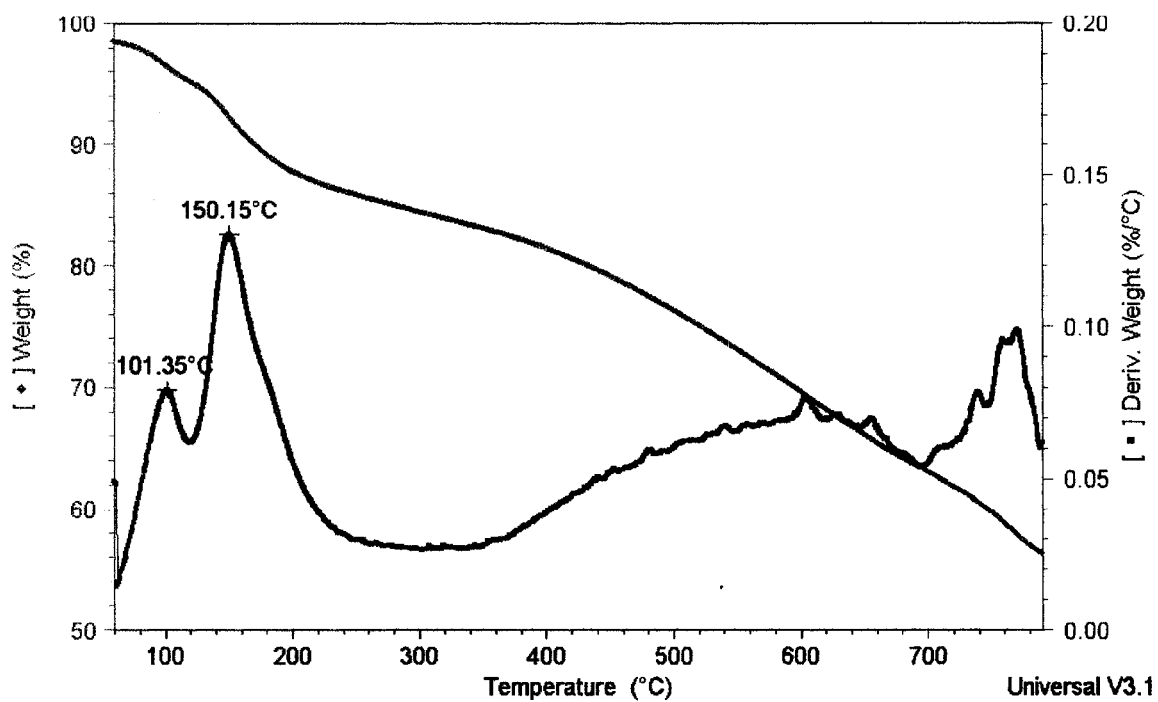


Figure 3-6 TGA of ozone treated bucky-paper during annealing. (Red curve: percentage weight loss; blue curve: temperature derivate weight loss.)

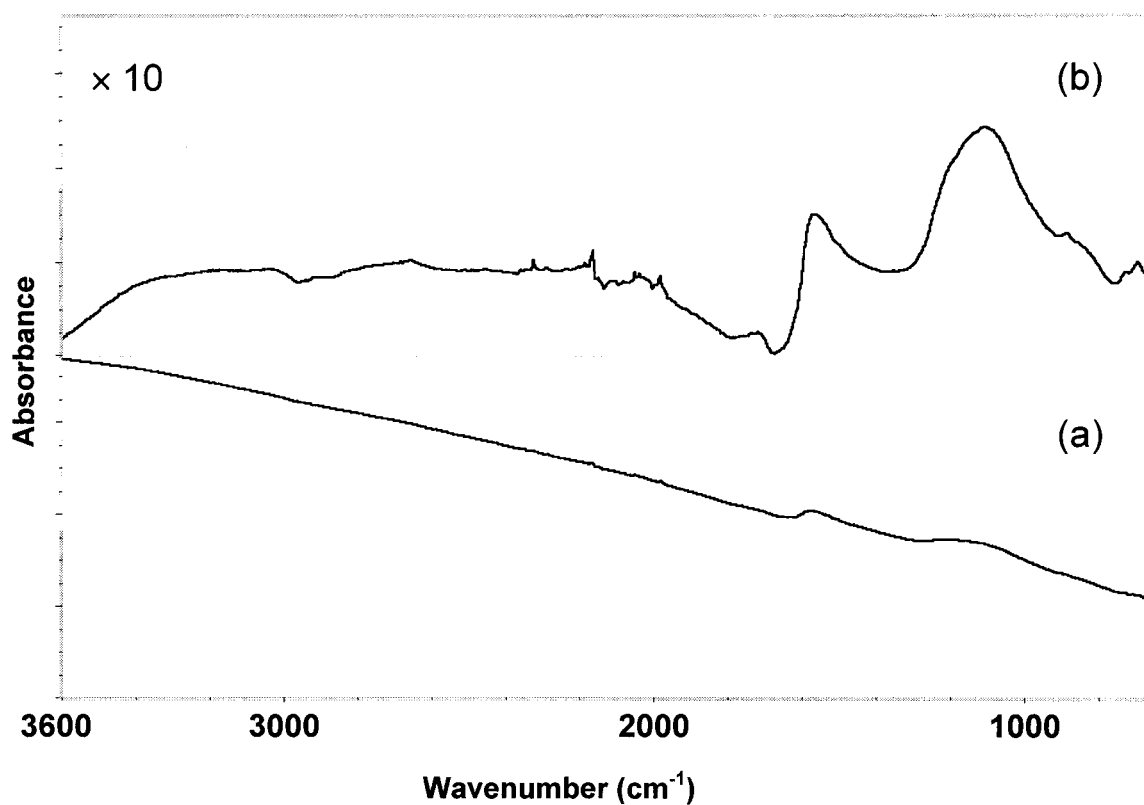


Figure 3-7 ATR-IR spectra of ozone treated bucky-paper SWNTs sample after annealing. (a): original spectrum; (b): (a) after baseline correction and scaled up.

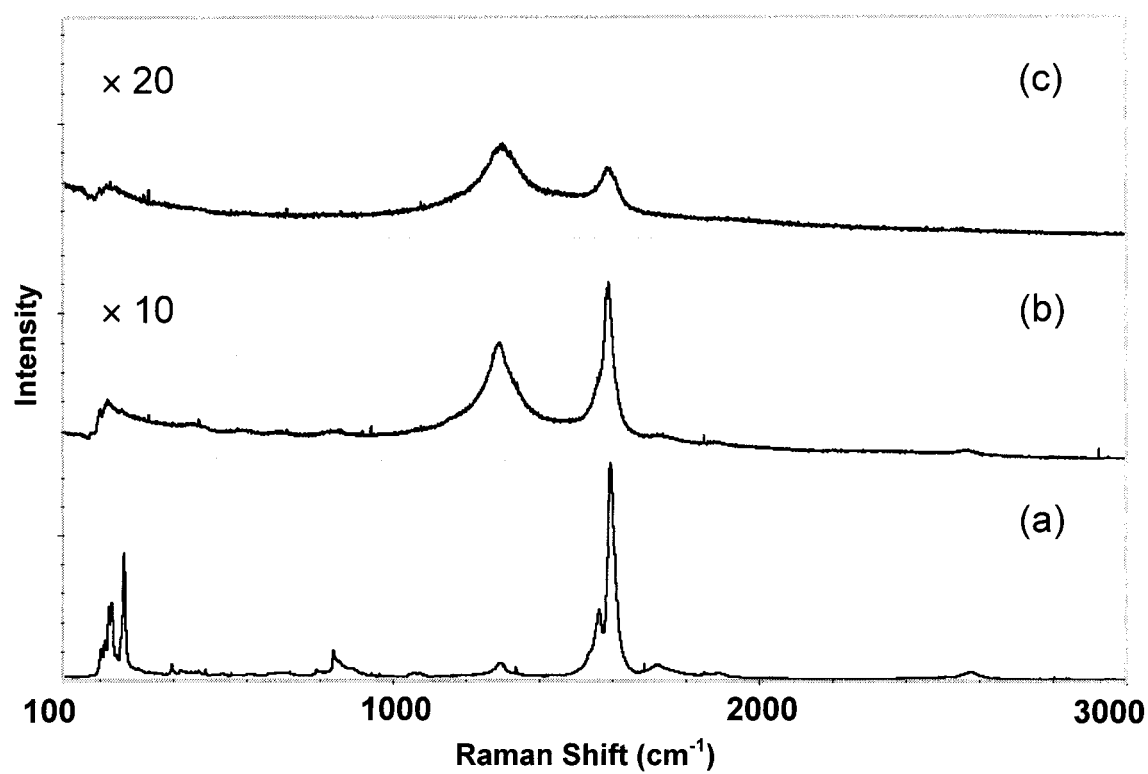


Figure 3-8 Raman spectra of ozone treated bucky-paper SWNTs sample after annealing. (a), (b) and (c) represent various parts of the same sample.

the annealing created high density of defect sites, which was not “self-healed” even up to 800 °C.

3.2.3 Conclusion

Our experiments on reaction between ozone and SWNTs on a gas-solid interface at 50 °C show that ozone chemically attaches to SWNTs (both ends and sidewall) under the reaction conditions. However, no uniform reaction circumstance throughout the bucky-paper could be reached under such conditions. The ozonation occurs mostly on the surface of the sample and forms highly derivatized surface layer and almost intact inner part. Annealing the ozone treated bucky-paper in argon up to 800 °C removes most of the oxygen containing functionalities from the SWNTs, most probably as CO₂ and CO. There is small amount of C – O – C functionalities that survives the annealing. Some of the SWNT structures are severely damaged during the annealing due to the removal of carbon atoms from the structure, and the damage could not be recovered through the “self-healing” process even at 800 °C.

3.3 INTERMITTENT OZONOLYSIS OF INDIVIDUALLY DISPERSED SWNTS ON GAS-AQUEOUS SOLUTION INTERFACE: CUTTING EFFECTS

3.3.1 Experimental

The individually dispersed SWNTs in sodium dodecyl sulfate (SDS) solution used

in the study were prepared as follows. 40 mg as prepared HiPco SWNTs were added to 200 ml 1 wt % SDS solution. The mixture was then ultrasonicated in a cuphorn sonicator (Cole Palmer CPX600) for 10 min at a power level of 540 W. Immediately after sonication, samples were centrifuged (Sovall 100S Discovery Ultracentrifuge with a Model T-1250 rotor) at 163,000g for 2 hours. The upper 80% of supernatant was then carefully decanted, which contained micelle isolated nanotube suspensions at a typical mass concentration of 15 to 20 mg/l. To be concise, such prepared SWNTs suspension is named *SWNTs/SDS* in the rest of the chapter.

The experiment of studying the ozone reaction with *SWNTs/SDS* on the gas-solution interface was carried out at room temperature. The gas mixture of ozone/oxygen was bubbling through the suspension that was constantly stirred with a magnet bar. The container for the suspension was sealed so that *SWNTs/SDS* was isolated from the environmental air. The *SWNTs/SDS* sample was treated with ozone for three intermittent sections. The experimental conditions during each section are listed in Table 3-1. The suspension was purged with oxygen and exposed to air between each section. Raman spectra of the sample after each section were collected with Renishaw micro-Raman spectrometer using a 780 nm laser. The incident laser radiated directly through the surface of the suspension and the distance between the objective lens and the suspension surface was adjusted until the maximum Raman signal of tangential mode was obtained before Raman spectra were collected. UV-vis.-NIR spectra of the sample before and after the ozone treatment were also collected. In order to compare the absorption quantitatively in both spectra, the pH of the suspension was adjusted to ~10.4 with NaOH solution before each spectrum was taken. The precursor *SWNTs/SDS* and the ozone treated

Table 3-1 Experimental conditions used in the intermittent ozone reactions with *SWNTs/SDS*.

	O ₃ conc. (gram/m ³)	Total flow rate (ml/min.)	Total flow time (min.)	Total amount of O ₃ (mole)
Section 1	35	31	30	6.78×10^{-4}
Section 2	54	31	30	1.05×10^{-3}
Section 3	54	31	60	2.09×10^{-3}

suspension were deposited onto the APTES monolayer coated silicon wafer (using the “dip-rinse-blow dry” process) and examined with TM-AFM, respectively. The statistical size distribution of SWNTs in both samples was obtained with AFM analysis.

3.3.2 Results and Discussions

The Raman spectrum of the untreated *SWNTs/SDS* is shown in Figure 3-9(a). The notable difference between this spectrum and that from the solid SWNTs includes the extraordinarily strong Breathing mode, the nearly absent disorder mode and the broad fluorescence features falling into the detected range of Raman frequency. The former two features suggest that the SWNTs in the suspension are almost free of impurities on their sidewalls. They could even be free of van der Waals force from surrounding SWNTs, which means that most of these SWNTs are individually suspended in the solution. Details about the fluorescence from the individually dispersed SWNTs was described elsewhere⁸⁹. Since they are not the Raman scattering signals, their real frequencies could not be read through the Raman shift scale. The real wavelengths of each of the fluorescence modes, after a simple transversion, turned out to be ~874 nm, ~914 nm, ~955 nm, ~977 nm, respectively, with the shortest-wavelength fluorescence appearing at the lowest Raman shift scale. Since only individual SWNTs show fluorescence features, it is believed that the fluorescence from SWNTs is even more sensitive to the chemical environment of nanotube sidewalls than van Hove singularities. Even van der Waals force driven bundling would quench the fluorescence quickly.

Figure 3-9(b) is the Raman spectrum of *SWNTs/SDS* after the first section of ozone

treatment. The overall Raman intensity of the sample decreased considerably. It indicates that the sidewall structure of the SWNTs was somehow modified, which weakened the resonant Raman modes. It was noticed that the fluorescence was almost completely quenched, which also suggests that the chemical environment around the individual SWNTs varied. Also the Breathing mode intensity decreased dramatically and was lower than that of the tangential mode. In the enlarged $180 - 280 \text{ cm}^{-1}$ region of the spectra, it was found that the peak shape of the Breathing mode changed significantly: the 215 cm^{-1} mode disappeared, the two major peaks up-shifted from 225 to 229 cm^{-1} , and from 232 to 236 cm^{-1} , respectively, also a plateau arose around 267 cm^{-1} . The disappearance of the low-frequency Breathing mode indicates that the chemical process occurred has sort of preference towards smaller diameter SWNTs, which is reasonable because smaller diameter SWNTs are widely accepted to be more reactive than the larger diameter ones. The frequency shift of the breathing modes implies that there was physically adsorbed species. We've already known from previous discussion that the adsorption of ozone onto the sidewall of SWNTs is energetically facile. In the current experiment, the result indicates that the micelles surrounding the SWNTs don't prevent ozone from adsorbing onto the SWNTs. The arisen 267 cm^{-1} mode was normally assigned as the "roping" peak. Its appearance implies that the ozone treatment might somehow opened up the micelles and caused certain degree of bundling between individual SWNTs. However, there was no detectable disorder mode in Figure 3-9(b), which suggests that whatever chemical process happened during the ozone treatment, it did not building up functionalities onto the nanotube sidewall.

Figure 3-9(c) is the Raman spectrum of *SWNTs/SDS* after second section of ozone

treatment. The decrease of Raman modes intensity continued during this section. The fluorescence had completely vanished on the spectrum. The relative intensity of the Breathing mode decreased more, and only the strongest 235 cm^{-1} mode was discernable. The broad plateau-like feature at $\sim 267\text{ cm}^{-1}$ was more clearly seen. Apparently, the chemical modification was continuing during this section. But the disorder mode is still very low in intensity. After the third ozone treatment, the Raman modes of SWNTs was abruptly recovered, especially the Breathing mode, which almost reached the same intensity as that of the tangential mode, as shown in Figure 3-9(d). However, the Breathing modes only had two component peaks in this spectrum, at 228 and 235 cm^{-1} , respectively. It was apparently not the same as the starting *SWNTs/SDS*. In addition, the disorder mode (around 1295 cm^{-1}) had never substantially increased its intensity, which suggests that even though the ozone had modified the chemical properties of the nanotube sidewalls, it didn't create large amount of permanent functionalities. It is very interesting finding and other characterization techniques would provide additional information about the process.

In Figure 3-10, the UV-vis.-NIR spectra of the *SWNTs/SDS* before and after the intermittent ozone treatment were compared. We've mentioned in the introduction part of this chapter that the individually dispersed SWNTs in SDS solution have strongly enhanced van Hove singularity features. It can be clearly seen in Figure 3-10 (the red curve) that the first van Hove singularities from the semiconductor SWNTs between 900 and 1300 cm^{-1} are well resolved. The UV spectrum of the ozone treated *SWNTs/SDS* sample (blue curve in Figure 3-10) looks very similar to that of the purified SWNT bundles dispersed in *o*-dichlorobenzene⁷⁵. The features between $900 - 1100\text{ nm}$ were

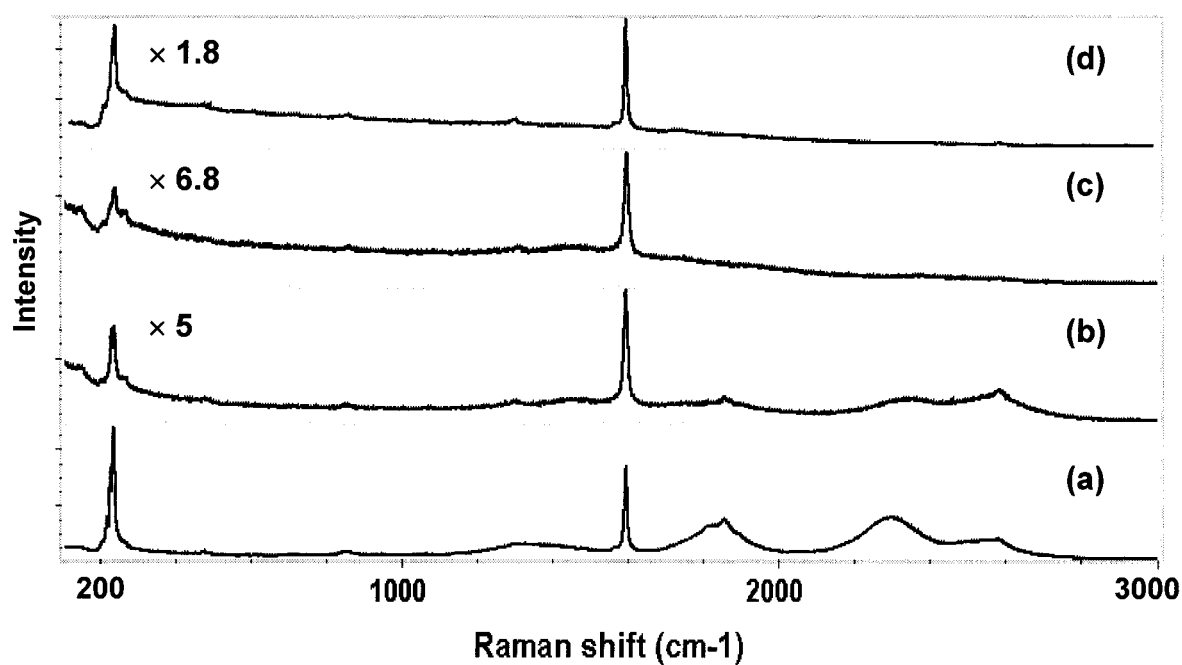
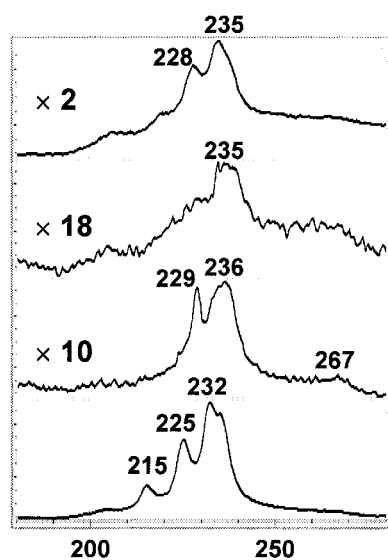


Figure 3-9 Raman of *SWNTs/SDS* at each stage of the intermittent ozone treatment. (a) untreated decant; (b) after 1st dose ozone (2.26×10^{-5} mol/min. for 30 min.); (c) after 2nd dose ozone (3.49×10^{-5} mol/min. for 30 min.); (d) after 3rd dose ozone (3.49×10^{-5} mol/min. for 60 min.).



Left plot: the enlarged part of Fig. 3-9 in the range of $180-280 \text{ cm}^{-1}$.

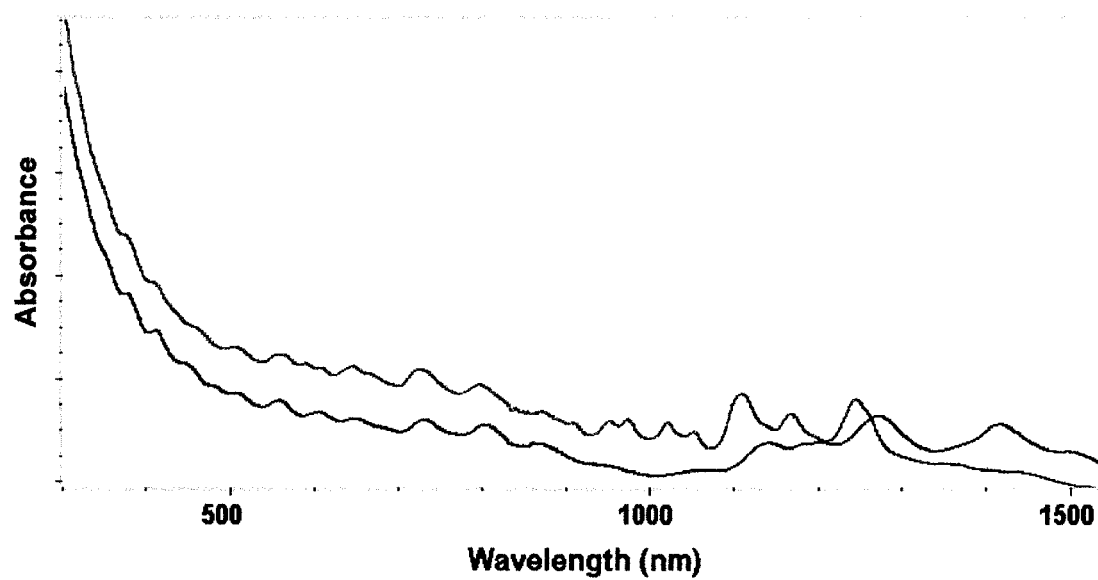


Figure 3-10 UV spectra of *SWNTs/SDS* before and after the intermittent ozone treatment. (red: before ozone treatment; blue: after the three-dose ozone treatment.)

absent in this spectrum. Instead, there are three broad features at ~ 1140 nm, ~ 1270 nm, and 1415 nm. These features could not match those of individually dispersed SWNTs. It implies that the roping of SWNTs causes significant change of their van Hove transitions. But the presence of the van Hove features over the region between $300 - 1400$ nm in the ozone treated *SWNTs/SDS* sample confirmed that there was not much covalent functionalization occurred onto the SWNTs, because the disappearance of the van Hove features has been used as an indicator of covalent sidewall derivatizations³⁴. Another information can be obtained from the UV-vis.-NIR spectra of SWNTs is the approximate mass concentration of the SWNTs. The absorption indexes (ϵ) between two adjacent van Hove features ~ 630 nm could be used to compare the relative concentrations of SWNT suspensions (using same solvent and/or surfactant and at same pH condition). In present experiment, $\epsilon = 1.015$ at 626 nm for the untreated *SWNTs/SDS* sample, and $\epsilon = 0.786$ at 630 nm for the ozone treated *SWNTs/SDS* sample. Since the total volume of the suspension did not changed during the experiment, the amount of SWNTs decreased $\sim 23\%$ during the ozone treatment. We've already known from the gas-solid reaction between ozone and SWNTs that ozone treatment is able to remove carbon from nanotubes. The fact that the suspension still showed van Hove features indicates that the nanotube structures were not destroyed by the carbon removal. Then, it would be informative to know what exactly happened to the SWNTs. In other words, is it true that all of the nanotubes were "etched" to $\sim 77\%$ of their original length, or some nanotubes were completely consumed and others were almost intact, or the removal of carbon on specific sites along the nanotube sidewall actually "cut" the nanotubes into much shorter pieces without consuming most of them?

The AFM analysis of the *SWNTs/SDS* before and after ozone treatment answered the questions above. The typical AFM image of the untreated *SWNTs/SDS* is shown in Figure 3-11. The AFM height analysis indicates that the average bundle size of the SWNTs is 1.63 nm, which means that most of the nanotubes in this sample are individual SWNTs or very small bundles of 2-3 individual SWNTs. The average length of the SWNTs in this sample is ~512 nm. The AFM image of the ozone treated *SWNTs/SDS* is shown in Figure 3-12, 3-13, 3-14. The latter two are the enlarged portions of Figure 3-12 for more accurate measurements. It is clearly seen that there is not any longer nanotubes in this sample. But the bundle sizes of the SWNTs are significantly larger. Statistical analysis of the length and bundle size distribution of this sample was shown in Figure 3-15. With over 90% SWNTs shorter than 200 nm, the average length of nanotubes is ~134 nm in this sample, which is ~26% their original length. Also, over 60% of the nanotubes have a bundle size between 6-10 nm, which are considerably larger than that of the precursor nanotubes. Apparently, significant roping had occurred during the ozone treatment. The 74% decrease in average length of the SWNTs with only 23% decrease in total amount of the SWNTs in the suspension rules out both the possibility that the nanotubes were “etched” to the short length, and the possibility that some nanotubes were completely etched away whereas others were intact during the ozone treatment. This leaves one reasonable explanation: the carbon removal on individually dispersed SWNTs by ozone treatment could be site specific that “cut” SWNTs into much shorter pieces without damaging their tubular structures.



Figure 3-11 AFM image of SWNTs SDS decant. (area: $10\text{ }\mu\text{m} \times 10\text{ }\mu\text{m}$)

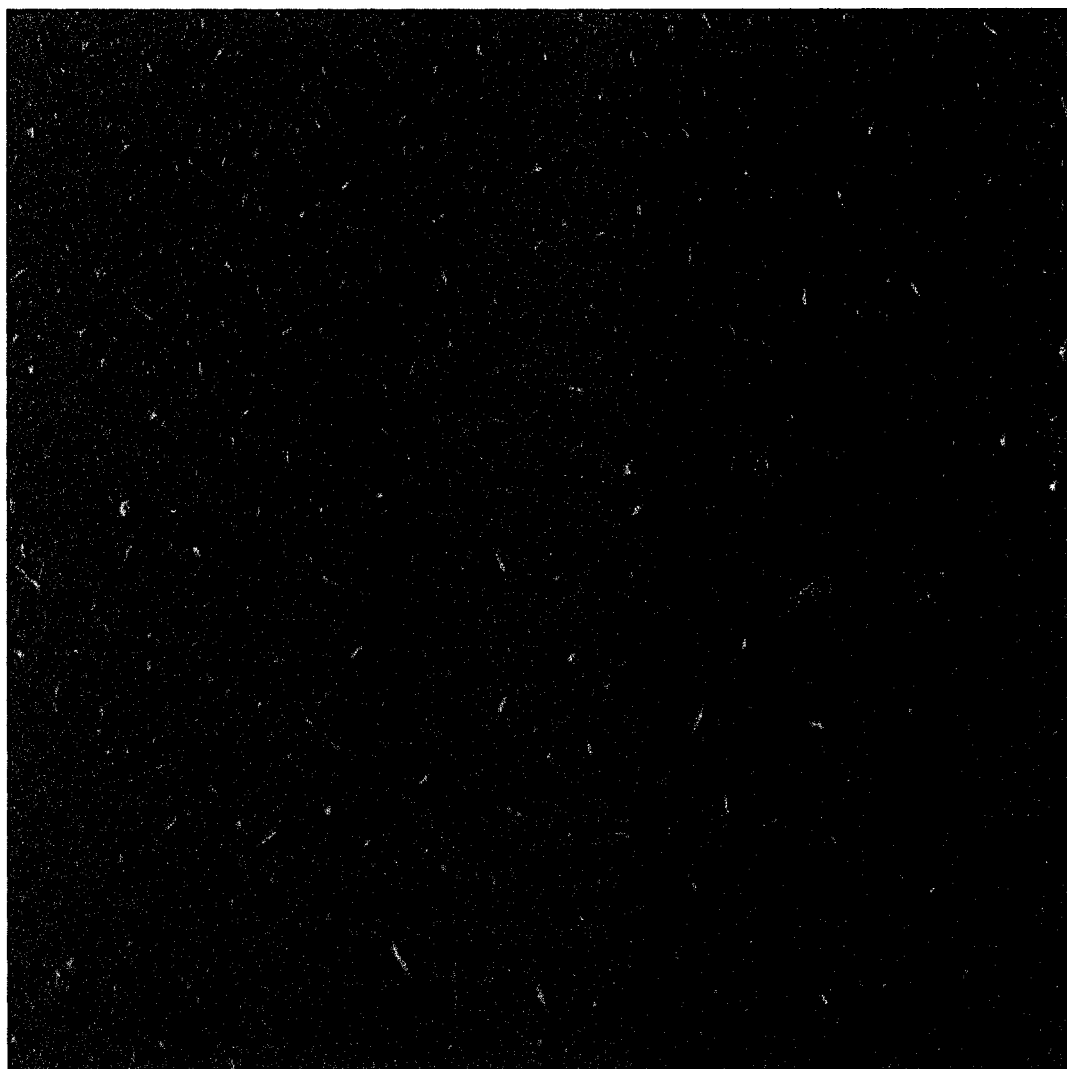


Figure 3-12 AFM image of intermittent ozone treated SWNTs SDS decant. (area: $10\ \mu\text{m} \times 10\ \mu\text{m}$)



Figure 3-13 AFM image of intermittent ozone treated SWNTs SDS decant. (area: $5\text{ }\mu\text{m} \times 5\text{ }\mu\text{m}$)

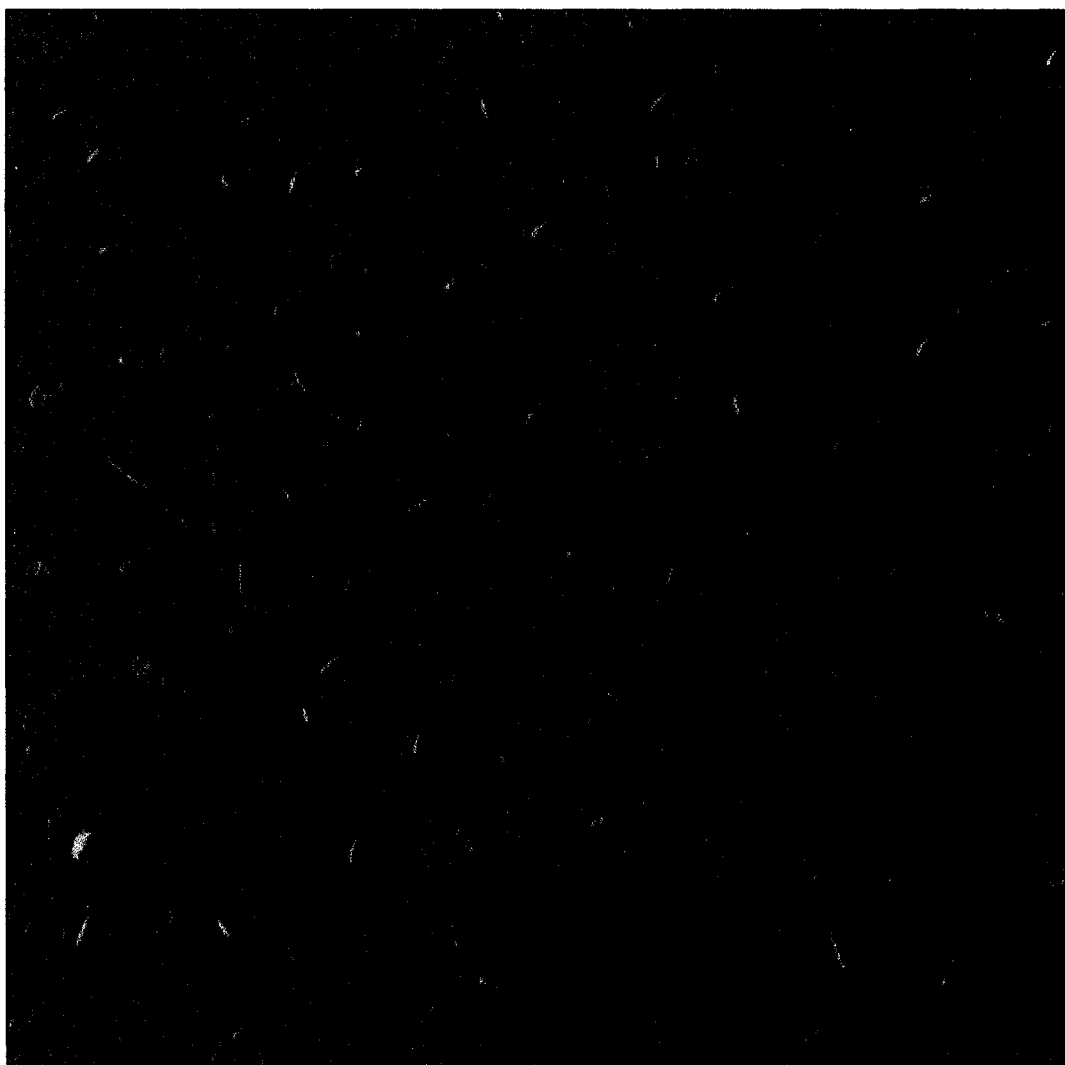


Figure 3-14 AFM image of intermittent ozone treated SWNTs SDS decant. (area: $5\text{ }\mu\text{m} \times 5\text{ }\mu\text{m}$)

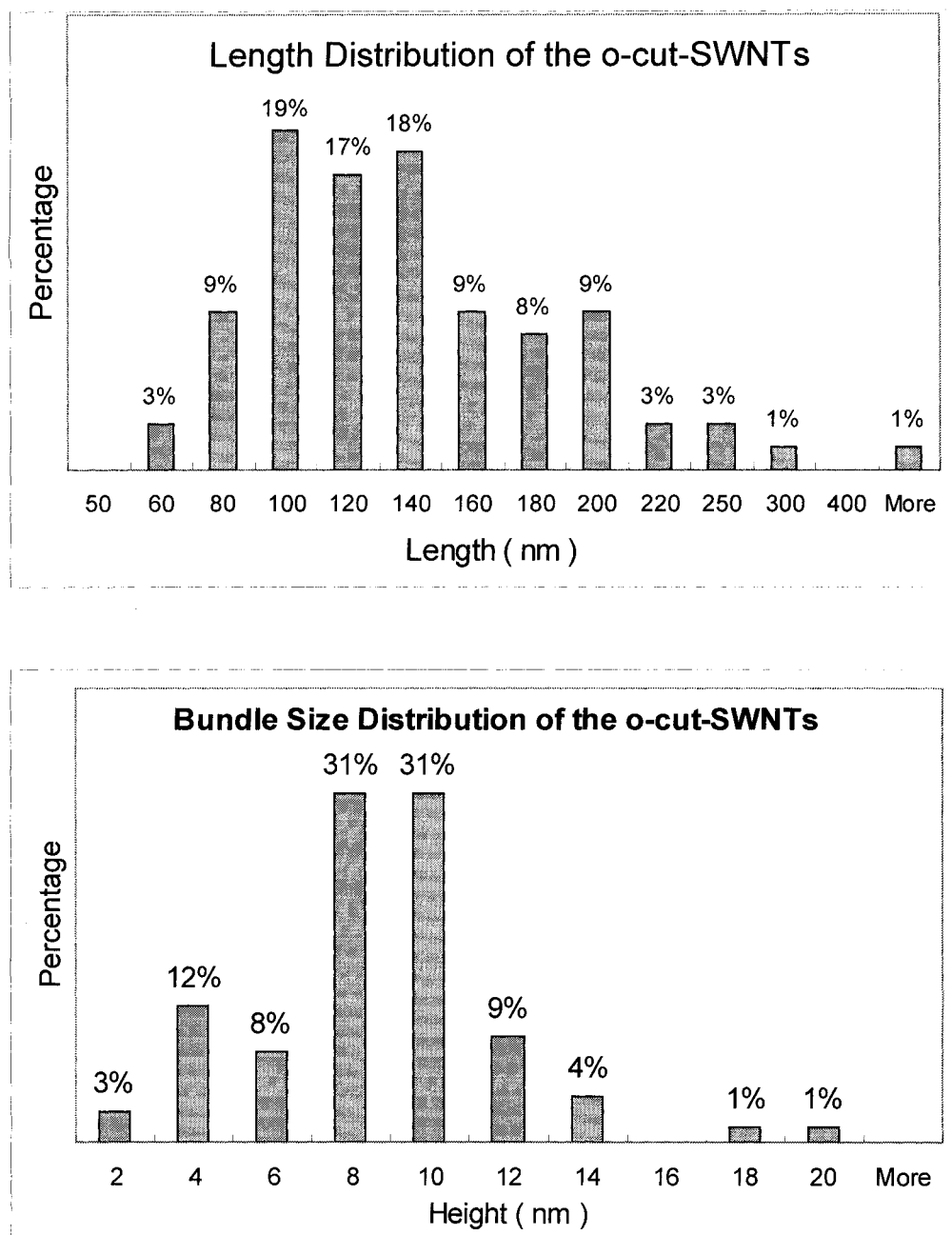


Figure 3-15 Statistical data on size distribution of the ozone-cut-SWNTs (*o-cut-SWNTs*)

3.3.3 Conclusion

The intermittent ozone treatment of *SWNTs/SDS* at room temperature was studied. The three-section ozone exposure resulted 23% loss of total mass of nanotubes in the suspension with little covalent functionalization occurred on sidewall of the SWNTs. The average length of the nanotubes in the suspension decreased to 26% that of the precursor. Significant bundling also happened during the process. The dramatic length decrease with relatively small amount of total mass loss of SWNTs suggests that the nanotubes were “cut” into short pieces instead of being “etched” away by the ozone treatment. The special micelle surroundings in the suspension, as well as the intermittence of ozone exposure might have prevented the SWNTs from being quickly “etched” away. It could be a promising chemical method of cutting SWNTs in aqueous solution.

3.4 SPECTROSCOPIC STUDY OF CONTINUOUS OZONOLYSIS OF INDIVIDUALLY DISPERSED SWNTS

3.4.1 Experimental

The individually dispersed SWNTs (will be called *SWNTs/surfactant* dispersion below) used in this study were prepared similarly as above. One extra step before the ultrasonication was highshear mixing the dispersion of HiPco SWNTs in surfactant solution for 1 hour (Polyscience X520). Three different types of surfactants, the anionic surfactant SDS, nonionic surfactant Pluronic-108, and cationic surfactant dodecyltrimethylammonium bromide (DTAB) had been used to prepare individually dispersed SWNTs. The concentration of the surfactant solutions was 1 wt % for SDS, 2

wt % for Pluronic-108, and 1 wt % for DTAB. Same ultrasonication and centrifuging conditions were used to prepare all the samples for this study. The concentration of SWNTs in the resulted *SWNTs/surfactant* dispersion varies with the surfactant used. Generally, with SDS the most concentrated SWNTs dispersions could be prepared. With DTAB, the resultant dispersions had the lowest SWNT concentration.

The experimental set up for in-situ monitoring the spectra of the SWNTs during ozone treatment was demonstrated in Figure 3-16. The *SWNTs/surfactant* dispersion was held in a Teflon cap sealed deep glass dish and was constantly stirred with a magnet stir bar during the experiment. Silicone lines were used to create a circuit for the SWNTs dispersion to flow from the glass dish to a peristaltic pump, to a quartz flow-cell in Raman spectrometer, to another quartz flow-cell in UV spectrometer (only used in some experiments), and back to the glass dish. The Raman spectra were collected with a Kaiser fiber Raman spectrometer using 785 nm laser excitation. The interval for Raman spectra collection was 1 minute, and that for UV spectra collection was about 4 minutes.

The pH adjustment of the dispersions was approached by using NaOH solution and Gram-Pac buffers from Fisher Scientific.

3.4.2 Results and Discussions

3.4.2.1 Spectra Analysis

The major information we could obtain from the Raman spectra of *SWNTs/surfactant* dispersion is demonstrated in Figure 3-17. The spectra range is set at $100 - 3450 \text{ cm}^{-1}$. The three specific Raman modes of SWNTs, the RBM, the disorder

mode and the tangential mode, are in the range of $180 - 1650 \text{ cm}^{-1}$. The variation of these modes provides important information about the chemical modifications on the sidewall of SWNTs. There also are six detectable fluorescence modes from semiconducting HiPco SWNTs in the range of $1200 - 3450 \text{ cm}^{-1}$ labeled as F #1 to F #6. The real wavelength of these emission modes is 874 nm, 914 nm, 955 nm, 977 nm, 1027 nm, and 1058 nm, respectively. They have been assigned to SWNTs with structure index (6,4), (9,1), (8,3), (6,5), (7,5), and (10,2), respectively ⁹⁷. As mentioned in last section, the fluorescence modes of SWNTs are very sensitive to the variation of the chemical circumstance around the SWNTs. They will provide supplemental information on the subtle change around the SWNTs in the dispersion during the ozone treatment. The different quenching rates of the fluorescence during the experiments might also reflect certain selectivity of the processes involved.

The information included in a UV-vis.-NIR spectrum of the *SWNTs/surfactant* dispersion is demonstrated in Figure 3-18. The van Hove singularities from various types of SWNTs are observable in the range of 300 – 1350 nm. The E_{11} transition absorptions from semiconducting SWNTs in the range of 900 – 1300 nm are greatly enhanced in the individually dispersed SWNTs, which can be used tracking changes of different SWNTs during a reaction. The six modes enclosed in the green-dash-line square are the absorptions from the same SWNTs from which the strong fluorescence modes are observed in the Raman spectra range. The E_{22} transition absorptions from semiconducting SWNTs in the range of 500 – 900 nm are partially overlapped with the E_{11} transition absorptions from metallic SWNTs in the range of 300 – 600 nm. Absorptions in these

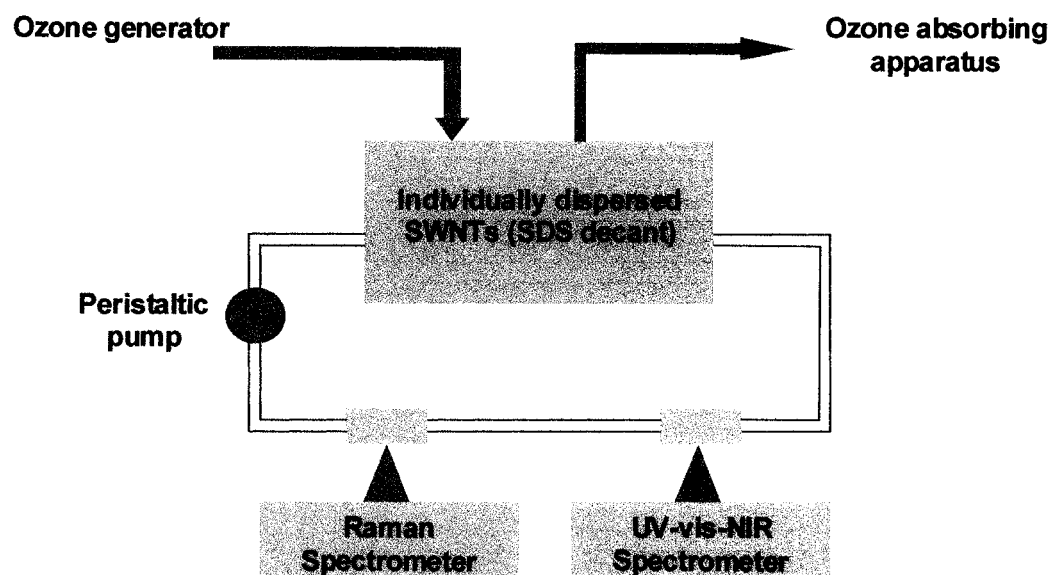


Figure 3-16 Schematic demonstration of the experiment set-up for spectroscopic monitoring the ozone reaction with individually dispersed SWNTs.

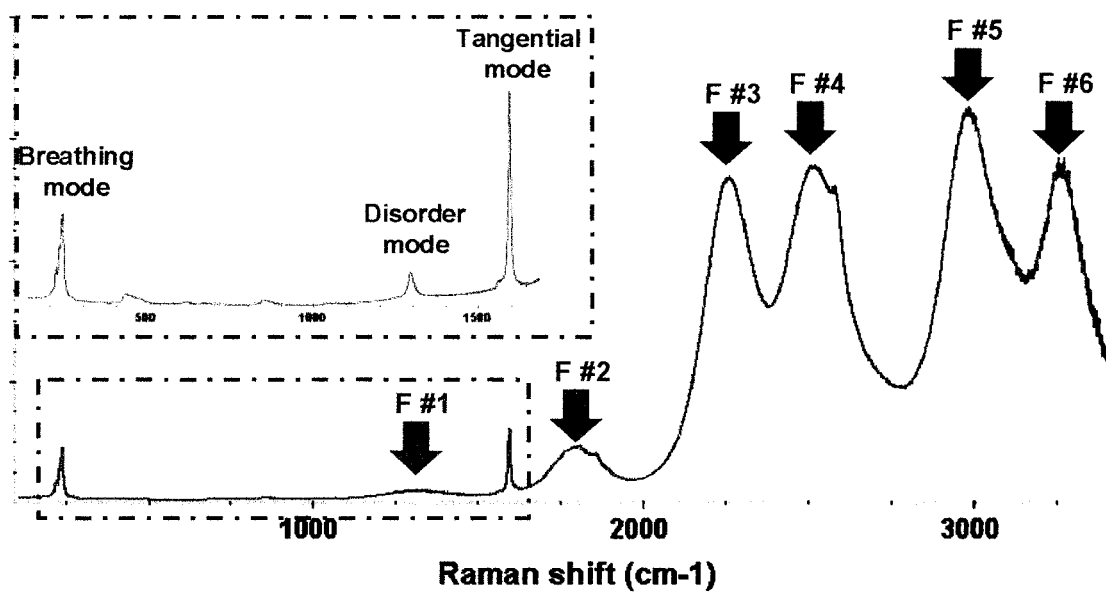


Figure 3-17 Peak identities in Raman and fluorescence spectra of individually dispersed SWNTs.

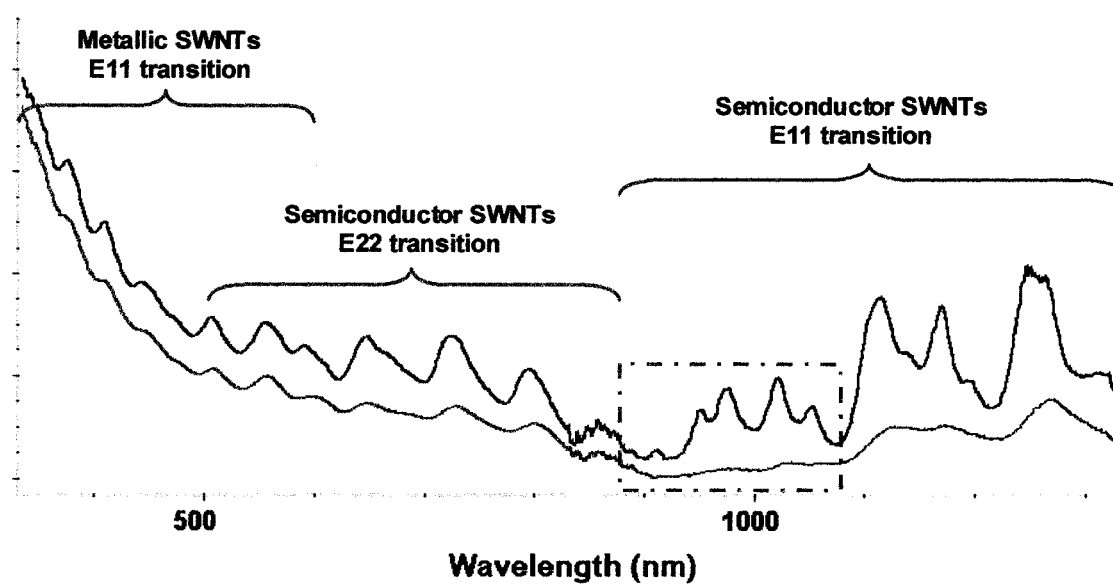


Figure 3-18 UV-vis.-NIR spectrum of *SWNTs/SDS* dispersion (blue curve) and a typical spectrum of *SWNTs/surfactant* dispersion after 2-hour ozone exposure (red curve).

two regions were less affected by the ozone treatment we studied. A typical absorption spectrum of the ozone treated *SWNTs/SDS* dispersion is also shown in Figure 3-18. Besides the decrease in overall absorbance that indicates the decrease in total amount of SWNTs in the dispersion, the van Hove features, especially the ones in the range of 900 – 1300 nm, have significantly changed. The sharp features between 1100 – 1300 nm were broadened. The features in the green-dash-line square were almost completely flattened. These changes in absorption spectra indicate that the chemical circumstance of the SWNTs in the dispersion have varied during the ozone treatment. For example, the SWNTs might not be individually dispersed any more. The sidewall of the SWNTs had been modified with chemicals, either physically absorbed or chemically bound to the nanotubes.

2.4.2.2 Non-buffered System

In Experiment 1, *SWNTs/SDS* dispersion (prepared with SWNTs HPR85) with pH adjusted to 10 (with NaOH) was exposed to ozone (ozone conc.: 55 gram/m³; total gas flow rate: 62 ml/min.) in the dark environment for ~5.5 hours. The pH value of the dispersion at the end of the experiment was ~5. Apparently, acidic products were created during the ozone treatment that changed the pH of the dispersion. Breakdown of the Raman spectra during the first hour of the ozone exposure is shown in Figure 3-19. The red curve on the top of the series represents the start of the ozone treatment. The fluorescence features gradually quenched with time and almost vanished from the spectrum after one hour. Various quenching rates were observed among the six

fluorescence features. For example, F #5 and F #6 (see label definitions in Figure 3-17) quenched faster than F #3 and F #4. It might be SWNT diameter related because F #5 and F #6 are from SWNTs with the largest diameters among those the fluorescence was detectable. The Raman spectra of the sample before and after the 5.5-hour ozone treatment were compared in Figure 3-20. We've already known that the fluorescence was completely quenched during the first hour or so. The overall intensity of the phonon modes of SWNTs decreased over an order of magnitude with the ozone treatment. In Figure 3-20(b), the distinct disorder mode around 1300 cm^{-1} indicates that there was certain amount of sidewall derivatization occurred. Based on the pH change of the dispersion, it is reasonable to believe that there were carboxylic acid groups formed on the SWNTs. The Breathing modes were very low in intensity and had two discernable components: the 235 cm^{-1} mode and the 268 cm^{-1} one. The 235 cm^{-1} mode is typical in Raman spectra of HiPco SWNTs. The 268 cm^{-1} mode was not in presence in Figure 3-20(a), which means it was resulted from the ozone treatment. It might indicate the roping of individual SWNTs during the process. Another distinct mode in Figure 3-20(b) was the one at 2590 cm^{-1} . It was up-shifted from 2577 cm^{-1} compared with the spectrum in Figure 3-20(a). This mode is usually low in intensity in the spectra of *SWNTs/surfactant* dispersion and is overlapped with the F #4 mode. It is also presented in the solid SWNT samples and is assigned as the overtone phonon mode. The behavior of this mode with ozone treatment in this experiment hasn't been clearly understood. It might be related to the variation of long-range phonon transport properties.

Breakdown of the UV-vis.-NIR spectra (500 – 1600 nm) of *SWNTs/SDS* dispersion during the first 2 hours of ozone treatment is shown in Figure 3-21. The pink spectrum at

the top of the series represents the start of the experiment. Preferential weakening of some absorption bands was observable. For example, the vanishing rates of the 1376, 1170, 1051, and 950 nm bands are significantly higher than their neighboring bands. Also among the four bands in the range of 950 – 1051 nm, the 1020, 1051 nm bands vanished faster than the 950, 973 nm bands, which is in consistent with the observation in the corresponding fluorescence modes. The UV-vis.-NIR spectra of the sample before and after the 5.5-hour ozone treatment were compared in Figure 3-22. Actually the spectra didn't change much after the first 135 minutes. The region between 900 and 1250 nm was featureless in Figure 2-22(b), indicating the modification of sidewall electronic states with covalent functionalization. The broad band around 1314 nm and the feature at 1406 nm seemed as van Hove transitions from bundled SWNTs. Also by comparing the UV-vis.-NIR spectra before and after the ozone exposure, it was found that there was a 30% loss on total amount of SWNTs in the dispersion. We believed it was due to consumption of carbon atoms from nanotubes by ozone in the reactions forming CO₂. It could be the other reason for the pH decrease of the dispersion.

In Experiment 2, *SWNTs/SDS* dispersion (prepared with SWNTs HPR1061) with pH adjusted to 10 (with NaOH) was exposed to ozone (ozone conc.: 55 gram/m³; total gas flow rate: 62 ml/min.) in the dark environment for ~2 hours. After ozone was turned off, the dispersion was purged with oxygen for more than 2 hours. The pH value of the dispersion at the end of the experiment was ~5. Raman spectrum of the dispersion was collected at one-minute intervals during the overall process. Variation in intensity (measured by peak area) of tangential mode (T-mode), Breathing modes (B-modes), disorder mode (D-mode) and the fluorescence bands from the Raman spectra of SWNTs

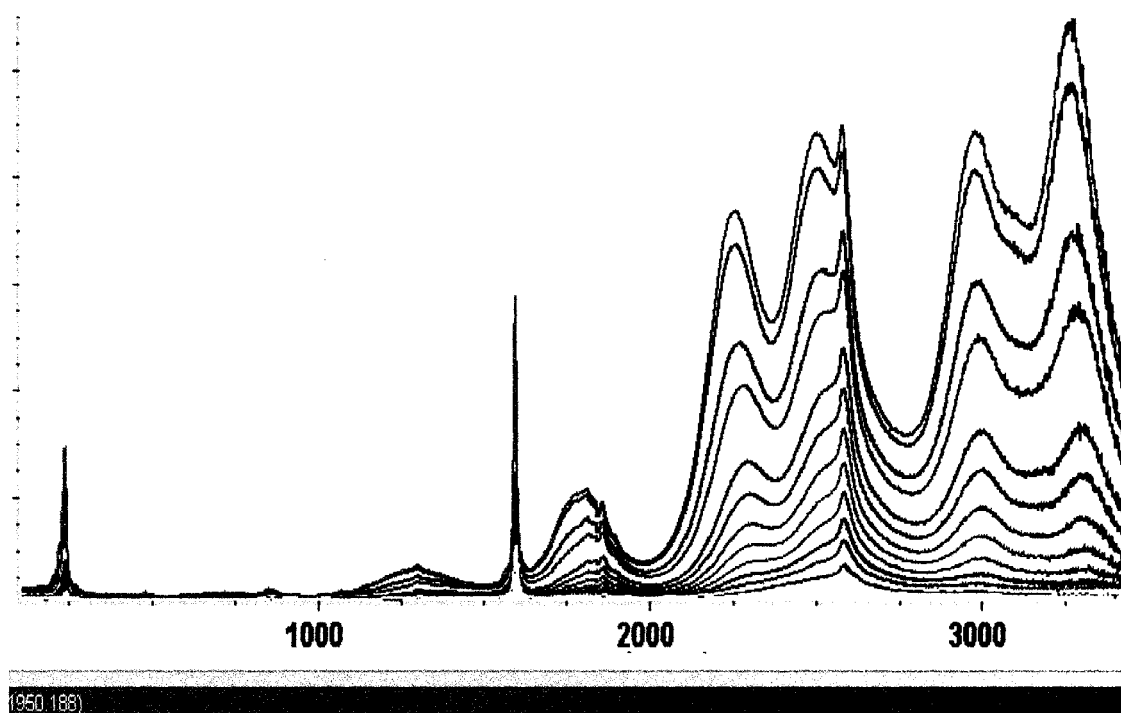


Figure 3-19 Breakdown of the Raman spectra of SWNTs/SDS (unbuffered) during the first hour ozone treatment.

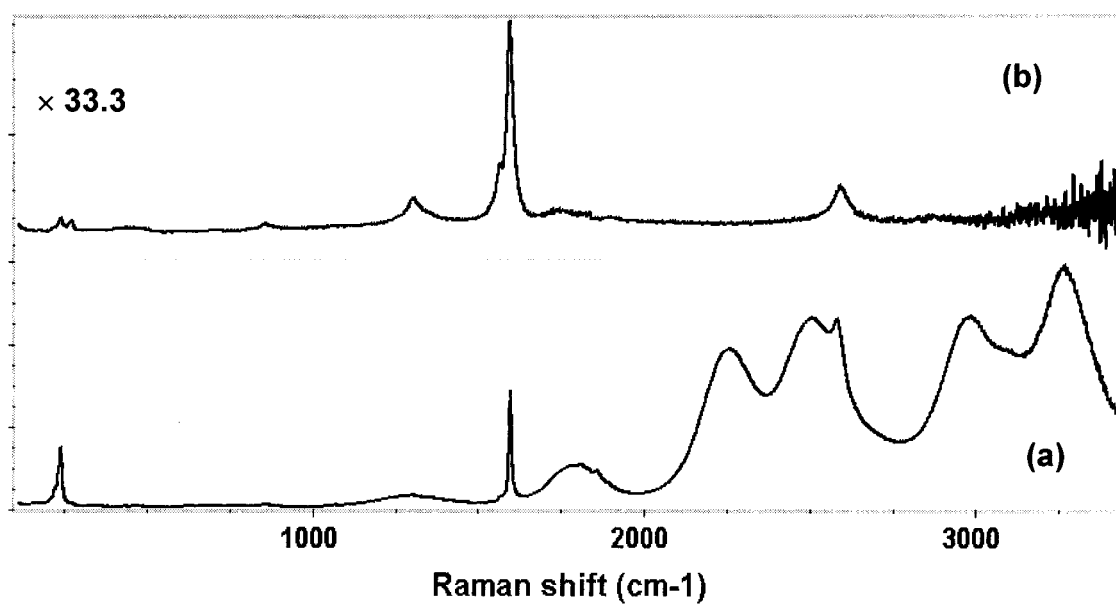


Figure 3-20 Raman spectra of SWNTs/SDS (unbuffered) with 5.5-hour ozone treatment.

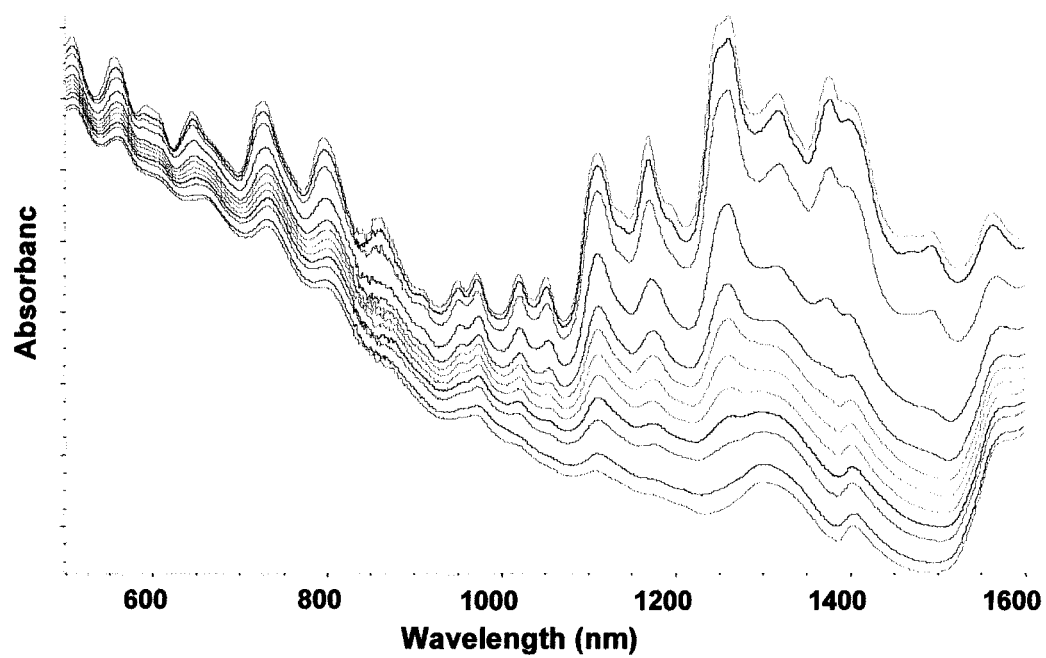


Figure 3-21 Breakdown of the UV-vis.-NIR spectra of *SWNTs/SDS* (unbuffered) During the first 2 hours of ozone treatment.

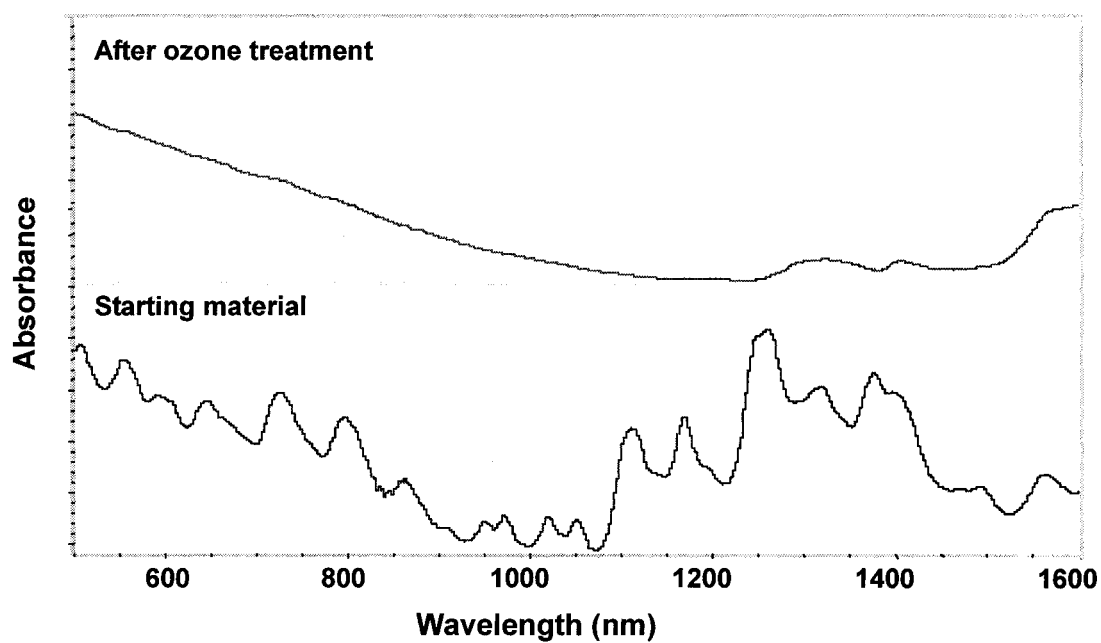


Figure 3-22 UV-vis.-NIR spectra of SWNTs/SDS (unbuffered) with 5.5-hour ozone treatment.

was measured and plotted, as shown in Figure 3-23(a) – (c). The plot showed that intensity of T-mode decreased rapidly upon ozone exposure. B-modes were more sensitive towards ozone treatment compared to T-mode. Because the D-mode is overlapped with fluorescence band F #1, it is difficult to measure its intensity before F #1 was completely quenched. The first part of the D-mode curve [the bottom plot in Figure 3-23(b)] actually reflected the quenching of F #1. After that, it can be seen that the D-mode was increasing with ozone treatment. After the first 75 minutes of ozone treatment, the overall intensity of Raman modes decreased to a level at least one order of magnitude lower than the original value. The deviation of intensity measurement became too large, as reflected from the widely scattering of the data points in the D-mode trend. The fluorescence bands quenched much faster than the resonant Raman modes from SWNTs, as shown in Figure 3-23. In the top plot, it seems all fluorescence bands quenched at similar rates. Replot the data using $\ln(\text{peak area})$ instead of peak area as Y axis linearized the curves, and the difference among the fluorescence bands showed up [bottom plot in Figure 3-23(c)]. The fluorescence bands could be divided into three groups according to their quenching rates: the 955 nm and 1058 nm bands seem to have the highest quenching rates, followed by the 914 nm and 1027 nm bands. The 977 nm bands showed the lowest quenching rate among the observable fluorescence bands. The result was very proximate, but it reflects certain level of selectivity on the ozonolysis reaction in question. In Figure 3-24, the Raman spectra of this sample before and after the ozone treatment were compared. The bottom spectrum was from the starting *SWNT/SDS* dispersion. It is notable that the B-modes has almost equivalent intensity as that of the T-mode, which was not the case in Experiment 1. Raman spectra of solid SWNT samples

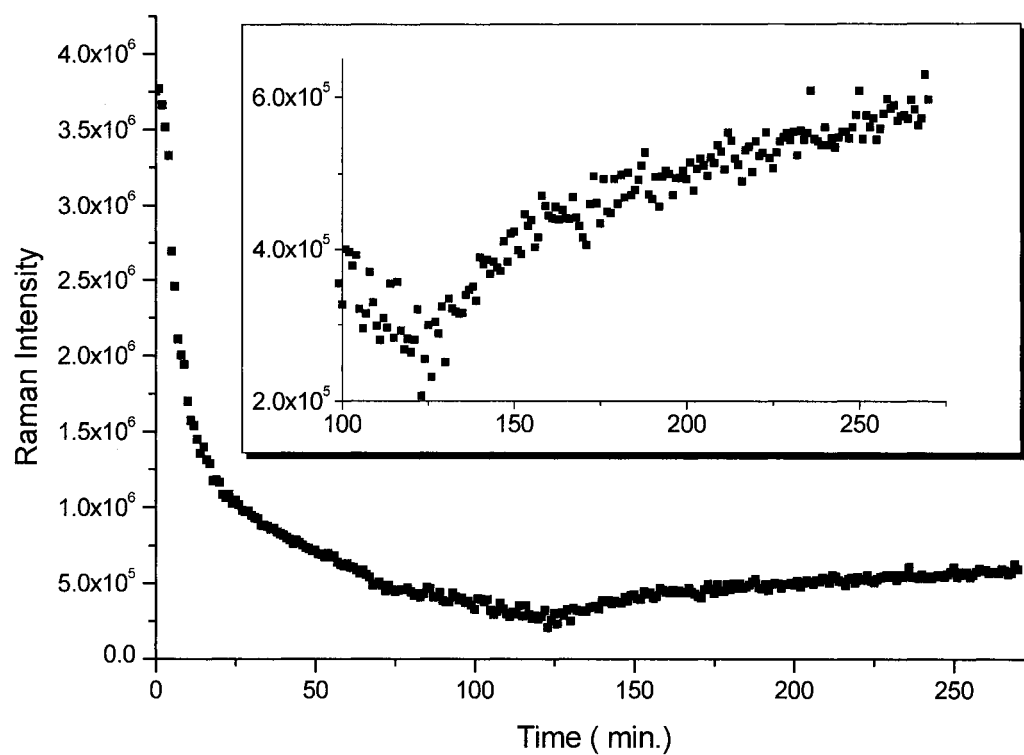


Figure 3-23(a) Raman intensity trendline (tangential mode) during a 2-hour continuous ozone treatment of SWNTs/SDS (unbuffered).

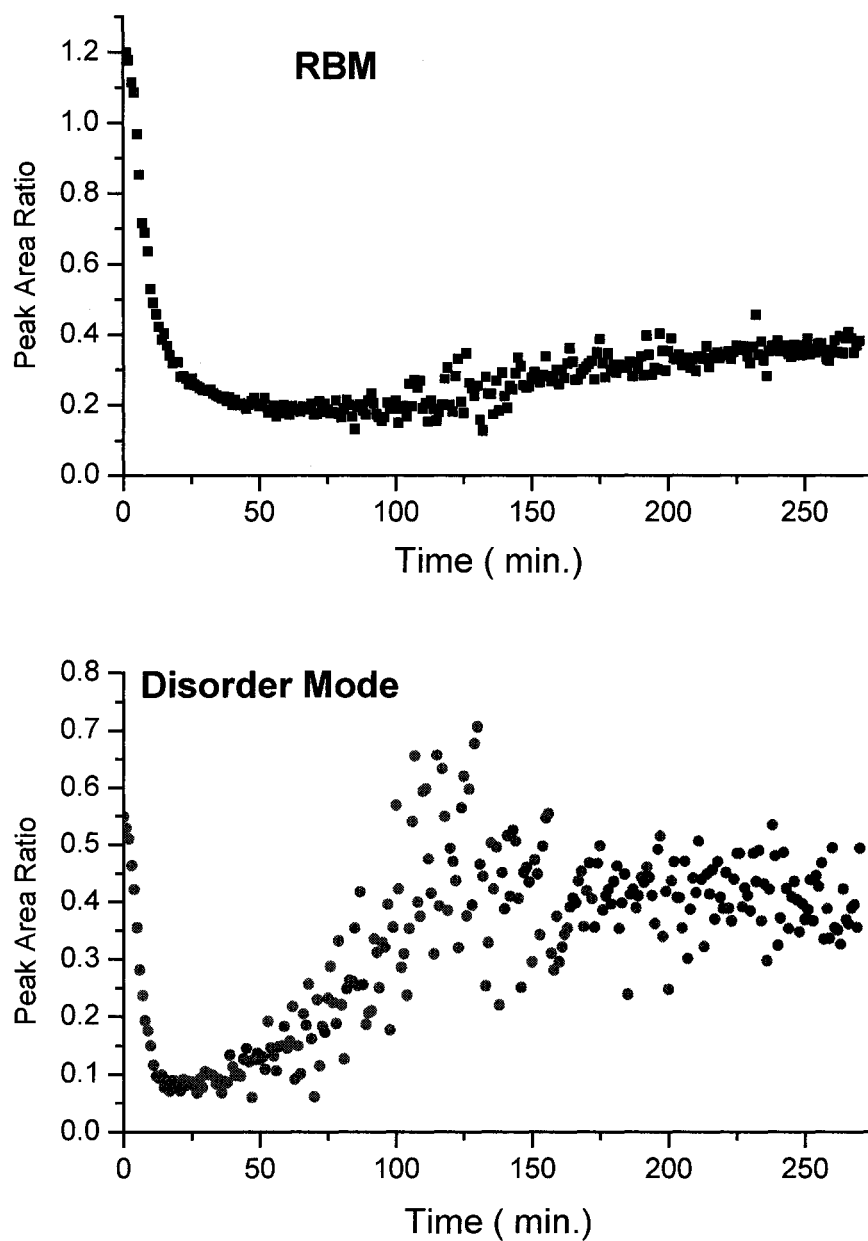


Figure 3-23(b) Raman intensity trendline (Y scale is the peak area ratio relative to the tangential mode. Top: the Breathing mode; bottom: disorder mode) during a 2-hour continuous ozone treatment of SWNTs/SDS (unbuffered).

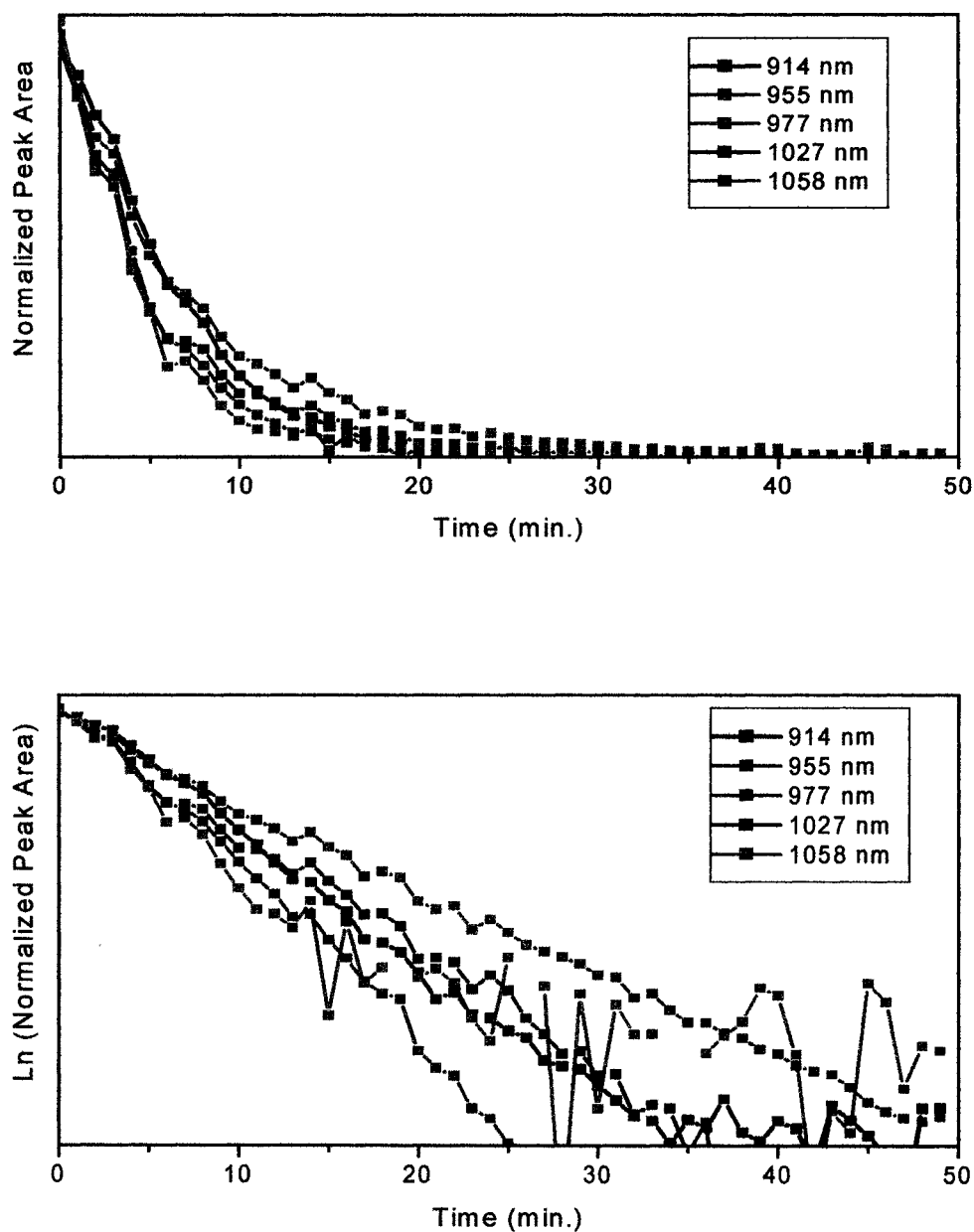


Figure 3-23(c) Top plot: the fluorescence intensity trendline during a 2-hour continuous ozone treatment of SWNTs/SDS (unbuffered); bottom plot: same data as the top plot, but plot with natural logarithm of peak intensity as Y axis.

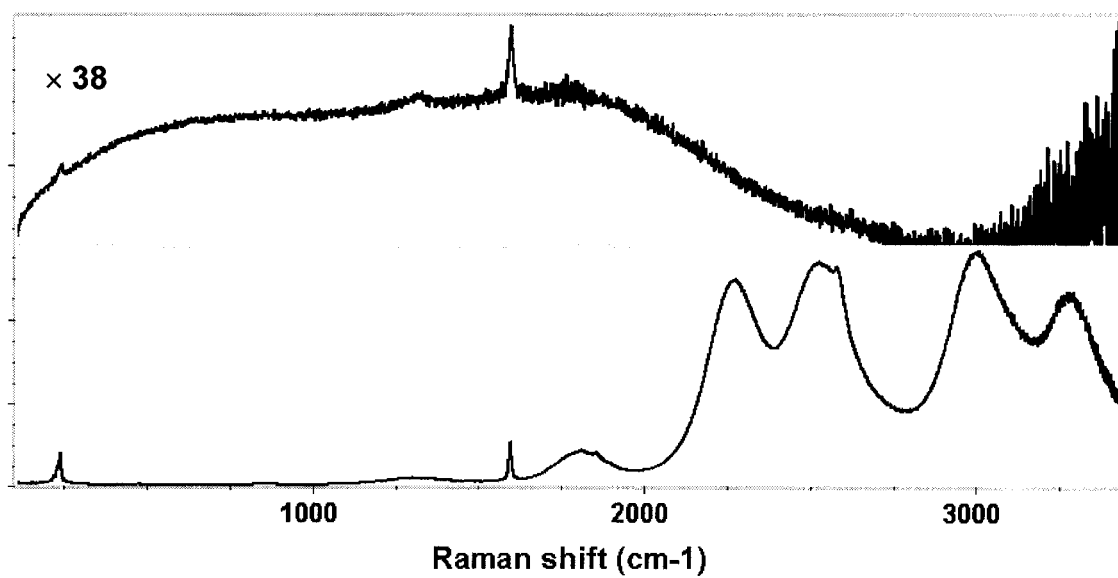


Figure 3-24 Raman spectra of SWNTs/SDS (unbuffered) with 2-hour ozone treatment.

always show considerably higher intensity T-mode compared with B-modes. We also found that *SWNT/SDS* dispersions prepared from purified SWNTs show higher intensity of T-mode relative to B-modes in Raman spectra. We believe bundling is the reason for relatively higher intensity of T-mode. The top spectrum in Figure 3-24 showed that the resonant Raman modes from SWNTs decreased dramatically after the 2-hour ozone exposure. However, there was not corresponding increase in the D-mode, which suggests that the change in Raman mode was not caused by the covalent sidewall derivatization. Also the B-modes in this spectrum was very low in intensity, which indicates significant distortion of the tubular structure of SWNTs. The broad background in the spectrum was believed caused by the ozone adsorption in the dispersion because it disappeared with oxygen purging. The purging also resulted in slow and partial recovery in intensity of both the T-mode and B-modes. For example, the intensity of T-mode increased to about twice the lowest level after 2-hour purging with oxygen, as shown in inset of Figure 3-23(a). It suggested that the reversible physical adsorption of ozone onto sidewall of nanotubes contributes to the decrease of the resonant Raman modes, but it was only one of the multi processes occurred during the ozone experiment. There was no recovery of any fluorescence band during the oxygen purging.

The AFM images of the *SWNT/SDS* dispersion before and after Experiment 2 are shown in Figure 3-25. The SWNTs in the starting dispersion were mostly over micron in length and height analysis indicated that they were mostly individual nanotubes or very small bundles with 2 to 3 nanotubes. After the ozone exposure, the average length of the SWNTs apparently decreased, which might be the result of the oxidative “etching” by continuous ozonolysis.

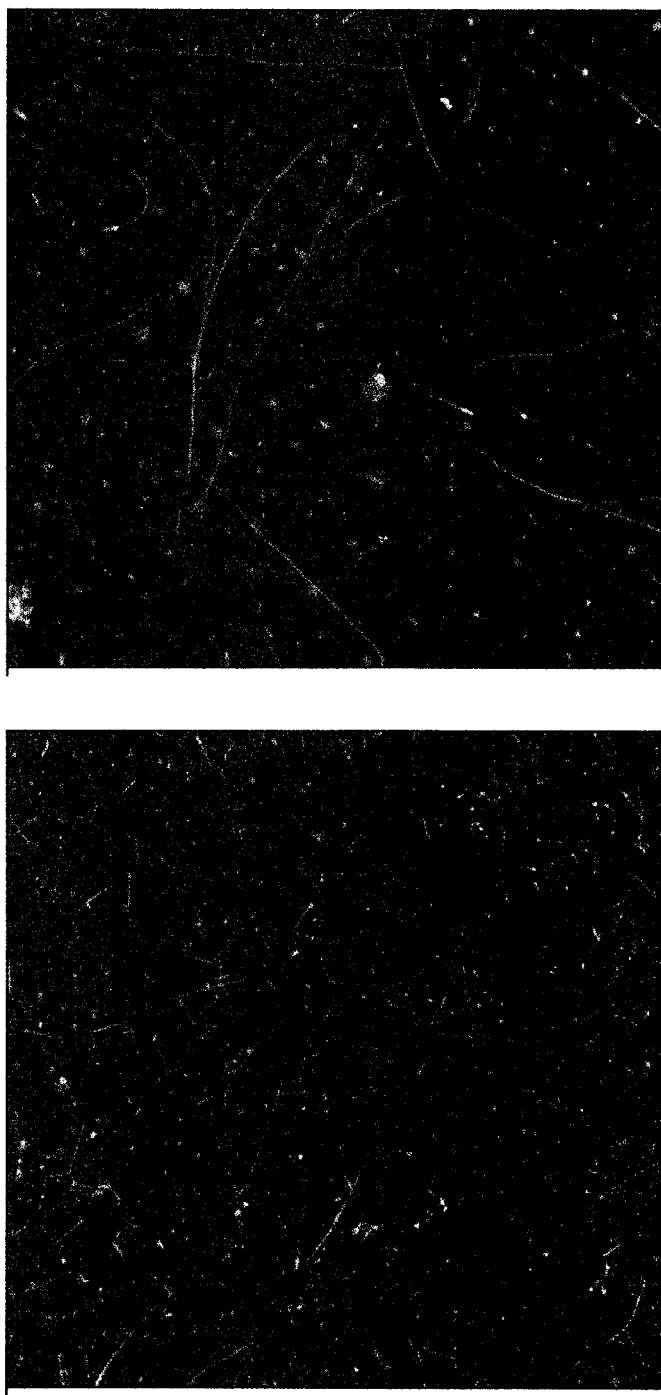


Figure 3-25 AFM images of SWNTs/SDS (unbuffered) with 80-minutes ozone treatment.

3.4.2.3 Buffered System

In Experiment 3, *SWNTs/SDS* dispersion (prepared with SWNTs HPR1061) buffered at pH ~10.4 was exposed to ozone (ozone conc.: 55 gram/m³; total gas flow rate: 62 ml/min.) in the dark environment for ~2 hours. After ozone was turned off, the dispersion was purged with oxygen for 2 hours. The pH value of the dispersion at the end of the experiment was ~6, which implies that the acidic substance formed during the ozone treatment could even break the pH equilibrium established with buffer. Variation in intensity of T-mode, B-modes, D-mode and the fluorescence bands was measured and plotted, as shown in Figure 3-26(a) – (d). Reaction rates in this system were apparently much lower than those in Experiment 2. The intensity of T-mode and B-modes dropped to half of their original value after 2-hour ozone exposure. The very interesting find is that behavior of intensity from all three Raman modes is linear, which is a sharp contrast to the observations in Experiment 2. The linear decrease in T-mode and D-mode with the corresponding linear increase in D-mode suggests that they are resulted from the same chemical process – covalent sidewall derivatization. There was no recovery of Raman intensity observed during the post-ozonation purging, which indicates that there is no unreacted ozone physically adsorbed on the SWNTs during the experiment. The fluorescence bands quenched much more slowly in this experiment, as shown in Figure 3-26(d). The enlarged part of the plot indicates the difference in quenching rates of these fluorescence bands. The 914 and 955 nm bands had slightly higher quenching rates than that of the 1058 nm band. The 977 nm band showed similar tendency, but slightly lower than that of the 1058 nm band. The data points from the 1027 nm band stayed at the top of the series, indicating the lowest quenching rates. The Raman spectra of the dispersion

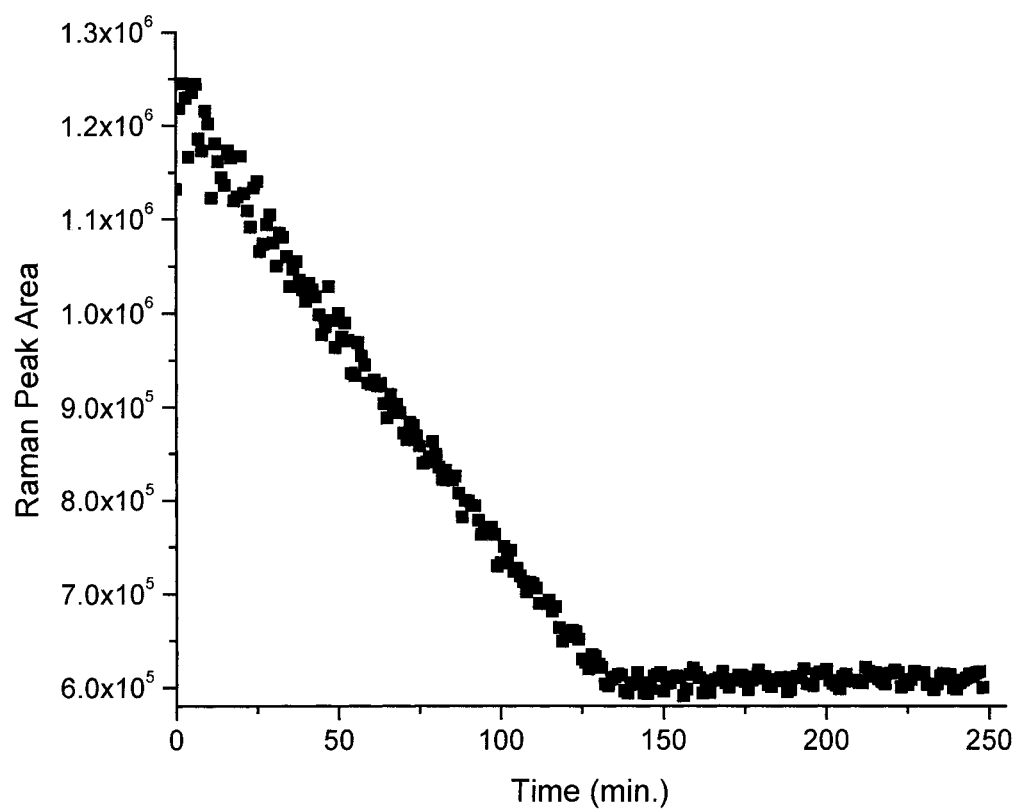


Figure 3-26(a) Raman intensity trendline (disorder mode) during a 2-hour continuous ozone treatment of SWNTs/SDS (buffered).

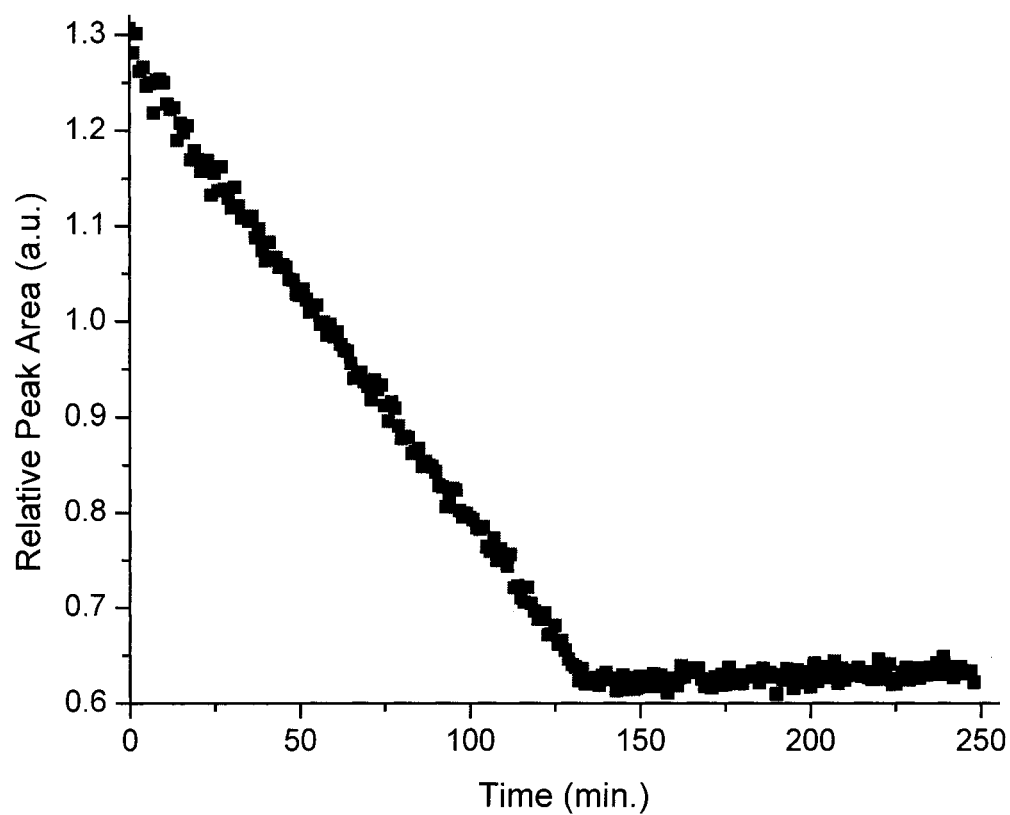


Figure 3-26(b) Raman intensity trendline (the Breathing mode) during a 2-hour continuous ozone treatment of SWNTs/SDS (buffered).

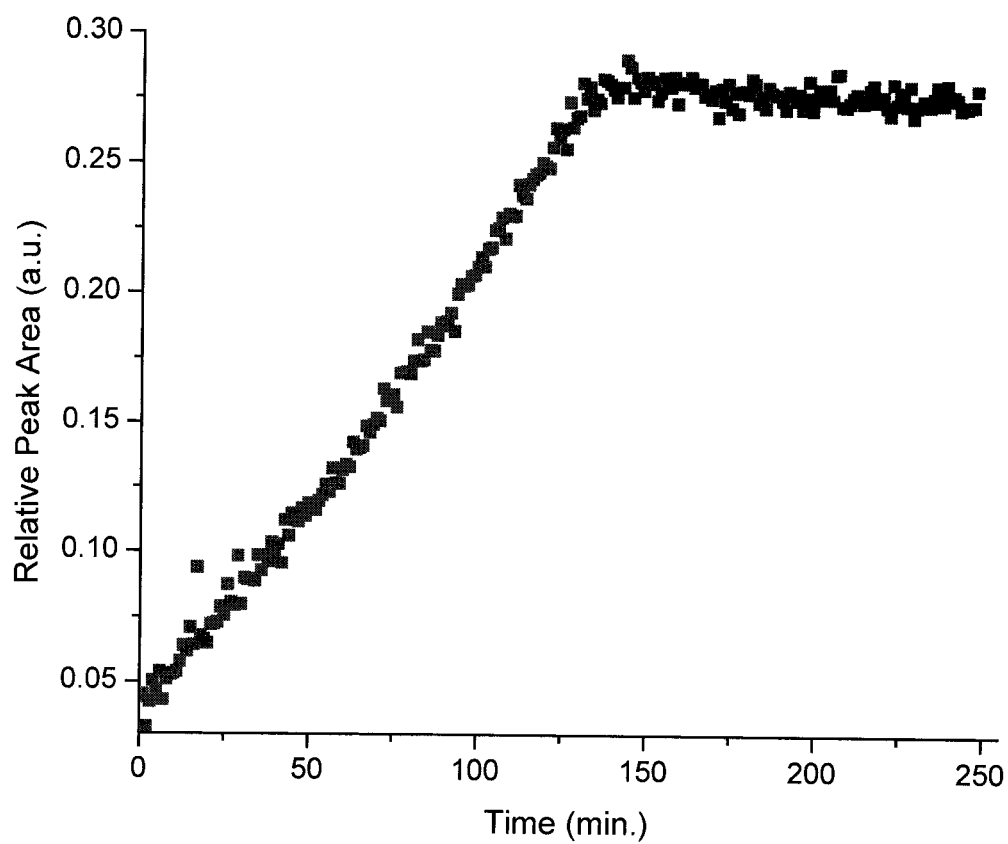


Figure 3-26(c) Raman intensity trendline (disorder mode) during a 2-hour continuous ozone treatment of SWNTs/SDS (buffered).

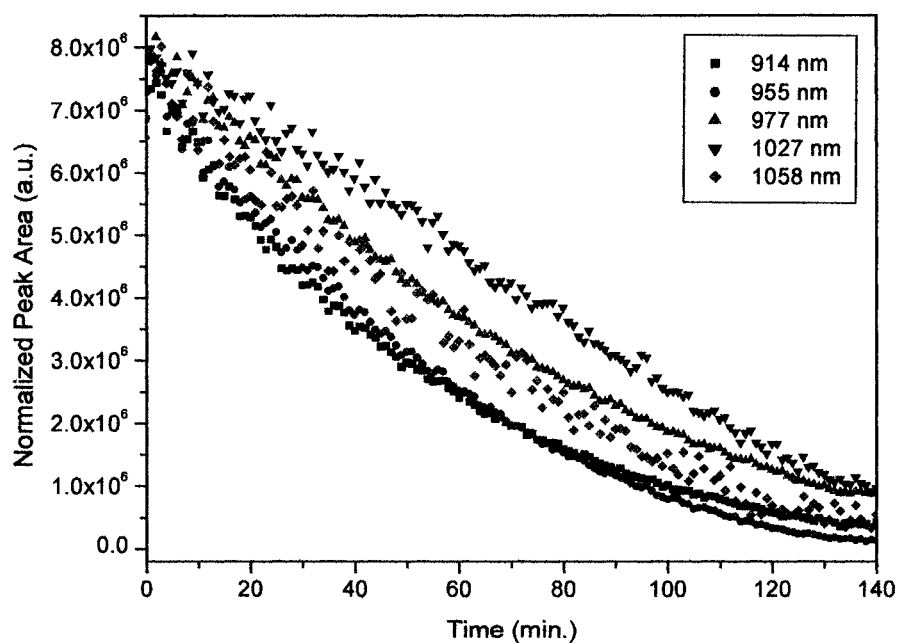
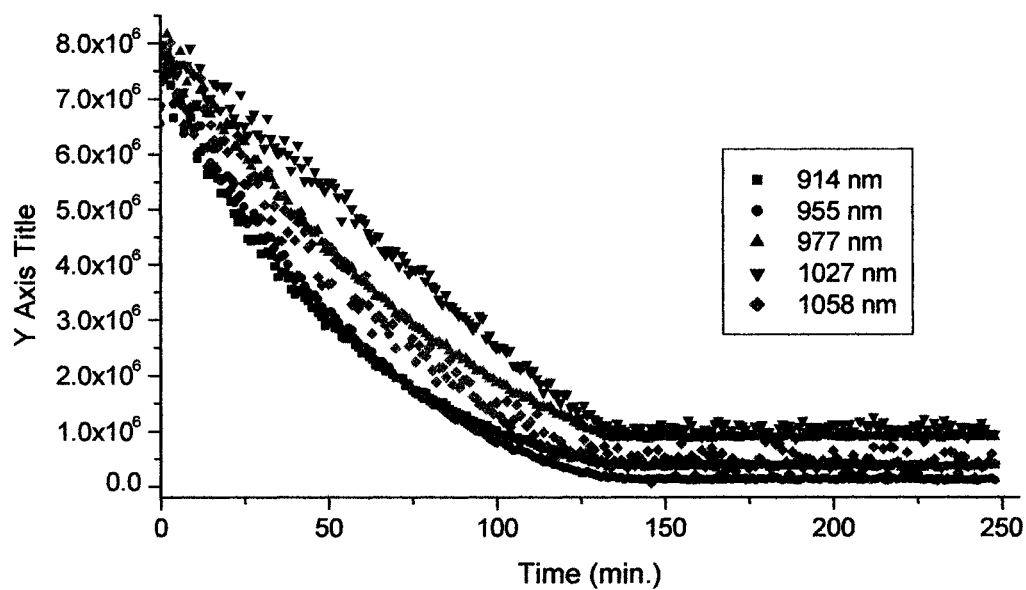


Figure 3-26(d) Top plot: the fluorescence intensity trendline during a 2-hour continuous ozone treatment of SWNTs/SDS (buffered); bottom plot: the enlarged part (0 – 140 in X axis scale) of the top plot.

before and after the experiment were demonstrated as two parts in Figure 3-27 for a better comparison of the fluorescence region and the resonant Raman modes region. From the top spectrum window, it was clearly seen the growth of D-mode with ozone treatment. The intensity of B-modes decreased to the level lower than that of the T-mode. But their shape didn't change, and there was no appearance of the "roping" mode at $\sim 268\text{ cm}^{-1}$, either. It implies that there was no bundling up of the SWNTs in this experiment. The bottom spectrum window showed that there were two broad fluorescence bands survived the 2-hour ozone treatment. They don't look like the original fluorescence bands. Their presence might represent the emission from SWNTs with sparsely derivatized sidewall. The observations from this experiment are very important. They demonstrated that the ozonolysis of *SWNTs/SDS* dispersion is controllable with pH adjustment. Exclusive chemical derivatizations could be achieved through this way, and the extent of such derivatizations, i.e. the amount of functionalities attached to the sidewall of SWNTs, can also be controlled by terminating the experiment timely. Quantity controlled derivatization of SWNT sidewalls is very important. It offers possibility of creating reactive sites quantitatively along SWNTs, which then can be used for further chemical modifications of SWNTs, for example, secondary derivatization induced cutting of SWNTs, etc. However, all the controlling is based on the results from the 2-hour experiment. Whether or not the same tendency will continue in longer time experiment is discussed below with further experiment.

The AFM images of the *SWNT/SDS* dispersion before and after Experiment 3 are shown in Figure 3-28. The SWNTs in the starting dispersion had similar length and bundle size distribution as those in non-buffered dispersion. After the 2-hour ozone

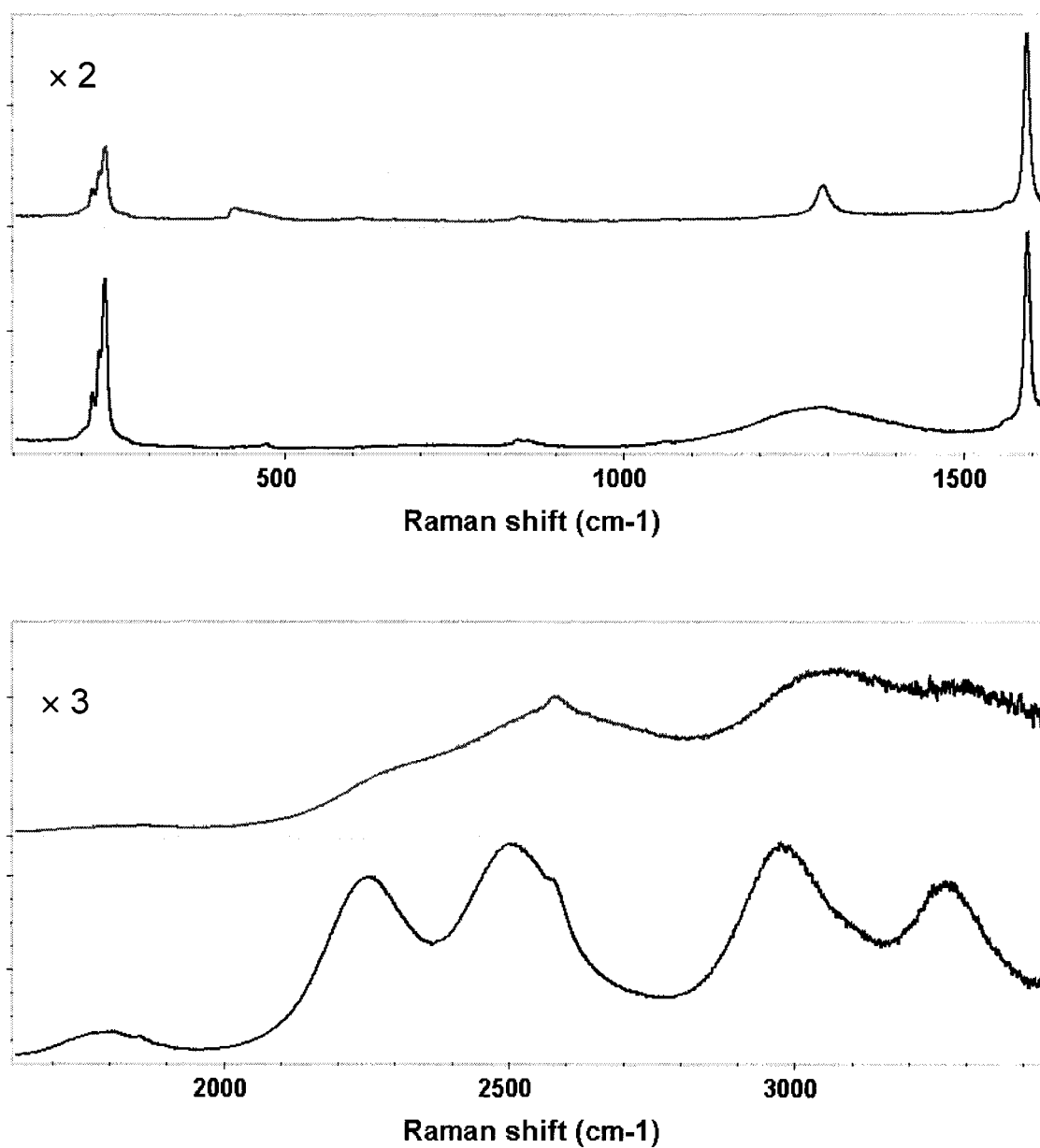


Figure 3-27 Raman spectra of *SWNTs/SDS* (buffered) with 2-hour ozone treatment.

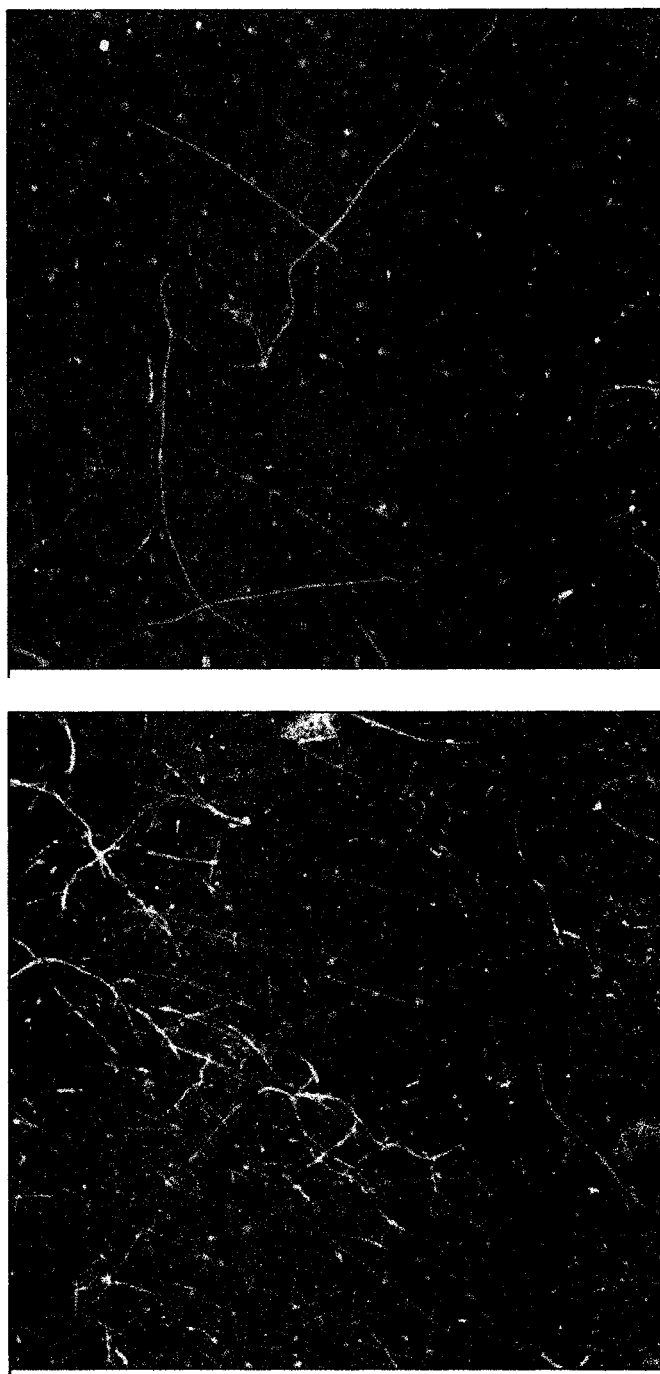


Figure 3-28 AFM comparison: Buffered. Ozone treated for 2 hours (area: $5\text{ }\mu\text{m} \times 5\text{ }\mu\text{m}$ in both images).

treatment, there was no visible length decrease of the SWNTs. But they seem to be more tangled with each other and some large bundles were observed. It implies that the sidewall properties of the SWNTs have been modified and that might cause change in micelle structures that protect SWNTs from roping up. Therefore, stronger interactions between individual SWNTs occurred.

In Experiment 4, a longer period experiment under the same conditions as Experiment 3 was conducted. The total ozone exposure time was ~220 minutes in this experiment. The comparison of the Raman spectra before and after the ozone treatment was demonstrated in Figure 3-29. The fluorescence bands were completely disappeared in the spectrum from ozone treated sample. The D-mode was higher than that in Figure 3-27, which indicates that more sidewall derivatizations could be achieved with longer reaction time. The tendency of T-mode shown in Figure 3-30(a) is mostly linear except a slight curvature around the end of the experiment time. However, the tendency of D-mode shown in Figure 3-30(b) indicates that the sidewall derivatization was actually saturated from the 167 minute of the experiment time. Therefore, further decrease in T-mode was caused by processes other than sidewall covalent derivatization. From this experiment we found the saturation point of the linear sidewall derivatization of SWNTs in the buffered system, which is very important for the controlling of the ozonolysis reaction.

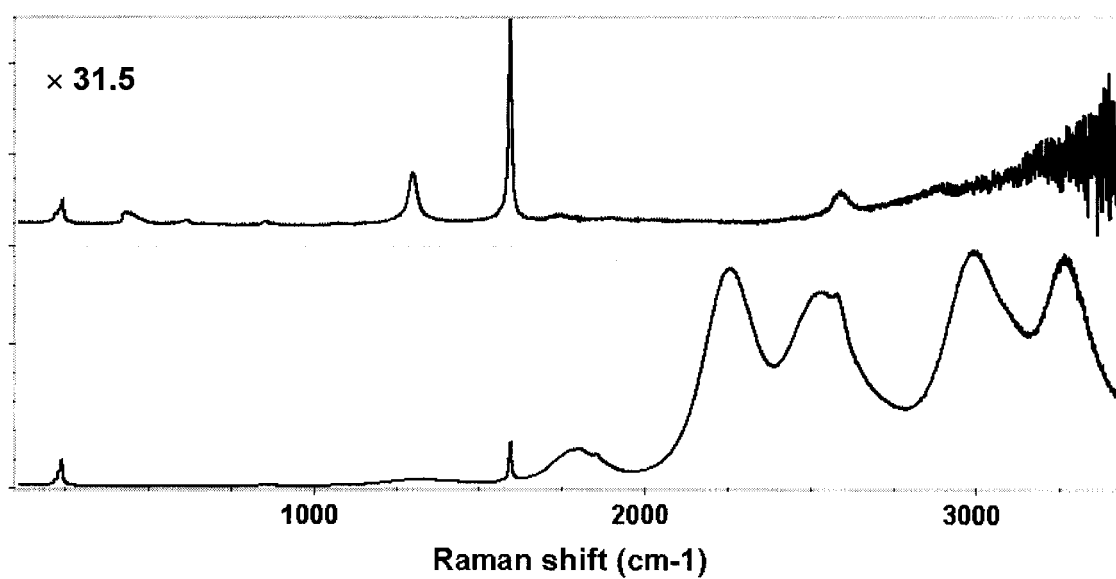


Figure 3-29 Raman spectra of *SWNTs/SDS* (buffered) with 215-minute ozone treatment. (Bottom spectrum: before ozone treatment; top spectrum: after ozone treatment.)

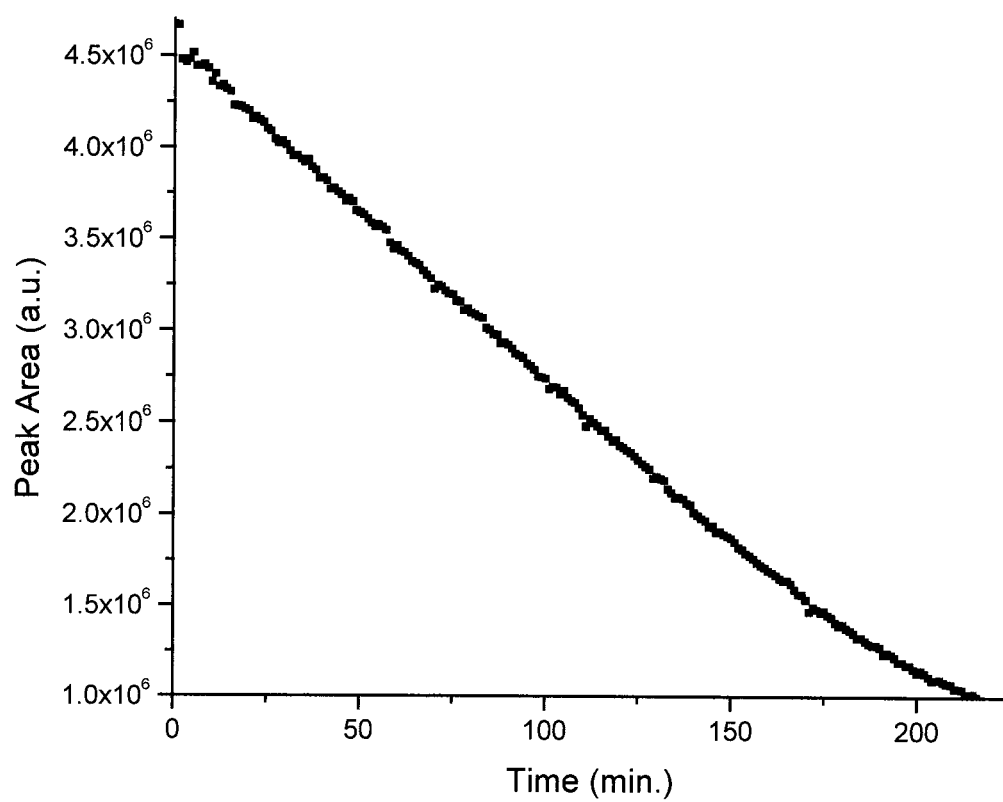


Figure 3-30(a) Raman intensity trendline (tangential mode) of *SWNTs/SDS* (buffered) with 215-minute ozone treatment.

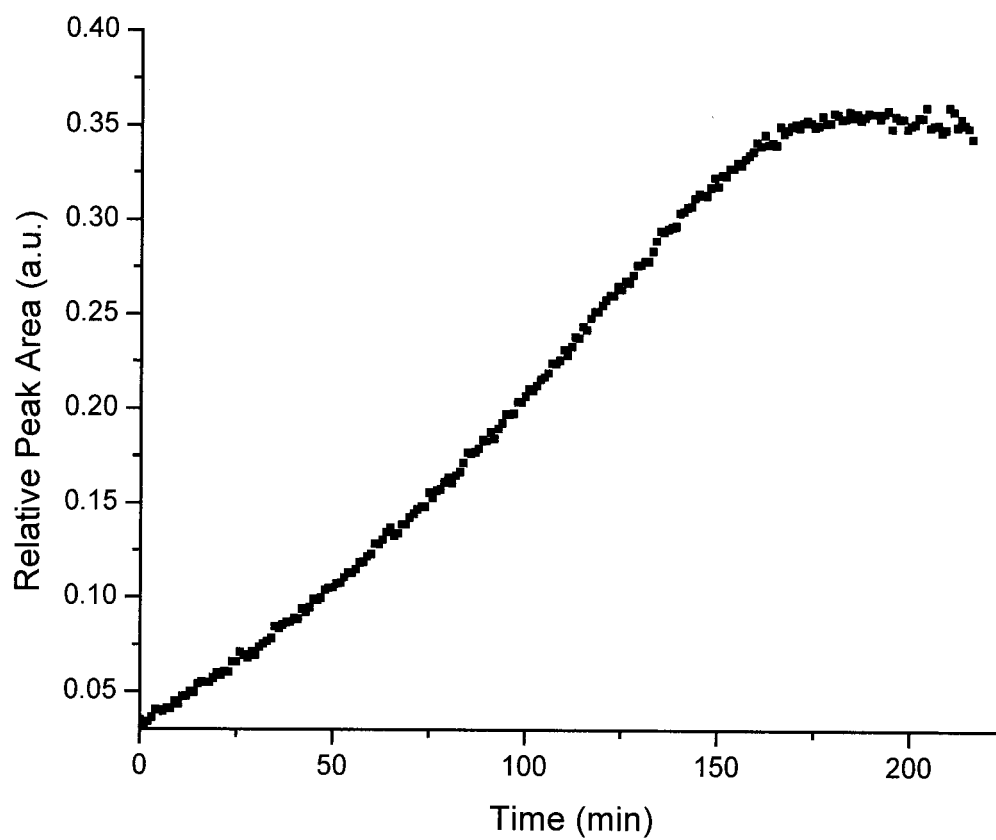


Figure 3-30(b) Raman intensity trendline (disorder mode) of SWNTs/SDS (buffered) with 215-minute ozone treatment.

3.4.2.4 Ozonolysis of the *Purified-SWNTs/SDS* dispersion

In Experiment 5, *Purified-SWNTs/SDS* dispersion (prepared with purified-SWNTs HPR1061) with pH adjusted to ~ 10.4 was exposed to ozone (ozone conc.: 55 gram/m³; total gas flow rate: 62 ml/min.) in the dark environment for ~ 2 hours. The pH value of the dispersion at the end of the experiment was ~ 5 . The comparison of the Raman spectra before and after the ozone treatment was demonstrated in Figure 3-31. Raman spectrum of the *Purified-SWNTs/SDS* dispersion has several different features compared with that of the dispersion prepared from as prepared SWNTs. The B-mode is always lower in intensity than the T-mode, and the roping mode at 267 cm⁻¹ is in presence. It suggests most SWNTs in the dispersion are in bundles. The intensity of fluorescence bands was also much lower in this case. The overtone mode at 2588 cm⁻¹ is very strong and exceeds the fluorescence band in the same region. The overall Raman intensity decreased after the 2-hour ozone treatment, and all the fluorescence bands vanished. There was no distinct D-mode growth, which suggests there was not much sidewall derivatization occurred. The trend of T-mode intensity during ozone treatment was plotted and compared with that from the as prepared SWNTs system, as shown in Figure 3-32(a). It was clearly seen from the plot that duration of the first part of the reaction where the Raman intensity dropped dramatically was much shorter in the purified-SWNTs system than that in the as prepared SWNTs system. It resulted in an overall lower rate of intensity decrease during the 2-hour experiment in the purified-SWNTs system. The same comparison of D-mode intensity was demonstrated in Figure 3-32(b). The D-mode growth varied at similar tendency, but the rate was lower in the purified-SWNTs system. The results of this experiment indicate that there is no substantial difference in the ozonolysis between

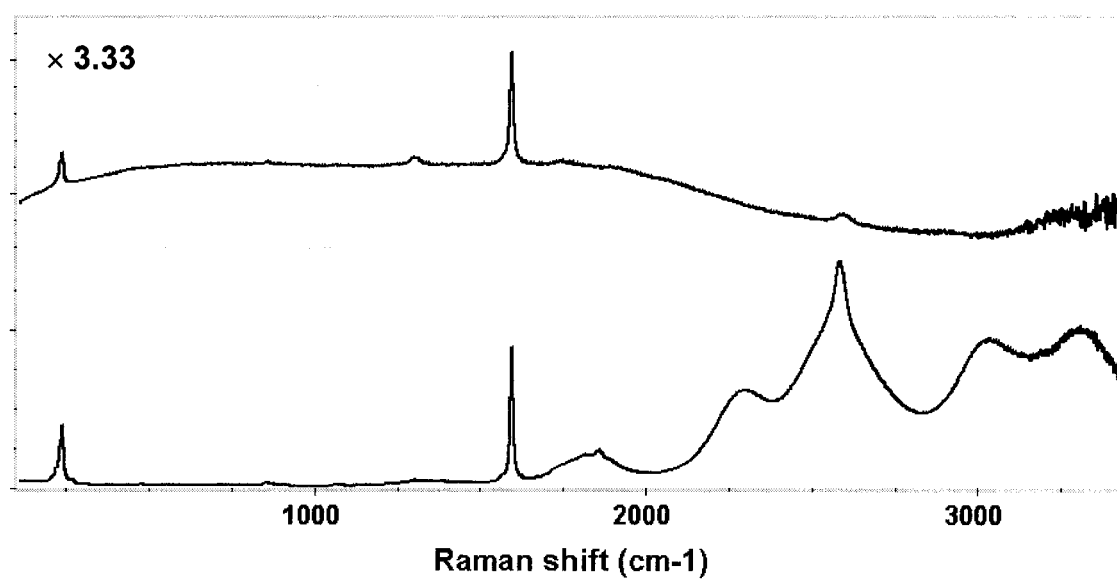


Figure 3-31 Raman spectra of purified SWNTs/SDS (unbuffered) with 2-hour ozone treatment.

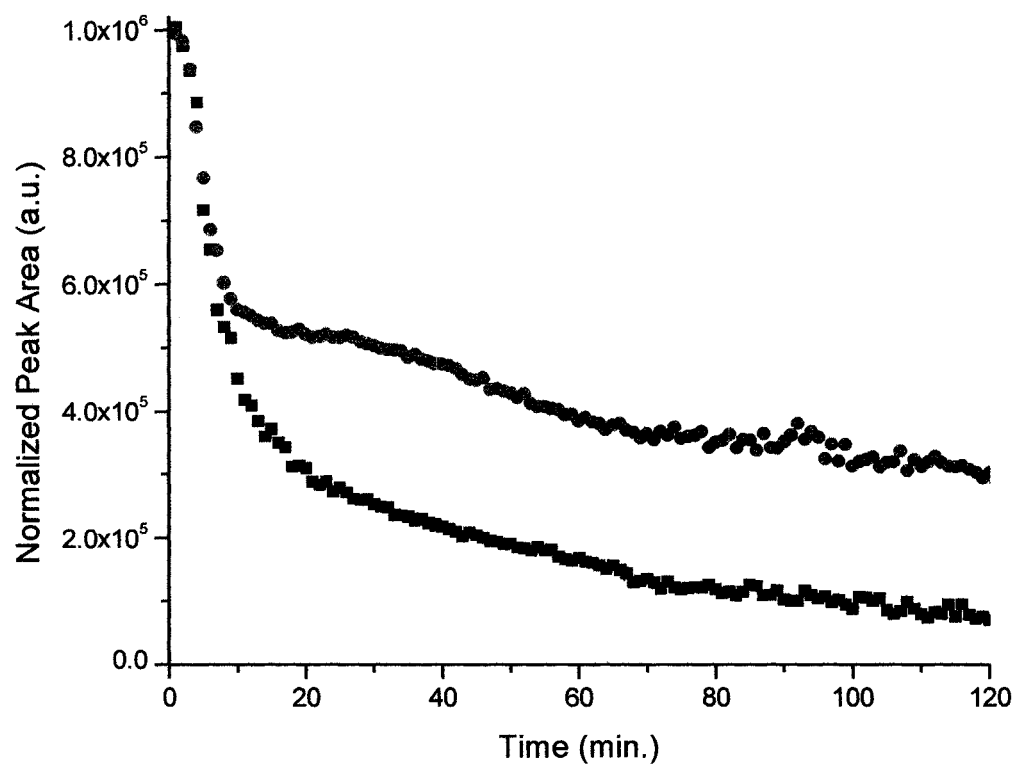


Figure 3-32(a) Comparison of Raman intensity trendlines (tangential mode) of as-prepared (black) and purified (red) *SWNTs/SDS* with ozone treatment.

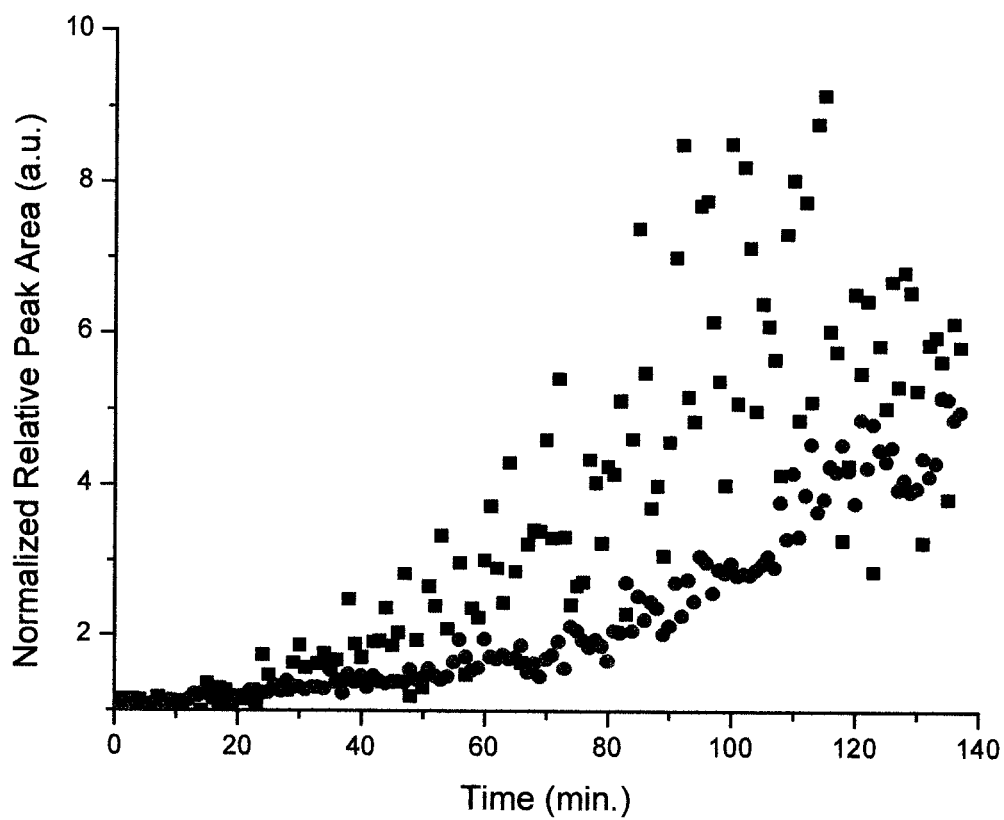


Figure 3-32(b) Comparison of Raman intensity trendlines (disorder mode) of as-prepared (black) and purified (red) *SWNTs/SDS* with ozone treatment.

the purified-SWNTs and as prepared SWNTs dispersions. The different reaction rates might come from the bundling of nanotubes in the purified-SWNTs dispersion system.

3.4.2.5 pH effect in *SWNTs/Pluoronic-108* dispersion system

In Experiment 6, three *SWNTs/Pluoronic-108* dispersions (prepared with SWNTs HPR1061) with pH adjusted differently were used for the study. *Dispersion I* was adjusted to pH 11, *Dispersion II* was buffered at pH ~10.4, *Dispersion III* was buffered at pH ~7. The three dispersions were exposed to ozone (ozone conc.: 55 gram/m³; total gas flow rate: 62 ml/min.) in the dark environment for ~2 hours, respectively. The variation of T-mode and D-mode during ozone treatment from all three samples were plotted and compared in Figure 3-33(a) and (b). The pH effect on the ozonolysis was apparent and consistent in both plots. The reaction rates were highest in *Dispersion III*, second highest in *Dispersion I*, and lowest in *Dispersion II*. The T-mode intensity decayed linearly in *Dispersion II*, and decayed exponentially in the other two systems. There was a linear “induction” period at the initial part of the reaction in the case of *Dispersion I*, which was not observed in that of *Dispersion III*. The influence of environmental pH on the ozonolysis reactions is similar in SDS and Pluoronic systems, which indicates that the pH effect is independent of the charge of the surfactants. Controlled linear modification of SWNTs in the dispersion can be achieved by buffering the pH of the system around 10, whereas buffering the pH around 7 doesn’t work. Figure 3-33(b) shows that the relative intensity of D-mode in *Dispersion I* and *III* systems was considerably higher than that in *Dispersion II*. But considering the total loss of SWNTs during the ozonolysis in the case

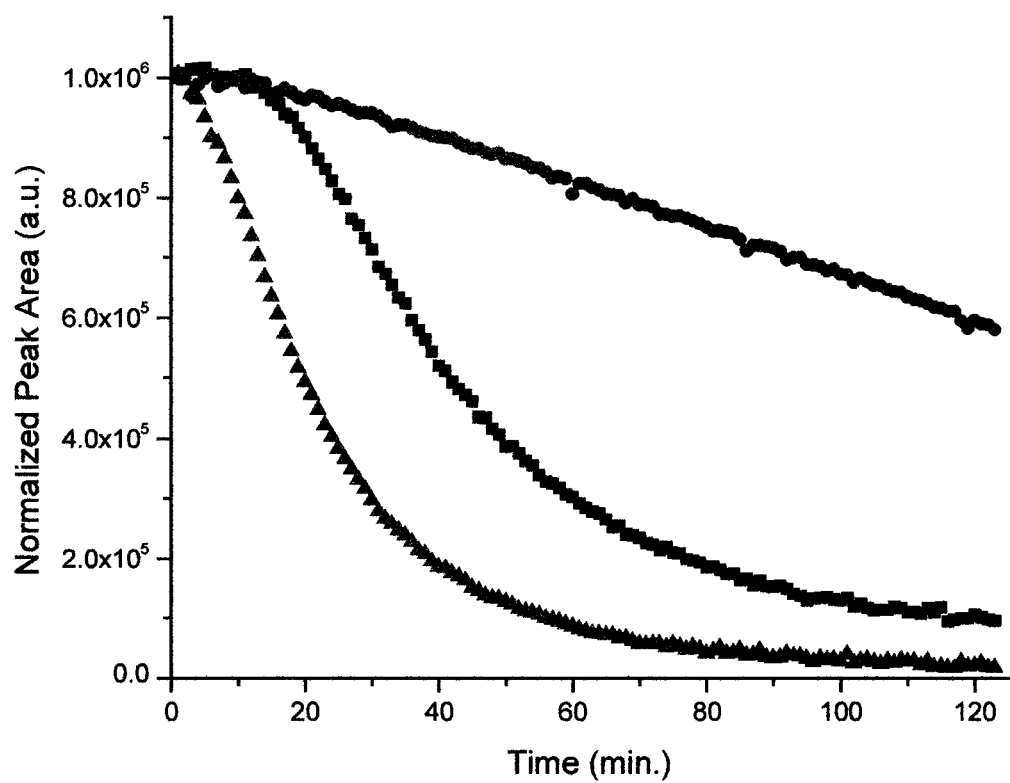


Figure 3-33(a) The pH effect on Raman intensity (tangential mode) of *SWNTs/Pluoronic-108* with ozone treatment (Red: buffered at pH 10; Black: pH 11, unbuffered; Green: buffered at pH 7).

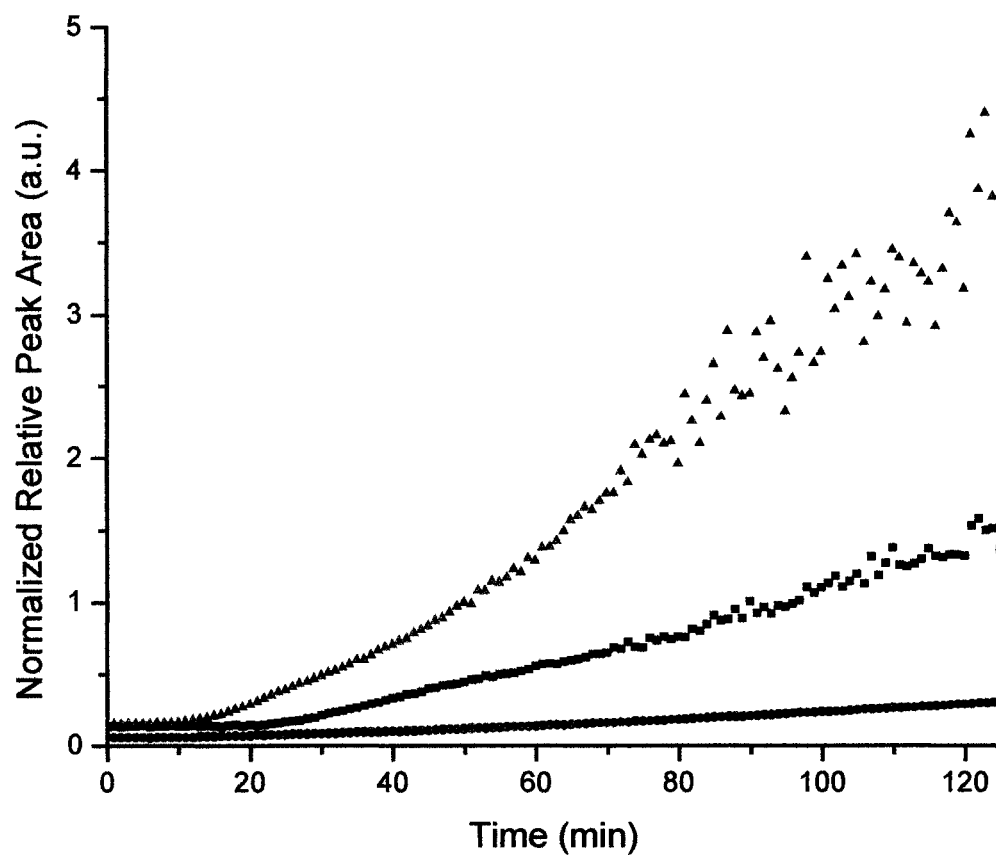


Figure 3-33(b) The pH effect on Raman intensity (disorder mode) of *SWNTs/Pluoronic-108* with ozone treatment (Red: buffered at pH 10; Black: pH 11, unbuffered; Green: buffered at pH 7).

of *I* and *II*, *Dispersion II* is the best system for controlled sidewall derivatization without high consumption of SWNTs.

3.4.2.6 Influence of surfactants

In Experiment 7, *SWNTs/DTAB* dispersion (prepared with SWNTs HPR1061) with pH buffered at ~ 10.4 was exposed to ozone (ozone conc.: 55 gram/m³; total gas flow rate: 62 ml/min.) in the dark environment. Surprisingly, the dispersion turned into almost colorless within less than half an hour of ozone treatment. The Raman spectra became completely featureless around the same time. Apparently, all the SWNTs in the dispersion were swiftly consumed within this time. The variation of T-mode and D-mode during the ozone treatment of the *SWNTs/DTAB* dispersion was plotted and compared with the data from experiments under same pH conditions with SDS and Pluoronic-108 in Figure 3-34(a) and (b). It can be seen that the decay rates of T-mode were very close in SDS system and Pluoronic-108 system, except that the “induction” period was slightly longer in the Pluoronic-108 system. Whereas the decay rate was surprisingly high in DTAB system, and it didn’t seem to be linear. The D-mode trends shown in Figure 3-34(b) indicate that the relative intensity of D-mode in SDS and Pluoronic-108 system was also close, with that in Pluoronic-108 system slightly higher. It suggests that the relative ratio of sidewall derivatization versus other processes such as physically adsorption and secondary oxidation that leading to the “etching” of SWNTs is higher in the Pluoronic-108 system than that in the SDS system. The growth rate of D-mode in DTAB system was particularly high in the 25 minutes of the experiment. And the fact is

that there was almost no SWNTs in the system after the first 25 minutes. It means that in the DTAB system, the ozone had significantly high reactivity with nanotubes. This not only resulted highly sidewall derivatization, but also developed further and “etched” nanotubes away at very high rates. The Raman spectra of the *SWNTs/DTAB* dispersion before and after the 25-minute ozone treatment were shown in Figure 3-35. The low concentration of SWNTs in the ozone treated dispersion was reflected by the absence of B-mode in the top spectrum. The intensity ratio of D-mode to T-mode indicates the high level of derivatization. The surprisingly high reactivity of ozone in the *SWNTs/DTAB* dispersion was believed related to the bromine ions (Br^-) presented in the system. Br^- might be easily oxidized by ozone to form BrO^- , even BrO_3^- . Both are very strong oxidizing reagents and they might rapidly oxidize carbon from SWNTs forming CO_2 .

3.4.3 Conclusion

We’ve investigated the continuous ozonolysis of individually dispersed SWNTs on a gas-aqueous solution interface with in-situ Raman and UV-vis.-NIR spectroscopy techniques. We found that multiple processes were involved in the interaction between ozone and SWNTs, for example, physical adsorption, covalent sidewall derivatization, and reactive oxidative “etching”. These processes influence the Raman and UV-vis.-NIR spectra of the SWNTs extensively and many information about the processes could be learnt by examining the variation in the in-situ recorded spectra. The ozone was found reacting with SWNTs at higher rate in non-buffered pH ~10 system without creating much sidewall derivatization on the nanotube sidewall. We believe that it was because

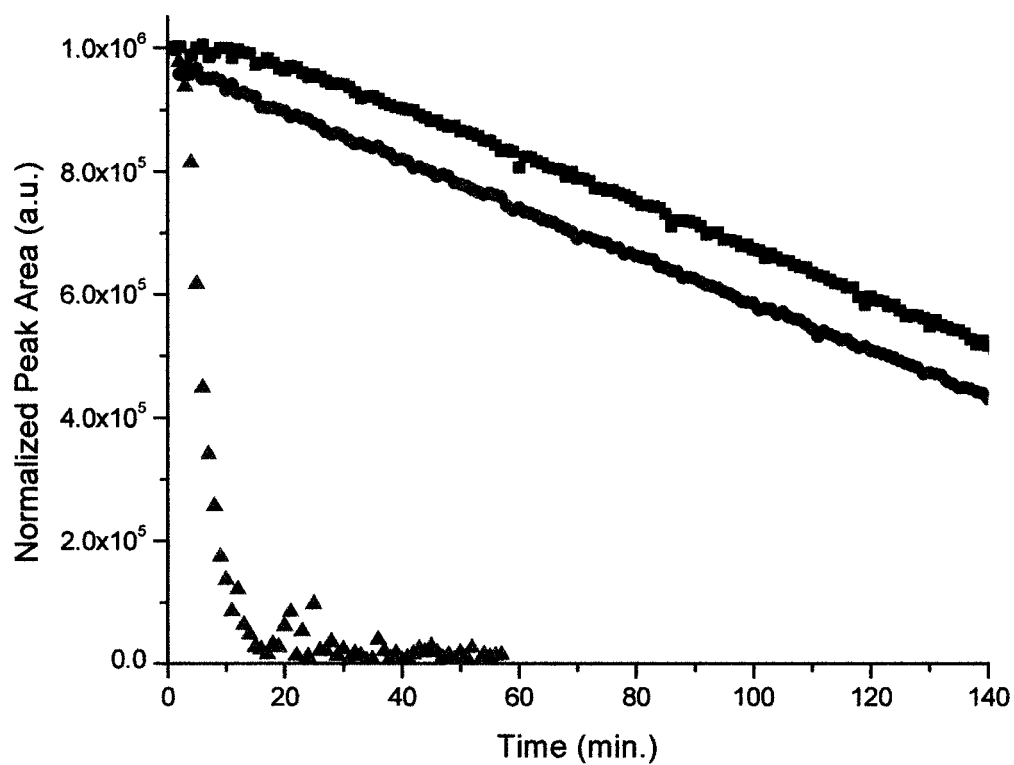


Figure 3-34(a) The effect of surfactants on Raman intensity (tangential mode) of *SWNTs/surfactant* with ozone treatment. (Black: Pluronic-108; Red: SDS; Green: DTAB).

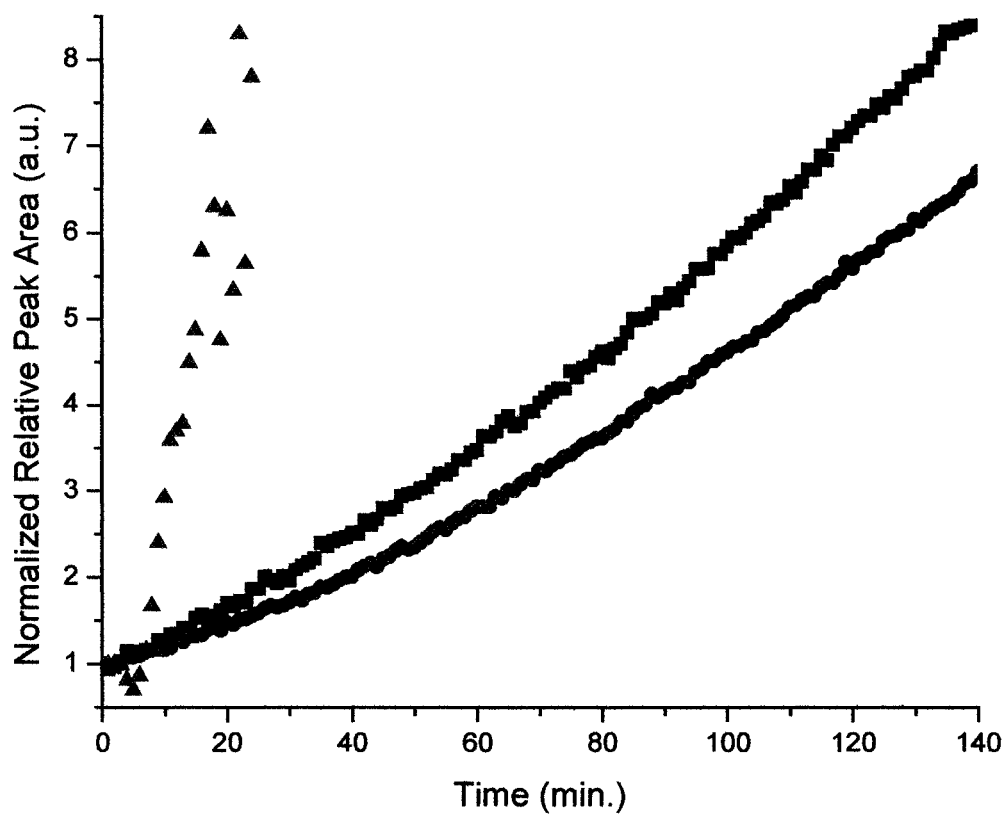


Figure 3-34(b) The effect of surfactants on Raman intensity (disorder mode) of *SWNTs/surfactant* with ozone treatment. (Black: Pluoronic-108; Red: SDS; Green: DTAB).

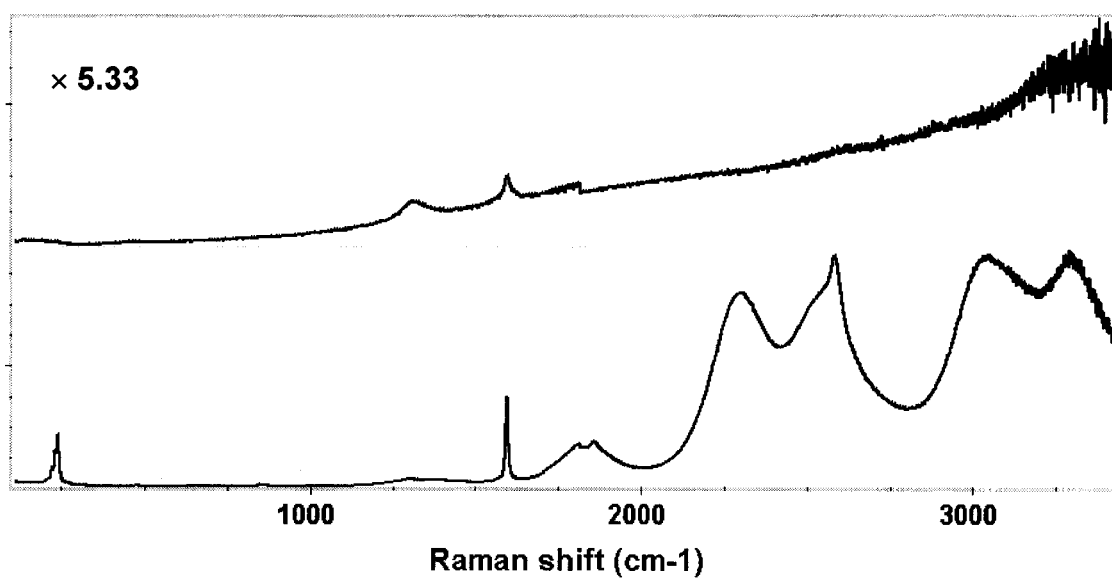


Figure 3-35 Raman spectra of *SWNTs/DTAB* (buffered) with 25-minute ozone treatment. (Bottom spectrum: before ozone treatment; top spectrum: after ozone treatment).

continuous ozone attack on the initial sidewall derivatives resulted removal of carbon from nanotubes and “etched” the SWNTs gradually. In pH \sim 10.4 buffered system, the ozone reacted with SWNTs at significantly lower rate. The reactions built up covalent sidewall derivatizations at a linear rate, which suggest better control of the reactions under these conditions. Reaction of ozone in the *SWNTs/DTAB* dispersion resulted unusually rapid consumption of SWNTs. It was believed related to the formation of highly oxidative species such as BrO^\cdot , even BrO_3^\cdot from the reaction between ozone and Br^- ions presented in the system.

3.4.4 Future Work

The reaction system of ozone and surfactant dispersed individual SWNTs can provide important information on sidewall modifications of SWNTs. What have been learnt from the above study will lead to controllable sidewall derivatization. It can be used to intentionally create reactive sites along the nanotubes with certain distribution. Then activation of further reaction could “cut” SWNTs to specific length at the reactive sites. To achieve that, further study is needed to understand the mechanism behind the phenomena observed here so that real control of the ozonolysis could be realized.

Chapter 4

OTHER CHEMISTRY OF HIPCO SWNTS

4.1 HIGH TEMPERATURE GASEOUS HYDROGEN CHLORIDE PROCESS

4.1.1 Introduction

As described previously in this thesis, HiPco process can produce SWNTs with high quality and smaller diameter (1 nm in average). As prepared HiPco SWNTs generally contain 20 – 30 wt % Fe catalysts, most of which are encapsulated in graphene carbon shells. To take full advantages of the remarkable mechanical, physical and chemical properties of SWNTs, the Fe catalyst has to be removed from the SWNT samples as thoroughly as possible. One of the successful purification processes⁷⁵ includes “soft-baking” the raw material in a wet Ar/O₂ environment at elevated temperatures to selectively oxidize the non-SWNT carbon, to break the carbon shells surrounding Fe particles and oxidize the metal impurity. Then sonicating and stirring the “soft-baked” sample in concentrated HCl solution can extract the oxidized Fe species. Finally, the samples were annealed at 800 °C in argon atmosphere for one hour. This process was found to reduce the wt % of Fe from ~20 wt % to ~0.03 wt %. Because SWNTs are dispersed in solution phase in one of the purification steps, this process is also referred as “wet” purification process. This section of the thesis describes a “dry” purification process that involved converting oxidized Fe species into vapor-phased FeCl₃ with gaseous HCl at temperatures over 600 °C. The FeCl₃ vapor is purged off the SWNT sample with flowing argon and this leaves behind the purified SWNTs. There is no liquid

phase processing involved in this method where the circumstance facilitates the SWNTs moving towards each other and forming huge bundles. Instead, the morphology of the SWNT sample would remain nearly unchanged during the “dry” process. The purity and quality of thus purified SWNTs were examined with TGA, ESEM/EDAX, Raman and UV-vis.-NIR.

4.1.2 Experimental

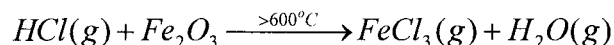
The “soft-baked” SWNTs materials were loaded in the quartz chamber of a tubular furnace. The design of the quartz chamber ensures the maximum exposure of SWNT sample to the gaseous HCl/Ar mixture. Samples were purged with pure argon at 50 °C for 1 hour for degassing. Then another stream of 10 % HCl/Ar gas mixture started flowing through the sample while the heating began. The flow rates were set at 70 cm³/min. for 10 % HCl/Ar and 50 cm³/min. for pure argon. The heating program was ~10 °C/min. to 800 °C. Once the temperature reached 800 °C, the HCl/Ar gas was turned off, the sample was isothermal at 800 °C for one hour purging with pure argon. Then the furnace was turned off and the sample was cooled down to room temperature naturally.

UV-vis.-NIR spectra of the purified SWNTs were collected with suspension of the SWNT sample in *o*-dichlorobenzene (ODCB).

4.1.3 Results and Discussions

The chemical reaction involved in the gaseous HCl purification process can be

expressed as:



The b.p. of $FeCl_3$ is $316^\circ C$, when HCl contacts Fe_2O_3 at temperatures over $600^\circ C$, $FeCl_3$ vapor forms. The vapor is taken away from the hot sample zone by the purging argon and condenses at cooler area of the system. Yellowish to light-brownish crystalline substance was observed at the quartz tube portion that is outside the furnace, which was a clear evidence that Fe was removed from the SWNTs. SEM image of the gaseous HCl purified SWNTs is shown in Figure 4-1. The surface of the sample looks porous and bundle size of the SWNTs is not as large as that from a “wet” purification process. A Raman spectrum of the purified SWNTs is shown in Figure 4-2. The sharp and strong resonant Raman modes with the low intensity disorder mode from SWNTs suggest that the quality of the SWNTs is high. In the inset of Figure 4-2, the well resolved components of the Breathing modes confirm that the sidewall of the SWNTs is free of chemical derivatives. The UV-vis.-NIR spectrum of the purified SWNTs is shown in Figure 4-3. The broad van Hove features in the range of $1000 - 1600$ nm indicate that the SWNTs in ODCB are bundled. The continuously distributed van Hove absorption modes from 400 to 1600 nm also suggest that the sidewall of SWNTs is clean and nearly defectless. The thermal decomposition behavior of the purified SWNTs in air was recorded with TGA. Generally, there are several important factors from TGA data that indicate the quality of the SWNTs. The thermal decomposition onset temperature can tell if there is catalytic oxidation caused by the metal impurities; the residue percentage tells the exact amount of Fe_2O_3 in the sample; the temperature derivative weight loss curve indicates maximum weight loss temperature, which is also indicative of the quality of the SWNTs; the peak width of the

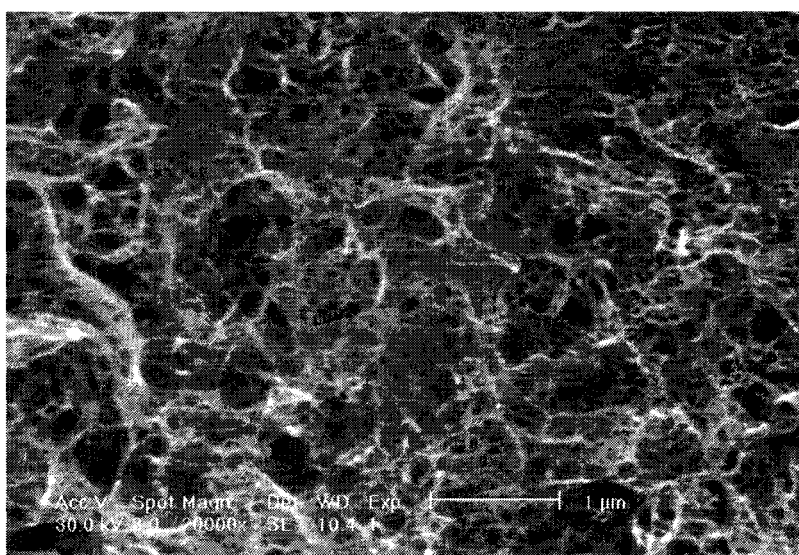


Figure 4-1 SEM image of gaseous HCl purified HiPco SWNTs.

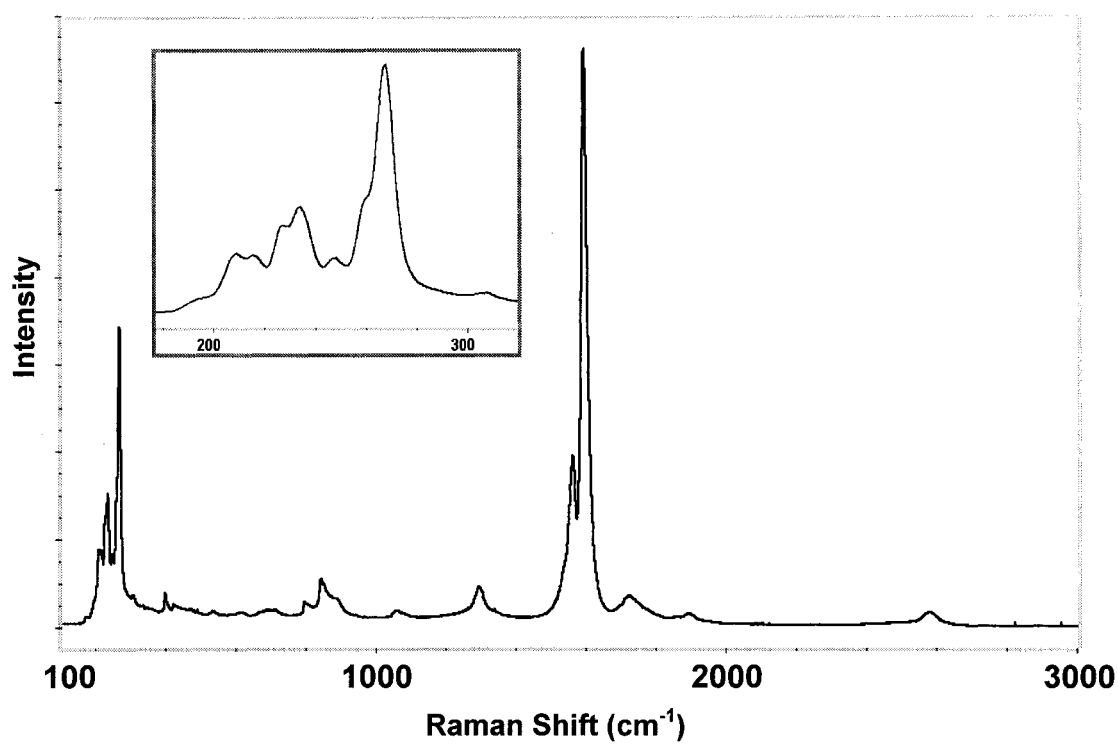


Figure 4-2 Raman spectrum of gaseous HCl purified HiPco SWNTs. (Inset: enlarged part of the Breathing mode region of the spectrum)

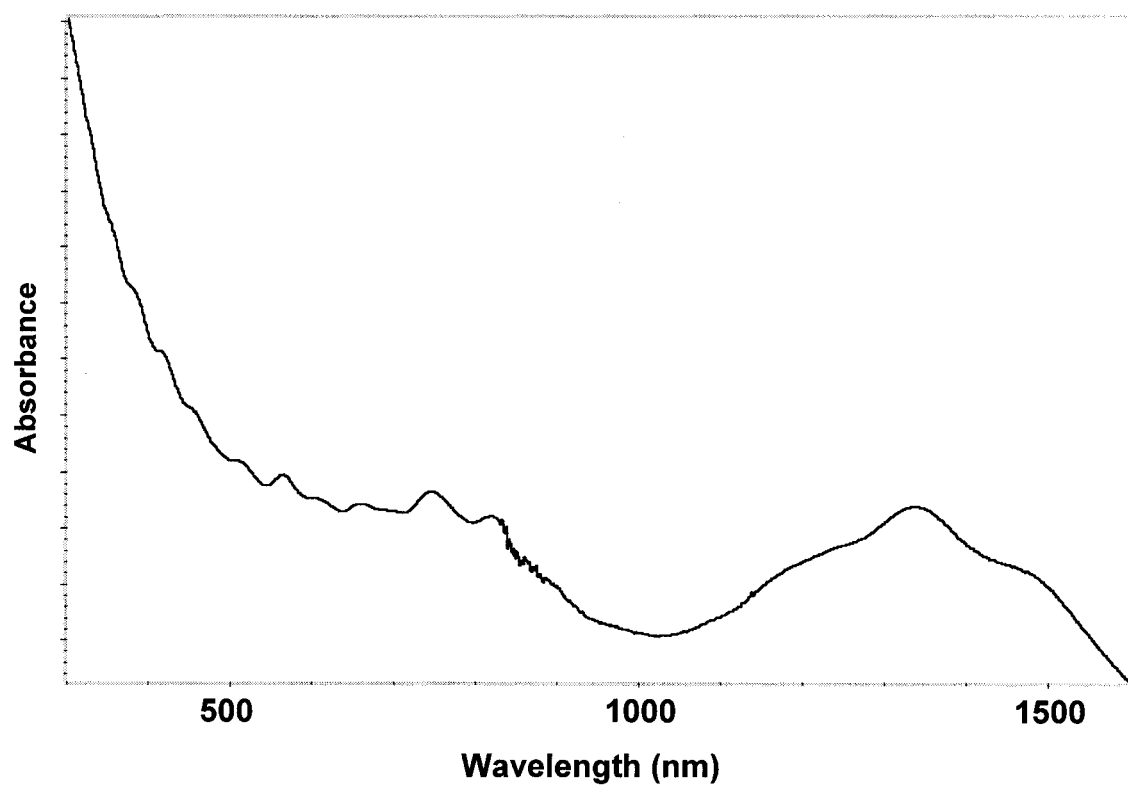


Figure 4-3 UV-vis.-NIR spectrum of gaseous HCl purified HiPco SWNTs.

temperature derivative weight loss curve indicates the size uniformity of the SWNTs. The TGA plot of the gaseous HCl purified SWNTs in Figure 4-4 shows that the thermal decomposition onset temperature of the purified SWNTs was 479 °C, the temperature of the maximum weight loss was 523 °C. These values are close to those from the “wet” process purified SWNTs. The residue weight percentage is 1.825 when the sample was heating to 800 °C, which corresponds to 1.28 wt % of Fe impurity.

4.1.4 Conclusions

The experiments showed that gaseous HCl process (“dry” purification process) can effectively remove Fe catalyst from HiPco SWNTs sample. The morphology of the “dry” process purified SWNTs is quite different from the hydrochloric acid soaking process (“wet” purification process). The “dry” process purified SWNTs are more porous and don’t form as dense layers of tangled thick bundles as those from the “wet” process. Also, the high temperature process prevents HCl from adsorbing or intercalating into nanotube ropes that was found influencing the optical absorption spectra of the SWNTs⁷⁵.

4.2 DILUTE HNO₃ REFLUXING PROCESS

4.2.1 Introduction

Nitric acid (2 - 3 M) has been used in the initial purification of laser-oven grown SWNTs to oxidize and remove metal catalysts and other non-nanotube carbon species. The raw materials had to be refluxed in nitric acid for 45 hours for an effective

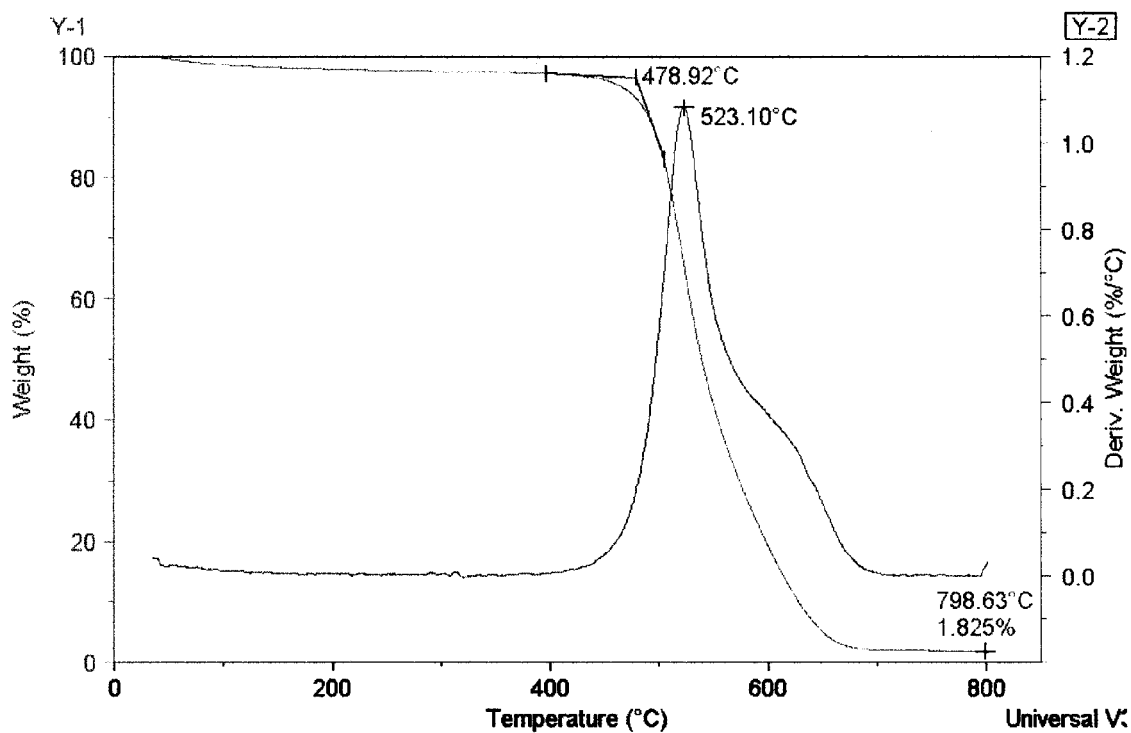


Figure 4-4 TGA of gaseous HCl purified HiPco SWNTs heated in air up to 800 °C. (Red curve: percentage weight loss; blue curve: temperature derivative weight loss)

purification result^{108,109}. The mixture of concentrate sulfuric acid (98% conc.) and nitric acid (70% conc.) was found creating short pieces of nanotubes when purified laser-oven grown SWNTs were sonicated in the mixture for long period of time at 40 °C¹⁰⁸. These processes were found too harsh for HiPco SWNTs that most of the nanotubes were “digested” during the prolonged refluxing. In this section, a modified HNO₃ refluxing process was described that was found removing almost all the Fe catalysts and amorphous carbons from raw HiPco SWNTs as well as forming oxygen containing functionalities onto the nanotubes that greatly improve their solubility. Thermal desorption of the attached functionalities was studied by annealing the functionalized SWNTs in argon atmosphere up to 600 °C. The annealing was found removing all functionalities on the nanotubes and recovering the pristine SWNT structure as confirmed with Raman spectra analysis.

4.2.2 Experimental

100 mg HiPco SWNTs raw material was added to ~100 ml 1M HNO₃ solution. The mixture was stirred constantly and refluxed for ~20 hours. The solution turned into light yellowish color during the refluxing. The SWNTs samples was then collected by vacuum filtering the solution through the 1 µm pore-sized PTFE membrane, and rinsing with large amount of DI water until the pH of the filtration close to 7. The solid SWNTs were then collected and vacuum dried at 70 °C overnight before further analysis.

The functionalization of SWNTs during the HNO₃ refluxing was examined with ATR-IR and Raman spectroscopy. The amount of metal impurity in the HNO₃ treated

SWNTs was determined by burning the sample in air in a TGA furnace up to 800 °C and examine the residue percentage. Thermal stability of the sample in air was also obtained from the TGA analysis. The mass spectrometer coupled with the TGA instrument provided detailed information about the species evolved from the sample during the heating process. Similar thermogravimetric analysis was also used to investigate the thermal desorption of the functionalities on the sample in an inert atmosphere (argon) up to 600 °C.

4.2.3 Results and discussions

The HNO₃ treated SWNTs showed greatly improved solubility in solvents such as ethanol. They can form dark brownish suspension with brief sonication and the suspension was stable over months. Apparently, the sidewall derivatives formed during the refluxing had changed the affinity of nanotube sidewalls towards ethanol. ATR-IR spectra of the HNO₃ treated SWNTs are shown in Figure 4-5. The original spectrum (the bottom one) was processed and scaled up (the top one) to show the weakly absorbed IR modes from the functionalities on the SWNTs. The features between 1100 – 1250 cm⁻¹ indicate there are C – O – C groups on the nanotube structure, the C = O feature (at 1733 cm⁻¹) and the O – H feature (3000 – 3600 cm⁻¹) indicate that there are carboxylic acid groups. The C = C feature at 1582 cm⁻¹ confirmed that there are functionalities covalently attached to the SWNTs. Raman spectra of the SWNTs before and after the HNO₃ refluxing are compared in Figure 4-6. The decrease in overall intensity of Raman modes is typical for derivatized SWNTs because of the weakening of resonant Raman

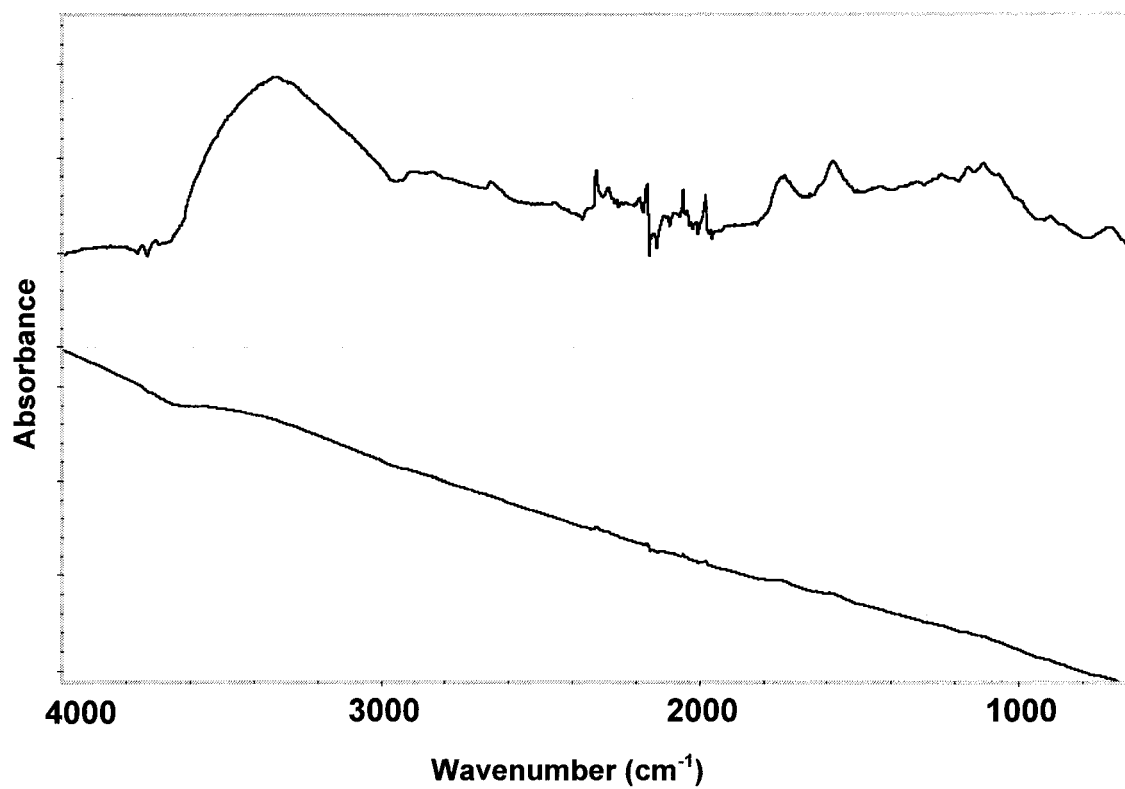


Figure 4-5 Bottom spectrum: ATR-IR spectra of HNO_3 treated as-prepared HiPco SWNTs; Top plot: bottom spectrum after baseline correction and enlargement.

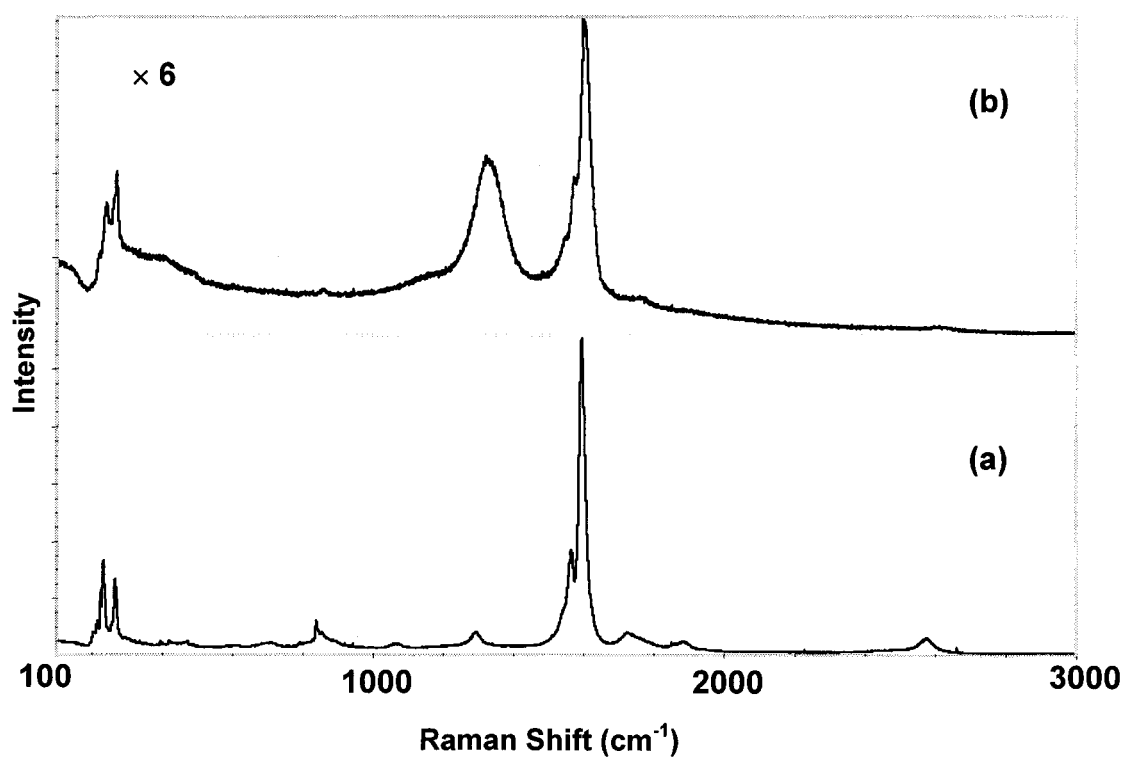


Figure 4-6 Raman spectra of as-prepared HiPco SWNTs before (a) and after (b) HNO₃ treatment.

enhancement effect. The distinct disorder mode at 1319 cm^{-1} in Figure 4-6(b) is indicative of the covalent sidewall functionalization. It was noticed that it shifted from 1292 cm^{-1} to 1319 cm^{-1} . The Breathing modes from SWNTs were modified, with the highest frequency component shifted from 265 cm^{-1} to 269 cm^{-1} . There was also an 8 cm^{-1} upshift in the tangential mode from 1592 to 1600 cm^{-1} . Apparently the oxygen containing functional groups caused the Raman modes of the SWNTs shifted to higher frequency. Such Raman shift variation caused by oxidative functionalities was studied and was attributed to the change in intertube interaction¹¹⁰. TGA result of the HNO_3 treated SWNTs heated in air is demonstrated in Figure 4-7. Although slow weight loss was observed at lower temperatures, the major weight loss onset temperature of the sample was $\sim 480^\circ\text{C}$, which is similar to that of the purified SWNTs. The residue was $\sim 0.20\%$ of the total mass, which is corresponding to 0.04 atomic percentage of Fe impurity. It suggests that the HNO_3 refluxing had removed almost all the Fe particles from the SWNTs.

According to the temperature derivative weight loss curve in Figure 4-7, there were two weight loss steps during the process. The maximum weight loss occurred about 530°C contributes to $\sim 70\%$ of the total mass decrease, the second major weight loss occurred about 646°C accounts for $\sim 20\%$ of total mass decrease. TGA-MS data in Figure 4-8 provide information on the identities of the volatile species evolved from the sample during the heating. The two species contributed to the major weight loss of the sample had m/z values of 44 and 46 , respectively. Considering the possible species involved in the process, CO_2 and NO_2 were identified as the molecules released from the HNO_3 treated SWNT sample. It suggests that there are carbon-oxygen containing groups and

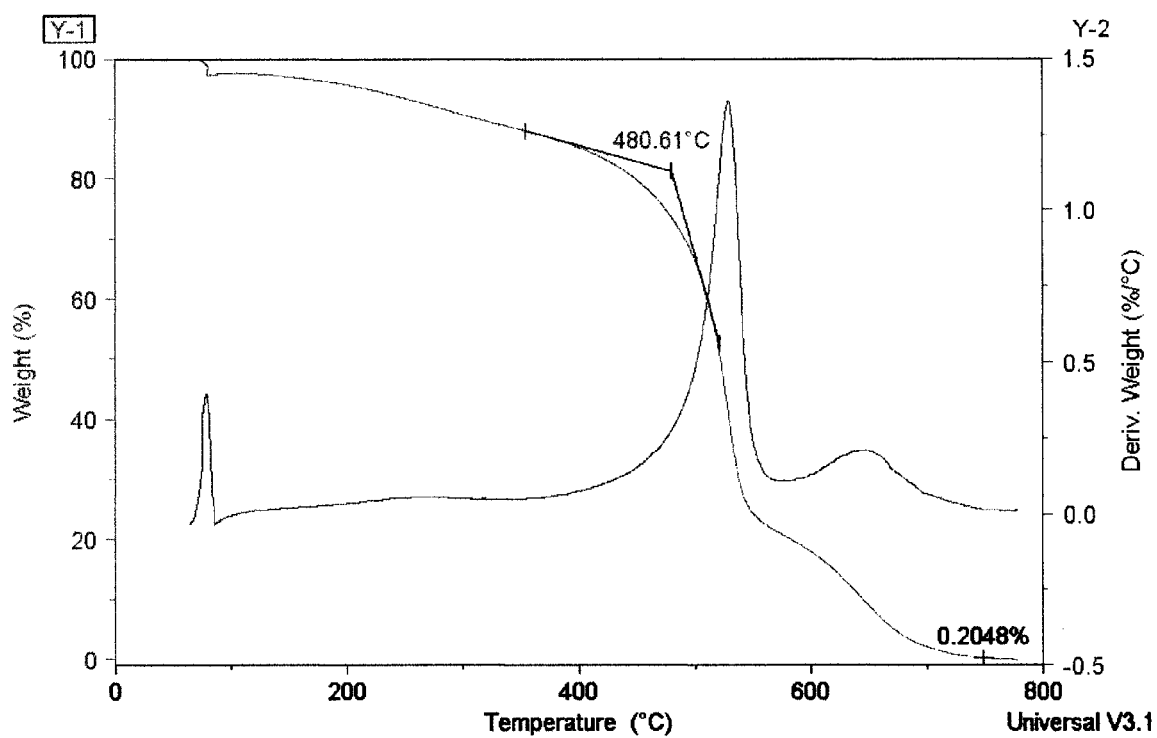


Figure 4-7 TGA of HNO_3 treated as-prepared HiPco SWNTs heated in air up to 780 °C. (Red curve: percentage weight loss; blue curve: temperature derivative weight loss)

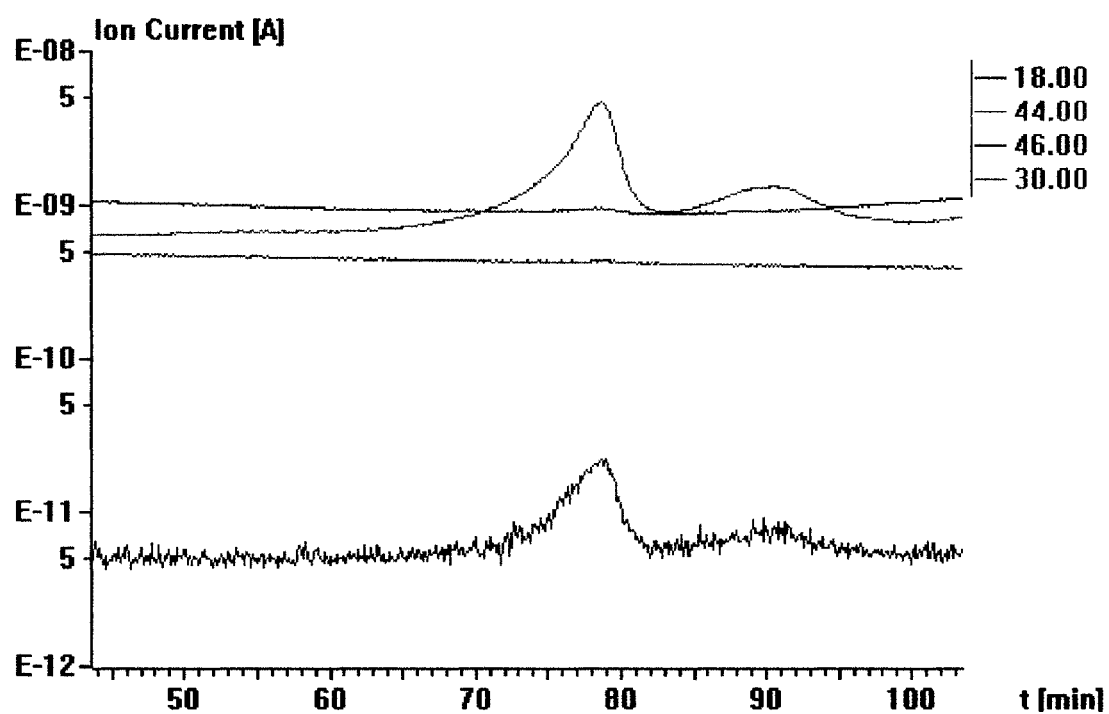


Figure 4-8 TGA-MS plot of HNO₃ treated as-prepared HiPco SWNTs heated in air up to 780 °C. (Labeled numbers are m/z number of the detected ions.)

nitrogen-oxygen containing groups covalently attached to the nanotubes. It was known from the IR spectrum that there were carboxylic acid functionalities on the nanotubes, which corresponds to the CO_2^+ detected by mass spectrometer. Although there was no apparent signs in IR showing that there were nitrogen-oxygen containing groups on the nanotubes, the MS data showed evidence that there was NO_2 volatilized from the sample at relatively high temperature ($\sim 530^\circ\text{C}$), which can only be attributed to the desorption of covalently attached functional groups.

The thermal desorption behavior of the functional groups on the HNO_3 treated SWNTs was also examined by annealing the nanotube sample in argon atmosphere up to 600°C . There was $\sim 40\%$ weight loss of the sample during the process that was mainly due to the volatilizing of CO_2 and NO from the nanotubes. The annealed nanotubes were examined with Raman and UV-vis.-NIR. The spectra were compared with those of the sample before annealing in Figure 4-9 and Figure 4-10, respectively. It was surprising to see in Figure 4-9(b) that the Raman spectrum of the annealed nanotube sample looked almost exactly the same as the purified SWNTs, with strong and sharp resonant features of the Breathing modes and tangential mode. Even the disappeared low frequency component in Breathing modes and the 1564 cm^{-1} branch in tangential mode were restored. UV-vis.-NIR spectrum of the annealed SWNTs in Figure 4-10 shows that the van Hove transition features of the SWNTs were also restored with annealing, which indicates that the sidewall of nanotubes are free of covalently bound derivatives. The spectra analysis suggests that desorption of the functional groups from the nanotube structure in an inert atmosphere had reinstated the pristine nanotube structure without any major modification. Although the observation of CO_2 volatilized from the nanotubes

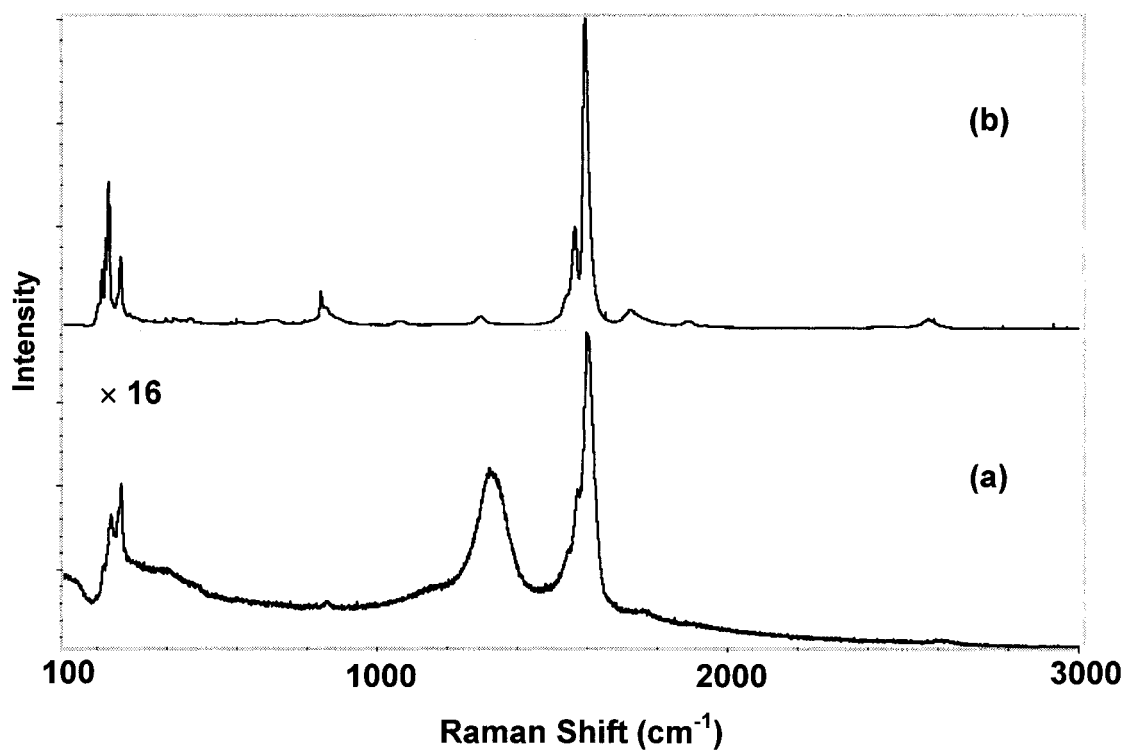


Figure 4-9 Raman spectra of HNO_3 treated as-prepared HiPco SWNTs (a) with annealing in argon up to 600 $^{\circ}\text{C}$ (b).

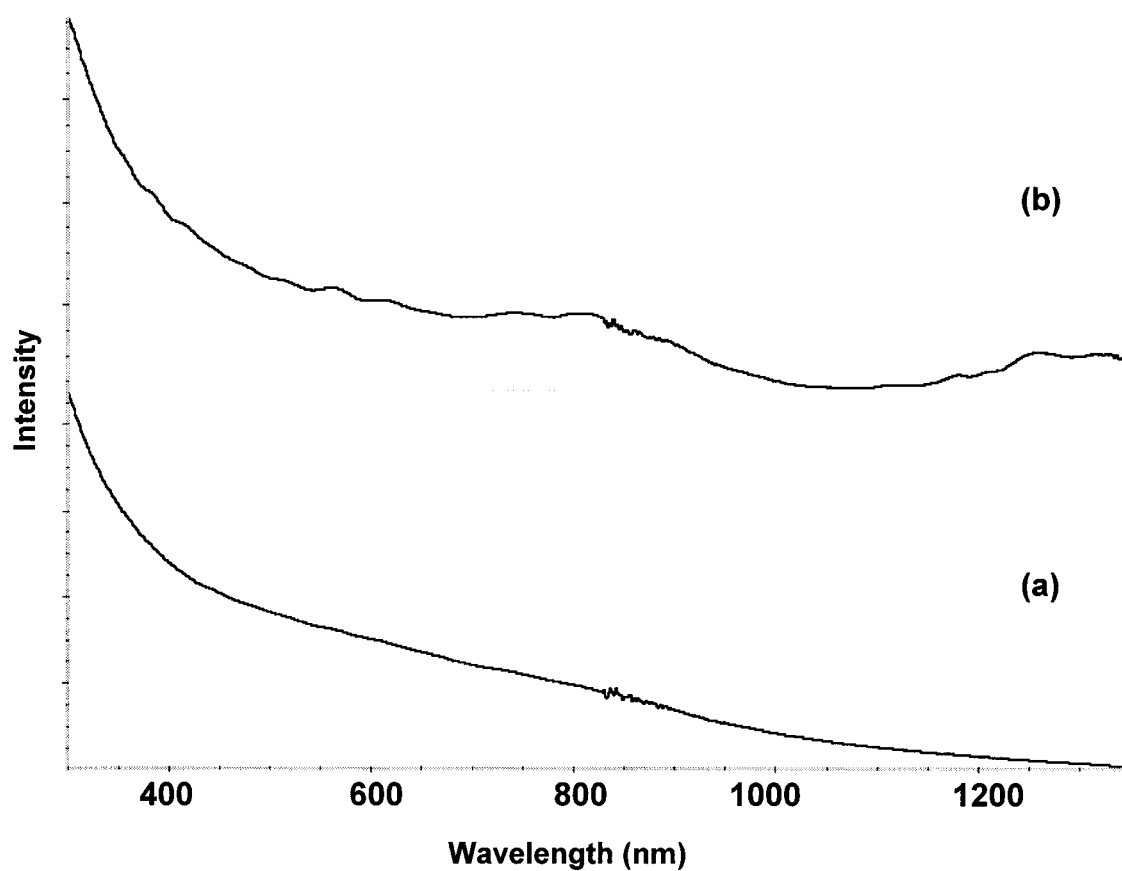


Figure 4-10 UV-vis.-NIR spectra of HNO₃ treated as-prepared HiPco SWNTs (a) with annealing in argon up to 600 °C (b).

indicates that there were carbon atoms removed from the structure, it might happen at the ends of the SWNTs that wouldn't affect their resonant Raman modes significantly.

4.2.4 Conclusions

Raw HiPco SWNTs refluxing in 1 M HNO_3 solution for ~20 hours was found removing almost all the Fe impurities and amorphous carbon from the sample. The process also derivatized the SWNTs with nitrogen and oxygen containing functional groups, which greatly improved the solubility of the SWNTs in ethanol. Annealing the HNO_3 treated SWNTs in argon atmosphere desorbed all the functionalities and restore the pristine SWNT structures. This process would be useful in reversibly manipulating SWNTs.

4.3 EXTRACTION AND CHARACTERIZATION OF GIANT FULLERENE SPECIES FROM HIPCO PROCESS

4.3.1 Introduction

High pressure CO disproportionation (HiPco) process produces high purity and high quality SWNTs in larger scale than previous arc or laser discharge process. The catalytic SWNT growth process also creates ~10% non-nanotube carbon products. The non-nanotube carbon impurities have been identified with TEM to be a mixture of the following: Fe encapsulated multilayered graphene shells, amorphous carbon, or hollow, monoshelled, close-caged structures known as giant fullerenes. Laser desorption /

ionization time-of-flight mass spectrometry (LDI-TOFMS) study ⁵ of the as prepared HiPco materials had revealed that there was a series mass peaks spanning between 1800 – 4500 a.m.u. that were evenly separated at a spacing of 24 a.m.u.. As described in the Introduction Chapter, this is a typical pattern in the mass spectra of fullerene species due to the continuous loss of C₂ species. The observations of fullerenes formation in carbon nanotubes synthesis process is significant as the presence of fullerenes in SWNTs formed by any method will influence the properties of the resultant carbon composites. For example, any physical measurements obtained from SWNTs containing fullerenes must inevitably include some component from the incorporated molecules. Furthermore, with respect to the filling of SWNTs with metals and metals halides, the presence of fullerenes could affect both the yield and homogeneity of halide / nanotube composites. Whereas understanding of the specific properties of giant fullerene species might lead to useful applications of this special class of fullerene molecules. In this section, part of the published work on the identification of large fullerenes formed during HiPco process ⁵ was included. It describes a process of extracting giant fullerene species from as prepared HiPco nanotube materials with fluorination and/or alkylation. The extracted species was characterized with Raman and IR spectroscopy. The thermal desorption behavior of the alkylated giant fullerenes in argon atmosphere was investigated with TGA. What is believed to be the pristine giant fullerenes that were obtained from the annealing were also characterized with IR and Raman spectroscopy.

4.3.2 Experimental

The as prepared material from HiPco process was fluorinated at 150 °C for 12 hours under similar conditions described earlier in this thesis. The fluorine take-up ratio was higher in this case compared with that of the purified SWNTs because the Fe catalysts were believed preferably fluorinated to FeF_3 . Two extraction approaches were conducted with the fluorinated raw material. In the first approach, the fluorinated raw material was suspended in dry tetrahydrofuran (THF) with brief sonication. The suspension was then filtered through a 0.2 μm PTFE membrane. The filtration containing mainly the fluorinated giant fullerenes was processed to evaporate the solvent, vacuum oven dried over night before further analysis. In the second approach, the fluorinated raw material was hexylated with hexyl lithium. Then the hexylated material was suspended in chloroform to extract the more soluble hexylated giant fullerenes following the similar separation steps described above.

4.3.3 Results and Discussions

Raman spectra of the fluorinated HiPco raw material, the extracted fluorinated giant fullerenes, and the extracted hexylated giant fullerenes were compared in Figure 4-11. The Breathing modes with poor resolution in Figure 4-11(a) were due to the distortion fluorination had caused on the fullerene structures. The barely resolved features at 217 cm^{-1} , 236 cm^{-1} and 260 cm^{-1} probably have contribution from both SWNTs and giant fullerenes. Both the disorder mode centered around 1305 cm^{-1} and the tangential mode centered $\sim 1586 \text{ cm}^{-1}$ in Figure 4-11(a) are several wavenumbers higher in frequency than

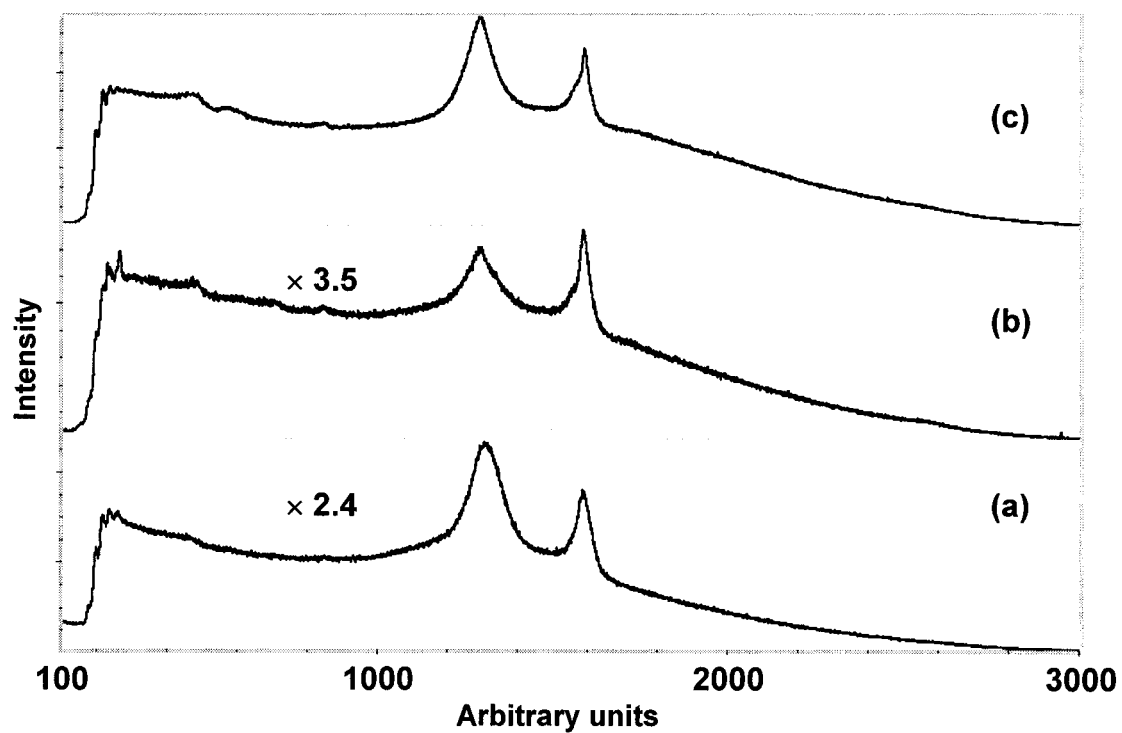


Figure 4-11 Raman spectra of as-prepared HiPco SWNTs samples at various stages of giant fullerene extraction. (a): fluorinated as-prepared HiPco SWNTs; (b): extracted fluorinated giant fullerenes; (c): hexylated giant fullerenes.

those from fluorinated purified SWNTs ($C_{2.5}F$), in which the disorder mode is generally centered around 1298 cm^{-1} and the tangential mode is centered around 1583 cm^{-1} . It suggests that the fluorinated giant fullerene species contributed to the upshift of both the disorder mode and tangential mode in Figure 4-11(a). We've known that fluorination caused upshift of disorder mode and downshift of tangential mode in SWNTs. The different Raman shifts between fluorinated SWNTs and the fluorinated giant fullerenes might be related to the lower aspect ratio of molecule geometry in giant fullerenes than that in SWNTs. Raman spectrum of the extracted fluorinated giant fullerenes in Figure 4-11(b) shows that there are two resolved components in the Breathing modes range: one at 229 cm^{-1} and the other one at 265 cm^{-1} . The position of the disorder mode ($\sim 1300\text{ cm}^{-1}$) and the tangential mode ($\sim 1586\text{ cm}^{-1}$) was considerably different from those of the fluorinated SWNTs, which explains what was observed in Figure 4-11(a). In Raman spectrum of the hexylated giant fullerenes [Figure 4-11(c)], no detectable peaks could be seen in the Breathing modes region. The disorder mode and the tangential mode are located at $\sim 1290\text{ cm}^{-1}$ and 1590 cm^{-1} , respectively. Compared with those in Figure 4-11(b), the disorder mode downshifted ~ 10 wavenumbers and the tangential mode upshifted ~ 4 wavenumbers. The disorder mode in Figure 4-11(c) should have contribution from the sp^3 carbon on the hexyl groups, which explains part of the frequency shift. Also the electron withdrawing effect of fluorine functionalities is expected to be much stronger than that of the hexyl functionalities, which suggests that the fluorination would cause a greater downshift effect of the tangential mode than hexylation. This speculation is consistent with our observation on the difference between Figure 4-11(b) and (c).

The thermal desorption behavior of the hexylated giant fullerenes in argon atmosphere was demonstrated in Figure 4-12. The weight loss curve indicates that annealing the sample up to 800 °C resulted ~33.4% decrease of the total mass. If the weight loss is merely due to the chemical desorption of the hexyl groups from the giant fullerenes, it can be calculated that in the hexylated giant fullerene sample, one out of every 14 carbon atoms on the giant fullerene molecules was attached with a hexyl group. The temperature derivative weight loss curve indicates that there were three weight loss maxima during the process: the first occurred at ~213 °C, the second occurred at ~368 °C, and the last one occurred at ~730 °C. This might be due to the fractional desorption of the hexyl groups on different giant fullerenes.

The IR spectra of the hexylated giant fullerenes before and after annealing were compared in Figure 4-13. Most features in Figure 4-13(a) belong to the hexyl groups attached on the giant fullerenes. For example, the set of peaks at 2852, 2920 and 2954 cm^{-1} are typical C – H stretching modes of alkyl groups. The peaks between 790 – 1460 cm^{-1} belong to C – H non-stretching modes. The broad feature at ~1589 cm^{-1} might be related to the C = C bonds on giant fullerenes that was activated with sidewall derivatization. All these features are absent in Figure 4-11(b), which suggests the complete desorption of the hexyl groups. The Raman spectrum of the annealed hexylated giant fullerenes is shown in Figure 4-14. In general, the spectrum closely resembles that of SWNTs, except in the following aspects. The Breathing modes of the giant fullerenes have only two features: one at 230 cm^{-1} , the other one at 262 cm^{-1} . These modes are analogical to the typical radial modes of lower closed shell or curved graphene structures such as fullerenes^{111,112}. There is also a low intensity mode at ~301 cm^{-1} that is not

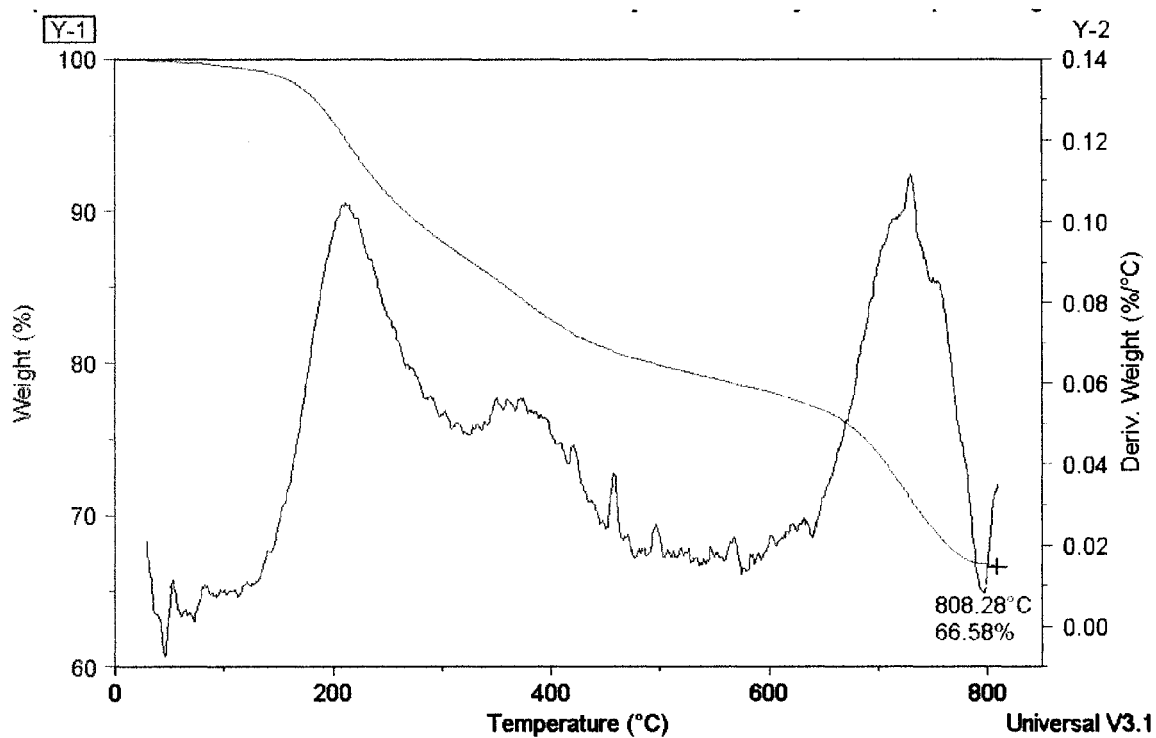


Figure 4-12 TGA of hexylated giant fullerenes annealed up to 800 °C. (Red curve: percentage weight loss; blue curve: temperature derivative weight loss)

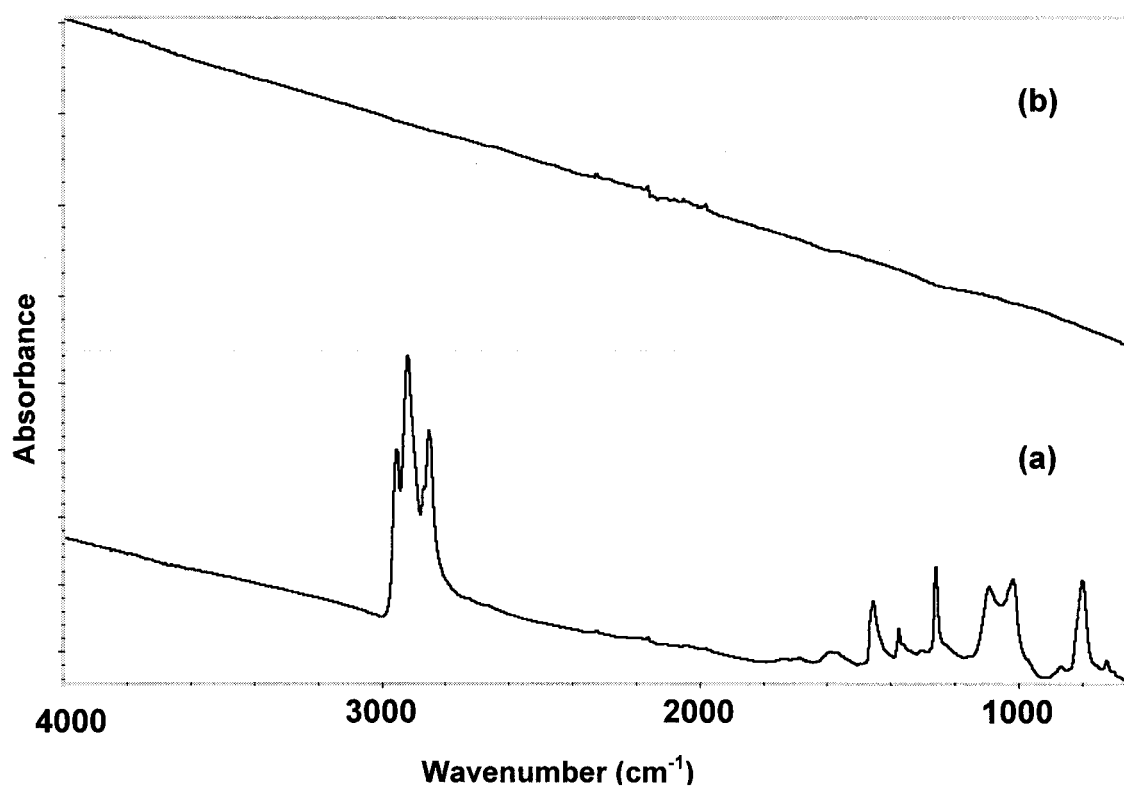


Figure 4-13 ATR-IR spectra of hexylated giant fullerenes (a) and after annealed up to 800 °C (b).

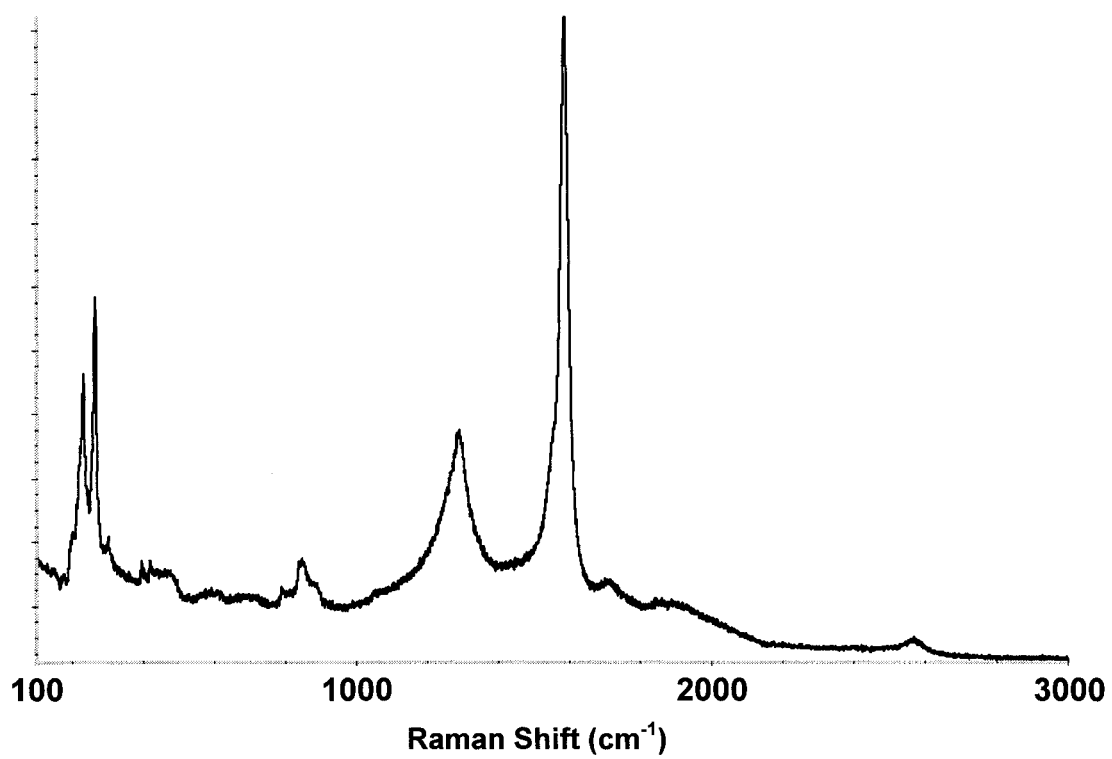


Figure 4-14 Raman spectrum of hexylated giant fullerenes after annealing.

usually seen in spectra of SWNTs. There is still a fairly distinct disorder mode in Figure 4-14, which could be attributed to interlinking between giant fullerene molecules formed during annealing. The tangential mode in Figure 4-14 is located at 1585 cm^{-1} , which is typically lower in frequency than that of the SWNTs.

4.3.4 Conclusions

A small portion of giant fullerenes formed as byproduct in the HiPco SWNT synthesis process was extracted and analyzed. The giant fullerenes were separated from SWNTs according to different solubility of their fluorinated and/or hexylated derivatives. The separated giant fullerene derivatives were characterized with ATR-IR and Raman spectroscopy and compared with those of SWNTs. It was found that the fluorination affects the Raman features of giant fullerenes and SWNTs differently. The thermal desorption behavior of the hexylated giant fullerenes was investigated by annealing the sample in argon atmosphere up to $800\text{ }^{\circ}\text{C}$ and monitoring the process with TGA. The annealed product was also examined with Raman and compared with that of SWNTs. Finding of the comparison is that the Raman features of the giant fullerenes closely resemble those of HiPco SWNTs except the line shape in the Breathing modes and the position of the tangential mode.

Chapter 5

CHARACTERIZATION OF THE HIGH PRESSURE-HIGH TEMPERATURE TREATED SWNTS

5.1 INTRODUCTION

The high curvature of SWNTs suggests the distorted sp^2 electron configuration of carbon atoms in the network, which provides the possibility of crosslinking intertube carbons through 2 + 2 cycloaddition. Such created SWNTs based materials are expected to be superhard and have highly anisotropic mechanical and electrical properties¹³. One of the approaches to create cross-linked SWNTs involves high temperature-high pressure treatment (HPHTT). New phases of materials have been found to form during the HPHT treatment of *fcc* crystalline C_{60} ⁷⁰, which were identified as polymerized C_{60} because 1D or 2D networks were formed across neighboring C_{60} cages through 2 + 2 cycloaddition¹⁰. In this chapter, part of the published work on the characterization of HPHTT polymerized SWNTs¹⁴ is included. Variation in bonding and crystalline structures of SWNTs under HPHTT was investigated with micro-Raman and powder XRD. The depolymerization of the HPHT treated SWNTs with ultrasonication was studied with Raman, SEM and AFM analysis.

5.2 EXPERIMENTAL

Details about the preparation of polymerized SWNTs under HPHTT was described

elsewhere¹⁴. XRD patterns of the samples were collected with a General Area Detector Diffraction System (GADDS) from Bruker AXS Inc. using Cu K α radiation as X-ray source. The depolymerization of the HPHTT SWNTs was studied by dispersing the SWNT sample in 2-isopropanol (IPA) and sonicating for 2 hours in a 17 W cup sonicator. For AFM imaging, one drop of the suspension was deposited onto a fresh mica surface, the solvent was removed immediately with ultra-spinner. For micro-Raman analysis, the SWNT samples from the sonicated suspension were collected by vacuum filtering to remove the solvent. The samples were then vacuum dried at 70 °C for 2 hours before spectroscopy analysis.

5.3 RESULTS AND DISCUSSIONS

The Raman spectra of SWNTs treated under 1.5 GPa and at various temperatures were shown in Figure 5-1. The strong and sharp Breathing modes ($\sim 200\text{ cm}^{-1}$) and tangential mode ($\sim 1590\text{ cm}^{-1}$) in Figure 5-1(a) are typical resonant Raman modes from 1D nanotube structures. The low intensity of the disorder mode at 1295 cm^{-1} suggests the low defect site density as well as the small amount of sp^3 type carbon along the nanotubes. With the increasing temperature treatment under the pressure of 1.5 GPa, one can see the gradual decrease in the overall Raman intensity and the increase of disorder mode relative to the tangential mode in Figure 5-1(b), (c) and (d). These observations suggest formation of sidewall covalent bonding, which, under the specific experiment conditions, can only be attributed to covalent crosslinking between carbon atoms on sidewalls of the neighboring nanotubes. The energetic drive behind the crosslinking could be that the high

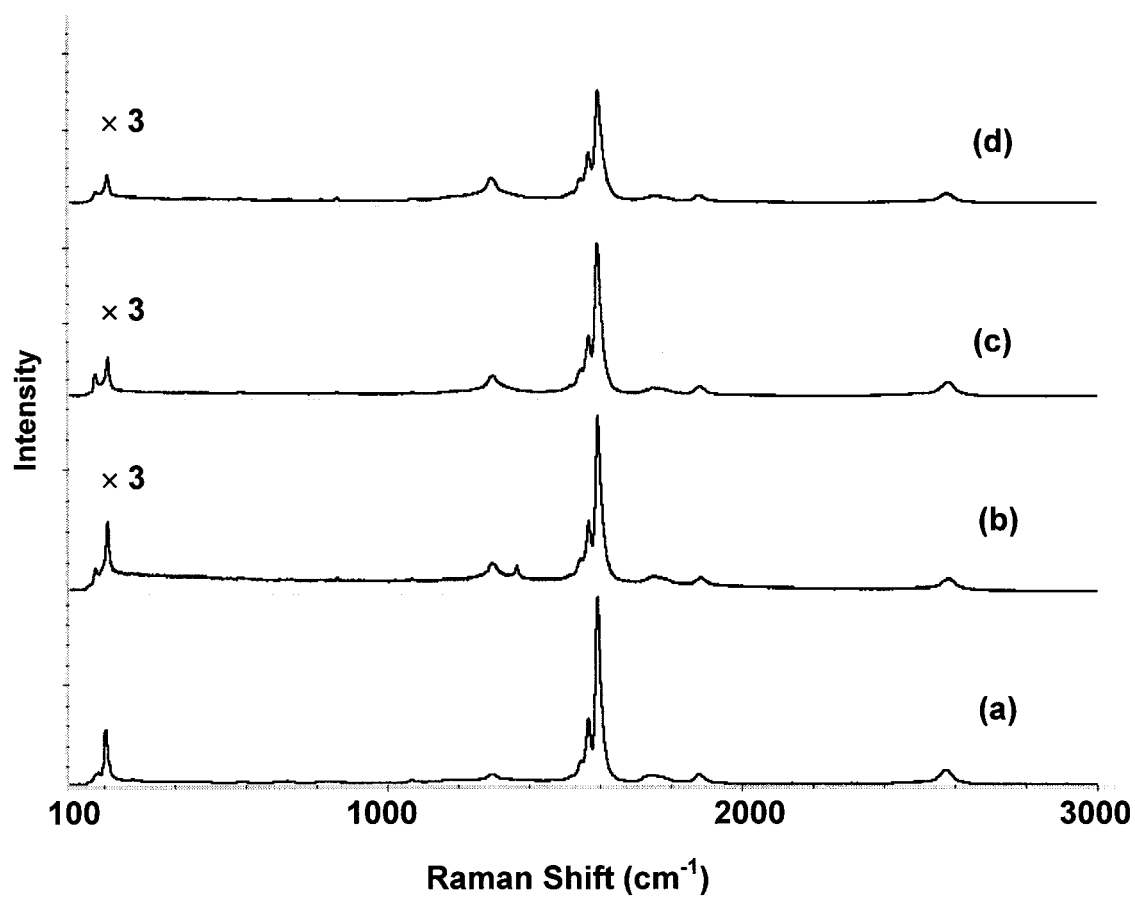


Figure 5-1 Raman spectra of SWNTs treated under 1.5 GPa at various temperatures. (a) precursor SWNTs; (b) 300 °C; (c) 500 °C; (d) 700 °C.

pressure treatment caused the distortion of the cylindrical structure of SWNTs and created localized higher curvature. The sp^2 configuration of the carbon atoms at the high-curvature sites was more distorted towards a pyramidal geometry that at certain degree resembled the sp^3 configuration. The overlap of electron density between such distorted sp^2 carbon on neighboring nanotubes would result in the formation of the crosslinking bonds via a 2+2 cycloaddition route. According to the increasing intensity of the disorder mode with temperature from Figure 5-1(b) to (d), the crosslinking bond formation was facilitated with the higher temperature. The decrease in intensity of the Breathing modes indicates that the cylindrical geometry was broken down under the HPHT treatment, which was a reasonable consequence of intertube covalent bond formation.

The examination of the above samples with XRD analysis revealed the formation of graphite-like lattice structures. As shown in Figure 5-2(a), the pristine SWNTs have no features in the 2θ range of 7 – 70 degree. After the HPHT treatment at 1.5 GPa and 300 °C, sharp peaks appeared at $2\theta = 26.6^\circ$ and $2\theta = 44.4^\circ$. Additional peaks were observed at $2\theta = 32.8^\circ$ and 38.8° for the sample treated at 1.5 GPa and 500 °C. In the sample treated at 1.5 GPa and 700 °C, the peak at $2\theta = 26.6^\circ$ has grown so high in intensity that it became the only distinct feature in the XRD pattern. The feature at $2\theta = 26.6^\circ$ is a typical XRD pattern of graphite that is corresponding to the layered structure with the interlayer spacing $d = 0.355$ nm. The appearance of this feature in XRD of the HPHT SWNT samples suggests that the distortion of the cylindrical geometry and crosslinking between nanotubes has changed the packing of carbon atoms towards the stacking of planar graphene network structure. The results from Raman and XRD analysis were

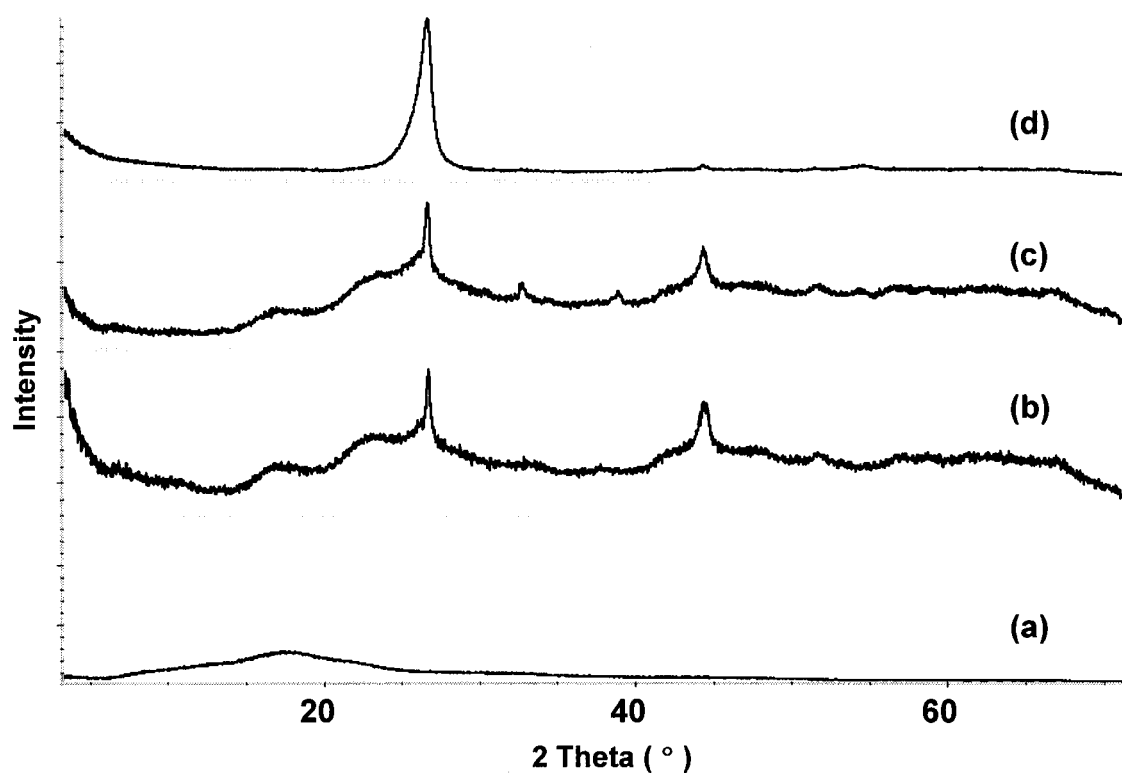


Figure 5-2 XRD patterns of SWNTs treated under 1.5 GPa at various temperatures. (a) precursor SWNTs; (b) 300 °C; (c) 500 °C; (d) 700 °C.

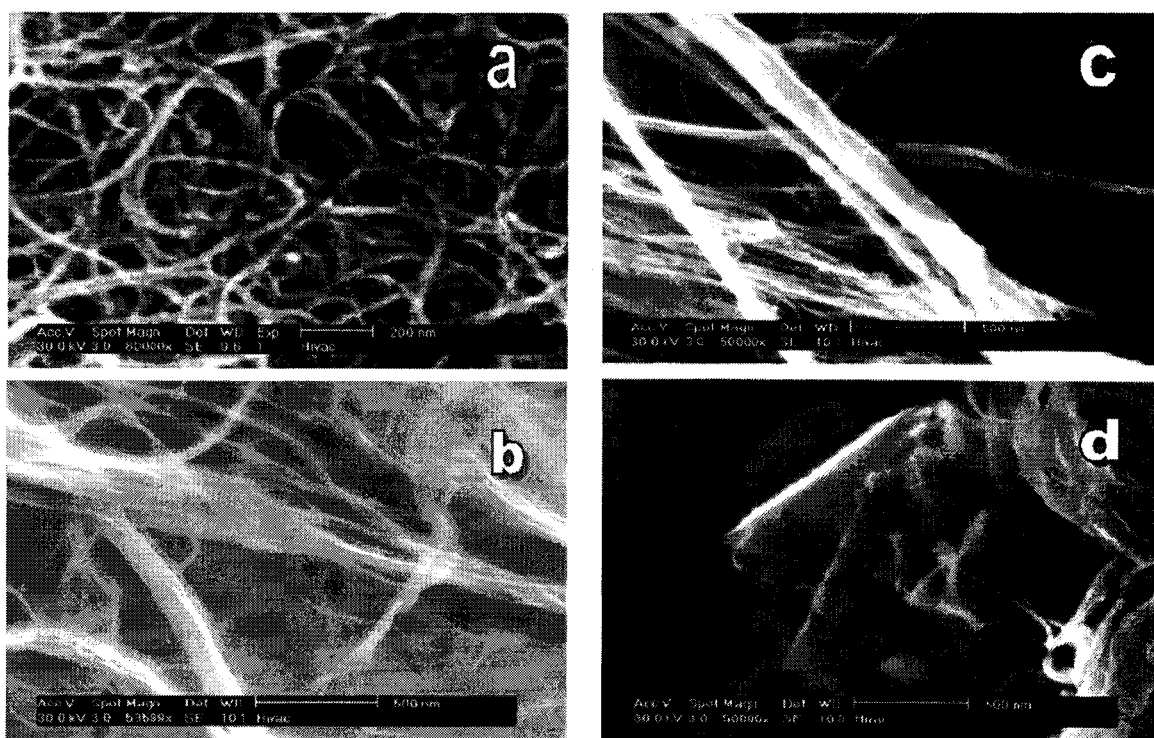


Figure 5-3 SEM images of SWNTs precursor (a) and of that treated under 1.5 GPa at 300 °C (b), at 500 °C (c), and at 700 °C (d). (adapted from Khabashesku, V. N.; Gu, Z.; Brinson, B.; Zimmerman, J. L.; Margrave, J. L.; Davydov, V. A.; Kashevarova, L. S. and Rakhmanina, A. V. *J. Phys. Chem. B* **2002**, *106*, 11155.)

supported by SEM observations ¹⁴ (shown in Figure 5-3) that under 1.5 GPa denser structures were formed at higher temperatures.

Ultrasonication of the above covalently crosslinked SWNT samples in IPA for 2 hours resulted substantial depolymerization. It was demonstrated by the Raman spectra shown in Figure 5-4. The decrease in intensity of disorder mode and the restoration of the Breathing modes indicate the breaking of wall-to-wall covalent bonding. It seems that under the same sonication conditions, the sample treated at lower temperature shows a more complete restoration of nanotube features. SEM investigation of the sonicated samples shows the results consistent with the Raman observation. As shown in Figure 5-5(a), SWNTs treated under 1.5 GPa at 300 °C, after the 2-hour sonication, looked very similar to precursor SWNTs. No compact packing of SWNTs was seen in this sample. The sample treated under 1.5 GPa at 500 °C, as shown in Figure 5-5(b), had a more densified packing after the sonication. Some large-size bundles could be seen in this sample implying that nanotubes strongly interacted with each other within such bundles. It is consistent with the Raman observation in Figure 5-4(b) that indicating certain amount of crosslinking bonds has survived the sonication. SEM image of the sample treated under 1.5 GPa at 700 °C after sonication was shown in Figure 5-5(c). Apparently, SWNTs in this sample maintained a much denser packing pattern. Even after the sonication, there was still a high ratio of large bundles observed, which implies that some covalent crosslinking has survived the sonication. AFM of the sonicated sample treated under 1.5 GPa at 300 °C, as shown in Figure 5-6, more clearly demonstrates the breaking down of the crosslinking between SWNTs. Most of the SWNTs in the image appear individually, but there are still a few distinct bundles observed. Actually if the bundles in

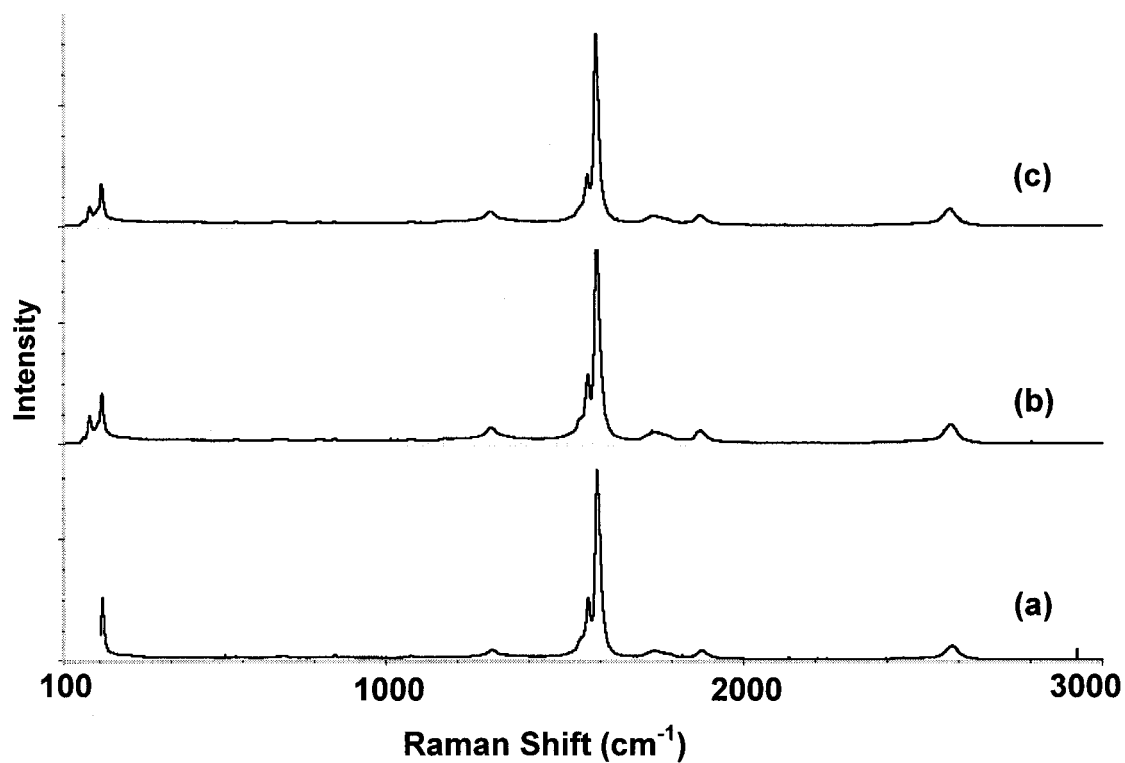


Figure 5-4 Raman spectra of the HPHTT treated SWNTs with 2-hour ultrasonication. (a) originally treated at 1.5 GPa, 300 °C; (b) originally treated at 1.5 GPa, 500 °C; (c) originally treated at 1.5 GPa, 700 °C.

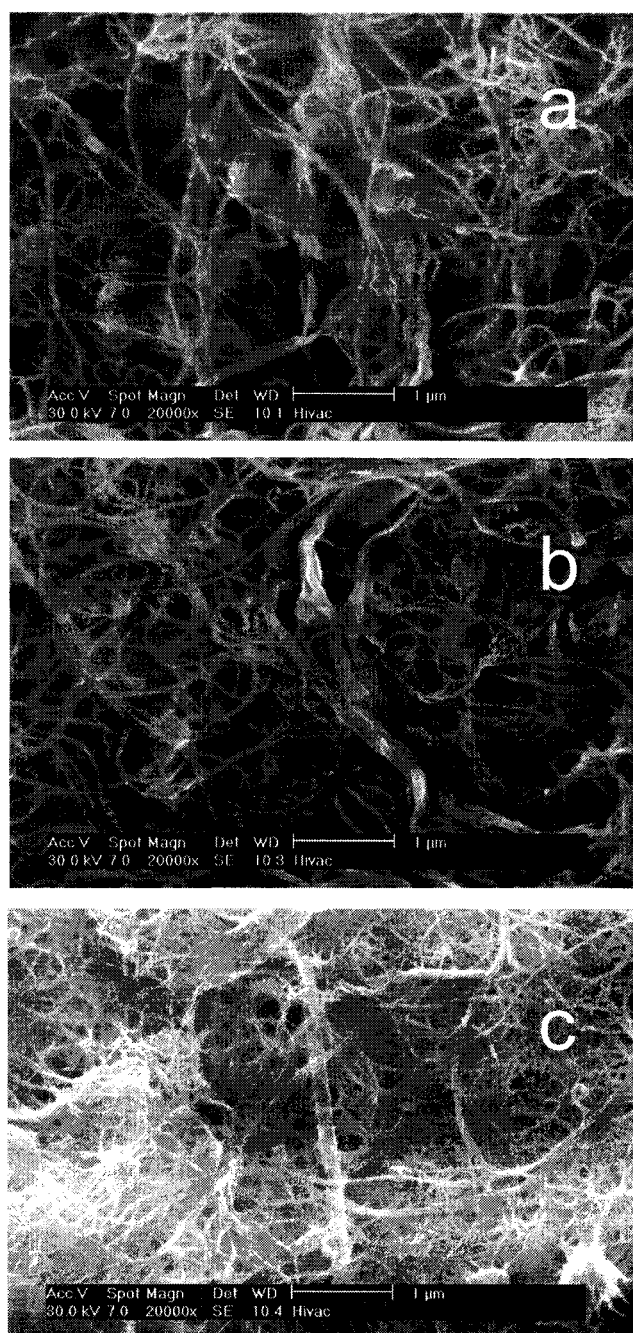


Figure 5-5 SEM images of the HPHTT treated SWNTs with 2-hour ultrasonication. (a) originally treated at 1.5 GPa, 300 °C; (b) originally treated at 1.5 GPa, 500 °C; (c) originally treated at 1.5 GPa, 700 °C.

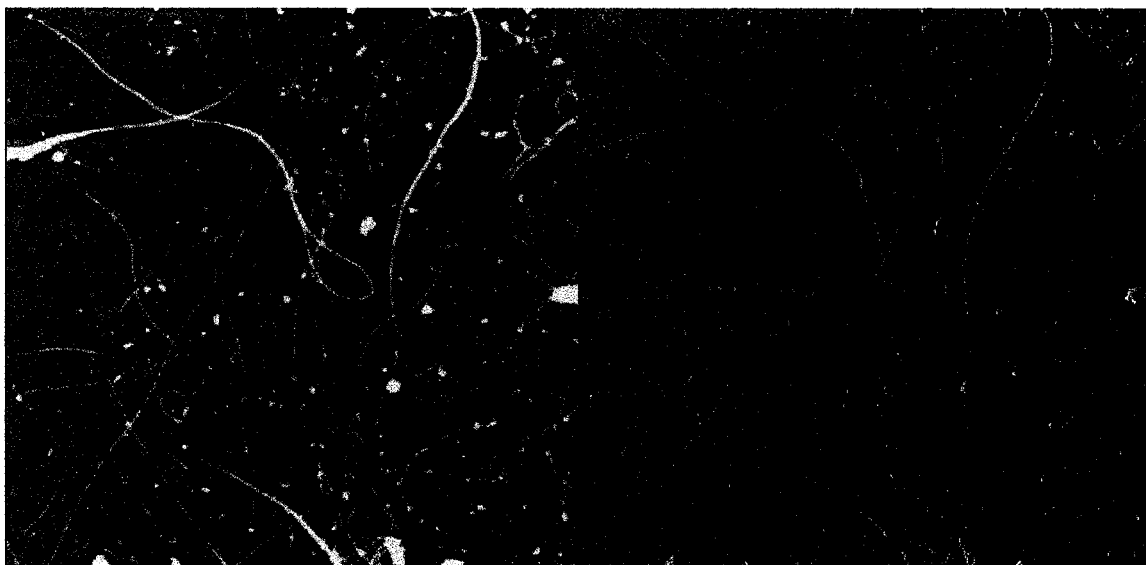


Figure 5-6 SEM images of the HPHTT (1.5 GPa, 300 °C) treated SWNTs with 2-hour ultrasonication. (a) originally treated at 1.5 GPa, 300 °C.

the image are examined more carefully, it can be seen that most of them were in the process of breaking into smaller bundles or individual SWNTs.

The XRD patterns of the SWNTs treated under 8 GPa and at various temperatures were shown in Figure 5-7. Patterns in Figure 5-7(a) and (b) resemble those in Figure 5-2(b) and (c). They indicate the local transformation of carbon packing pattern towards layered graphite structure. The broad features appearing in 2θ range of $20 - 30^\circ$ in Figure 5-7(c) and (d) suggest that a high ratio of microcrystallization occurred when the high pressure treatment was conducted at 800 and 1200 $^\circ\text{C}$. After treatment at the highest temperature, 1500 $^\circ\text{C}$, the observed XRD pattern [Figure 5-6(e)] indicates that the crystalline structure became a graphite phase. Figure 5-7(a) to (e) clearly demonstrate the phase transition of nanotubular structure to microcrystalline graphite, then to large graphite network under high pressure treatment at increasing temperatures. The phase transition has been confirmed by results from Raman and SEM analysis of the same samples¹⁴. This series of results suggest that under pressure as high as 8 GPa, the large scale phase transition from nanotube structure to graphite structure only occurs at temperatures over 1500 $^\circ\text{C}$.

The XRD patterns of SWNTs treated under 9.5 GPa and at 400 $^\circ\text{C}$ and 600 $^\circ\text{C}$ were shown in Figure 5-8. It was found that under this high pressure, the microcrystallization of the SWNT sample occurred at much lower temperature. There was already significantly strong feature appeared between $2\theta = 20$ and 30° at 400 $^\circ\text{C}$. And when the high pressure treatment was conducted at 600 $^\circ\text{C}$, a sharp new peak showed up at $2\theta = 32.8^\circ$ as well as some low intensity peaks at 43.2, 47, and 54.5° . Microdiffraction analysis of the sample with TEM¹⁴ implies that there were single-phased cubic structure

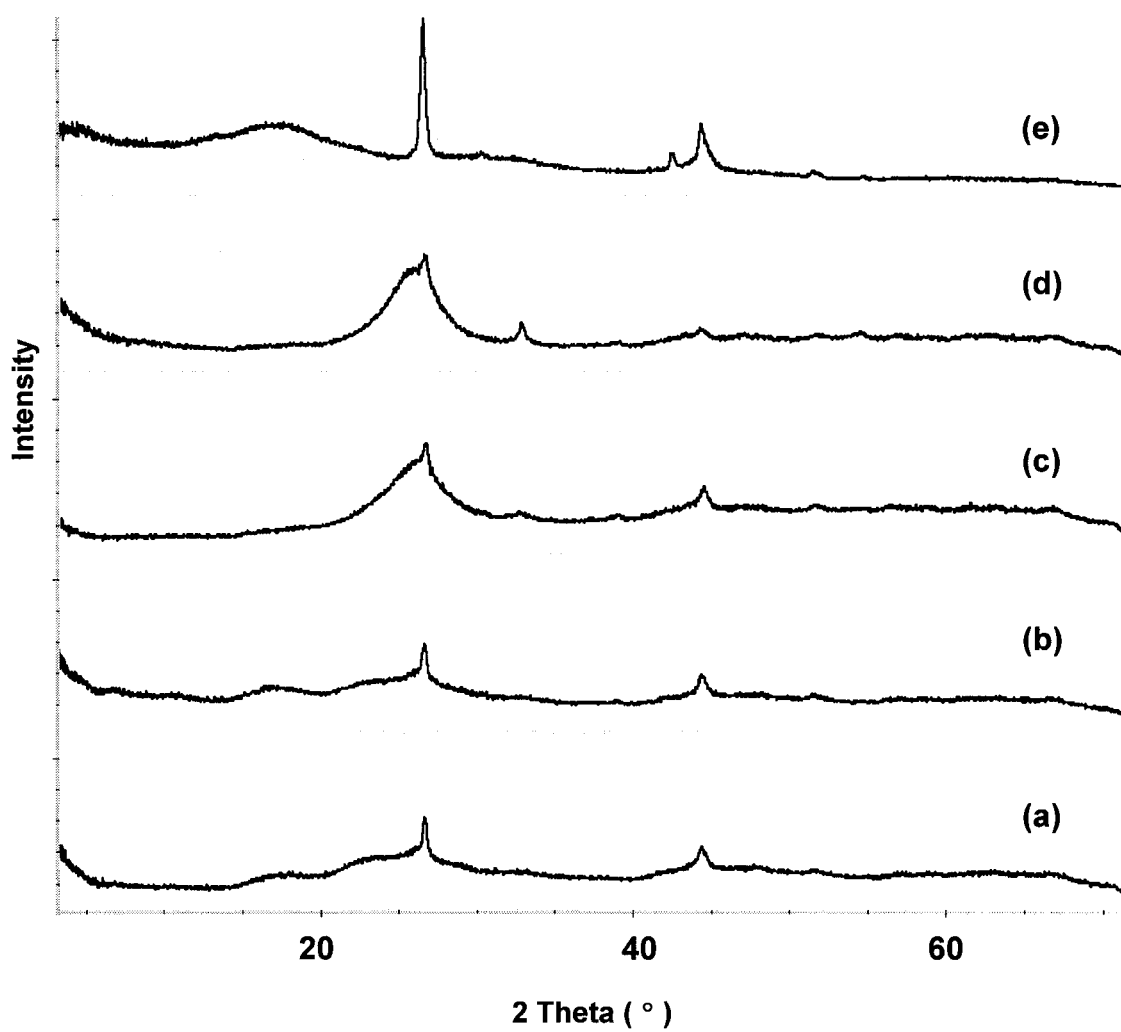


Figure 5-7 XRD patterns of SWNTs treated under 8 GPa at various temperatures. (a) 200 °C; (b) 500 °C; (c) 800 °C; (d) 1200 °C; (e) 1500 °C.

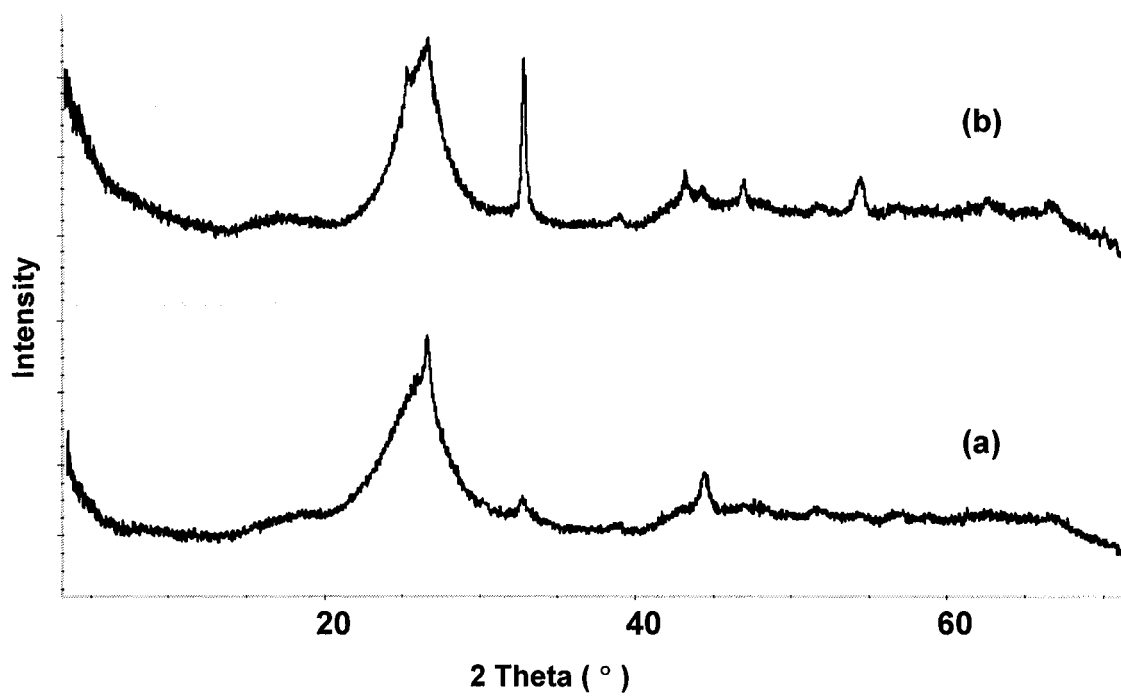


Figure 5-8 XRD patterns of SWNTs treated under 9.5 GPa at 400 °C (a) and 600 °C (b).

and a polycrystalline phase formed under these conditions, both of which were identified as nanocrystalline diamond-like structures. These new nanodiamond phases are expected to be ultrahard materials.

5.4 CONCLUSIONS

The irreversible phase transition of SWNTs under HPHTT has been studied with Raman spectroscopy, XRD analysis, SEM and AFM. Formation of covalent crosslinking between carbon atoms on neighboring nanotubes was confirmed by spectroscopy data. The depolymerization of the crosslinked SWNT polymers by the ultrasonication was investigated. The crosslinking bonds formed in the SWNTs treated under the same high pressure conditions but at the higher temperatures were found to be more resistant to ultrasonication treatment. Transformation from carbon nanotube structures to microcrystalline graphite structures and to larger scale graphite network structures was observed when SWNT samples were treated under 8 GPa and at increasing temperatures. At even higher pressure, 9.5 GPa, such transformations were found to occur at much lower temperatures, and nanocrystalline diamond phases could be formed. The study revealed the possibility of converting SWNTs to ultrahard nanocrystalline materials through the HPHT treatment.

Chapter 6

FLUORINATION AND CHARACTERIZATION OF POLYMERIC C₆₀

6.1 INTRODUCTION

High temperature-high pressure treatment (HPHTT) of crystalline C₆₀ created new forms of structures, which have been confirmed to be the polymeric forms of C₆₀. Although the crystalline packing patterns, the spectroscopy as well as the electric, and magnetic properties of the polymeric C₆₀ phases have been extensively studied (see references in Chapter 1), little has been done towards understanding the chemical properties of the polymeric C₆₀. In this paper, we reported the study on the reactivity of the polymeric C₆₀ using gaseous fluorine as reagent. The reactions were conducted at several temperatures ranging from 50 to 250 °C for relatively short period of time, i.e. one hour. It was found that the fluorination of the polymeric C₆₀ phases started at 100 °C. Different stoichiometries have been obtained from different polymer phases under the same fluorination conditions, while the R-phase polymer gained the highest fluorine weight content at the most optimal temperature. Monomeric C₆₀ was observed when the fluorination was carried out at 250 °C indicating that the polymers were depolymerized at this temperature under fluorine atmosphere. Powder X-ray diffraction examination showed that except for one product all fluorinated polymers consist of the mixtures of several polycrystalline phases. SEM analysis suggested that the microcrystalline patterns remained after fluorinations carried out at temperatures between 100 and 200 °C.

6.2 EXPERIMENTAL

The polymeric C₆₀ phases used in this study were prepared from high-purity, small crystalline fullerite C₆₀ by the high-pressure high-temperature treatment (HPHTT). The p , T parameters for the synthesis of the O-, T- and R-phase were 1.5 Gpa, 720 K; 2.3 Gpa, 775 K; and 6 Gpa, 873 K, respectively. The purity of the polymers was 95%, 98%, and 99.5% for O-, T- and R-phase, respectively. All the samples were carefully ground to fine powders before transferring into the fluorination chamber to maximize the exposure area to fluorine gas. Also, under each set of reaction conditions, the samples from the three phases were separately loaded into a small Monel foil boats and then transferred into the reactor to guarantee that all the samples be treated equally. Once the samples were loaded, the reactor was sealed and purged with helium at room temperature for 2 hours to remove the residue air and moisture adsorbed on the samples. The reactor was then heated to the reaction temperature under continuous helium flow before fluorine and hydrogen were introduced into the reactor. The flow rates of fluorine and hydrogen were 3 cc/min and 1 cc/min, respectively. Hydrogen was used to react with fluorine to produce HF to facilitate the fluorination. The concentrations of fluorine and HF in the final gas mixture (helium diluted) were both 10%. The reaction was conducted at 50 °C, 100 °C, 150 °C, 200 °C and 250 °C, respectively, for one hour.

The samples for transmission mode IR measurement were prepared by mixing the samples with KBr powder and pressing into pellets. A PERKIN ELMER PARAGON 1000PC FT-IR spectrometer was used to record spectra. The powder X-ray diffraction analysis of the polymers and the fluorinated products was carried out using a General

Area Detector Diffraction System (GADDS) from Bruker AXS Inc. and an INEL CPS 120 position-sensitive detector with $\text{CuK}\alpha_1$ radiation. A Philips environmental mode SEM with energy disperse X-ray elemental analysis (EDAX) accessories was used to investigate the microcrystalline structure and to determine the stoichiometries of the samples.

The sample preparation for UV-vis.-NIR spectra collection was as follows. For C_{60} , sample was dissolved in ODCB, the spectrum range started at 290 nm. For all three polymeric C_{60} phases and their fluorinated derivatives, the samples were suspended in hexane or in other solvents such as ethylenediamine, then only the clear supernates were used for spectra measurements. The starting wavelength for the spectra collection was varied according to the solvent absorption.

The variable temperature probe-electron ionization-mass spectra (VTP-EIMS) were collected using Finnigan MAT 95 mass spectrometer. Tiny amount of powdered sample was loaded into a 2 mm-diameter quartz sampling tube. The sampling tube was fit into the heating tip on the probe and then heated according to a preset program. Only the vaporized species were ionized by electron bombardment and detected by mass spectrometer system. Information about the vaporization temperatures of the detected species can be obtained from VTP-MS analysis.

6.3 RESULTS AND DISCUSSION

All three phases of the polymeric C_{60} were found not to be affected by fluorine / HF treatment at 50 °C for one hour. The polymers reacted with fluorine / HF reagents at

temperatures starting from 100 °C. The stoichiometries of the fluorine / HF treated polymers were determined by EDAX. The results are listed in Table 6-1. According to Table 6-1, under each set of the fluorination conditions, the three polymer phases reacted to different extents. At 100 °C, fluorine addition to the T-phase polymer was very low, with less than three fluorine atoms per C₆₀ cage in average; O-phase polymer had about six fluorine atoms added to every C₆₀ cage; however, R-phase obtained a relatively high fluorine uptake, about ten fluorine atoms per C₆₀ cage. At 150 °C, the fluorine uptake amounts were close for all three polymers, which is 16 – 19 fluorine atoms per C₆₀ cage. This means that for the O- and T- phase polymers, there is a large increase in fluorine uptake between 100 °C and 150 °C. The similar increase in fluorine uptake amounts was observed in all three polymers when temperature jumped from 150 °C to 200 °C, where the number of fluorine atoms per C₆₀ cage became 30 for O-phase polymer, 38 for T-phase polymer, and 42 for R-phase polymer. Even though these are just average values, we noticed that all three polymers have higher reactivity towards fluorination compared to the C₆₀ monomers treated under the same temperature and reaction time^{113,114}. It is believed that the cross-linking between the C₆₀ cages distorts the overall electron density distribution around the C₆₀ sphere and thus creates more reactive sites on the cages. At 250 °C, the fluorine uptake amounts showed a sharp decrease of all three polymers, which, as confirmed by spectroscopy data, was due to the decomposition of the polymers at this temperature and under fluorine atmosphere. Overall, the R-phase polymer seems to have the highest reactivity towards fluorine addition. This could be because with 12 carbon atoms per C₆₀ cage forming cross-linking bonds with surrounding C₆₀ molecular units, the extent of distortion of the electron density geometry in R-phase polymer is the

Table 6-1 F/C Ratio (in atomic %) of C₆₀ Polymers fluorinated at various temperatures.

	100 °C	150 °C	200 °C	250 °C
O-phase poly-C ₆₀	9.9	29.9	51.8	43.4
T-phase poly-C ₆₀	4.3	32.7	63.5	42.1
R-phase poly-C ₆₀	17.3	27.1	70.6	50.6

highest among all three polymers. This relationship between the cross-linking pattern and the reactivity towards fluorination is consistent with the tendency of fluorine uptake amounts among the three polymers observed in our experiment, i.e. O-phase polymer, with 4 carbon atoms per C_{60} cage forming cross-linking bonds with other C_{60} units, has the lowest fluorine uptake, and T-phase polymer, with 8 carbon atoms per C_{60} cage forming cross-linking bonds with other C_{60} s, has fluorine uptake amounts being somewhere between O- and R-phase polymers. It is a very interesting finding because it demonstrates the effects the covalent bonds between C_{60} cages within the polymers have on the chemical properties of the buckyballs.

Scanning electron microscope images of the polymer C_{60} phases were used as experimental verification of their crystalline structure assignments based on calculated XRD patterns⁶⁴. Our SEM observations of these polymers before fluorination were consistent with the previous work [Figure 6-1(a) and Figure 6-2(a)]. We could even capture the large symmetric crystallites under microscope that represent the lattice structure of the polymers, as shown in Figure 6-2(a). Some of the fluorinated polymers were also investigated with SEM in this work. Figure 6-1(b) shows the microscope image of the T-phase polymer fluorinated at 100 °C. Figure 6-2(b) and (c) show the images of R-phase polymer fluorinated at 150 °C. Based on the SEM images, addition of small amount of fluorine did not change the morphology of the crystalline polymers. As can be clearly seen from Figure 6-1(b), the typical crystalline pattern was maintained during fluorination. However, discontinuity in the long range crystalline structure was observed. The discontinuity as well as the hexagonal microcrystallites, observed in Figure 6-2(b) and (c), suggests the disintegration of larger crystallites caused by the repulsive

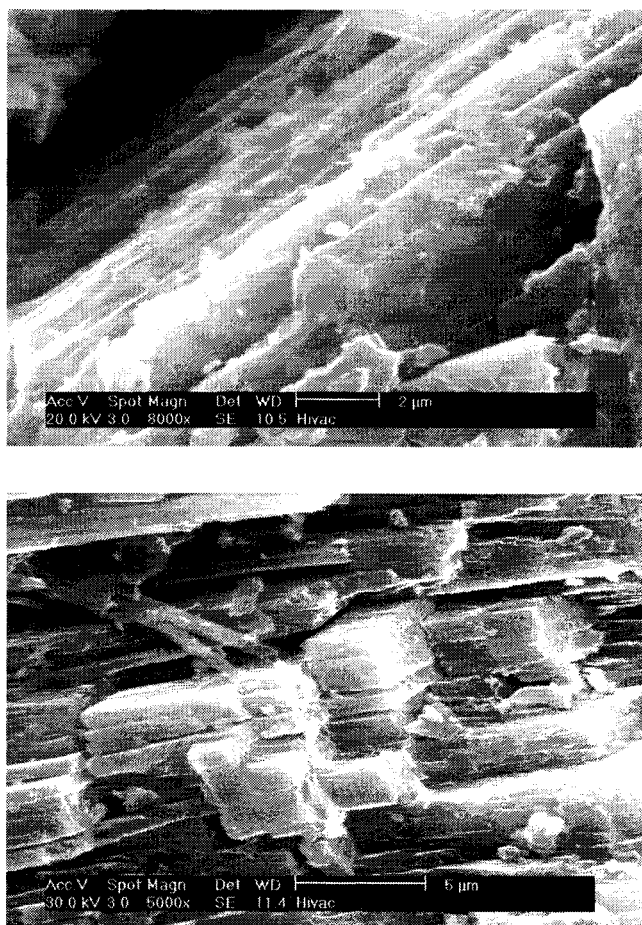


Figure 6-1 SEM images of the T phase polymeric C₆₀ (top) and after fluorination (bottom).

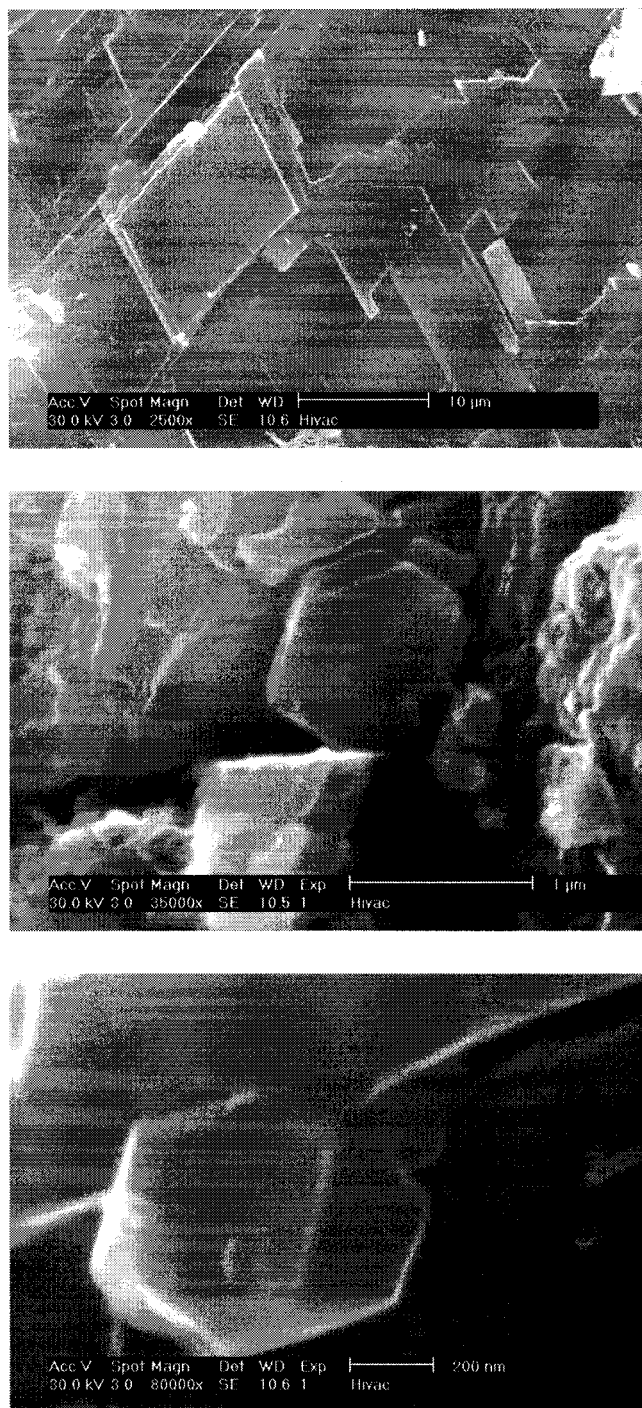


Figure 6-2 SEM images of the R phase polymeric C₆₀ (top) and after fluorination (middle and bottom).

interaction between fluorine atoms added along the edges of crystalline grains.

Infrared Spectra The IR spectra provide important information about the bonding between fluorine and carbon within the fluorinated polymers and the effects of such bonding on the molecular symmetry and therefore the vibrational spectra of the polymers. Also by comparing the IR spectra of the polymers fluorinated at increased temperatures, tendency of reactivity and chemical stability of the polymers could be found.

O-phase C₆₀ polymer. The IR spectrum of the pristine O-phase polymer [Figure 6-3(a)] is compared with published data ⁶⁴. In general, the IR modes are consistent with the published data with few exceptions. For example, the 576 cm⁻¹ F_{1u} mode splits into 571 and 576 cm⁻¹ bands. The IR-silent F_{1g}(2) mode at 965 cm⁻¹ was activated in our spectrum. The difference might be caused by the trace amount of impurities.

After fluorination at 100 °C for one hour, a broad and low-intensity C-F stretching mode showed up in the range of 1050 – 1200 cm⁻¹, centering around 1120 cm⁻¹ [Figure 6-3(b)]. Broad features are typical of fluorinated fullerene products with variable stoichiometry ^{114,115}. Differing from the fluorination of C₆₀ monomer, where besides C-F stretching mode there are other new modes shown in IR spectrum ¹¹⁴, the fluorination of O-polymer at 100 °C did not result in detectable new modes in IR spectrum except the C-F mode. Since the appearance of new modes is due to the activation of the silent modes by fluorination, it is reasonable to explain that the polymerization of C₆₀ monomer already activates those modes so that fluorination of these polymers will not bring up new features. As a result of fluorination, all modes belonging to the pristine polymer have broadened. The intensity of these modes apparently weakened, especially the ones above 900 cm⁻¹. Some split modes such as the ones at 531, 576, 717, 736 cm⁻¹ disappeared after

fluorination. Because the split modes in pristine polymers are due to the symmetry breakdown, it is possible that various fluorination patterns on different C_{60} cages within the polymer evened out such splitting. Another notable effect is that most modes downshifted by 1 - 4 cm^{-1} , for example, the 543, 657, 710, 777, 1324 cm^{-1} modes downshifted by 2 cm^{-1} , the 923 mode downshifted by 3 cm^{-1} , and the 1422 cm^{-1} mode downshifted by 4 cm^{-1} . It is within our expectation that the formation of C-F bonds should weaken the C - C bond strength throughout the polymer.

Fluorination of O polymer at 150 °C for one hour brought up a broad, higher intensity C - F mode centering around 1150 cm^{-1} [Figure 6-3(c)]. It shifted about 30 cm^{-1} towards higher frequency compared with the one in Figure 6-3(b). It is an indication of the higher C - F bond strength in average. Also there is a very slight shoulder at ~1210 cm^{-1} observed on the band of the C - F mode in Figure 6-3(c). Its increase with fluorination temperature, as shown by the other spectra in Figure 6-3, suggests that it represents another type of C - F bonding pattern, which is more covalent in bonding nature. In the fingerprint range (400 - 900 cm^{-1}), the intensity of the features was further decreased, with the 668 cm^{-1} mode completely disappeared. It is apparently the result of more fluorine addition to the polymer because in this case the average atomic F/C ratio is three times higher than the polymer represented by the spectrum in Figure 6-3(a). However, the fact that features in this range are not broader than those in Figure 6-3(a), implied that the higher fluorine addition did not cause more randomness of fluorine distribution on the C_{60} cages.

The IR spectrum of O-polymer fluorinated at 200 °C [Figure 6-3(d)] is quite different from those shown in Figure 6-3(b) and (c) in several aspects. First, the C - F

stretching mode, which is still broad and centered around 1155 cm^{-1} , shows three fine structures at 1144 , 1164 and 1220 cm^{-1} , respectively. Such fine structures are typical indications of better defined fluorine addition patterns, i.e. fewer variably fluorinated components¹¹⁴. Second, in $400 - 900\text{ cm}^{-1}$ fingerprint range, instead of being broadened and non-split bands, all original features of pristine polymers appear to be almost as sharp as they are in Figure 6-3(a). These sharp peaks are overlapped by two broad features, one at $580 - 650\text{ cm}^{-1}$, the other at $700 - 800\text{ cm}^{-1}$. The spectrum is believed to characterize a mixture of the unchanged polymer and the highly fluorinated polymer. It is probably because that at $200\text{ }^{\circ}\text{C}$ the diffusion of fluorine into the crystalline polymer was greatly hindered due to the vigorous lattice vibration. As a result, the rate of fluorine addition on the surface of the polymer greatly exceeded that of the fluorine diffusion. Within the one hour reaction time a product with highly fluorinated surface layer and barely affected inner polymer was formed. There was similar observation in the fluorination of pure crystalline C_{60} ¹¹³, where because of the molecules being packed together so well that fluorine was unable to penetrate the fullerene lattice under mild reaction conditions, the outer layer of molecules became highly fluorinated before the inner ones were even touched.

When O polymer was fluorinated at $250\text{ }^{\circ}\text{C}$ for one hour, the C – F mode, which is now centered around 1160 cm^{-1} , shows more defined three peaks at 1146 , 1174 and 1215 cm^{-1} [Figure 6-3(e)]. According to the analysis given above, fewer differently fluorinated components were formed at $250\text{ }^{\circ}\text{C}$. This observation is consistent with the results of monomer C_{60} fluorination where high purity single isomer were only obtained at temperatures over $200\text{ }^{\circ}\text{C}$ ¹¹⁵. In contrast to the continuous broadening of the C – F mode

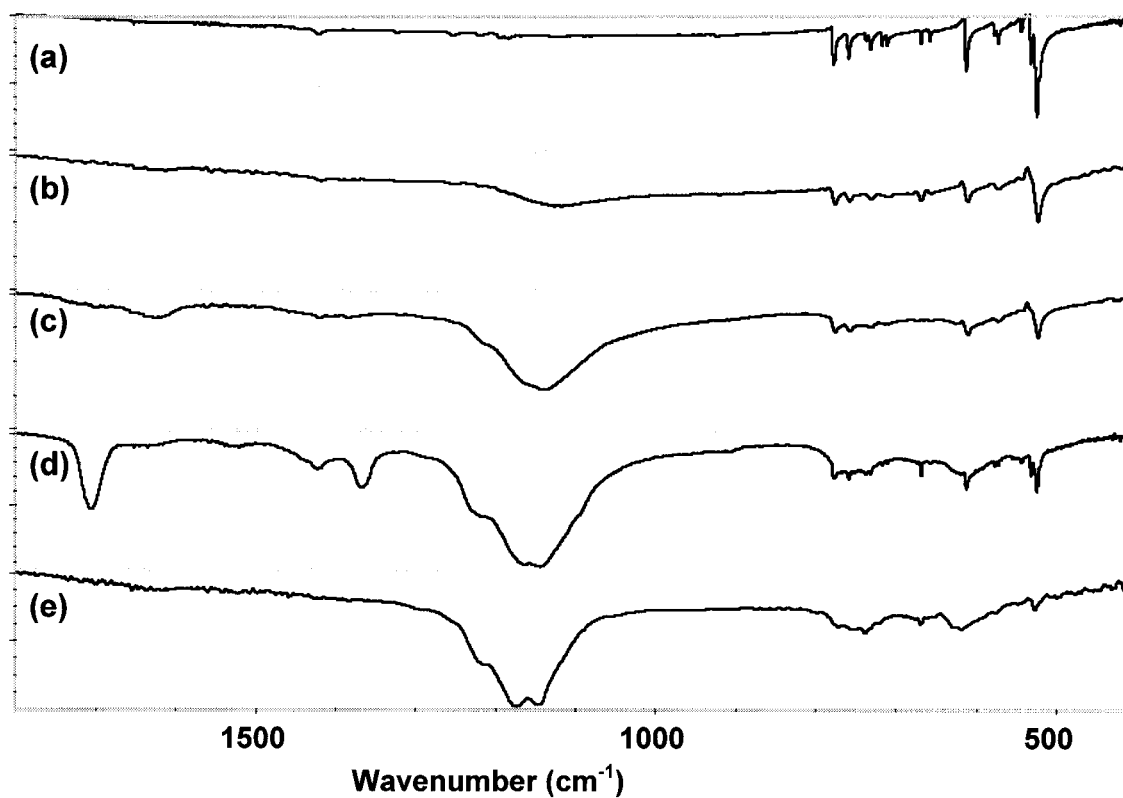


Figure 6-3 IR spectra of O phase polymer. (a) pristine; (b) fluorinated at 100 °C for one hour (twice the original intensity); (c) fluorinated at 150 °C for one hour (twice the original intensity); (d) fluorinated at 200 °C for one hour; (e) fluorinated at 250 °C for one hour (twice the original intensity).

with increasing temperature in previous spectra, the width of the C – F mode in current spectrum was $\sim 30 \text{ cm}^{-1}$ less than that in the above ones. EDAX results also indicated that the fluorine amount in this sample was $\sim 9\%$ less than that of the sample fluorinated at 200°C . Other features of the IR spectrum showed evidence that it actually belongs to a mixture of two phases: the fluorinated O-polymer and pure C_{60} . The existence of C_{60} was determined from its typical modes at 527 and 574 cm^{-1} , which were absent in products fluorinated at lower temperatures. X-ray diffraction analysis of the sample confirmed that it was the fcc crystalline C_{60} . Apparently the monomeric C_{60} resulted from the depolymerization of the polymer. However, it is unusual that thus formed C_{60} was not sufficiently fluorinated under the specific condition (i.e. at 250°C and in a fluorine atmosphere).

T-phase C_{60} polymer. Similar spectra analysis is carried out for the T-phase polymer. All expected odd modes⁶⁴ were shown in IR spectrum of the pristine T polymer [Figure 6-4(a)] except that the $\text{G}_u(3)$ doublet at 762 and 765 cm^{-1} was missing. Instead, a 759 cm^{-1} mode appeared with no definite assignment. Also, low intensity of this spectrum caused absence of some split modes. For example, the $\text{H}_u(3)$ doublet was shown as singlet at 641 cm^{-1} , the $\text{H}_u(4)$ triplet appeared as singlet at 932 cm^{-1} , and the $\text{F}_{2u}(5)$ doublet appeared as singlet at 1340 cm^{-1} in our spectrum.

Fluorination of T polymer at 100°C brought up the appearance of a shallow and broad band of the C – F stretching mode centering at about 1116 cm^{-1} in spectrum shown in Figure 6-4(b), very similar to that of O polymer. Other similar changes in this spectrum include intensity weakening and peaks downshifting of most IR modes. But no significant broadening of the peaks and no disappearing of the split modes were observed.

Considering that T polymer has 2D polymerization pattern, the number of possible fluorine attack sites on it are more limited than that on the 1D O-phase polymer. It explains the less effect the fluorine addition has on the existing IR modes.

Fluorination of T polymer at 150 °C shifted the center of the C – F mode to $\sim 1150\text{ cm}^{-1}$ [Figure 6-4(c)], which is a 35 cm^{-1} upward shift compared to the sample fluorinated at 100 °C. The low frequency mode at 483 cm^{-1} is also activated. Similarly, the band of the C – F mode shows very “shallow” shoulder on its high frequency side, implying a more covalent bond nature. The detectable broad feature between 710 and 780 cm^{-1} is indicative of the formation of new bonding structure due to the fluorine addition.

Fluorination of the T polymer at 200 °C caused another 10 cm^{-1} up-shift of the C – F mode. With the further weakening of the modes in the fingerprint region ($400 - 800\text{ cm}^{-1}$), two broad features appeared at $580 - 640\text{ cm}^{-1}$ and $720 - 780\text{ cm}^{-1}$, respectively. As we discussed in the O polymer section, the two features implied the formation of a highly fluorinated polymer-phase. Based on the IR spectrum alone, there is a much less intact polymer content in this sample, as compared with the O polymer, which is due to more covalent bonds formed between C_{60} cages in T polymer. The effect of temperature on the lattice vibration is much less than that in the case of O polymer. This could be a critical factor that determines a more sufficient diffusion of fluorine into the crystal lattices, and thus a more complete fluorination throughout the sample.

When the T polymer was fluorinated at 250 °C for an hour, in the IR spectrum the C – F mode became a very broad feature over 200 cm^{-1} in width and centered at about 1170 cm^{-1} with no improved fine structure. IR spectrum also showed apparent evidence of C_{60} formation, with the specific modes at 526 , 574 , and 1427 cm^{-1} . Besides that, the

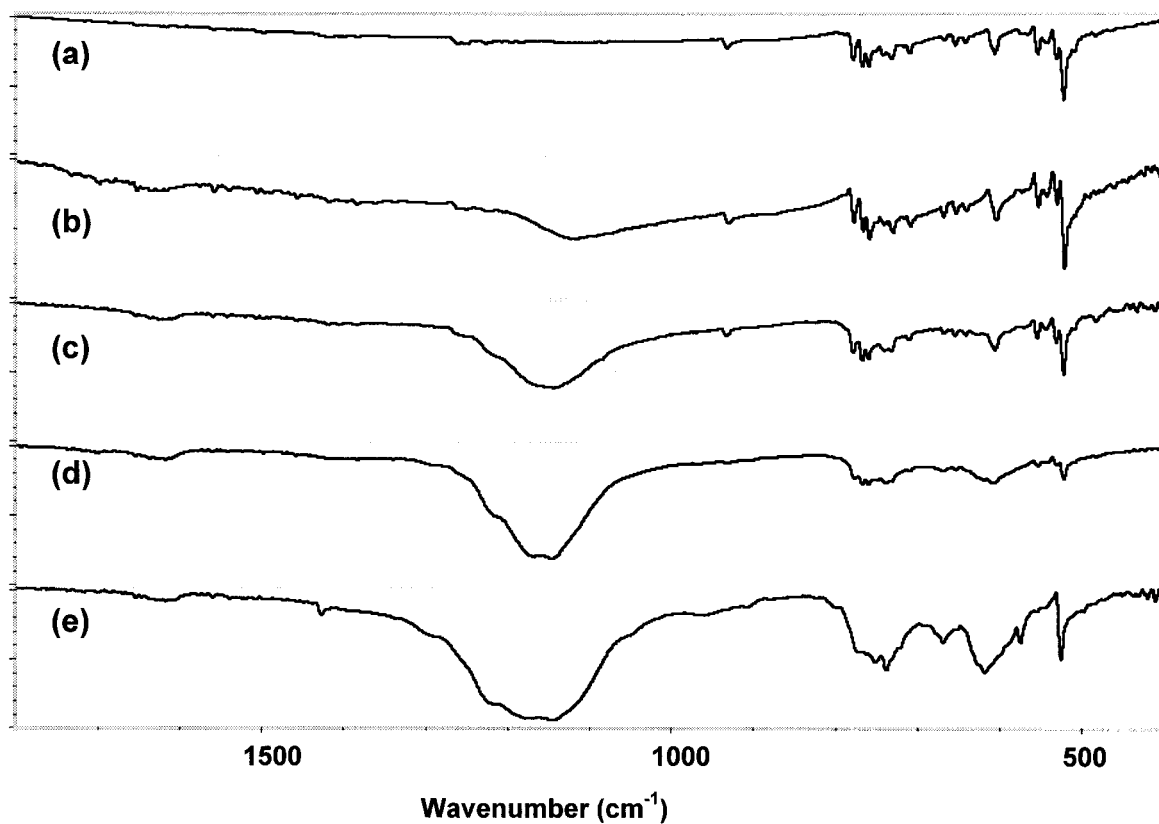


Figure 6-4 IR spectra of T phase polymer. (a) pristine; (b) fluorinated at 100 °C for one hour (four times the original intensity); (c) fluorinated at 150 °C for one hour; (d) fluorinated at 200 °C for one hour; (e) fluorinated at 250 °C for one hour.

broad features between $580 - 640\text{ cm}^{-1}$ and $710 - 790\text{ cm}^{-1}$ were enhanced.

R-phase C_{60} polymer. The IR of the pristine R polymer [Figure 6-5(a)] is in very good agreement with the published data. After fluorination at $100\text{ }^{\circ}\text{C}$ for one hour, broad and asymmetric feature of the C – F mode showed up between 1020 and 1200 cm^{-1} , with a steep edge at the low frequency end and an extended tail at the high frequency end, as shown in Figure 6-5(b). It indicates that the C – F bonds formed under these conditions are mostly semi-covalent. Another notable change is the activation of several IR-silent even modes: the $F_{2g}(1)$ mode at 534 cm^{-1} , which appeared as a fairly strong mode, the $F_{1g}(3)$ mode at 1495 cm^{-1} , the $F_{2g}(4)$ at 1524 cm^{-1} , and the $G_g(6)$ mode at 1619 cm^{-1} . All the pristine polymer modes experienced an intensity drop but remained well defined.

Fluorination of the R polymer at $150\text{ }^{\circ}\text{C}$ for an hour resulted in a broader C – F feature in the IR spectrum which extended from 1010 to $\sim 1230\text{ cm}^{-1}$, as shown in Figure 6-5(c). Compared with Figure 6-5(b), the broadening is mainly on the high frequency side, and the intensity of the C – F mode is increased. Apparently, at $150\text{ }^{\circ}\text{C}$, not only more C – F bonds were formed, but the bond strength enhanced. There is no further intensity decrease of all polymer fingerprint features observed. Instead, the intensities are higher than those in Figure 6-5(b). This seems inconsistent with the fact that the fluorine addition amount was found to be $\sim 10\%$ higher at $150\text{ }^{\circ}\text{C}$, unless at this temperature the fluorination is highly localized in a certain part of the sample and the other part are left intact. It is very possible that the competition between fluorine addition and fluorine diffusion caused such result.

The IR spectrum of the sample fluorinated at $200\text{ }^{\circ}\text{C}$ is quite simple, as shown in Figure 6-5(d). The C – F mode became more symmetric and its center shifted to about

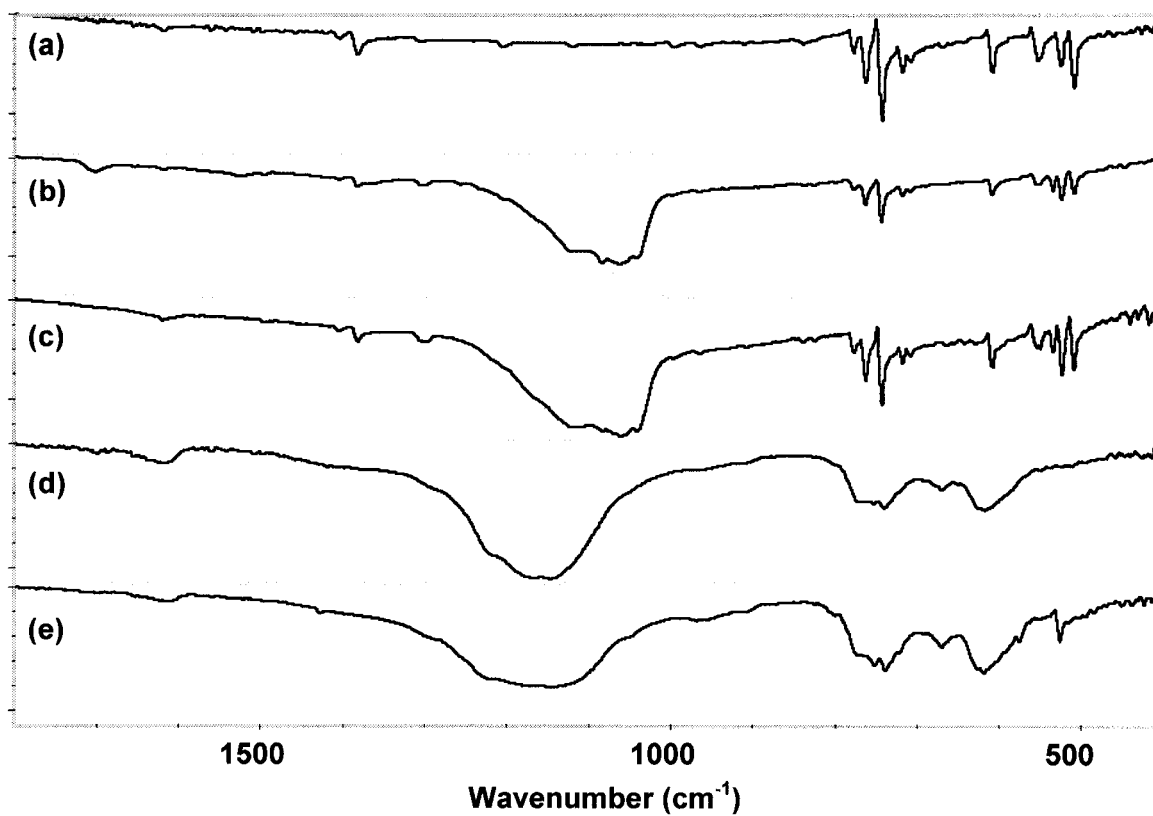


Figure 6-5 IR spectra of R phase polymer. (a) pristine (twice the original intensity); (b) fluorinated at 100 °C for one hour (twice the original intensity); (c) fluorinated at 150 °C for one hour (twice the original intensity); (d) fluorinated at 200 °C for one hour; (e) fluorinated at 250 °C for one hour.

1160 cm^{-1} . All fingerprint features of the pristine polymer are covered by three broad “humps” in 400 – 800 cm^{-1} range, centered at 617 cm^{-1} , 669 cm^{-1} and 755 cm^{-1} , respectively. The general features of the IR suggested a single phase product, which was consistent with the XRD result.

There is no shift of the C – F mode between the sample fluorinated at 250 °C [Figure 6-5(e)] and the one fluorinated at 200 °C, although the C – F peak was even broader, and the intensity lower. The latter is consistent with the elemental analysis results which show that the F/C ratio in this sample was lower than in the sample fluorinated at 200 °C. Also, similar to the fluorination of O and T polymer at 250 °C there are features of C_{60} found in the spectrum.

XRD According to the established structure parameters⁶⁴, the distances between the covalently bonded C_{60} cages in all three C_{60} polymers (9.0 – 9.2 Å) are much shorter than the cell parameter of fcc C_{60} (14.17 Å). The packing patterns of the buckyballs within various polymers apparently would influence the diffusion of fluorine into the crystalline structure and therefore affect the fluorine addition reaction. The detailed discussion of the XRD patterns of products formed at various temperatures is given below.

O-phase polymer. The XRD patterns of O-phase polymer and its fluorination products are shown in Figure 6-6. Fluorination at 100 °C does not change the XRD pattern much, as follows from comparing Figure 6-6 (a) and (b). We have already known from the elemental analysis that the average fluorine addition amount at this temperature is only ~10 fluorine atoms per C_{60} cage. The XRD result implies that most of the fluorine is only attached to the surface or interstitial space of the polymer, which will not change

the crystalline structure of the polymer. Starting from Figure 6-6 (c), new feature appeared at $2\theta = 9^\circ$. It has been reported ¹¹⁶ that all XRD patterns of fluorinated C_{60} ($C_{60}F_x$) have this feature. It was believed that the effective size of the fluorinated C_{60} molecules was essentially the same regardless of the number of fluorine atoms attached to them, as long as $x \geq 20$. However, it will not be true in the case of fluorinated C_{60} polymer, since due to the covalent bonding between the C_{60} cages, the number of sites available for fluorine addition without affecting the inter-cage bonding is limited. Beyond that limit, the polymers will either experience significant change of crystalline structure or depolymerize. In Figure 6-6 (c) there is a broad feature showing up between $2\theta = 14 - 17^\circ$. It narrowed into a new peak at $2\theta = 14.8^\circ$ in Figure 6-6 (d). Crystalline fluorinated C_{60} phases ¹¹⁷ also have a feature in this range. It implies the formation of new crystalline structure due to fluorine addition. The feature at $2\theta = 9^\circ$ is increased in intensity in Figure 6-6 (d), implying increased amount of fluorine addition. The XRD pattern in Figure 6-6 (e) is changed dramatically compared to other spectra in Fig 6-6: all pristine O-phase features have completely disappeared. Instead, a strong and sharp features of fcc C_{60} showed up, i.e. $2\theta = 10.88^\circ$ (very strong), $2\theta = 17.87^\circ$ (very strong), $2\theta = 20.95^\circ$ (very strong), $2\theta = 21.82^\circ$ (strong), $2\theta = 27.68^\circ$ (medium), $2\theta = 28.36^\circ$ (medium), $2\theta = 31.19^\circ$ (medium), and $2\theta = 33.15^\circ$ (medium). Also, the two features ($2\theta = 9^\circ$ and 15°) representing the fluorinated fullerene species are presented. It is noted that the feature at $2\theta = 9^\circ$ has decreased in intensity, which is consistent with the EDAX results which show that the fluorine amount is lower in this sample.

T-phase polymer. The XRD patterns of T-phase polymer and its fluorination products are shown in Figure 6-7. The variation of XRD patterns of T-phase polymer

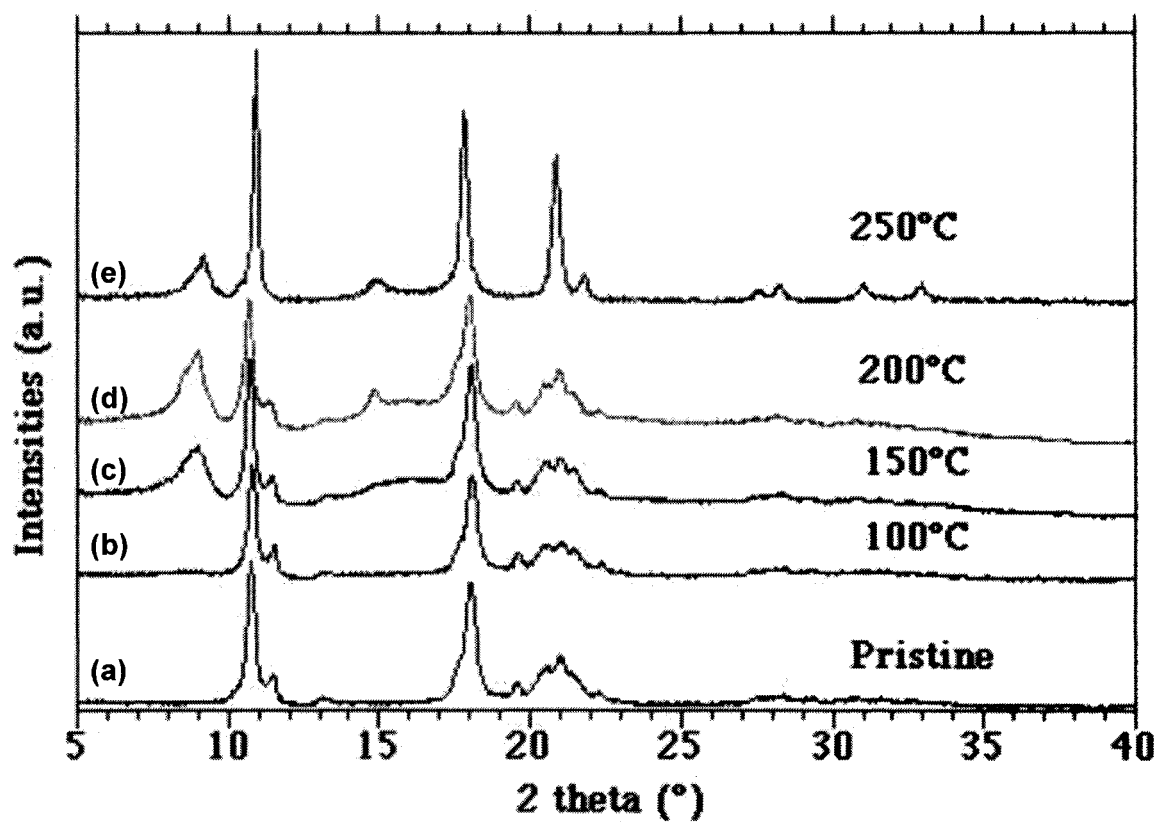


Figure 6-6 XRD patterns of O phase polymer with fluorination.

fluorinated at different temperatures shows very similar behavior as in case of O-phase. There is no detectable change when T-phase polymer was fluorinated at 100 °C [Figure 6-7(b) vs. Figure 6-7(a)]. The $2\theta = 9^\circ$ feature appeared when the sample was fluorinated at 150 °C (Figure 6-7 (c)). Its intensity is increased in Figure 7 (d) but decreased more in Figure 6-7 (e). Broad feature also showed up in the range of $2\theta = 14 - 17^\circ$ in Figure 6-7 (c) and developed into a narrow peak at $2\theta = 14.9^\circ$. When fluorinated at 250 °C, the XRD pattern also looks like one representing the mixture of fluorinated fullerenes and the unfluorinated fcc C₆₀.

R-phase polymer. The XRD patterns of O-phase polymer and its fluorination products are shown in Figure 6-8. Fluorination of R-phase polymer at 100 °C has already brought up the feature at $2\theta = 9^\circ$. With the highest fluorine uptake ratio among the three polymers at this temperature along with the fewer sites per C₆₀ cage available, the influence of fluorine addition to the crystalline structure is within expectation. Fluorination at 150 °C did not change the XRD pattern further, except the $2\theta = 9^\circ$ feature increases in intensity. However, the fluorination at 200 °C “wiped” out all features of the pristine R-phase polymer and produced the spectrum consisting of only a strong $2\theta = 9^\circ$ feature and two overlapped broad features at $2\theta = \sim 14.8^\circ$ and $2\theta = \sim 17.2^\circ$. Apparently, a new phase that is completely different from the pristine polymer has formed under these conditions. We believed that this is a highly fluorinated R polymer. According to EDAX, the formula of the fluorinated product corresponds to C₆₀F₄₂. Since R polymer only has 48 sites per C₆₀ cage available for fluorine addition, there is little chance of forming multiple isomers with formula C₆₀F₄₂. It could be the reason why only R polymer forms the single-phase fluorinated product. Figure 6-8 (e) shows that the fluorination of R

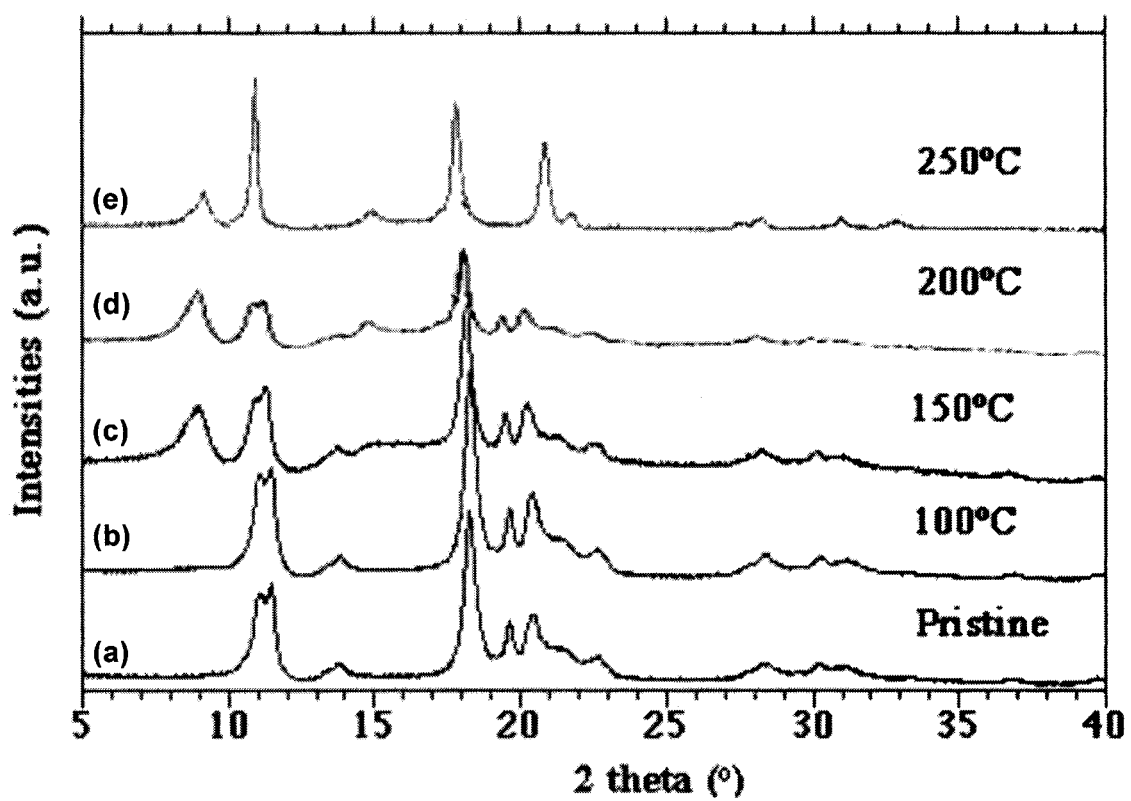


Figure 6-7 XRD patterns of T phase polymer with fluorination.

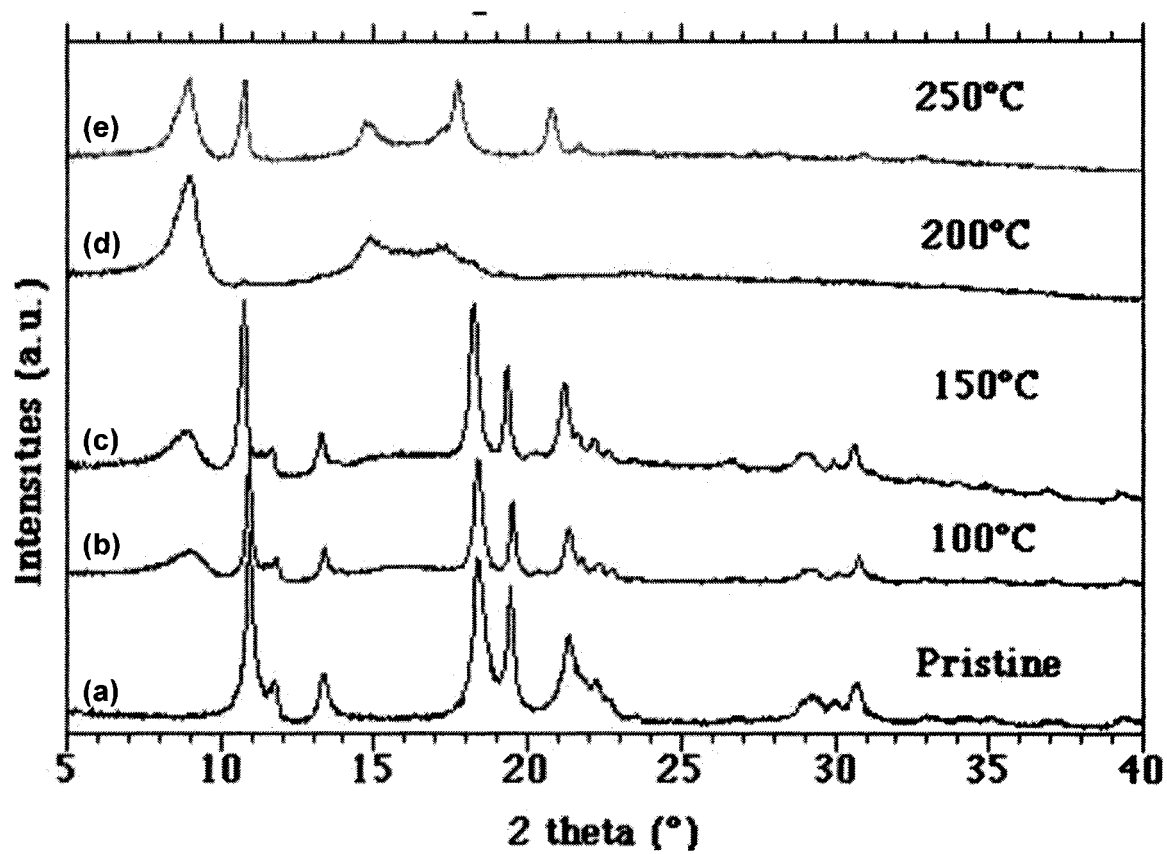


Figure 6-8 XRD patterns of R phase polymer with fluorination.

polymer at 250 °C also resulted in C₆₀. But according to the relative intensity, the content of the fluorinated species is higher in this sample than in the fluorinated O and T polymers.

IR and XRD results have confirmed that all three C₆₀ polymers decompose to monomeric C₆₀ at 250 °C in a fluorine atmosphere. But the fact that the thus formed C₆₀ monomers were not fluorinated under these conditions is somewhat unexpected. It has been reported that fcc C₆₀ gets fluorinated very slowly at temperatures lower than 300 °C¹¹³. Our observation in this work is that fluorination reaction rates of the C₆₀ polymers are significantly higher than that of the monomeric C₆₀. We interpret this as the result of reactive sites creation on the C₆₀ cages due to the covalent bonds formation between the C₆₀ molecules. It is reasonable that once the polymers decomposed into C₆₀ monomers, the reactive sites caused by the inter-cage bonding also disappear, therefore no notable fluorination would occur on the *fcc* C₆₀ within 1 hour.

UV-vis.-NIR C₆₀ has several strong typical absorption bands in the UV range, as shown in Figure 6-9¹¹⁸. When the spectrum was collected using *n*-hexane as solvent, the absorption bands were usually located at 195 nm, 211 nm, 227 nm (shoulder), 257 nm (main band), 328 nm, and 404 nm. The positions of absorption bands may vary with the solvent used. For example, when ODCB was used as solvent in our study [Figure 6-10(a)], the 329 nm band shifted to 334 nm, the 404 nm band shifted to 407 nm, etc. Inset of Figure 6-10(a) shows the interesting absorption features of C₆₀ in visible spectrum region (400 – 700 nm). These absorption bands are theoretically assigned as orbitally forbidden, but they can be partially activated by excitations of some symmetry suitable vibration modes¹¹⁸.

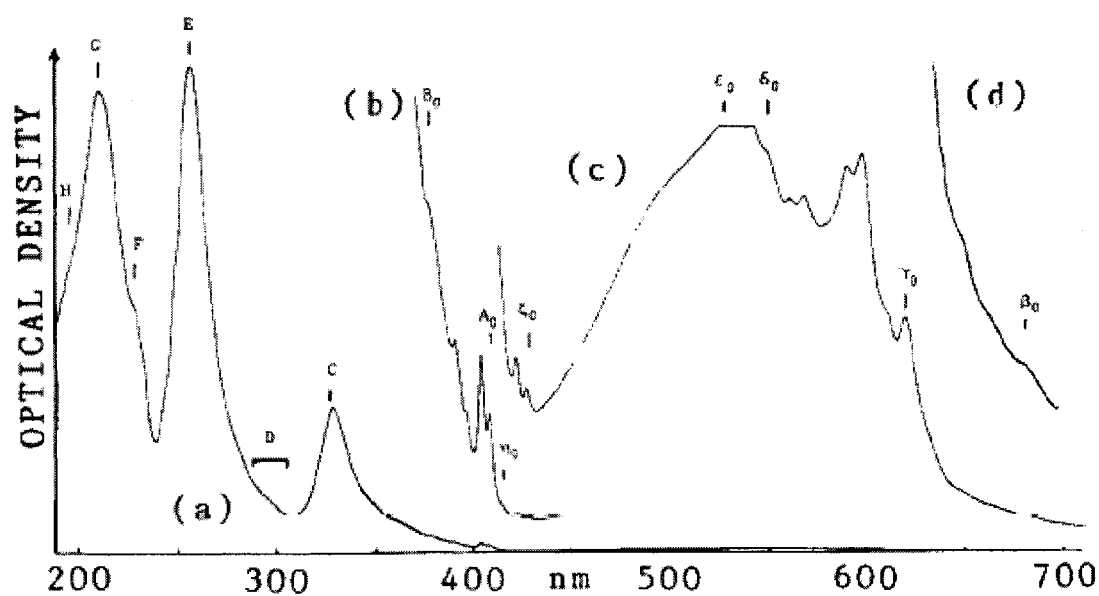


Figure 6-9 UV spectrum of C₆₀-n-hexane solution (adapted from Leach, S. et al *Chem. Phys.* **1992**, 160, 451).

The UV-vis.-NIR spectra from hexane suspensions of O, T, and R-phase-polymeric C_{60} are shown in Figure 6-10(b), (c) and (d), respectively. The spectrum regions between 200 – 420 nm of Figure 6-10(b) and (c) look similar to those in Figure 6-9, except that an additional feature in the shoulder range of the 258 nm band seem to appear in both Figure 6-10(b) and (c), which might belong specifically to the polymers. Also in the visible spectrum region the features were absent both in Figure 6-10(b) and (c). The optical absorption of R-phase polymer shown in Figure 6-10(d) is interesting. Besides the similar features to other two polymers and C_{60} in the region of 200 – 350 nm, the R-phase polymer had some continuous absorption from 350 nm to 1600 nm! The absorption in vis.-NIR region suggests that there are closely distributed energy levels in this sample. The covalent crosslinking between C_{60} cages in R-phase polymer might be the result of “communications” of π electrons among different C_{60} molecules over the polymer network, which could lower the energy gap between electron states. No similar low energy absorption was observed from the other two polymers. It might be because that the scale of polymerization in O and T-phase polymers is not as large as in the R-phase polymer.

The UV-vis. spectra from hexane suspensions of fluorinated C_{60} (stoichiometry $\sim C_{60}F_{44}$), O, T, and R-phase polymeric C_{60} were shown in Figure 6-11(a) - (d), respectively. The influence of fluorination on the electronic structure of C_{60} was extensively studied¹¹⁹, and it was found that the fluorination reduces the size of the π -conjugated system and also lowers the energy levels of π and π^* bands on the C_{60} . It was reflected on the optical absorption spectrum of fluorinated C_{60} by the vanishing of some distinct bands and red-shift of existing bands. Our observation in Figure 6-11(a)

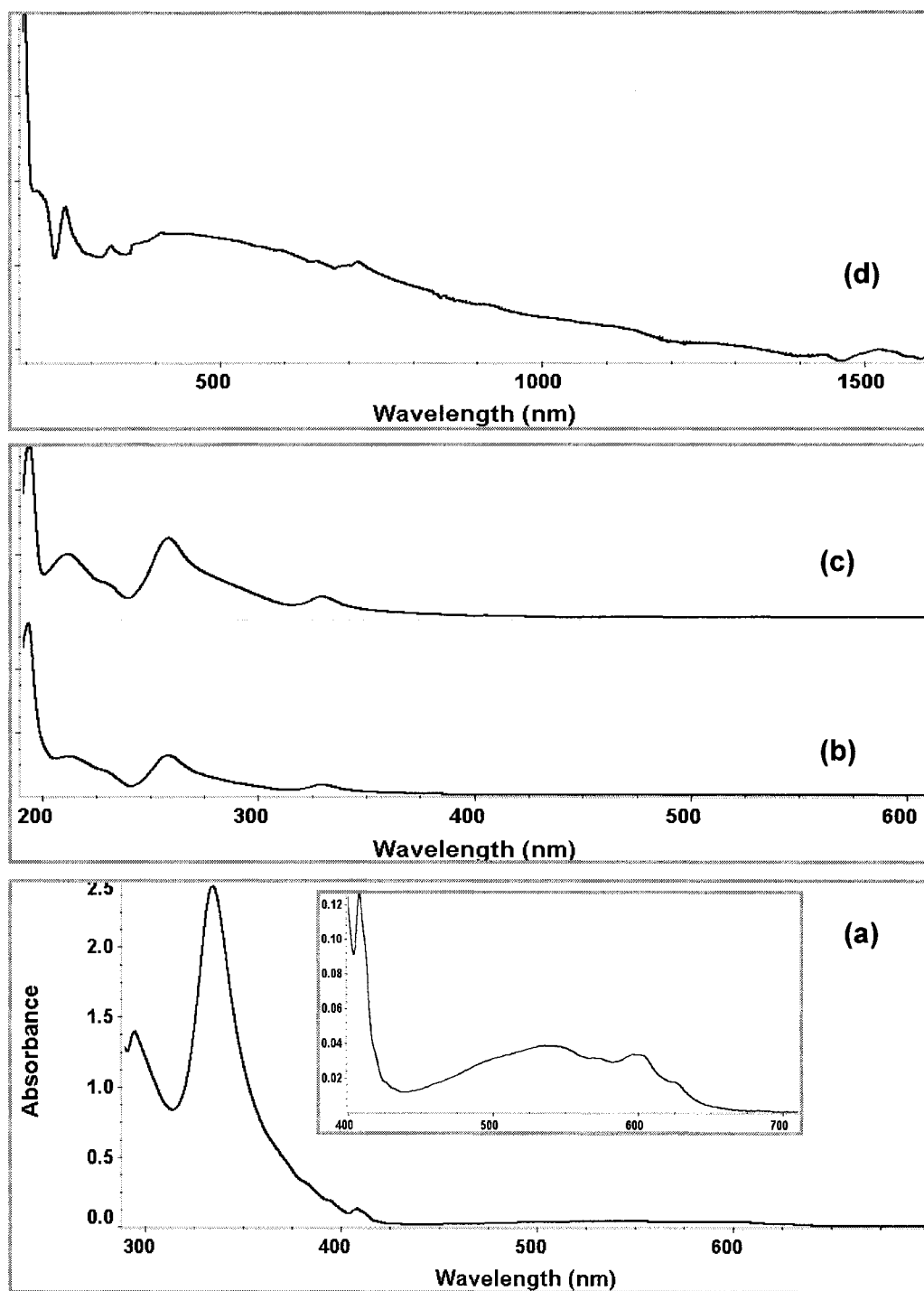


Figure 6-10 UV spectra of C_{60} -ODCB (a) and of polymeric $C_{60}S$ - *n*-hexane. (b) T phase; (c) R phase.

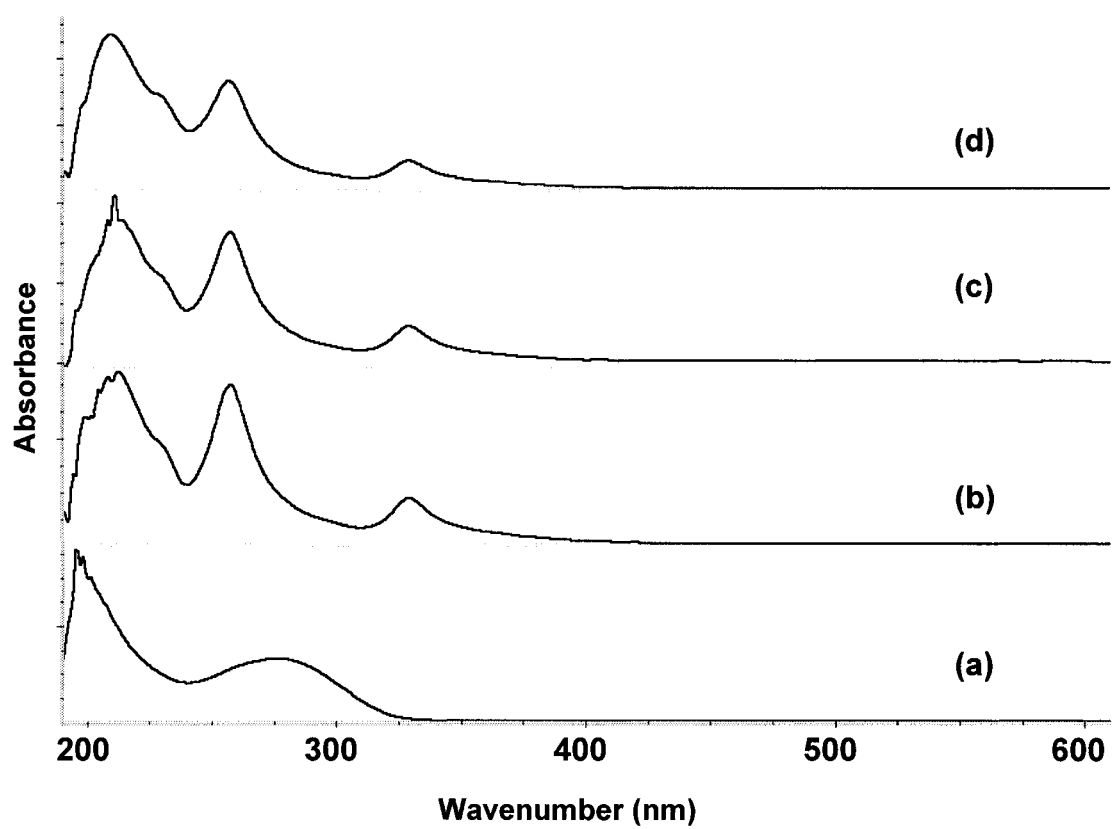


Figure 6-11 UV spectra of fluorinated C₆₀ (a) and polymeric C₆₀s in *n*-hexane. (b) O phase; (c) T phase; (d) R phase.

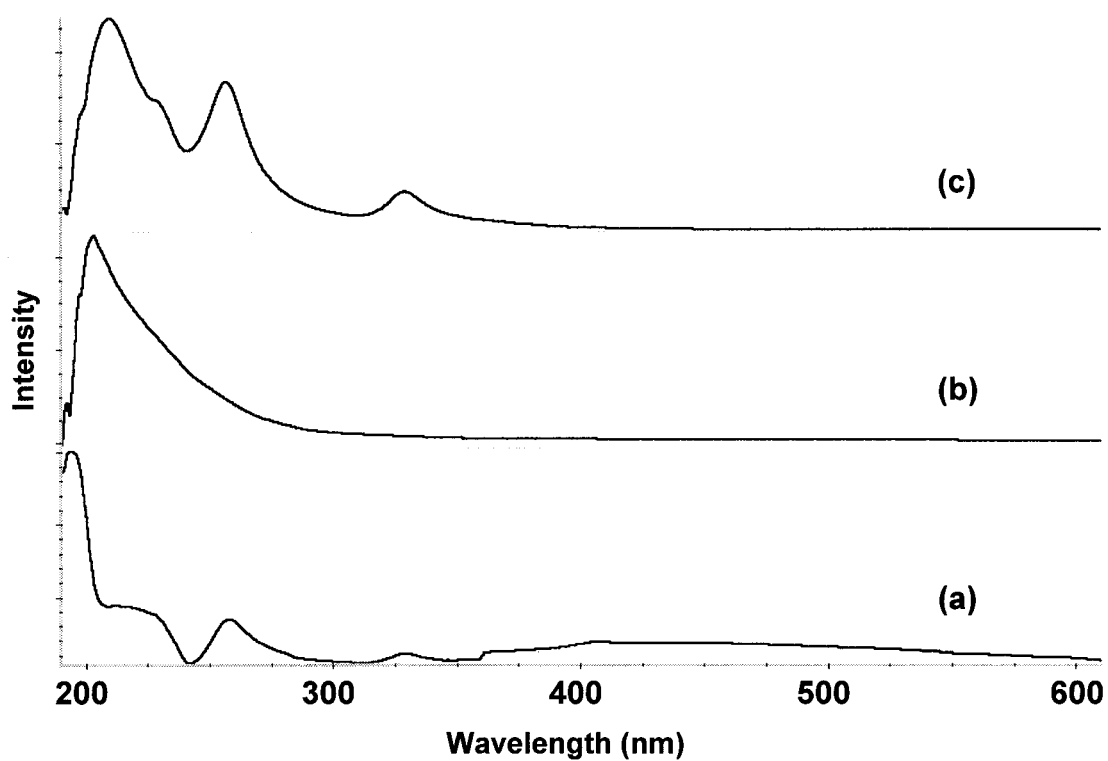


Figure 6-12 UV spectra of R phase C₆₀ polymer with various fluorination extents (in *n*-hexane). (a) pristine; (b) C₆₀F₄₂; (d) C₆₀F₃₀.

was consistent with the above analysis. The spectra of the fluorinated C₆₀ polymers did not change much as compared with that of the precursor polymers, except the disappearance of the high absorbing tails at ~194 nm, the increase of relative intensity of the broad bands at ~212 nm. It is probably caused by the isolation of the C = C bonds due to fluorination. The retaining of the bands at 257 and 329 nm might be attributed to the fact that the polymers were not evenly fluorinated, and there are still some π -conjugation areas on the samples.

When we compared the UV-vis. spectra of the R-phase polymers with various fluorine contents, as shown in Figure 6-12, it was found that when the polymer was heavily fluorinated, the spectrum became a continuous, featureless absorption band with only one distinct peak at ~205 nm. According to the above analysis, this might be because of small number of isolated C = C bonds left on C₆₀ cages. In the spectrum of the sample fluorinated at 250 °C, the features of monomer C₆₀ were clearly seen. It was consistent with our observations from the IR spectra.

The comparison of UV-vis. spectra of fluorinated O-phase polymeric C₆₀ suspended in different solvents were shown in Figure 6-13. The influence of solvent-sample interaction on the optical absorption properties of the C₆₀ polymers can be seen from the spectra. When hexane was used as solvent, the absorption band at ~329 nm was clearly seen. However, when IPA was used as solvent, the 329 nm band weakened significantly. We believe that this is because the interaction between the IPA molecules and C = C bonds on C₆₀ cages has localized the π -conjugation system, in other words, created isolated π bonds, which eliminate the absorption at ~329 nm. When ethylenediamine was used as solvent, apparently this effect was stronger, because the 329 nm absorption band

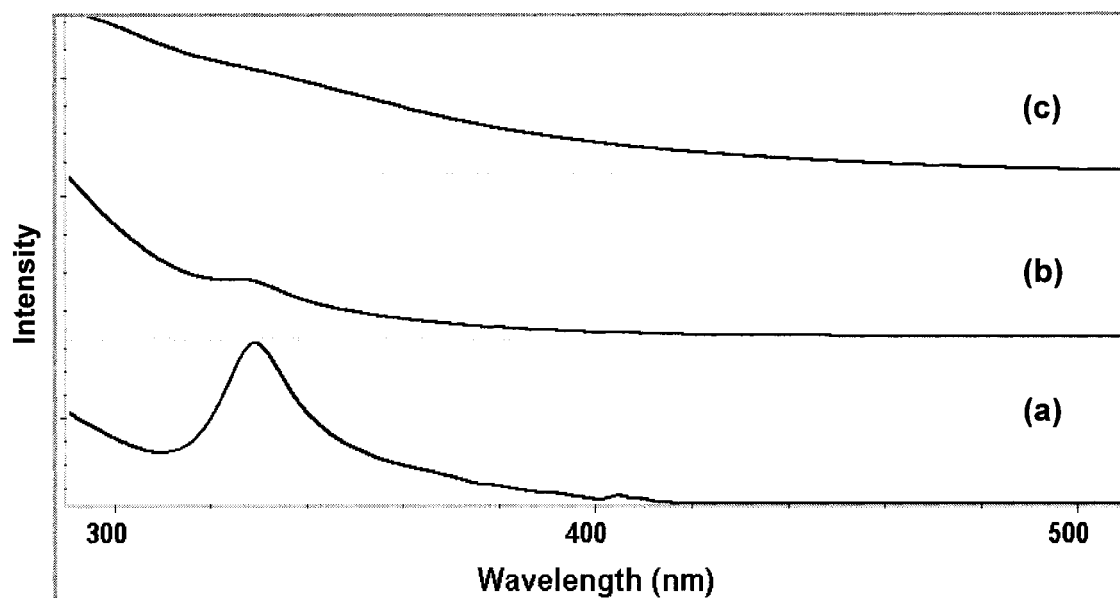


Figure 6-13 UV spectra of fluorinated R phase C_{60} polymer in various solvents. (a) in hexane; (b) in IPA; (c) in ethylenediamine.

has almost completely disappeared.

VTP-MS The thermal decomposition behavior of the polymeric C_{60} phases and their fluorinated derivatives in vacuum ($\sim 10^{-5}$ torr.) was investigated with VTP-MS. The thermal decomposition onset temperatures of these samples were listed in Table 6-2. It was found that R-phase polymer decomposed at lower temperature (~ 400 °C) than the other two polymers (~ 475 °C). Fluorinated O and T polymers started decomposing at temperatures over 100 degrees lower than those of their precursors. But the decomposition temperature of R-phase polymer didn't change much upon fluorination. The mass spectrum of the fluorinated R-phase polymer at ~ 600 °C was shown in Figure 6-14. Fragments such as fluorinated monomer C_{60} (m/z range: 1406 – 1558) and C_{60} (m/z: 720) can be seen. The signals in the m/z range of 1406 – 1558 formed an ordered pattern with an m/z interval of 38. It is the typical pattern seen in the mass spectra of fluorinated C_{60} , representing the desorption pattern of fluorine from C_{60} cages. The signals shown in the inset of Figure 6-14 corresponded to ions from $C_{60}F_{36}^{+}$ to $C_{60}F_{44}^{+}$, with $C_{60}F_{42}^{+}$ having the highest intensity. The mass spectrum confirmed that this specific sample was heavily fluorinated.

6.4 CONCLUSION

To conclude, we investigated the fluorination reaction of O, T, and R-phases of polymeric C_{60} at temperatures ranging from 50 to 250 °C. There were no signs of fluorination observed at 50 °C within one hour for all three polymers. The C_{60} polymers

Table 6-2 Thermal decomposition temperatures of C60 polymers and their fluorinated derivatives.

Polymer Type	Decomposition Temp. (°C)	Fluorinated Polymer	Decomposition Temp. (°C)
O phase	475	O phase	350
T phase	475	T phase	370
R phase	400	R phase	400

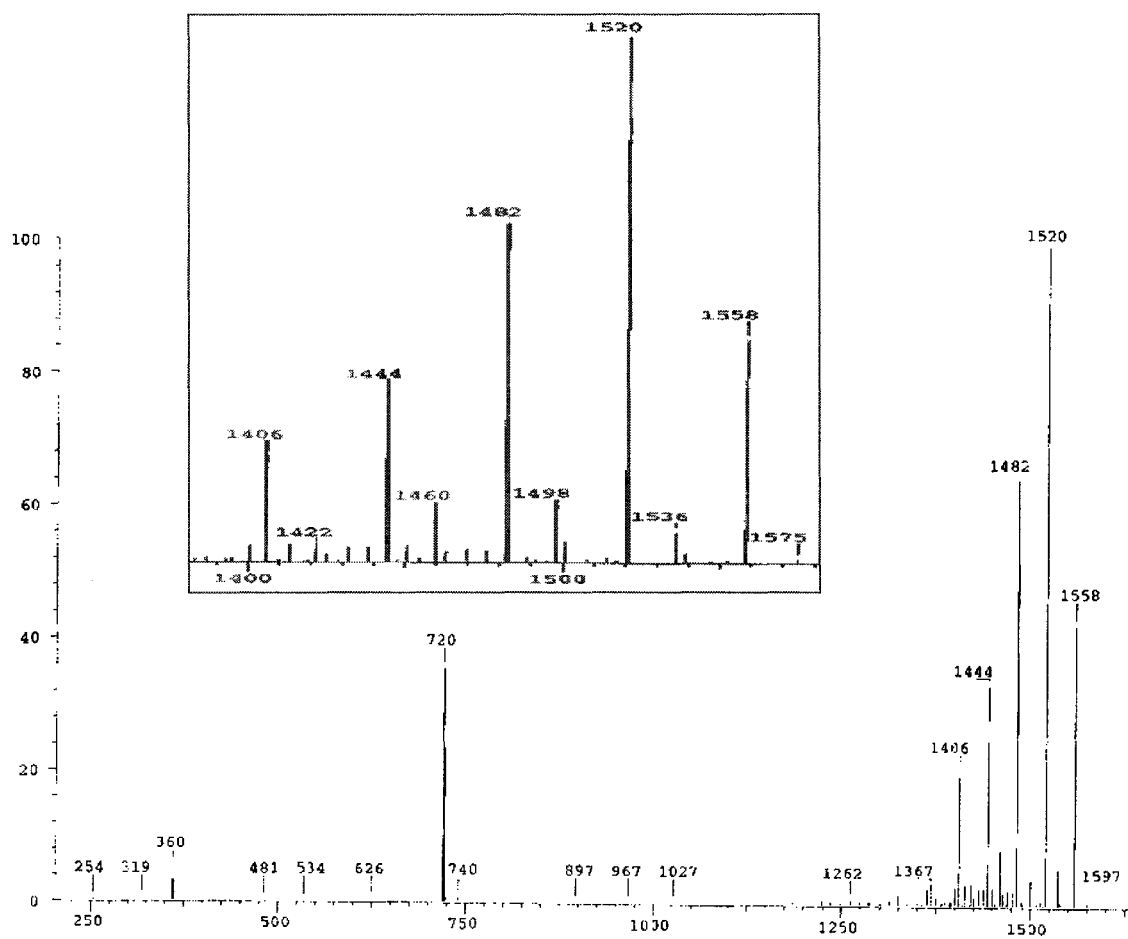


Figure 6-14 VTP-MS of fluorinated R phase C₆₀ polymer at 600 °C.

were found to be fluorinated at significantly higher rates than the C_{60} monomer between 100 and 200 °C. In this temperature range, the amount of fluorine addition increased with the temperature for all three polymers, and the R-phase polymer obtained the highest fluorine addition ratio among them. Also, stronger C – F bonds were formed in all polymers fluorinated at higher temperatures. There were no abrupt crystalline phase transitions due to the fluorination observed in most samples between 100 and 200 °C, except that the fluorination of R polymer at 200 °C seemed to create a pure single phase product with a completely different crystalline structure. At 250 °C all three polymers decomposed into monomeric C_{60} in a fluorine atmosphere and thus formed C_{60} monomers were not sufficiently fluorinated within one hour. The fluorinated polymers showed improved solubility in polar solvents such as alcohols and have strong interactions with nucleophiles such as ethylenediamine. Studies on the thermal decomposition of the polymers and their fluorinated derivatives indicates that R-phase polymer has the lowest thermal decomposition temperature among the three phases, and the fluorinated O and T-phase polymers decompose at lower temperatures than their precursor polymers. The VTP-MS pattern of the fluorinated R-phase polymer showed heavily fluorinated C_{60} fragments, confirming that the polymer was highly fluorinated.

References

- (1) Kroto, H. W.; Heath, J. R.; O'Brien, S. C.; Curl, R. F. and Smalley, R. E. *Nature* **1985**, 318, 162.
- (2) Diederich, F.; Ettl, R.; Rubun, Y.; Whetten, R. L.; Beck, R.; Alvarez, M.; Anz, S.; Sensharma, D.; Wudl, F.; Khemani, K. C. and Koch, A. *Science* **1991**, 252, 548.
- (3) Smalley, R. E. *Accounts of Chem. Res.* **1992**, 25, 98.
- (4) Lamb, L. D.; Huffman, D. R.; Workman, R. K.; Howells, S.; Chen, T.; Sarid, D. and Ziolo, R. F. *Science* **1992**, 255, 1413.
- (5) Ramesh, S.; Brinson, B.; Johnson, M. P.; Gu, Z.; Saini, R. K.; Willis, P.; Marriott, T.; Billups, W. E.; Margrave, J. L.; Hauge, R. H. and Smalley, R. E. *J. Phys. Chem. B* **2003**, 107, 1360.
- (6) Iijima, S. *Nature* **1991**, 354, 56.
- (7) Iijima, S. and Ichihashi, T. *Nature* **1993**, 363, 603.
- (8) Ugarte, D. *Nature* **1993**, 359, 707.
- (9) Ugarte, D. *Chem. Phys. Lett.* **1993**, 207, 473.
- (10) Iwasa, Y.; Arima, T.; Fleming, R. M.; Siegrist, T.; Zhou, O.; Haddon, R. C.; Rothberg, L. J.; Lyons, K. B.; Carter, H. L.; Hebard, A. F.; Tycko, R.; Dabbagh, G.; Krajevski, J. J.; Thomas, G. A. and Yagi, T. *Science* **1994**, 264, 1570.
- (11) Oszlanyi, G. and Forro, L. *Solid State Commun.* **1995**, 93, 265.
- (12) Xu, C. H. and Scuseria, G. E. *Phys. Rev. Lett.* **1995**, 74, 274.
- (13) Popov, M.; Kyotani, M.; Nemanich, J., R. and Koga, Y. *Phys. Rev. B* **2002**, 65, 033408.
- (14) Khabashesku, V. N.; Gu, Z.; Brinson, B.; Zimmerman, J. L.; Margrave, J. L.;

- Davydov, V. A.; Kashevarova, L. S. and Rakhmanina, A. V. *J. Phys. Chem. B* **2002**, *106*, 11155.
- (15) White, C. T. and Todorov, T. N. *Nature* **1998**, *393*, 240.
- (16) Bockrath, M.; Cobden, D. H.; Lu, J.; Rinzler, A. G.; Smalley, R. E.; Balents, L. and McEuen, P. L. *Nature* **1999**, *397*, 598.
- (17) Yakobson, B. I. and Smalley, R. E. *American Scientist* **1997**, *85*, 500.
- (18) Ajayan, P. M. *Chem. Rev.* **1999**, *99*, 1787.
- (19) Dresselhaus, M. S.; Dresselhaus, G. and Eklund, P. C. *Science of Fullerenes and Carbon Nanotubes*; Academic: San Diego, 1996.
- (20) Wildoer, J. W. G.; Venema, L. C.; Rinzler, A. G.; Smalley, R. E. and Dekker, C. *Nature* **1998**, *391*, 59.
- (21) Odom, T. W.; Huang, J. L.; Kim, P. and Lieber, C. M. *Nature* **1998**, *391*, 59.
- (22) Charlier, J. C.; Vita, A. D.; Blase, X. and Car, R. *Science* **1997**, *275*, 646.
- (23) Thess, A.; Lee, R.; Nikolaev, P.; Dai, H. J.; Petit, P.; Robert, J.; Xu, C. H.; Lee, Y. H.; Kim, S. G.; Rinzler, A. G.; Colbert, D. T.; Scuseria, G. E.; Tomanek, D.; Fischer, J. E. and Smalley, R. E. *Science* **1996**, *273*, 483.
- (24) Kiang, C. H. and Goddard, W. A. *Phys. Rev. Lett.* **1996**, *76*, 2515.
- (25) Saito, R.; Fujita, M.; Dresselhaus, G. and Dresselhaus, M. S. *Appl. Phys. Lett.* **1992**, *60*, 2204.
- (26) Blase, X.; Benedict, L. X.; Shirley, E. L. and Louie, S. G. *Phys. Rev. Lett.* **1994**, *72*, 1878.
- (27) Rochefort, A.; Salahub, D. S. and Avouris, P. *Chem. Phys. Lett.* **1998**, *297*, 45.
- (28) Kazumov, A. Y.; Deblock, R.; Kociak, M.; Reulet, B.; Bouchiat, H.; Khodos, I. I.;

- Gorbatov, Y. B.; Volkov, V. T.; Journet, C. and Burghard, M. *Science* **1999**, *284*, 1508.
- (29) Tans, S. J.; Verschueren, A. R. M. and Dekker, C. *Nature* **1998**, *393*, 49.
- (30) Cobden, D. H.; Bockrath, M.; McEuen, P. L.; Rinzler, A. G. and Smalley, R. E. *Physical Review Letters* **1998**, *81*, 681.
- (31) Mickelson, E. T.; Huffman, C. B.; Rinzler, A. G.; Smalley, R. E.; Hauge, R. H. and Margrave, J. L. *Chemical Physics Letters* **1998**, 296.
- (32) Chen, Y.; Haddon, R. C.; Fang, S.; Rao, A. M.; Eklund, P. C.; Lee, W. H.; Dickey, E. C.; Grulke, E. A.; Pendergrass, J. C.; Chavan, A.; Haley, B. E. and Smalley, R. E. *J. Mat. Res.* **1998**, *13*, 2423.
- (33) Boul, P. J.; Liu, J.; Mickelson, E. T.; Huffman, C. B.; Ericson, L. M.; Chiang, I. W.; Smith, K. A.; Colbert, D. T.; Hauge, R. H.; Margrave, J. L. and Smalley, R. E. *Chemical Physics Letters* **1999**, *310*, 367.
- (34) Bahr, J. L.; Yang, J.; Kosynkin, D. V.; Bronikowski, M. J.; Smalley, R. E. and Tour, J. M. *J. Am. Chem. Soc.* **2001**, *123*, 6536.
- (35) Baughman, R. H.; Zakhidov, A. A. and Heer, W. A. d. *Science* **2002**, *297*, 787.
- (36) Wong, S. S.; Joselevich, E.; Woolley, A. T.; Cheung, C. L. and C.M. Lieber *Nature* **1998**, *394*, 52.
- (37) Hafner, J. H.; Cheung, C. L. and Lieber, C. M. *Nature* **1999**, *398*, 761.
- (38) Choi, W. B.; Chung, D. S.; Kang, J. H.; Kim, H. Y.; Jin, Y. W.; Han, I. T.; Lee, Y. H.; Jung, J. E.; Lee, N. S.; Park, G. S. and Kim, J. M. *Appl. Phys. Lett.* **1999**, *75*, 20.
- (39) M.J. Biercuk and al., e. *Appl. Phys. Lett.* **2002**, *80*, 2767.

- (40) Collins, P. G.; Bradley, K.; Ishigami, M. and Zettl, A. *Science* **2000**, 287, 1801.
- (41) Kong, J. and al., e. *Science* **2000**, 287, 622.
- (42) Ajayan, P. M.; Stephan, O.; Redlich, P. and Colliex, C. *Nature* **1995**, 375, 564.
- (43) Guerret-Plecourt, C.; Le Bouar, Y.; Loiseau, A. and Pascard, H. *Nature* **1994**, 372, 761.
- (44) Fowler, P. W.; Cremona, J. E. and Steer, J. I. *Theor. Chim. Acta* **1988**, 73, 1.
- (45) Iijima, S. *J. Cryst. Growth* **1980**, 5, 675.
- (46) Ugarte, D. *Europhys. Lett.* **1993**, 22, 45.
- (47) Kroro, H. W. and McKay, K. *Nature* **1988**, 331, 328.
- (48) Scuseria, G. E. *Chem. Phys. Lett.* **1995**, 243, 193.
- (49) Pierson, H. O. *Handbook of Carbon, Graphite, Diamond and Fullerenes. Properties, Processing and Applications*; Noyes Publications: Park Ridge, NJ, 1993.
- (50) Edgar, J. H. *Properties of Group III Nitrides*; INSPEC, IEE Publ.: London, U. K., 1994.
- (51) Yildirim, T.; Gülseren, O.; Kilic, C. and Ciraci, S. *Phys. Rev. B* **2000**, 62, 12648.
- (52) Chernozatonskii, L. A. *Chem. Phys. Lett.* **1998**, 297, 257.
- (53) Wood, J. R.; Frogley, M. D.; Meurs, E. R.; Prins, A. D.; Peijs, T.; Dunstan, D. and Wagner, H. D. *J. Phys. Chem. B* **1999**, 103, 10388.
- (54) Venkateswaran, U. D.; Rao, A. M.; Richter, E.; Menon, M.; Rinzler, A.; Smalley, R. E. and Eklund, P. C. *Phys. Rev. B* **1999**, 59, 10928.
- (55) Chesnokov, S. A.; Nalimova, V. A.; Rinzler, A. G.; Smalley, R. E. and Fischer, J. E. *Phys. Rev. Lett.* **1999**, 82, 343.

- (56) Tang, J.; Qin, L.-C.; Sasaki, T.; Yudasaka, M.; Matsushita, A. and Iijima, S. *Phys. Rev. Lett.* **2000**, 85.
- (57) Sharma, S. M.; Karmakar, S.; Sikka, S. K.; Teredesai, P. V.; Sood, A. K.; Govindaraj, V. and Rao, C. N. R. *Phys. Rev. B* **2001**, 63, 205417.
- (58) Teredesai, P. V.; Sood, A. K.; Muthu, D. V. S.; Sen, R.; Govindaraj, V. and Rao, C. N. R. *Chem. Phys. Lett.* **2000**, 319, 296.
- (59) Nunez-Regueiro, M.; Marques, L.; Hodeau, J.-L.; Berthous, O. and Perroux, M. *Phys. Rev. Lett.* **1995**, 74, 278.
- (60) Davydov, V. A.; Kashevarova, L. S.; Rakhmanina, A. V.; Agafonov, V.; Ceolin, R. and Szwarc, H. *Carbon* **1997**, 35, 735.
- (61) Blank, V. D.; Popov, M.; Pivovarov, G. I.; Lvova, N. A.; Gogolinsky, K. and Reshetov, V. *Diamond Relat. Mater.* **1998**, 7, 427.
- (62) Marques, L.; Hodeau, J.-L.; Nunez-Regueiro, M. and Perroux, M. *Phys. Rev. B* **1996**, 54, R12633.
- (63) Davydov, V. A.; Agafonov, V.; Dzyabchenko, A. V.; Ceolin, R. and Szwarc, J. *Solid State Chem.* **1998**, 141, 164.
- (64) Davydov, V. A.; Kashevarova, L. S.; Rakhmanina, A. V.; Senyavin, V. M.; Ceolin, R.; Szwarc, H.; Allouchi, H. and Agafonov, V. *Phys. Rev. B* **2000**, 61, 11936.
- (65) Marques, L.; Hodeau, J.-L. and Nunez -Regueiro, M. *Molec. Mater.* **1996**, 8, 49.
- (66) Arvanitidis, J.; Meletov, K. P.; Papagelis, K.; Ves, S.; Kourouklis, G. A.; Soldatov, A. and Prassides, K. *J. Chem. Phys.* **2001**, 114, 9099.
- (67) Long, V. C.; Musfeldt, J. L.; Kamara's, K.; Adams, G. B.; Page, J. B.; Iwasa,

- Y.and Mayo, W. E. *Phys. Rev. B* **2000**, *61*, 13191.
- (68) Makarova, T. L.; Sundqvist, B.; Scharff, P.; Gaevski, M. E.; Olsson, E.; Davydov, V. A.; Rakhmanina, A. V.and Kashevarova, L. S. *Carbon* **2001**, *39*, 2203.
- (69) Makarova, T. L.; Sundqvist, B.; Höhne, R.; Esquinazi, P.; Kopelevich, Y.; Scharff, P.; Davydov, V. A.; Kashevarova, L. S.and Rakhmanina, A. V. *Nature* **2001**, *413*, 716.
- (70) Sundqvist, B. *Adv. Phys.* **1999**, *48*, 1.
- (71) Chernozatoskii, L. A.; Serebryanaya, N. R.and Mavrin, B. N. *Chem. Phys. Lett.* **2000**, *316*, 199.
- (72) Serebryanaya, N. R.and Chernozatoskii, L. A. *Solid State Commun.* **2000**, *114*, 537.
- (73) Tans, S. J.and al., e. *Nature* **1997**, *386*, 474.
- (74) Nikolaev, P.; Bronikowski, M. J.; Bradley, R. K.; Rohmund, F.; Colbert, D. T.; Smith, K. A.and Smalley, R. E. *Chem. Phys. Lett.* **1999**, *313*, 91.
- (75) Chiang, I. W.; Brinson, B. E.; Huang, A. Y.; Willis, P. A.; Bronikowski, M. J.; Margrave, J. L.; Smalley, R. E.and Hauge, R. H. *J. Phys. Chem. B* **2001**, *105*, 8297.
- (76) Zimmerman, J. L.; Bradley, R. K.; Huffman, C. B.; Hauge, R. H.and Margrave, J. L. *Chem. Mater.* **2000**, *12*, 1361.
- (77) Hirsch, A. *Angew. Chem. Int. Ed.* **2002**, *41*, 1853.
- (78) Mickelson, E. T.; Chiang, I. W.; Zimmerman, J. L.; Boul, P. J.; Lozano, J.; Liu, J.; Smalley, R. E.; Hauge, R. H.and Margrave, J. L. *J. Phys. Chem. B* **1999**, *103*, 4318.

- (79) O'Connell, M. J.; Boul, P.; Ericson, L. M.; Huffman, C.; Wang, Y. H.; Haroz, E.; Kuper, C.; Tour, J.; Ausman, K. D. and Smalley, R. E. *Chemical Physics Letters* **2001**, 342, 265.
- (80) Chen, R. J.; Zhang, Y.; Wang, D. and Dai, H. *J. Am. Chem. Soc.* **2001**, 123, 3838.
- (81) Saini, R. K.; Chiang, I. W.; Peng, H.; Smalley, R. E.; Billups, W. E.; Hauge, R. H. and Margrave, J. L. *J. Am. Chem. Soc.* **2003**, *in press*.
- (82) Kudin, K. N.; Bettinger, H. F. and Scuseria, G. E. *Phys. Rev. B.* **2001**, 63, 045413.
- (83) Bettinger, H. F.; Kudin, K. N. and Scuseria, G. E. *J. Am. Chem. Soc.* **2001**, 123, 12849.
- (84) Peng, H.; Gu, Z.; Liu, Y.; Chiang, I. W.; Smalley, R. E.; Hauge, R. H.; Khabashesku, V. N. and Margrave, J. L. *J. Nanosci. Nanotech.* **2003**, *in press*.
- (85) Mickelson, E. T. In *Chemistry*; Rice University: Houston, 1999.
- (86) Chiang, I. W. In *Chemistry*; Rice University: Houston, 2001, p 156.
- (87) Nakajima, T. *Fluorine-Carbon and Fluoride-Carbon Materials, Chemistry, Physics, and Applications.*; Marcel Dekker, Inc., 1995.
- (88) Journet, C.; Maser, W. K.; Bernier, P.; Loiseau, A.; Chapelle, M. L. d. l.; Lefrant, S.; Deniard, P.; Lee, R. S. and Fischer, J. E. *Nature* **1997**, 388, 756.
- (89) O'Connell, M. J.; M. Bachilo, S.; B. Huffman, C.; C. Moore, V.; S. Strano, M.; H. Haroz, E.; L. Rialon, K.; J. Boul, P.; H. Noon, W.; Kittrell, C.; Ma, J.; H. Hauge, R.; Weisman, R. B. and E. Smalley, R. *Science* **2002**, 297, 593.
- (90) Liu, Z.; Shen, Z.; Zhu, T.; Hou, S.; Ying, L.; Shi, Z. and Gu, Z. *Langmuir* **2000**, 16.
- (91) Brown, G.; Bailey, S. R.; Sloan, J. and Green, M. L. H. *Chem. Commun.* **2001**,

845.

- (92) Sloan, J.; Novotny, M. C.; Bailey, S. R. and Hutchison, J. L. *Chem. Phys. Lett.* **2000**, 329, 61.
- (93) Liu, J.; Rinzler, A. G.; Dai, H.; Hafner, J. H.; Bradley, R. K.; Boul, P. J.; Lu, A.; Iverson, T.; Shelimov, K.; Huffman, C. B.; Rodriguez-Macias, F.; Shon, Y.-S.; Lee, T. R.; Colbert, D. T. and Smalley, R. E. *Science* **1998**, 280, 1253.
- (94) Yudasaka, M.; Zhang, M.; Jabs, C. and Iijima, S. *Appl. Phys. A* **2000**, 71, 449.
- (95) Zhao, W.; Song, C.; Zheng, B.; Liu, J. and Viswanathan, T. *J. Phys. Chem. B* **2002**, 106, 293.
- (96) Kelly, K. F.; Chiang, I. W.; Mickelson, E. T.; Hauge, R. H.; Margrave, J. L.; Wang, X.; Scuseria, G. E.; Radloff, C. and Halas, N. J. *Chem. Phys. Lett.* **1999**, 313, 445.
- (97) Bachilo, S. M.; Strano, M. S.; Kittrell, C.; Hauge, R. H.; Smalley, R. E. and Weisman, R. B. *Science* **2002**, 298, 2361.
- (98) McElvany, S. W.; Callahan, J. H.; Ross, M. M.; Lamb, L. D. and Huffman, D. R. *Science* **1993**, 260, 1632.
- (99) Chibante, L. P. F. and Heyman, D. *Geochemica et Geophysica Acta* **1993**, 57, 1879.
- (100) Malhotra, R.; Kumar, S. and Satyam, A. *J. Chem. Soc. Chem. Commun.* **1994**, 1339.
- (101) Criegee, R. *Angew. Chem. Int. Ed. Engl.* **1975**, 14, 745.
- (102) Heymann, D.; Bachilo, S. M.; Weisman, R. B.; Cataldo, F.; Fokkens, R. H.; Nibbering, N. M. M.; Vis, R. D. and †, L. P. F. C. *J. Am. Chem. Soc.* **2000**, 122,

11473.

- (103) Weisman, R. B.; Heymann, D. and Bachilo, S. M. *J. Am. Chem. Soc.* **2001**, *123*, 9720.
- (104) Mawhinney, D. B.; Naumenko, V.; Kuznetsova, A.; John T. Yates, J.; Liu, J. and Smalley, R. E. *J. Am. Chem. Soc.* **2000**, *122*, 2383.
- (105) Cai, L.; Bahr, J. L.; Yao, Y. and Tour, J. M. *Chem. Mater.* **2002**, *14*, 4235.
- (106) Banerjee, S. and Wong, S. S. *J. Phys. Chem. B* **2002**, *106*, 12144.
- (107) Lu, X.; Zhang, L.; Xu, X.; Wang, N. and Zhang, Q. *J. Phys. Chem. B* **2002**, *106*, 2136.
- (108) Liu, J.; Rinzler, A. G.; Dai, H. J.; Hafner, J. H.; Bradley, R. K.; Boul, P. J.; Lu, A.; Iverson, T.; Shelimov, K.; Huffman, C. B.; Rodriguez-Macias, F.; Shon, Y. S.; Lee, T. R.; Colbert, D. T. and Smalley, R. E. *Science* **1998**, *280*, 1253.
- (109) Rinzler, A. G.; J. Liu; H. Dai; P. Nikolaev; Huffman, C. B.; F. J. Rodríguez-Macias; P. J. Boul; A. H. Lu; D. Heymann; Colbert, D. T.; R. S. Lee; Fischer, J. E.; A. M. Rao; Eklund, P. C. and Smalley, R. E. *Appl. Phys. A* **1998**, *67*, 29.
- (110) Kukovecz, A.; Kramberger, C.; Holzinger, M.; Kuzmany, H.; Schalko, J.; Mannsberger, M. and Hirsch, A. *J. Phys. Chem. B* **2002**, *106*, 6374.
- (111) Meilunas, R.; Chang, R. P. H.; Liu, S.; Jensen, M. and Kappes *J. Appl. Phys.* **1991**, *70*, 5128.
- (112) Wang, K. A.; Zhou, P.; Rao, A. M.; Eklund, P. C.; Jishi, R. A. and Dresselhaus, M. S. *Phys. Rev. B* **1993**, *48*, 3501.
- (113) Taylor, R.; Langley, G. J.; Holloway, J. H.; Hope, E. G.; Brisdon, A. K.; Kroto, H. W. and Walton, D. R. M. *J. Chem. Soc. Perkin Trans. 2* **1995**, 181.

- (114) Boltalina, O. V.; Sidorov, L. N.; Bagryantsev, V. F.; Seredenko, V. A.; Zapol'skii, A. S.; Street, J. M. and Taylor, R. *J. Chem. Soc. Perkin Trans. 2* **1996**, 2275.
- (115) Taylor, R. *Russian Chemical Bulletin* **1998**, 47, 823.
- (116) Okino, F.; Touhara, H.; Seki, K.; Mitsumoto, R.; Shigematsu, K. and Achiba, Y. *Fullerene Sci. & Tech.* **1993**, 1, 425.
- (117) Kawasaki, S.; Aketa, T.; Touhara, H.; Okino, F.; Boltalina, O. V.; Gol'dt, I. V.; Troyanov, S. I. and Taylor, R. *J. Phys. Chem. B* **1999**, 103, 1223.
- (118) Leach, S.; Vervloet, M.; Despres, A.; Breheret, E.; Hare, J. P.; Dennis, T. J.; Kroto, H. W.; Taylor, R. and Walton, D. R. M. *Chem. Phys.* **1992**, 160, 451.
- (119) Mitsumoto, R.; Araki, T.; Ito, E.; Ouchi, Y.; Seki, K.; Kikuchi, K.; Achiba, Y.; Kurosaki, H.; Sonoda, T.; Kobayashi, H.; Boltalina, O. V.; Pavlovich, V. K.; Sidorov, L. N.; Hattori, Y.; Liu, N.; Yajima, S.; Kawasaki, S.; Okino, F. and Touhara, H. *J. Phys. Chem. A* **1998**, 102, 552.